

https://dspace.org/

Metal hydroxide modified functionalized onion-like carbons for use in supercapacitors

Libale, Marvin Embodokah

2025-03

University of the Witwatersrand, Johannesburg

https://hdl.handle.net/10539/50306

Libale, Marvin Embodokah. (2025). Metal hydroxide modified functionalized onion-like carbons for use in supercapacitors. [Master's dissertation, University of the Witwatersrand, Johannesburg]. WIReDSpace. https://hdl.handle.net/10539/50306

Downloaded from a DSpace repository. https://dspace.org/

Metal hydroxide modified functionalized onion-like carbons for use in supercapacitors



UNIVERSITY OF THE
WITWATERSRAND,
JOHANNESBURG

Marvin Embodokah Libale (2534021)

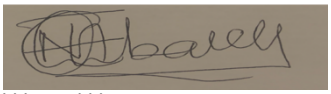
A research dissertation submitted to the Faculty of Science at the University of the Witwatersrand, Johannesburg, in partial fulfillment of the requirements for the Master of Science degree in Chemistry

Supervisors: Prof John Moma, Dr. Manoko Maubane-Nkadimeng and Prof Katlego Makgopa

Johannesburg, March 2025

Declaration

I declare that this thesis is my own, unaided work. It is being submitted for the Degree of Masters of dissertation in chemistry at the University of the Witwatersrand, Johannesburg. It has not been submitted before for any degree or examination at any other University.

Signature: … …  Date: ...19 August 2025…

Dedication

I dedicate this research work to Almighty God and my loving family for their endless support and inspiration.

"Success is not the work of one, but the strength of many. With faith and family, all things are possible."

Acknowledgements

I sincerely express my heartfelt gratitude to all those who supported me throughout my master's studies. Their encouragement, guidance, and belief in me were instrumental in my success.

I declare deep appreciation to the Almighty God for bestowing upon me wisdom and knowledge, forte, and guidance throughout my academic journey. His presence and grace provided me with hope and determination in moments of difficulty.

I extend my deepest appreciation to my supervisor, Prof John Moma, for his faith in me, his invaluable mentorship, and for providing me with the freedom to explore my research ideas. His guidance and encouragement played a crucial role in my academic growth.

I am also grateful to my co-supervisors, Dr. Manoko Maubane-Nkadimeng, Prof Katlego Makgopa, and Dr. Thapelo Mofokeng, for their patience, constructive feedback, insightful discussions, and expertise, all of which contributed significantly to my research.

I am thankful to my laboratory colleagues, Clinton and Bokome, for their assistance in material synthesis and analysis, as well as to the members of the CATMAT and Carbo Nano groups for their discussions and support.

Heartfelt appreciation goes to the team at the MMU and the Chemistry Department at the University of the Witwatersrand for their guidance and skill-building with electron microscopy, which greatly enhanced my research.

A heartfelt thank you to my family my parents Manoah and Dorothy Libale, my sister Cynthia Libale, and my wife Chania Wairimu for their unwavering love, financial and emotional support, and sacrifices. Their encouragement kept me motivated throughout this journey.

I also extend my gratitude to Dr. Aluha and Dr. Kennedy Otwombe for their support in integrating me into the university community and guiding me toward new opportunities.

Finally, my appreciation goes to my friends Sharon, Kabelo, Zongezile, Clementine, Mhlangabenzi, and Lesego for their friendship, emotional support, and shared experiences.

To all who have guided and enriched my academic pursuits, I am deeply grateful. Your support and kindness have left an everlasting impact on my life. Thank you.

Prizes and awards

1. Awarded the Penny Hurdle Memorial Award in 2023 for excellence as the best Teaching Assistant.
2. Awarded a certificate in 2023 for serving as a House Committee Member in International House.

Student supervision

1. Supervised one Honors student at the University of the Witwatersrand, Johannesburg South Africa.

Abstract

This presents an in-depth analysis of the fundamental properties and innovations in electrode materials for supercapacitor technology. The research examines the synthesis and investigation of several electrode materials for applications in supercapacitor stratagems, exploring their electrochemical characteristics and performance improvements. A methodical approach was used to synthesize and analyze these materials, aiding the evolution of high-performance energy storing devices. The flame pyrolysis process synthesized pristine onion-like carbons (P-OLCs). Oxidized onion-like carbons (Ox-OLCs) were subsequently synthesized by functionalization with hydrogen peroxide (H_2O_2). Further modifications resulted in synthesizing of nitrogen-doped onion-like carbons (N-OLCs) and (B-OLCs) B-doped onion-like carbons through the CVD technique, employing melamine and boric acid respectively as precursors.

A hydrothermal synthesis method was used to fabricate boron and nitrogen co-doped onion-like carbons (B, N-OLCs) utilizing ammonium pentaborate tetrahydrate ($NH_4B_5O_8.4H_2O$). Another variant, activated oxidized onion-like carbons (AcOx-OLCs), was synthesized by the CVD process utilizing potassium hydroxide (KOH) and Ox-OLCs, formulated explicitly as the anode electrode material. The synthesized N-OLCs, B-OLCs, B, N-OLCs, and AcOx-OLCs demonstrated increased surface area and elevated porosity relative to the pristine Ox-OLCs, resulting in enhanced electrochemical characteristics. These materials were used to fabricate composites by integrating alpha nickel hydroxide (α-Ni $(OH)_2$) to augment their electrochemical performance. Composites including N-OLCs/Ni $(OH)_2$, B-OLCs/Ni $(OH)_2$, B, N-OLCs/Ni $(OH)_2$, and Ox-OLCs/Ni $(OH)_2$ were fabricated using nickel (II) nitrate hexahydrate. The interaction between

doped carbon materials and alpha nickel hydroxide (α-Ni $(OH)_2$) markedly enhanced the electrochemical steadiness and electrical conductivity of the composites in comparison to the Ox-OLCs/Ni $(OH)_2$. The composite materials exhibited incomparable electrochemical performance, showcasing a high bidirectional specific capacitance, superior rate capability, and prolonged cycle stability.

Multiple analytical techniques comprehensively characterized the synthesized materials, including P-XRD, FE-SEM, Raman spectroscopy, TEM, BET surface area analysis, and XPS. These approaches provide comprehensive insights into the morphology, flaws, crystallinity, structural porosity, and elemental makeup. Furthermore, electrochemical characterization was performed via cycle stability analysis, EIS, CV, and GCD experiments in a 6M KOH aqueous electrolyte employing both two- and three-electrode configurations.

This study primarily examined the electrochemical characteristics of N-OLCs/Ni $(OH)_2$ in asymmetric capacitors. An asymmetric supercapacitor (ASC) device was fabricated, using N-OLCs/Ni $(OH)_2$ as the cathode and AcOx-OLCs as the anode. The ASC device, identified as N-OLCs//AcOx-OLCs, demonstrated a specific capacity of 20.38 mAh/g at a current density of 0.1 A/g, with a power density of 108.20 W/kg and an energy density of 18.34 Wh/kg at the same current density. At a current density of 2.00 A/g, the device exhibited a power density of 1856 W/kg and an energy density of 4.64 Wh/kg, indicating exceptional energy storage capabilities.

Conversely, the device AcOx-OLC//N-OLCs/Ni $(OH)_2$, operating within the voltage window 0.0–1.8 V, exhibited poor cyclic stability with only 22.45% capacity retention after 1000 charge–discharge cycles. The findings of this work demonstrate that N-OLCs/Ni $(OH)_2$ is an auspicious electrode material for supercapacitor applications. It's remarkable electrochemical performance, enhanced conductivity, and poor structural stability highlight its potential as a cathode material for asymmetric supercapacitors.This study enhances the advancement of sophisticated electrode materials, promoting the quest for high-performance energy storage solutions.

Table of Contents

Declaration ..... *ii*
Dedication ..... *iii*
Acknowledgements ..... *iv*
Prizes and awards ..... *vi*
Student supervision ..... *vi*
Abstract ..... *vii*
List of Tables ..... *xvii*
List of abbreviations ..... *xviii*
CHAPTER 1 ..... *1*
Introduction *1*
1.1. Background and motivation 1
1.2. Problem statement 7
1.3. Purpose of Research Project 8
1.3.1. Aims of the study 8
1.3.2. Objectives of this study 8
1.4. Outline of this study 9
1.5. References 11
Chapter 2 ..... *15*
Literature review *15*
2.1. Energy storage systems 15
2.2. Supercapacitors 19
2.2.1. Operational principle and storage methodology of supercapacitors 20
2.3. Mechanism of Supercapacitors Energy storage 23
2.3.1. Electric double-layer capacitance (EDLCs) 23
2.3.2. Pseudocapacitor 28
2.3.2.1. Surface - redox Pseudocapacitors 30
2.3.2.2. Intercalation Pseudocapacitors 32
2.3.2.3. Battery-type energy storage Faradaic reaction 33
2.3.2.4. Hybrid supercapacitors (HSCs) 35
2.3.2.5. Asymmetric supercapacitors 38
2.4. Distinguishing diffusion-governed processes from capacitive processes 41

2.5. Supercapacitor electrode materials 43
2.5.1. Carbon-based nano-structured materials 44
2.5.1.1. Activated carbon materials (ACs) 45
2.5.1.2. Graphene materials 48
2.5.1.3. Onion-like carbons (OLCs)/Carbon nano onions (CNOs) 50
2.5.1.3.1. Synthesis, functionalization, doping, and co-doping of onion-like carbons 54
2.5.1.4. Carbon nanotubes materials (CNTs) 58
2.5.2. Transition metal hydroxide and oxide-based materials 60
2.5.2.1. Ruthenium Oxide (RuO_2) 61
2.5.2.2. Manganese dioxide (MnO_2) 62
2.5.2.3. Nickel Oxide (NiO) 64
2.5.2.4. Nickel Hydroxide 65
2.5.3. Conducting polymers 67
2.5.4. Battery-type materials 68

2.6. Electrolytes for supercapacitors 69
2.6.1. Electrolyte features 70
2.6.1.1. Aqueous electrolyte 73
2.6.1.2. Organic electrolytes 76
2.6.1.3. Ionic liquid electrolytes 77

2.7. Designing, assessment, and analysis of supercapacitor systems and 78
2.7.1. Electrode designing for supercapacitors 78
2.7.2. Electrode analysis for supercapacitors 79

2.8. Electrochemical techniques 82
2.8.1. Cyclic voltammetry (CV) 82
2.8.2. Galvanostatic charge-discharge (GCD) 85
2.8.3. Electrochemical impedance spectroscopy (EIS) 87
2.8.4. An overview of the literature review 92

3.0. References 93

Chapter 3 118

Synthesis of Onion-like carbon by flame pyrolysis method, experimental methods and characterization techniques 118

3.0. Introduction 118

3.1. Reagents and materials 122

3.2. Flow diagram of synthesis and characterization of onion-like carbon 123

3.3. Synthesis methods used in the preparation of the samples 124
3.3.1. Synthesis of OLCs using flame pyrolysis 124
3.3.2. Functionalization of Pristine OLCs (P-OLCs) 125
3.3.3. Ex-situ nitrogen doping of Ox-OLCs 127
3.3.4. Boron doping 128
3.3.5. Boron and nitrogen co-doped Ox-OLCs preparation 129
3.3.6. Preparation of the OLCs/Ni $(OH)_2$ composites with the mass ratio of (1:4) 130
3.3.7. Preparation of activated carbon with the mass ratio of (1:3) 132

3.4. A concise summary of various characterization techniques 133

3.4.1. Scanning Electron Microscope (SEM) ... 133
3.4.2. Transmission Electron Microscope (TEM) ... 135
3.4.3. Raman Spectroscopy ... 138
3.4.4. X-ray diffraction (XRD) ... 140
3.4.5. X-ray photoelectron spectroscopy (XPS) ... 142
3.4.6. Brunauer – Emmet – Teller (BET) ... 145
3.4.7. Thermogravimetric analysis (TGA) ... 147

3.4. References ... **149**

Chapter 4 ... ***157***

Physicochemical and structural characterization of synthesized materials ... ***157***

4.1. Results and Discussion ... **157**
4.1.1. Scanning Electron Microscopy (SEM) imaging, Energy Dispersive Spectroscopy ... 157
(EDS) and elemental EDS mapping of pristine, oxidized, and doped onion-like ... 157
carbon. ... 157
4.1.2. TEM analysis and particle distribution graphs for onion-like carbon samples ... 163
4.1.3. BET surface area analysis ... 168
4.1.4. TGA and DTGA analysis of pristine, functionalized, and doped OLCs ... 172
4.1.5. XRD analysis ... 175
4.1.6. Raman Spectroscopy ... 181
4.1.7. X-ray Photoelectron Spectroscopy (XPS) ... 187

4.2. Synthesis technique of OLCs produced via flame pyrolysis ... **202**

4.3. Conclusion ... **203**

4.4. References ... **205**

Chapter 5 ... ***215***

Exploring the electrochemical performance of OLCs/Ni (OH)2 electrode materials for hybrid supercapacitor application ... ***215***

5.0. Introduction ... **215**

5.1. Development of enhanced Ox- OLCs/Ni $(OH)_2$, N- OLCs/Ni $(OH)_2$, B, N- ... **218**

OLCs/Ni $(OH)_2$, B-OLCs/Ni $(OH)_2$, and AcOx-OLCs electrode material ... **218**

used for three-electrode systems and two electrode systems ... **218**

5.2. Results and discussion. ... **221**
5.2.1. Cyclic voltammetry for a three-electrode system for Ox-OLCs/Ni $(OH)_2$, N- ... 221
5.2.2. Galvanostatic charge-discharge and specific capacitance of a three-electrode ... 225
5.2.3. Electrochemical impedance spectroscopy (EIS) for three-electrode system ... 229
5.2.4. Graphs of Trasatti and Dunn differentiation and the Randles-Sevcik plot ... 235

5.3. Cyclic voltammetry for two electrode system for N-OLCs/Ni $(OH)_2$ ... **238**
5.3.1. Galvanostatic charge-discharge, specific capacity, electrochemical impedance ... 241
spectroscopy, bode plots, cyclic performance plot ... 241
5.3.2. The Ragone Plot of N-OLCs/Ni $(OH)_2$ ... 248

5.4. Summary ... **251**

5.5. References **252**

Chapter 6 ..... *258*

Conclusions and recommendation *258*

6.1. Conclusions **258**

6.2. Future Works and Recommendations **259**

Appendix A *262*

Appendix B *264*

Appendix C *265*

List of Figures

FIGURE 2. 1: RAGONE MAP OF SEVERAL ENERGY STORAGE SYSTEMS[11] 18
FIGURE 2. 2: SCHEMATIC DIAGRAM OF (A) TRADITIONAL CAPACITOR (B) SUPERCAPACITOR[16][17]. 19
FIGURE 2. 3: HIERARCHY OF SUPERCAPACITORS COMPRISING THREE PRIMARY GROUPS, AND THEIR SUBCLASSES BASED ON POTENTIAL 22
FIGURE 2. 4: ELECTRIC DOUBLE-LAYER CAPACITOR WITH SIMPLE EQUIVALENT CIRCUIT[24] 24
FIGURE 2. 5: REPRESENTATIONS OF THE EDLC AT A POSITIVELY CHARGED INTERFACE (A) HELMHOLTZ MODEL (B) GOUY-CHAPMAN 25
FIGURE 2. 6: (A) SCHEMATIC DIAGRAM OF A PSEUDOCAPACITOR (B) EQUIVALENT CIRCUIT OF PSEUDOCAPACITOR[36][37] 30
FIGURE 2. 7: ENERGY STORAGE SYSTEMS AND THEIR ELECTROCHEMICAL CHARACTERISTICS: (A-C) EDLC, (D-F) SURFACE REDOX 32
FIGURE 2. 8: SCHEMATIC DIAGRAM OF A TYPICAL HYBRID SUPERCAPACITOR[56] 37
FIGURE 2. 9: ELECTROCHEMICAL MONOGRAMS FOR A HYBRID SUPERCAPACITOR[39] 38
FIGURE 2. 10: ELECTROCHEMICAL SIGNATURE OF A TYPICAL ASYMMETRIC SUPERCAPACITOR [39] 39
FIGURE 2. 11: SCHEMATIC DIAGRAM DEPICTING THE POROUS ARCHITECTURE OF ACTIVATED CARBONS[89] 47
FIGURE 2. 12: GRAPHENE CARBON ALLOTROPES 0D FULLERENE,1D CARBON NANOTUBES, AND 3D GRAPHITE 49
FIGURE 2. 13: SCHEMATIC ILLUSTRATION OF ONION-LIKE CARBON 53
FIGURE 2. 14: FLOW DIAGRAM SHOWING PRISTINE NI $(OH)_2$ PHASE SHIFTS DURING THE CHARGE-DISCHARGE PROCESS[179] 66
FIGURE 2. 15: FEATURES AFFECTING ELECTROLYTE CHARACTERISTICS[202] 71
FIGURE 2. 16: CATEGORIZATION OF ELECTROLYTES[202] 73
FIGURE 2. 17: SCHEMATIC DEPICTION OF A THREE-ELECTRODE AND TWO-ELECTRODES UTILIZING A BATTERY-TYPE SWAGELOK 81
FIGURE 2. 18: AN ILLUSTRATION OF CYCLIC VOLTAMMOGRAMS OF (A) IDEAL CAPACITOR (B) CAPACITOR WITH RESISTIVITY 84
FIGURE 2. 19: GCD GRAPH OF (A) EDLC DEPICTING IR DROP (B) REDOX PSEUDOCAPACITOR OR FARADAIC[4] 85
FIGURE 2. 20: PHASE CHANGE Φ IN THE CURRENT (I) DUE TO A SINUSOIDAL FLUCTUATION'S VOLTAGE (V) IN A PSEUDO-LINEAR 88
FIGURE 2. 21: NYQUIST PLOT WITH $R\Omega$ AND Rct [4] 90

FIGURE 3. 1: FLOW DIAGRAM OF THE SYNTHESIS PROCESS AND CHARACTERIZATION TECHNIQUES. 123
FIGURE 3. 2: THE SYNTHESIS OF OLCS USING THE FLAME PYROLYSIS TECHNIQUE. 124
FIGURE 3. 3: STEP BY STEP FLOW DIAGRAM OF P-OLCS FUNCTIONALIZATION 126
FIGURE 3. 4: SCHEMATIC DIAGRAM DEPICTING DOPING OF OX-OLCS WITH NITROGEN 127
FIGURE 3. 5: SCHEMATIC DIAGRAM DEPICTING DOPING OF OX-OLCS WITH BORON. 129

FIGURE 3. 6: SCHEMATIC DIAGRAM DEPICTING CO-DOPING OF OX-OLCS WITH BORON AND NITROGEN 130
FIGURE 3. 7: SCHEMATIC DIAGRAM DEPICTING DECORATION OF OX-OLCS, N-OLCS, B-OLCS AND B, N-OLCS. 131
FIGURE 3. 8: SCHEMATIC REPRESENTATION DEPICTING ACTIVE THEATION PROCESS OF OX-OLCS. 132
FIGURE 3. 9: (A) SCHEMATIC REPRESENTATION DEPICTING SCANNING ELECTRON MICROSCOPE (B) DEPICTS HOW A BEAM ACT ON 134
FIGURE 3. 10: SCHEMATIC REPRESENTATION DEPICTING TRANSMISSION ELECTRON MICROSCOPE[41] 136
FIGURE 3. 11: (A) SCHEMATIC REPRESENTATION OF RAMAN INSTRUMENT (B) SCHEMATIC DIAGRAM OF RAMAN PRINCIPLE[50][51]. 139
FIGURE 3. 12: (A) SCHEMATIC DIAGRAM OF X-RAY DIFFRACTION (B) SCHEMATIC REPRESENTATION OF BRAGG BONTENO 142
FIGURE 3. 13: (A) SCHEMATIC REPRESENTATION OF XPS PRINCIPLE (B) DEPICTION OF X-RAY PHOTOELECTRON 144
FIGURE 3. 14: (A) REPRESENTATION OF MONOLAYER FORMATION (B) DEPICTION OF BRUNAUER-EMMET-TELLER SURFACE AREA 146
FIGURE 3. 15: REPRESENTATION OF THERMOGRAVIMETRIC ANALYSIS INSTRUMENTS SET-UP[75] 148

FIGURE 4. 1: SEM IMAGES OF (A) P-OLCS (B) OX-OLCS (C) N-OLCS (D) B-OLCS (E) B, N-OLCS 158
FIGURE 4. 2: SEM IMAGES OF COMPOSITES AND ACTIVATED FUNCTIONALIZED ONION-LIKE CARBON (A) P-OLCS/NI $(OH)_2$ (B) OX-OLCS/NI 159
FIGURE 4. 3: EDS MAPPING AND ELEMENTAL EDS ANALYSIS FOR OX-OLCS/NI $(OH)_2$ (A) EDS MAPPING (B) ELEMENTAL EDS ANALYSIS 160
FIGURE 4. 4: (A) EDS MAPPED AREA OF N-OLCS/NI $(OH)_2$ (B) ELEMENTAL ANALYSIS FOR N-OLCS/NI $(OH)_2$ 160
FIGURE 4. 5: (A) EDS MAPPED AREA FOR ACOX-OLCS (B) EDS ELEMENTAL ANALYSIS FOR ACOX-OLCS 162
FIGURE 4. 6: (A) EDS MAPPED AREA FOR B, N-OLCS/NI $(OH)_2$ (B) ELEMENTAL ANALYSIS FOR B, N-OLCS/NI $(OH)_2$ 163
FIGURE 4. 7: TEM IMAGES FOR (A) P-OLCS (B) OX-OLCS (C) N-OLCS (D) B-OLCS (E) B, N-OLCS (F) P-OLCS/NI $(OH)_2$ (G) B- 166
FIGURE 4. 8: HISTOGRAMS PLOTS OF PARTICLE DISTRIBUTION FOR (A) P-OLCS (B) P-OLCS/NI $(OH)_2$ (C) OX-OLCS (D) N-OLCS 167
FIGURE 4. 9: HISTOGRAM PLOTS FOR (A) B, N-OLCS (B) B-OLCS (C) B-OLCS/ NI $(OH)_2$ 168
FIGURE 4. 10: N_2 ADSORPTION AND DESORPTION ISOTHERMS (A) COMPARISON OF DIFFERENT OLCS SAMPLES (B) COMPARISON OF DIFFERENT 171
FIGURE 4. 11: THERMOGRAVIMETRIC ANALYSIS GRAPH FOR OLCS (B) DIFFERENTIAL-THERMOGRAVIMETRIC GRAPH FOR OLC SAMPLES 172
FIGURE 4. 12: X-RAY DIFFRACTION (XRD) PATTERNS OF DIFFERENT OLCS SAMPLE (A) OLCS SAMPLES PRISTINE, FUNCTIONALIZED, DOPED AND 177
FIGURE 4. 13: RAMAN SPECTROSCOPY GRAPH OF DIFFERENT OLCS SAMPLES 183

FIGURE 4. 14 : COMPARISON OF EXPERIMENTAL XPS SPECTRA FOR O 1S, N 1S, C 1S, B 1S, NI2P, AND SURVEY DATA OF OX-OLCS, ... 190
FIGURE 4. 15 : X-RAY PHOTOELECTRON SPECTROSCOPY DATA FOR OX-OLCS (A), (B), (C) AND (D) DEPICTS DECONVOLUTED SPECTRA O1S, ... 191
FIGURE 4. 16 : X-RAY PHOTOELECTRON SPECTROSCOPY DATA FOR N-OLCS/NI $(OH)_2$ (A), (B), (C) DEPICT DECONVOLUTED SPECTRA O1S, ... 192
FIGURE 4. 17: X-RAY PHOTOELECTRON SPECTROSCOPY DATA FOR B-OLCS/NI $(OH)_2$, (A), (B), (C) AND (D) DEPICTS DECONVOLUTED SPECTRA 193
FIGURE 4. 18: X-RAY PHOTOELECTRON SPECTROSCOPY DATA FOR B, N-OLCS/NI $(OH)_2$, (A), (B), AND (C) DEPICTS DECONVOLUTED SPECTRA 194
FIGURE 4. 19: X-RAY PHOTOELECTRON SPECTROSCOPY DATA FOR (A) N-OLCS/NI $(OH)_2$ (B) B-OLCS/NI $(OH)_2$, AND (C) B, N-OLCS/NI 195
FIGURE 4. 20: X-RAY PHOTOELECTRON SPECTROSCOPY DATA FOR (A) N-OLCS/NI $(OH)_2$ (B) B-OLCS/NI $(OH)_2$ AND (C) B, N-OLCS/NI 196
FIGURE 4. 21: SCHEMATIC DIAGRAM OF THE MECHANISM OF SYNTHESIS OF ONION-LIKE CARBON BY FLAME PYROLYSIS[73] 203

FIGURE 5. 2: SCHEMATIC DIAGRAM FOR THREE-ELECTRODE SYSTEM [11] 219
FIGURE 5. 3: SCHEMATIC DIAGRAM FOR TWO ELECTRODE SYSTEM [11] 220
FIGURE 5. 4: CV GRAPHS FOR THREE-ELECTRODE SYSTEM (A) OX-OLCS/NI $(OH)_2$ (B) N-OLCS/NI $(OH)_2$ (C) B- OLCS/NI $(OH)_2$ 223
FIGURE 5. 5: (A) CV GRAPHS COMPARISON FOR THE THREE-ELECTRODE SYSTEM AT 1.0 MV/S (B) CV GRAPHS FOR ACOX-OLCS AT 224
FIGURE 5. 6: GCD GRAPHS FOR THE THREE-ELECTRODE SYSTEM AT DIFFERENT CURRENT DENSITIES (A) OX-OLCS/NI $(OH)_2$ 226
FIGURE 5. 7: (A) GCD GRAPHS COMPARISON FOR THREE-ELECTRODE SYSTEMS AT DIFFERENT CURRENT DENSITIES (B) GCD GRAPHS FOR 228
FIGURE 5. 8: EIS GRAPHS AND SERIES CIRCUITS FOR (A) OX-OLCS/NI $(OH)_2$ (B) N-OLCS/NI $(OH)_2$ (C) B-OLCS/NI $(OH)_2$ 231
FIGURE 5. 9: EIS GRAPHS AND SERIES CIRCUIT FOR (A) ACOX-OLCS (B) EIS COMPARISON GRAPHS 232
FIGURE 5. 10: EIS SERIES CIRCUITS FOR THREE-ELECTRODE SYSTEM (A) OX-OLCS/NI $(OH)_2$ (B) N-OLCS/NI $(OH)_2$ (C) B-OLCS/NI 232
FIGURE 5. 11: (A) RANDLES-SEVCIK PLOT FOR N-OLCS/NI $(OH)_2$ (B) TRASATTI AND DUNN DIFFERENTIATION METHOD FOR N-OLCS/NI 237
FIGURE 5. 12: (A) CV GRAPH COMBINATION OF THREE-ELECTRODE SYSTEM ACOX-OLCS AND TWO-ELECTRODE SYSTEM N-OLCS/NI 239
FIGURE 5. 13: (A) GCD GRAPHS FOR N-OLCS/NI $(OH)_2$ (B) SPECIFIC CAPACITY GRAPH FOR N-OLCS/NI $(OH)_2$ (C) NYQUIST PLOT 243
FIGURE 5. 14: BODE PLOTS COMPARISON OBTAINED BEFORE AND AFTER 6000 CYCLES FOR N-OLCS/NI $(OH)_2$ 244
FIGURE 5. 15: RAGONE PLOT FOR N-OLCS/NI $(OH)_2$ (ENERGY DENSITY VS POWER DENSITY) 249

FIGURE S 1: FOURIER TRANSFORMED INFRARED (FTIR) OF (A) WASTE ENGINE OIL, (B) ONION-LIKE CARBONS FOR (PRISTINE,..... 262
FIGURE S 2: TWO ELECTRODE CELL DATA FOR B, N-OLCS/NI (OH)2 (A) CV DATA (B) CV COMPARISON WITH THE ANODE ELECTRODE 264
FIGURE S 3: CAPACITY RETENTION PLOT FOR B, N-OLCS/NI $(OH)_2$ IN TWO ELECTRODE CELLS... 265

List of Tables

TABLE 3. 1: MATERIALS AND REAGENTS USED IN THIS RESEARCH..... 122

TABLE 4. 1: ATOMIC PERCENTAGE WEIGHTS OF DIFFERENT ATOMS IN OLCS MATERIALS 161
TABLE 4. 2: BET SURFACE AREA FOR PRISTINE, FUNCTIONALIZED, DOPED, CO-DOPED AND COMPOSITES OF OLCS 168
TABLE 4. 3 XRD DATA ANALYSIS FOR OLCS AND THE COMPOSITES OLCS/NI $(OH)_2$..... 178
TABLE 4. 4: REPRESENTATION OF RAMAN SPECTROSCOPY DATA FOR ONION-LIKE CARBON, DOPED, CO-DOPED AND..... 185
TABLE 4. 5: REPRESENTATION OF X-RAY PHOTOELECTRON SPECTROSCOPY DATA OF ONION-LIKE CARBON, ... 197

TABLE 5. 1: SPECIFIC CAPACITY AND CAPACITANCE OF DIFFERENT OLCS AT VARIOUS CURRENT DENSITIES. 229
TABLE 5. 2: EIS PARAMETERS OF DIFFERENT ELECTRODE MATERIALS 233
TABLE 5. 3: SPECIFIC CAPACITY AT DIFFERENT CURRENT DENSITIES FOR THE TWO-ELECTRODE DEVICE..... 244
TABLE 5. 4: EIS PARAMETERS FOR THE TWO-ELECTRODE MATERIAL 246
TABLE 5. 5: ENERGY DENSITY VS POWER DENSITY DATA AT DIFFERENT CURRENT DENSITIES..... 250

List of abbreviations

Symbols and units

θ:	Theta
ϕ:	Phase shift
α:	Alpha
β:	Beta
Ω:	Ohms
Π:	Pi
δ:	Sigma
λ	Wavelength
R_{ct}:	Charge-transfer resistance
R_{int}:	Interfacial resistance
R_s:	Solution resistance
Zω:	Warburg diffusion region
d_v/d_t:	Slope of the charge/discharge curve
°C:	Degrees Celsius
C_{diff}:	Capacitance of the diffusion region
C_{dl}:	EDLC capacitor
C_H:	Stern-type condensed model
C_{sp}:	Specific capacitance
C_T:	Total capacitance
F/g:	Farad per gram
k_1:	Capacitive contribution
k_2:	Faradaic contribution

α-Ni $(OH)_2$:	Alpha nickel hydroxide
β-Ni $(OH)_2$:	Beta nickel hydroxide
γ-NiOOH:	Gamma nickel oxyhydroxide
R_{ct}:	Charge transfer resistance
R_d:	Charge transfer loss
R_f:	Resistance of the electrode/electrolyte
R_s:	Equivalent series resistance
$V_o(V)$:	Amplitude of the voltage signal
$\omega(rad.s^{-1})$:	Angular frequency in radiants per second
$Z\|\omega\|$:	Impedance magnitude
ε:	Permittivity
ε_o:	Permittivity of free space
ε_r:	Relative permittivity

Δ

Δt:	Change in time
$\Delta V(V)$:	Voltage interval
$\Delta V(V)$:	Maximum voltage applied

A

A:	Surface area
Å:	Angstrom
AC:	Activated carbon, 30; Alternating current
ACFs:	Activated carbon fibers
ACN:	Acetonitrile
AcOx-OLCs:	Activated Oxidized onion-like carbons

Ag:	Silver
AgCl:	Silver chloride
Al:	Aluminium
Ar:	Argon gas
ASC:	Asymmetric supercapacitor
ASCs:	Asymmetric supercapacitors
Au:	Gold

B

B:	Boron
B, N-OLCs:	Boron and Nitrogen co-doped onion-like carbons
BET:	Brunauer-Emmett-Teller surface area analysis
BMIM-PF_6:	1-butyl-3-methylimidazolium hexafluorophosphate
B-OLCs:	B-doped onion-like carbons

C

C:	Carbon; Coulomb; specific capacitance
C^-:	Capacitance on negative electrode
C/g:	Specific charge
C^+:	Capacitance on positive electrode
C=O:	Carbonyl
$C_3H_6N_6$:	Melamine
CC:	Carbon cloth
CCVD:	Catalytic chemical vapor deposition
Cd:	Cadmium
CD:	Charge-discharge
cm:	Centimeter

CN-:	Cyanides
CNF:	Carbon nanofibers
CNOs:	Carbon nano-onions
CNTs:	Carbon nanotubes
Co:	Cobalt
Co $(OH)_2$:	Cobalt (II) hydroxide
Co_3O_4:	Cobalt (II, III) oxide
-COO:	Carboxylic functional group
-COOH:	Carboxyl
CPE:	Constant-phase element
CPs:	Conductive polymers
Cu:	Copper
Cu-Kα:	Copper potassium alpha radiations
CuO:	Copper (II) oxide
CV:	Cyclic voltammetry
CVD:	Chemical vapor deposition

D

d:	Distance; Spacing between diffracting planes
D:	Dimension
D-band:	Defect band
DL:	Double layer

E

e^-:	Electron
E:	Energy density
EASA:	Electrochemically active surface area

EC:	Ethylene carbonate
ECT:	Electrochemical charge transfer
EDL:	Electric double layer
EDS:	Energy dispersive spectroscopy
EEC:	Electric equivalent circuit
EEI:	Electrode-Electrolyte Interface
EFTEM:	Energy-filtering transmission electron microscopy
EIS:	Electrochemical impedance spectroscopy
EDLCs:	Electrochemical double-layer capacitors
ECs:	Electrochemical supercapacitors
EDLC:	Electrostatic double-layer capacitance
EMIM-PF_4:	1-ethyl-3-methylimidazolium tetrafluoroborate
EPR:	Electron Paramagnetic Resonance spectroscopy
ESPW:	Electrochemical stable potential window
ESR:	Equivalent series resistance
ESS:	Energy storage systems
eV:	Electron volt

F

f:	Frequency
F:	Farad; Faraday constant
Fe:	Iron
Fe_3O_4:	Iron (II, III) oxide
FEGs:	Field emission guns
FeOOH:	Iron (III) oxide-hydroxide
FE-SEM:	Field-emission scanning electron microscopy
FP:	Flame pyrolysis
FTIR:	Fourier Transform Infrared spectroscopy

FWHM:	Full Width at Half Maximum

G

g:	Grams
G-band:	Graphite band
GCD:	Galvanostatic charge-discharge
GDP:	Gross domestic product
GNRs:	Graphene nanoribbons
GPa:	Gigapascal
GQDs:	Graphene quantum dots

H

H^+:	Hydron
H_2O_2:	Hydrogen peroxide
H_2SO_4:	Sulfuric acid
H_3BO_3:	Boric acid
H_3PO_4:	Phosphoric acid
HECs:	Hybrid energy capacitors
Hg:	Mercury
HgO:	Mercury oxide
HNO_3:	Nitric acid
H-OLCs:	Hollow onion-like carbon
HSCs:	Hybrid supercapacitors
Hz:	Hertz

I

I:	Current; ionic stamina
I (A):	Applied Current density
ICPs:	Ionic conducting polymers
ICTAC:	International Confederation for Thermal Analysis and Calorimetry
I_D/I_G:	Ratio of defect and graphite
IEA:	International Energy Agency
ILs:	ionic liquids
IR:	Internal resistance
IrO_2:	Iridium (IV) oxide
IUPAC:	International Union of Pure and Applied Chemistry

J

JCPDS:	Joint Committee on Powder Diffraction Standards

K

K:	Potassium
K^+:	Potassium ion
KCL:	Potassium chloride
KOH:	Potassium hydroxide

L

LaB_6:	Lanthanum hexaboride
LDHs:	Layered double hydroxides
Li^+:	Lithium ion
Li_2SO_4:	Lithium sulphate
LIBs:	Lithium-ion batteries

LICs:	Lithium-ion capacitors
$LiPF_6$:	Lithium hexafluorophosphate
log f:	Logarithm of frequency

M

m:	Active mass
m^-:	Active mass on negative electrode
M:	Molar/Molarity
m^+:	Active mass on positive electrode
mAh/g:	Milliampere hour per gram
ml:	Millilitres
Mn:	Manganese
MnO_2:	Manganese (iv) Oxide
Mo:	Molybdenum
MoO_3:	Molybdenum trioxide
MWCNTs:	Multi-walled carbon nanotubes

N

N:	Nitrogen
N_2:	Nitrogen gas
Na^+:	Sodium ion
Na_2SO_4:	Sodium sulphate
$NaClO_4$:	Sodium perchlorate
NaOH:	Sodium hydroxide
Nb:	Niobium
Nb_2O_5:	Niobium pentoxide
$NH_4B_5O_8.4H_2O$:	Ammonium pentaborate tetrahydrate

Ni:	Nickel
$Ni(OH)_2$:	Nickel hydroxide
NICs:	Sodium-ion capacitors
NiO:	Nickel (II) Oxide
NiO_2:	Nickel (iv) Oxide
NiOOH:	Nickel oxyhydroxide
nm:	Nanometers
NMP:	N-methyl-2-pyrrolidone
NMR:	Nuclear Magnetic Resonance
NN*N:	Azide
N-OLCs:	Nitrogen-doped onion-like carbons

O

O:	Oxygen atom
O_2:	Oxygen
-OH:	Hydroxyl
OLCs:	Onion-like carbon
Ox-OLCs:	Oxidized onion-like carbons

P

P:	Power density
PA:	Polyacetylene
PANI:	Polyaniline
PC:	Propylene carbonate
Pd:	Palladium
PEDOT:	Polyethylene dioxythiophene
PF:	Polyfuran

pH:	Potential of Hydrogen
P-OLCs:	Pristine onion-like carbons
PPV:	Polyphenylene vinylene
PPy:	Polypyrrole
PTFE:	Polytetrafluoroethylene
PTh:	Polythiophene
PVDF:	Polyvinylidene flouride
P-XRD:	Powder X-ray diffraction, viii

Q

q:	Charge
q^-:	Charge on negative electrode
Q:	Charge density
q^+:	Charge on positive electrode

R

R:	Gas constant
Ru:	Ruthenium
Ru^{2+}:	Ruthenium ion
RuO_2:	Ruthenium (IV) oxide

S

s:	Seconds
SA:	Surface area
SC:	Supercapacitor
SCNMs:	Spherical carbon nano-structured materials

SCs:	Supercapacitors
Si:	Silicon
SIBs:	Sodium-ion batteries
S-OLCs:	Solid onion-like carbon
SSA:	Specific surface area
SWCNTs:	Single-walled carbon nanotubes

T

T:	Absolute temperature
$TEABF_4$:	Tetraethylammonium tetrafluoroborate
$TEAPF_6$:	Tetraethylammonium hexafluorophosphate
TEM:	Transmission electron microscopy
Ti:	Titanium
$TiO_2(B)$:	Polymorph of titanium dioxide
TM(OH)s:	Transition metal hydroxides
TMCs:	Transition metal compounds
TMOs:	Transition metal oxides

U

UPS:	Uninterruptible power systems
UV:	UltraViolet-Visible spectroscopy

V

v:	Scan rate
V:	Vanadium; Voltage
V^-:	Potential window on negative electrode

V/s:	Constant voltage rate of scanning
V^+:	Potential window on positive electrode
V_2O_5:	Vanadium Pentaoxide

W

W/kg:	Watts per Kilogram
Wh/kg:	Watts hour per kilogram

X

XPS:	X-ray photoelectron spectroscopy

Z

Z':	Real resistance
Z'':	Imaginary reactance
$ZnCl_2$:	Zinc chloride
$ZnSO_4$:	Zinc sulphate

CHAPTER 1

Introduction

1.1. Background and motivation

The global energy dilemma and pollution are some of the most significant issues that society is facing in the 21st century. Due to the mounting demand for energy and the perpetual burning of fossil fuels, many believe that the conventional perception of the production and use of power from fossil fuels is no longer feasible for sustainable development. The primary energy source most people use is electricity, which is spawned mainly by burning fossil fuels, for example, natural gas, coal, and petroleum, which are regarded as non-renewable energy sources. Since the rapid progression of the world's populace is causing quick resource depletion and increasing energy usage[1], the global energy crisis is a severe issue that requires immediate attention[2] because fossil fuels immensely contribute to the world's energy requirement[3].

Despite the varying estimates, the world still has over 1 trillion tons of coal, over a trillion drums of petroleum, and more than 150 trillion cubic meters of gas, besides more than 3 million tons of uranium reserves [4]. Over the past three decades, global oil consumption has augmented steadily, and in 2021, it was estimated that the world's oil consumption had risen by six percent from 2020 [5]. Notwithstanding the increase in oil consumption, reserves have also risen due to technological advancements that have occurred in the field of extraction and exploration. Besides, nuclear power

production has declined, possibly leading to the expansion of sustainable energy solutions[6]. Globally, the power generation industry is responsible for more environmental pollution than any other activity. Fossil fuels are also known to cause various ecological concerns, such as ocean pollution and the exoneration of greenhouse gases into the atmosphere [7].

Since fossil fuels are non-renewable, their supplies get depleted more rapidly than novel ones can be discovered, which presents a significant challenge for producing and storing renewable energy[1]. The predicament is expected to end the era of fossil fuels by 2030. The momentum of the clean energy movement has resulted in the global demand for coal, oil, and natural gas reaching a plateau. By then, the share of non-renewable fuels in global supply will drop to 73% from 80% by 2030. This represents a significant shift in the direction of fossil fuel consumption. However, if the current trends continue as they have in the past few years, it will be impossible to meet the global climate objectives [8].

The world needs an industrial revolution that will result in the accessibility of affordable and sustainable energy sources. Efficient energy use and decarbonization of sources are necessary to achieve this objective[9], and studies on alternative energy have increasingly become critical due to the importance of finding sustainable and affordable energy sources. One of the most essential factors to contemplate when choosing an alternative energy source is its environmental compatibility [10]. Different forms of renewable energy, including solar, geothermal, biomass, wind, and nuclear, can be utilized to address critical energy research issues. Researchers are exploiting the applications of these devices to improve their stability, processability, and efficiency[11][12].

The need for durable, long-lasting, and sustainable energy storage devices is increasingly becoming more prevalent. The increasing demands for energy and the environmental concerns surrounding it have created new obstacles that must overcome to achieve a sustainable and clean energy future [13]. Various factors currently hinder the development and production of renewable energy, including government policies, technological changes, and corporate influence. In addition to these, other factors, such as the lack of infrastructure and awareness, are also contributing to the slow growth of the industry[14]. In advancing renewable technologies, grid energy is a vital component as it ensures the distribution of renewable energy[15].

In South Africa, for example, countless areas have experienced electricity outages over the past two years, leaving many residents without power for up to 10 hours a day and 200 days in 2022 alone [16]. In 2021, the autonomous region of Austria became the first place in Europe to warn its residents about a potential blackout due to the lack of fuel supplies and the rising gas prices.

By 2025, it could be without power for several days. Switzerland's government is currently planning on utilizing renewable energy, such as hydroelectricity, but it might not need as much power as it used to. Like other countries preparing to implement renewable energy strategies, Spain was informed that it might experience power cuts for a few extra weeks[17]. This outage can harm different sectors, decreasing overall productivity [16].

Electrochemical energy production is considered an acceptable alternative power source if it is designed to be both eco-friendly and sustainable [18]. Using energy storage, we can now store the energy when available and provide a single household with electricity when needed. This technology has the potential to affect the way we live significantly. Energy storage is the crucial

component of an energy system that allows for efficient electricity production and sustainable transport. Using energy storage, electricity transmission, and dissemination can operate at total capacity, which can help decrease the need for new lines and improve plant efficiencies. For shorter periods, it can also help smooth out voltage sags and peaks in voltage[15][19].

Lithium batteries are commonly used in diverse applications owing to their small size and lightweight, with the ability to provide adequate power for multiple tasks. Unfortunately, people are used to handling these issues of their short cycle and shelf life. As a result of increasing power requirements in various applications, the demand for high-power batteries has increased. This has led to the development of pulse batteries, often accompanied by a sacrifice in cycle life and energy density, and supercapacitor development became the viable alternative to these types of batteries [20].

Ultracapacitors, also called supercapacitors, are high-capacity batteries with a capacitance value significantly higher than traditional solid-state capacitors but with decreased voltage limitations. Compared to rechargeable batteries, these supercapacitors can deliver faster charge rates and handle more discharge cycles [21]. An electrochemical capacitor utilizes a double layer composed of a solid interface and an electrolyte with negative and positive ionic charges at its surface. This allows the capacitor to store its electric energy [22].

Developing new materials is one of the most promising strategies for improving electrochemical supercapacitor (ES) electrode energy density and voltage. Most commonly, these materials involve carbon particles known for their high surface areas, which can be utilized for charge storage[23]. Three different kinds of electroactive materials can be used for supercapacitors. These include

EDLCs, which can retain energy by the charge accumulation at the boundary between the surface of conducting electrodes and electrolytes. Carbon or its derivatives are ideal for electrode materials with significantly higher electrostatic double-layered capacitances (EDLCs) for optimal energy storage[24].

Another type of EDLC is pseudocapacitors, designed to perform fast reversible redox reactions. "pseudo" refers to a device with behavior like a capacitor (e.g., RuO_2, NiO_2, MnO_2) [25]. These include electrodes with a linear dependence on the charge retained in their potential window. Compared to EDLCs, pseudocapacitors exhibit large capacitances, but their low conductivity makes them less effective in electron transmission[26]. Electrochemical pseudocapacitors utilize conducting polymers or metal oxides with high pseudocapacitance as electrode materials. This type of pseudocapacitance can be achieved through electrosorption, intercalation, or the transfer of electrons through a Faradaic charge transfer[27]. Another type of energy storage is the Faradaic reaction-based device, wherein the charge is strongly dependent on the electrode potentials. Hybrid capacitors, for example, those used for lithium-ion batteries, utilize electrodes with varying features. Typically exhibiting both electrochemical and electrostatic capacitance [28].

Carbon materials are used frequently in supercapacitors. These include fibers, composites, mats, foils, felts, powders, and mixtures[27]. An efficient supercapacitor requires materials with flexible pores and a high surface area to accommodate ions[23]. Due to their exceptional corrosion resistance, carbon materials are commonly utilized as electrode materials in supercapacitors designed for high energy density and specific capacitance. The main reason these materials are

broadly utilized in supercapacitors is their distinctive combination of chemical and physical properties. The other factors contributing to these materials' improved performance include their cost-effectiveness, stability, and ability to work well with composite materials[29].

Carbon nano-onions (CNOs) are nanoparticles typically less than 10 nanometers in size. They feature several disorganized and defective shells enclosed in a "Russian doll-like" manner. Their unique multilayer structure makes them an exciting addition to the carbon family[30]. Due to their exceptional physical characteristics, CNOs are known to be helpful in various areas, such as batteries and catalysts[31].

Multiple studies have been conducted on the chemical functionalization of CNOs nanostructures to improve their solubility and control their processability. Another approach to functionalization is by incorporating porosity into the CNOs' outer shells through chemical activation[32].

Heteroatom doping is a commonly used technique to eliminate the need for complex chemical synthesis routes. The actions of heteroatom doping generally influence the characteristics of carbon nanomaterials. This process can broaden their potential applications by introducing new active sites. Nitrogen and boron are among the elements commonly applied[33].

With the increasing global focus on sustainability and circular economy strategies, several studies have explored the use of waste-derived carbon sources for energy storage materials. For instance, carbon materials derived from agricultural biomass [34], plastic waste [35], and used motor oil [36]have been reported to demonstrate promising electrochemical properties while offering waste management solutions. However, these studies often focus primarily on performance metrics —

such as specific capacitance or surface area — with limited evaluation of the energy input, environmental impact, or scalability of the synthesis methods. In the case of flame pyrolysis or high-temperature carbonization, the energy demand and potential toxic emissions can undermine the sustainability claim if not properly accounted for [35][37].

In this research, waste engine oil was utilized as a carbon precursor to synthesize CNO-based materials. This approach is motivated by the desire to turn hazardous waste into value-added carbon structures and reduce environmental burden. While this method appears environmentally friendly on the surface — due to waste reuse and the avoidance of direct incineration or landfilling — it is essential to acknowledge that a more holistic assessment of the process is needed. Factors such as energy input, the use of high-temperature flame pyrolysis, chemical washing, potential emissions, and the handling of by-products could significantly affect the overall environmental footprint and commercial viability of the process. Therefore, while the method holds promise as a sustainable strategy, a detailed energy return analysis and comparison to conventional carbon materials such as activated carbon or graphene is necessary to validate its long-term green potential.

1.2. Problem statement

The growing global demand for efficient, low-cost, and environmentally friendly energy storage solutions has led to increased interest in supercapacitors due to their high-power density, long cycle life, and safety. However, current carbon-based materials—such as activated carbons—are limited by low energy densities and poor electrochemical performance, which restrict their commercial applicability[13].

Recent developments have explored hybrid systems involving metal hydroxides and carbon nanostructures to overcome these limitations. While metal hydroxides like Ni $(OH)_2$ offer improved pseudocapacitance, their inherent drawbacks, such as poor electrical conductivity and structural instability, remain significant challenges. Moreover, noble metal oxides, although effective, are cost-prohibitive and scarce, limiting their widespread use[34][35].

Among the emerging carbon nanomaterials, onion-like carbons (OLCs) have shown considerable promise due to their high electrical conductivity, accessible surface area, and potential for functionalization. However, the full potential of functionalized OLCs, especially when doped with heteroatoms such as nitrogen or boron, remains underexplored in the context of supercapacitor electrode materials [23][29]. The specific research gap lies in optimizing these functionalized OLCs to enhance energy and power density while maintaining cycling stability.

This study aims to address this gap by investigating the electrochemical performance of heteroatom-functionalized OLCs, both independently and in hybrid systems with transition metal hydroxides, for high-performance supercapacitor applications.

1.3. Purpose of Research Project

1.3.1. Aims of the study

This study aims to enhance the electrochemical performance of supercapacitors by developing cost-effective electrode materials through the functionalization of onion-like carbons (OLCs) with heteroatoms and surface decoration with transition metal hydroxides.

1.3.2. Objectives of this study

- To synthesize onion-like carbon (OLCs) using waste engine oil through flame pyrolysis without a catalyst.
- To functionalize the onion-like carbon by an acid treatment.

- Modify the onion-like carbon by post-doping with nitrogen and co-doping with boron as an added advantage.
- To make composites on the doped material using nickel hydroxide.
- Characterizing the produced materials using analytical techniques such as SEM, TEM, XPS, XRD, TGA, BET, FTIR, and Raman Spectroscopy methods.
- To examine the electrochemical and physiochemical performance of the materials on supercapacitors using techniques such as GCD, CV, and EIS.

1.4. Outline of this study

The study is divided into six sections and features the subjects' objectives and motivation in **Chapter 1**. It tackles global energy problems and discusses the ways renewable sources can replenish depleted systems and ensure that the energy supply lasts. Supercapacitors are then explored in this section.

A review of the literature that provides background information on the types of supercapacitors, the types of electrode materials used in supercapacitors, the varieties of electrolytes, and the fabrication of supercapacitors and electrodes is covered in **Chapter 2**.

The synthesis and characterization techniques employed in this investigation are reviewed in **Chapter 3**.

The discussion and outcomes of various characterization results of different onion-like carbons are covered in **Chapter 4**.

The electrode material fabrication process, the supercapacitors' setup, the electrochemistry results from the three electrode cells, and the electrode cells' use of battery-type and EDLC electrode materials in an asymmetric capacitor in a two-electrode system are all covered in **Chapter 5**.

The study's conclusion, recommendations, and future work are covered in **Chapter 6**, which is its last chapter.

1.5. References

[1] N. G. Sahoo, Y. Pan, L. Li, and S. H. Chan, “Graphene-based materials for energy conversion,” *Advanced Materials*, 24, no. 30, pp. 4203–4210, Aug. 2012, doi: 10.1002/adma.201104971.

[2] H. Huang and X. Wang, "Recent progress on carbon-based support materials for electrocatalysts of direct methanol fuel cells," *J. Mater. Chem. A*, 2, pp. 6266–6291, 2014, doi: 10.1039/c3ta14754a.

[3] X. Qiu and C. Burda, “Chemically synthesized nitrogen-doped metal oxide nanoparticles,” *Chem Phys*, 339, no. 1–3, pp. 1–10, Oct. 2007, doi: 10.1016/j.chemphys.2007.06.039.

[4] J. Chow, R. J. Kopp, and P. R. Portney, “Energy resources and global development,” *Science*. [Online]. Available: https://www.science.org. Accessed: Nov. 7, 2023.

[5] Statista, “Global oil consumption from 1970 to 2024,” Statista. [Online]. Available: https://www.statista.com/statistics/265261/global-oil-consumption-in-million-metric-tons/. Accessed: Jan. 10, 2024.

[6] S. Chu and A. Majumdar, "Opportunities and challenges for a sustainable energy future," *Nature*, 488, pp. 294–303, Aug. 2012, doi: 10.1038/nature11475.

[7] H. K. Bang, A. E. Ellinger, J. Hadjimarcou, and P. A. Traichal, "Consumer concern, knowledge, belief, and attitude toward renewable energy: An application of the reasoned action theory," *Psychol. Mark.*,17, no. 6, pp. 449–468, Jun. 2000, doi: 10.1002/(SICI)1520-6793(200006)17:6<449::AID-MAR2>3.0.CO;2-8.

[8] International Energy Agency, *World Energy Outlook 2023*. [Online]. Available: https://www.iea.org/reports/world-energy-outlook-2023. Accessed: May 2024.

[9] International Energy Agency and Organisation for Economic Co-operation and Development, *World Energy Outlook 2011*. Paris: IEA, 2011. [Online]. Available: https://www.oecd.org/en/publications/world-energy-outlook-2011_weo-2011-en.html. Accessed: May 2024.

[10] A. Midilli, M. Ay, I. Dincer, and M. A. Rosen, "On hydrogen and hydrogen energy strategies I: Current status and needs," *Renew. Sustain. Energy Rev.*, vol. 9, no. 3, pp. 255–271, 2005, doi: 10.1016/j.rser.2004.05.003.

[11] E. J. Yoo, J. Kim, E. Hosono, H. S. Zhou, T. Kudo, and I. Honma, "Large reversible Li storage of graphene nanosheet families for use in rechargeable lithium ion batteries," *Nano Lett*, 8, pp. 2277–2282, Aug. 2008, doi: 10.1021/nl800957b.

[12] A. V. Murugan, T. Muraliganth, and A. Manthiram, "Rapid, facile microwave-solvothermal synthesis of graphene nanosheets and their polyaniline nanocomposites for energy strorage," *Chemistry of Materials*, vol. 21, 21, pp. 5004–5006, Nov. 2009, doi: 10.1021/cm902413c.

[13] S. Jung *et al.*, "Carbon nano-onions from waste oil for application in energy storage devices," *New Journal of Chemistry*, 18, pp. 7369–7375, May 2020, doi: 10.1039/d0nj00699h.

[14] Regen Power, "What are the problems faced by renewable energy?" Regen Power. [Online]. Available: https://regenpower.com/what-are-the-problems-faced-by-renewable-energy/. Accessed: May 2024.

[15] B. Shaku, *Synthesis and Application of Boron-Nitrogen Doped Carbon Nano-Onions in Supercapacitors*, Ph.D. dissertation, University of the Witwatersrand, Johannesburg, South Africa, 2020. [Online]. Available: https://wiredspace.wits.ac.za/items/2858cb25-a64b-4af8-b0de-c67c3fde5293. Accessed: May 2024.

[16] R. Mathekga, "Southern Africa's energy crisis," *GIS Reports*, Aug. 31, 2023. [Online]. Available: https://www.gisreportsonline.com/r/southern-africa-energy/. Accessed: Mar. 15, 2024.

[17] World Population Review, "Blackout countries," *World Population Review*. [Online]. Available: https://worldpopulationreview.com/country-rankings/blackout-countries. Accessed: Apr. 15, 2024.

[18] M. Winter and R. J. Brodd, "What are batteries, fuel cells, and supercapacitors?," *Chem Rev*, 10, pp. 4245–4269, Oct. 2004, doi: 10.1021/cr020730k.

[19] Energy Storage Association, "Electrochemical capacitors," *Energy Storage Association*. [Online]. Available: http://energystorage.org/energy-storage/technologies/electrochemical-capacitors. Accessed: Apr. 10, 2024.

[20] S. Heyvaert, O. Hegazy, T. Coosemans, and J. Van Mierlo, "Social acceptance of wireless battery charging systems: Belgium case study," in *Proc. IEEE Int. Electric Vehicle Conf. (IEVC)*, Florence, Italy, May 2014, pp. 1–6, doi: 10.1109/IEVC.2014.7056075.

[21] J. Delsing and F. Häggström, “IoT energy storage - A forecast,” *Energy Harvesting and Systems*, 5, no. 3–4, pp. 43–51, Oct. 2018, doi: 10.1515/ehs-2018-0010.

[22] R. Kötz and M. Carlen, "Principles and applications of electrochemical capacitors," *Electrochim. Acta*, 45, no. 15–16, pp. 2483–2498, 2000. [Online]. Available: https://www.sciencedirect.com/science/article/pii/S0013468600003213. Accessed: April 2024.

[23] A. G. Pandolfo and A. F. Hollenkamp, "Carbon properties and their role in supercapacitors," *J. Power Sources*, 157, pp. 11–27, Jun. 2006, doi: 10.1016/j.jpowsour.2006.02.065.

[24] D. M. Bobrowska, K. Brzezinski, L. Echegoyen, and M. E. Plonska-Brzezinska, “A new perspective on carbon nano-onion/nickel hydroxide/oxide composites: Physicochemical properties and application in hybrid electrochemical systems,” *Fullerenes Nanotubes and Carbon Nanostructures*, 25, pp. 193–203, Mar. 2017, doi: 10.1080/1536383X.2016.1267151.

[25] T. Brousse, D. Bélanger, and J. W. Long, “To Be or Not To Be Pseudocapacitive?,” *J Electrochem Soc*, 162, pp. A5185–A5189, 2015, doi: 10.1149/2.0201505jes.

[26] M. Toupin, D. Bélanger, I. R. Hill, and D. Quinn, “Performance of experimental carbon blacks in aqueous supercapacitors,” *J Power Sources*, 140, pp. 203–210, Jan. 2005, doi: 10.1016/j.jpowsour.2004.08.014.

[27] E. Frąckowiak and F. Béguin, "Carbon materials for the electrochemical storage of energy in capacitors," *Carbon*, 39, pp. 937–950, 2001, doi: 10.1016/S0008-6223(00)00183-4.

[28] J. P. Zheng, “The Limitations of Energy Density of Battery/Double-Layer Capacitor Asymmetric Cells,” *J Electrochem Soc*,150, p. A484, 2003, doi: 10.1149/1.1559067.

[29] L. L. Zhang, R. Zhou, and X. S. Zhao, “Graphene-based materials as supercapacitor electrodes,” *J Mater Chem*, vol. 20, no. 29, pp. 5983–5992, 2010, doi: 10.1039/c000417k.

[30] M. Zeiger, N. Jäckel, V. N. Mochalin, and V. Presser, "Review: Carbon onions for electrochemical energy storage," *J. Mater. Chem. A*, 4, pp. 3172–3196, 2016, doi: 10.1039/c5ta08295a.

[31] "Fullerenes," in *Compendium of Chemical Terminology (Gold Book)*, Int. Union of Pure and Applied Chemistry, 2014, sourced from *Pure Appl. Chem.*, 67, pp. 1307–1375, 1995, doi: 10.1351/goldbook.F02547.

[32] R. Dubey, D. Dutta, A. Sarkar, and P. Chattopadhyay, "Functionalized carbon nanotubes: synthesis, properties and applications in water purification, drug delivery, and material and biomedical sciences," *Nanoscale Adv.*, 3, pp. 5722–5744, 2021, doi: 10.1039/d1na00293g.

[33] J. Goclon, B. Bankiewicz, P. Kolek, and K. Winkler, "Role of nitrogen doping in stoichiometric and defective carbon nano-onions: Structural diversity from DFT calculations," *Carbon N Y*, 176, pp. 198–208, May 2021, doi: 10.1016/j.carbon.2021.01.131.

[34] G. P. Ojha *et al.*, "In-situ fabrication of manganese oxide nanorods decorated manganese oxide nanosheets as an efficient and durable catalyst for oxygen reduction reaction," *Colloids Surf A Physicochem Eng Asp*, 568, pp. 311–318, May 2019, doi: 10.1016/j.colsurfa.2019.02.030.

[35] S. Herou *et al.*, "Ordered mesoporous carbons from lignin: A new class of biobased electrodes for supercapacitors," *Green Chemistry*, 21, no. 3, pp. 550–559, 2019, doi: 10.1039/c8gc03497d.

[36] M. Bhaumik *et al.*, "High-performance supercapacitors based on S-doped polyaniline nanotubes decorated with Ni(OH)2 nanosponge and onion-like carbons derived from used car tyres," *Electrochim Acta*, 342, May 2020, doi: 10.1016/j.electacta.2020.136111.

[37] L. Luo *et al.*, "High performance supercapacitor electrodes based on B/N Co-doped biomass porous carbon materials by KOH activation and hydrothermal treatment," *Int J Hydrogen Energy*, 46, no. 63, pp. 31927–31937, Sep. 2021, doi: 10.1016/j.ijhydene.2021.06.211.

Chapter 2

Literature review

2.1. Energy storage systems

Energy storage is essential for efficient, clean, and adaptable energy use and is a fundamental component in harvesting renewable energy. Global energy consumption has surged significantly due to heightened industrialization, rampant technical advancements, and economic expansion in developing nations[1]. The International Energy Agency's (IEA) survey report for 2024-2028 predicts substantial growth in the worldwide energy market, propelled by factors including rising demand, technological innovations, and governmental initiatives for sustainable energy solutions. Their analysis estimates that the global energy as a service market will be valued at 64.7 billion dollars in 2022 and is projected to reach 105.6 billion dollars by 2027. The Asia-Pacific region is anticipated to lead the worldwide energy market during the projected period, driven by the rising energy demand in nations such as India, China, and Japan[2].

International energy trends contextualize the forthcoming trajectory of the South African energy market. As the global community gravitates towards advancing renewable energy, South Africa's energy environment is set for a significant transformation. This transition is expected to be propelled by the nation's enormous solar and wind energy resources, which remain underutilized,

with the government's dedication to decreasing carbon emissions. The energy sector constitutes a substantial portion of South Africa's GDP in market size[3].

The market value is anticipated to rise, propelled by the growth of renewable energy, the upgrading of current infrastructure, and the investigation of novel energy technologies. The emphasis on renewable energy sources corresponds with the worldwide movement towards sustainability and the battle against climate change[3]. Energy storage can offer numerous economic, reliable, and environmental advantages. Nonetheless, this is contingent upon the degree of its deployment. Energy storage could enhance the operational efficiency of the utility grid, diminish the probability of blackouts during peak demand, and facilitate the integration and utilization of more renewable resources.

There are four primary classifications of energy retention systems: mechanical energy retention, thermal energy retention, chemical energy retention, and electrical energy retention[4]. This dissertation will concentrate on electrochemical energy retention systems. Energy retention in an electrochemical system occurs through two profoundly distinct mechanisms: Faradaic and non-Faradaic processes. The Faradaic charge transfer process entails electrochemical reactions that facilitate the interchange of electrons between the electrolyte and the electrode. The non-Faradaic charge transference process entails storage without substantial chemical reactions at the electrolyte/electrode contact[5].

In Faradaic processes, potential chemical energy is retained and discharged by reduction-oxidation processes of electrochemically functioning species, whereas in non-Faradaic interactions, energy is retained electrostatically[6]. Capacitors, lead-acid batteries, and lithium-ion batteries (LIBs) are the predominant electrochemical storage systems in contemporary life. High-energy-density batteries like LIBs have garnered increasing interest due to their aptitude to amass and release electrical energy safely. High-power density capacitors are in demand due to the proliferation of the magnitude of Things and the rapid advancement of sophisticated integrated electronic systems, which continually drive the advancement of high-energy density capacitors. There are three categories of capacitors: electrolytic capacitors, electrochemical capacitors, and electrostatic capacitors. ECs, called supercapacitors/ultracapacitors, are electrochemical storage devices characterized by exceptionally high capacitance[7][8].

Supercapacitors, frequently called ultracapacitors or electric double-layer capacitors (EDLC), lack a traditional solid dielectric. Instead, they utilize an electrolyte, which exhibits superior energy density compared to conventional capacitors, quick discharging and charging capabilities, extended cycle life, and high efficiency[9]. Nevertheless, they have numerous problems, such as comparatively poor energy density, voltage constraints, elevated self-discharge rates, expensive expenses, and restricted energy storage capacity. Research and development endeavors can mitigate concerns by creating electrolytes with limited ion mobility or incorporating gel or solid-state electrolytes to decrease self-discharge rates.

Furthermore, the advancement of electrode and the fabrication of electrode materials architectures, including asymmetric or hierarchical topologies, can improve the performance and energy density of electrochemical capacitors (ECs)[10]. The Ragone graphical record in **Figure 2.1** illustrates that batteries often possess greater energy densities than ultracapacitors but exhibit worse power densities. ultracapacitors exhibit excellent electrochemical features relative to subordinate batteries, including high power density and prolonged cycle performance.

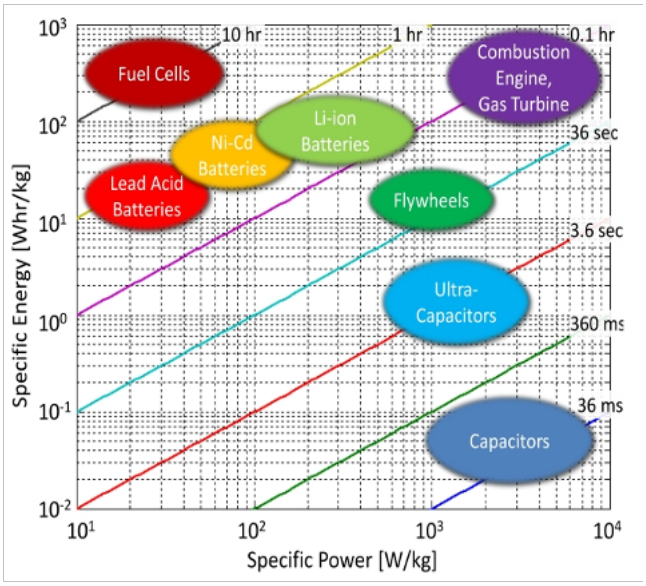


Figure 2. 1: Ragone map of several energy storage systems[11]

Moreover, supercapacitors exhibit superior temperature performance ranging from -40°C to 70°C, whereas battery materials undergo irreversible phase transitions throughout the charge-discharge cycle, significantly diminishing their lifespan. Formulating economical production processes and implementing efficient recycling procedures for electrode materials can lessen the overall expense of electrochemical capacitors (ECs) and mitigate their environmental footprint[12][13].

2.2. Supercapacitors

An ultracapacitor, or supercapacitor, is a device that occupies the intermediary position between lithium-ion batteries and conventional capacitors, possessing a capacitance that is considerably greater than that of traditional capacitors while exhibiting lower voltage limitations. It typically holds 10 to 100 times additional energy density than traditional capacitors. In contrast to batteries, it can accept and deliver a charge far more rapidly and endure a more significant number of recharge and discharge cycles. Unlike conventional capacitors, electrostatic double-layer capacitance and electrochemical pseudo-capacitance, utilized in supercapacitors, exert minimal influence on the total capacitance of the capacitor. Supercapacitors utilize two layers of solid dielectrics for energy storage. These are electrochemical double-layer capacitance and psuedocapacitance[14][15].

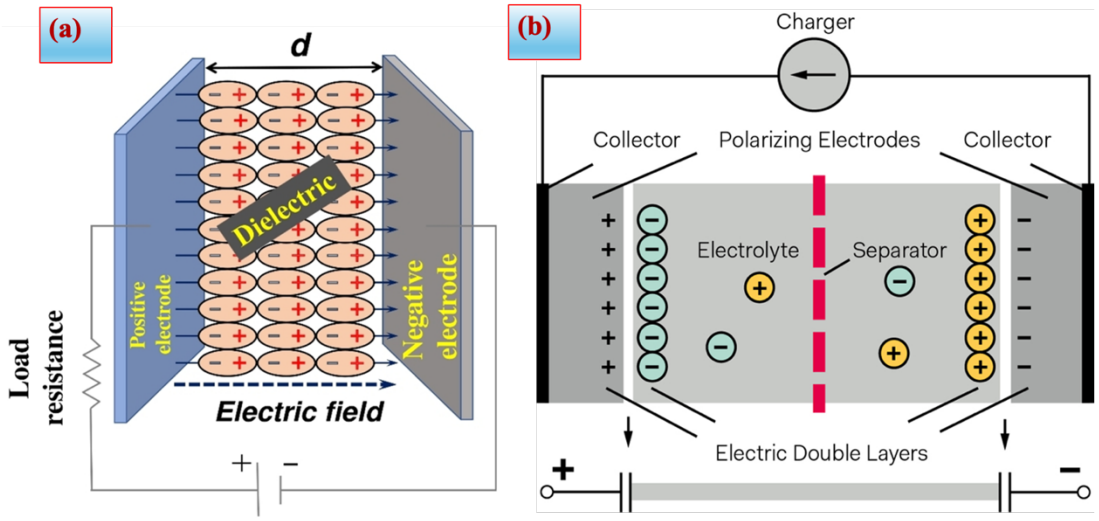


Figure 2. 2: Schematic diagram of (a) Traditional Capacitor (b) Supercapacitor[16][17].

The electrochemical double-layer capacitors utilize carbon materials, for example carbon nanofibers (CNF), CNOs, and CNTs, characterized by high surface area, where charge accumulates at the electrolyte-electrode boundary.

Pseudocapacitors exploits metal oxides or conductive polymers (CPs) as electrode materials for rapid and reversible redox processes. Hybrid capacitors integrate electrodes like those found in conventional capacitors within a single cell and pseudocapacitor electrodes, yielding an efficient and versatile power source [18].

2.2.1. Operational principle and storage methodology of supercapacitors

A supercapacitor comprises various components, as **Figure 2.2(b)** depicts. These encompass current collectors, electrodes, separators, and electrolytes. The battery's separator fulfills the same function in this usage as within the battery in question. Furthermore, it separates the two electrodes to suppress contact during a short circuit. The fundamental tasks of a ultracapacitor are energy retention and the dissemination of ions from the electrolyte to the electrode surface. The energy density of a supercapacitor is contingent upon its capacitance and voltage; an increase in any or both parameters will enhance the energy density[17]. In the subsequent **equation 2.1**, we have energy density (E), specific capacitance (C), charge density (Q), and voltage (V)[19]:

$$E = \frac{CV^2}{2} = \frac{QV}{2} \qquad \textit{Eqn (2. 1)}$$

The power density of a supercapacitor determines its discharge rate and is contingent upon the voltage and the equivalent series resistance, which should be minimized for optimal density. We present the power density (P) and equivalent series resistance R_s in **equation 2.2**, where[19]:

$$P = \frac{V^2}{4R_s} \qquad \textit{Eqn (2. 2)}$$

The two arithmetical formulas indicate that the power and energy densities of the capacitor can be enhanced by augmenting the capacitance and voltage while reducing the internal resistance.

Given the quadratic relationship between voltage and power and energy densities, expanding the capacitance to improve energy and power is more efficient. The potential difference depends on the electrode materials' characteristics and the electrolyte's potential windows [19]. Theoretical capacitance in a capacitor is expressed in **equation 2.3** as:

$$C_T = \frac{A\varepsilon}{4\pi d} \qquad \textit{Eqn (2. 3)}$$

Indicating that electrodes with a substantial surface area (A) and high permittivity (ε) yield greater capacitance; the distance (d) between the electrodes is inversely proportional to the capacitance. **Equation 2.4** depicts an experimental method for estimating capacitance represented by the calculation[19]:

$$C_E = \frac{I}{{}^{d_v}/_{d_t}} \qquad \textit{Eqn (2. 4)}$$

Where I, denote the current and d_v/d_t signifies the slope of the discharge/charge curve plotted against potential difference and time. It is advisable to calculate the power and energy of amassed supercapacitors and lithium-ion batteries derived from the total mass, volume, and area of the

capacitor rather than solely on the working electrode to convey their potential industrial applications [19] accurately.

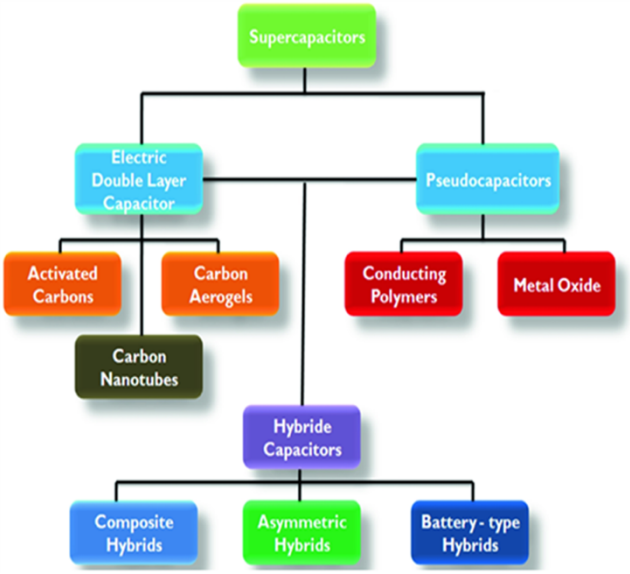


Figure 2. 3: Hierarchy of supercapacitors comprising three primary groups, and their subclasses based on potential materials for example, conducting polymers, metal oxides and carbon materials[20].

The performance metrics suggest that supercapacitors' power and energy of are primarily influenced by their cell capacitance, working voltage range, and cell equivalent series resistance. The energy retention method, the electrode materials, the electrolyte type, and the device assembly predominantly determine the supercapacitors' performance. **Figure 2.3** illustrates a flow chart delineating these supercapacitor categories concerning their charge storage mechanisms[21].

2.3. Mechanism of Supercapacitors Energy storage

2.3.1. Electric double-layer capacitance (EDLCs)

The electrolytes, electrodes, and separators in an (EDLC) consist entirely of carbon-based materials. No charge is exchanged amongst the electrolyte and electrode in EDLCs, either electrostatically or by a non-Faradaic method. EDLCs utilize the electrochemical double layer based on the 'Helmholtz double layer' for energy storage, as depicted in **Figure 2.4**. When voltage is introduced across the electrodes, charge accumulation transpires. This difference in potential attracts charges of opposing polarity, leading to ion migration from the electrolyte through the separator into the electrode pores. To avoid ion recombination, the electrodes are shielded by dual charge layers. EDLCs benefit from an enhanced specific surface area and reduced inter-electrode distances, leading to a higher energy density in the electric double layer. [22].

Energy may be retained and transmitted more rapidly and capably through the storage mechanism of EDLCs. This constitutes a significant benefit. Consequently, no chemical process is occurring at this moment. During battery charging or discharging, the operational material within the battery experiences expansion. EDLCs, in contrast to batteries, can endure millions of cycles. Conversely, batteries possess the highest capacity of merely a limited thousand[23]. Graphite-positive electrodes and high-potential negative electrodes in lithium-ion batteries facilitate the formation of the solid electrolyte interphase, indicating that no electrolyte solvent is necessary for charge retention. Electrostatic surface charging indicates that EDLCs can retain merely a limited total of energy; therefore, researchers are striving to enhance energy functioning and broaden the operational temperature range of EDLCs.

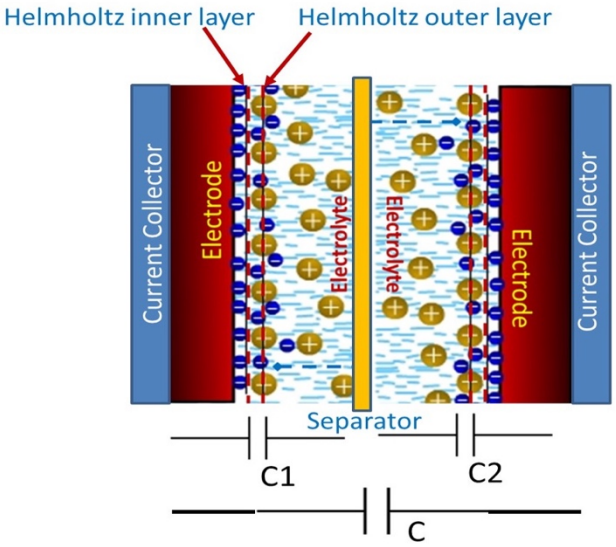


Figure 2. 4: Electric double-layer capacitor with simple equivalent circuit[24]

The functioning of EDLC is considerably swayed by the electrolyte employed[25]. Helmholtz (1871) initially elucidated the EDL, now called the Helmholtz model. Rendering to the Helmholtz model, the surface charges entirely counteract the involved ions with opposing charges; the exterior electrostatic force immobilizes the ions, forming an electric double layer, as illustrated in **Figure 2.5a**. According to the Gouy-Chapman hypothesis of the EDL, ions are not fixed to the surface due to their unsystematic thermal mobility. From that juncture, the notion of the diffuse Electric double layer emerges. The ions that neutralize the surface charge are not fixed to the surface; instead, they are dispersed in the solution, as shown in **Figure 2.5b**[26].

Stern (1924) suggested an ideal of the EDL that integrates both the Gouy-Chapman and Helmholtz mockups, wherein a portion of the charge on the surface is counteracted by stationary ions, albeit insufficient to counteract the entire charged surface entirely. The diffused layer neutralizes the remaining charge quantities. The diffusion process of ions with opposite charges near the

electrolyte-electrode boundary is driven by ion concentration or chemical potential. This absorption gradient is established owing to the desirability of charges with opposing polarities from the adjacent area of the polarized electrode in the electrolyte, as **represented in Figure 2.5b**[27].

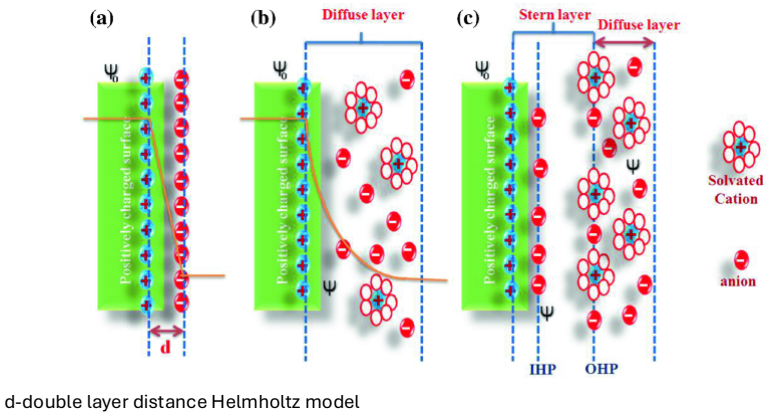


Figure 2. 5: representations of the EDLC at a positively charged interface (a) Helmholtz model (b) Gouy-Chapman model (c) Stern model[21]

Furthermore, to the absorption gradient, surface phenomena may occur owing to ordinary convection (the conveyance of ions resulting from vibrations, mechanical motion, etc.) and the effects of localized heating. The EDL exhibits two outcomes: electrocapillarity, which is challenging to identify with a stiff electrode, and the capacitive effect, upon which supercapacitors are founded. As previously stated, the double charge layer forms at the electrolyte-electrode boundary, functioning as an electric charge reservoir and exhibiting capacitive properties. The capacitance per unit area, as depicted in **equation 2.5**, is defined as[26]:

$$C = \frac{dq}{dQ} \qquad \textit{Eqn (2. 5)}$$

Where 'q' represents the particle's charge within the electrolyte. The Stern model suggests that the overall capacitance, (C_T), across the double layer, the synthesis of the Helmholtz and Gouy-Chapman effects, captured in **equation 2.6** as[26]:

$$C_T = C_H + \frac{\varepsilon\varepsilon_o}{X_d} \qquad \textit{Eqn (2. 6)}$$

Where:

$$X_d = \left[\frac{\varepsilon\varepsilon_o RT}{F^2 I}\right]^{1/2} \qquad \textit{Eqn (2. 7)}$$

Here, (ε) represents the dielectric continual of the intermediate, (ε_o) denotes the permittivity of free space, (R) is the gas constant, (T) signifies absolute temperature, (F) is the Faraday constant, and (I) indicate ionic stamina. The initial expression on the right-hand side of **equation 2.7** represents the capacitance outcome attributed to the Helmholtz layer, whereas the subsequent term signifies the Gouy-Chapman effect[26]. The Gouy-Chapman ideal of the (DL) double layer overstated the capacitance of the EDLC because it assumed point charges at the electrode surface. Stern subsequently addressed this issue by proposing synthesizing the Gouy-Chapman and Helmholtz mockups, resulting in an inside Stern layer (the Helmholtz layer) and an external diffuse layer. This model posits that ions possess a finite size, thereby establishing a geometric constraint on the adsorption region within the Helmholtz layer. The total capacitance is represented as a series of capacitances for the layers, where the most negligible capacitance exerts the most significant influence, as articulated in **equation 2.8**[28]:

$$\frac{1}{C_{dl}} = \frac{1}{C_H} + \frac{1}{C_{diff}} \qquad \textit{Eqn (2. 8)}$$

Where C_H denotes the Stern-type condensed C_{dl} and C_{diff} signifies the capacitance of the diffusion region. The spacing amongst the ion layers aligned parallelly is minimal, depending on the ionic radius order Å (Angstrom)[28]. Consequently, the capacitance of a double-layer capacitor is primarily enhanced by augmenting the electrode material, which for supercapacitors is activated carbon with a SSA of 1000-2000 m^2/g and a theoretical specific capacitance of up to $500F/g$. It is essential to annotate that ultracapacitors do not contain a distinct dielectric material[29].

A double layer of Helmholtz layers is established at the electrolyte/electrolyte boundary. This functions as a dielectric between the two, so constituting a capacitor. A comparable capacitor is based at the second electrode as well. The series combination of these two capacitors results in the overall capacitance. This configuration designates this category of ultracapacitors as electric double-layer capacitors, abbreviated as EDLC. The two capacitors, arranged in series at the electrodes, contribute to the effective capacitance between them. The voltage that either $(C1)$or $(C2)$ can endure is contingent upon the potential difference in the disintergration of the electrolyte. This restricts the rated voltages of EDLC to a range of $1.3V$ to $3.0V$[24].

The separator membrane maintains isolation between the two portions of the capacitor while permitting ion passage. The electrode's extensive porosity results in a substantial contact area between the electrolyte and the electrode material, determining the capacitance value and the energy stored in the capacitor. Initial capacitors were constructed from activated carbon, which continues to be utilized today. Various carbon-based constituents, comprising CNTs, CNFs, CNOs, and graphene, have been produced over the years, and research persists to enhance these materials

further. For an optimal EDLC, the specific capacitance C (F/g) adheres to the principles of a parallel-plate type capacitor, as expressed by the subsequent **equation 2.9**[30][31]:

$$C = \frac{\varepsilon_r \varepsilon_o A}{d} \qquad Eqn\ (2.\ 9)$$

Where ε_r denotes relative permittivity and ε_o represents absolute permittivity F/m in a vacuum. $A(m^2/g)$ indicates the accessible specific surface area of the electrode to the ions, whereas $d(m)$ represents the adequate width of the EDL.

2.3.2. Pseudocapacitor

'Pseudocapacitor' originates from the ancient Greek word 'Pseudes,' signifying 'False' or 'Erroneous.' The term pseudocapacitance derives from pseudocapacity, a concept introduced by David C. Grahame in 1941 to denote electrochemically reversible capacity that is not linked to the creation of the electric double layer (EDL). Pseudocapacitance was subsequently employed in the research of Conway and Gilead in the early 1960s to elucidate (ECT) electrochemical charge transfer mechanisms associated with surface adsorption. Pseudocapacitance was characterized initially by the fractional surface coverage (θ) of adsorbed species according to the Langmuir adsorption model. The capacitance originated from Faradaic reactions involving monolayers of electrochemically active species, distinguishing it from both double-layer capacitance, which was purely electrostatic, and the conventional behavior of battery materials, which, before the advent of lithium-ion chemistries, entailed substantial phase and structural transformations of the reactants. Pseudocapacitance refers to materials that have electrochemical characteristics (cyclic voltammetry and charge-discharge) akin to those of conventional capacitors (electric double-layer capacitors) yet employ distinct charge storage mechanisms[32][33].

In contrast to EDLC, pseudocapacitive reactions are Faradaic and retain electrical energy via rapid and bidirectional redox processes occurring at the surface of the electrode. Pseudocapacitive constituents demonstrate battery-like redox processes at elevated rates akin to capacitors, reflecting their electrochemical characteristics through quasi-rectangular cyclic CV and quasi-triangular GCD. The charge retention methods in pseudocapacitive constituents may involve surface redox or intercalation reactions. The charge transfer rates are elevated when a thinner redox material is applied to the electrode or ion penetration from the electrolyte is reduced into the structure. The capacitance values of pseudocapacitors are elevated due to the simultaneous operation of numerous charge storage mechanisms[34][35].

Pseudocapacitors utilize electrodes that function as capacitors, such as MnO_2, NiO_2, and RuO_2. These electrodes exhibit a linear correlation between the retained charge and the breadth of the potential window. Pseudocapacitors exhibit superior capacitance relative to EDLCs[38]. Their inadequate conductivity, however, leads to diminished electron transport rates. **Figure 2.6a** illustrates a pseudocapacitor cell. In the corresponding electrical circuit illustrated in **Figure 2.6b**, C_{dl} denotes an EDLC capacitor, which signifies the storage of electrostatic charge characteristic of an EDLC capacitor. R_s is the ESR of the entire capacitor. R_f denotes the resistance of the electrolyte/electrode, while R_d signifies losses incurred during charge transfer due to the Faradaic component of capacitance, which pertains to charge transfer via the Faradaic process[39].

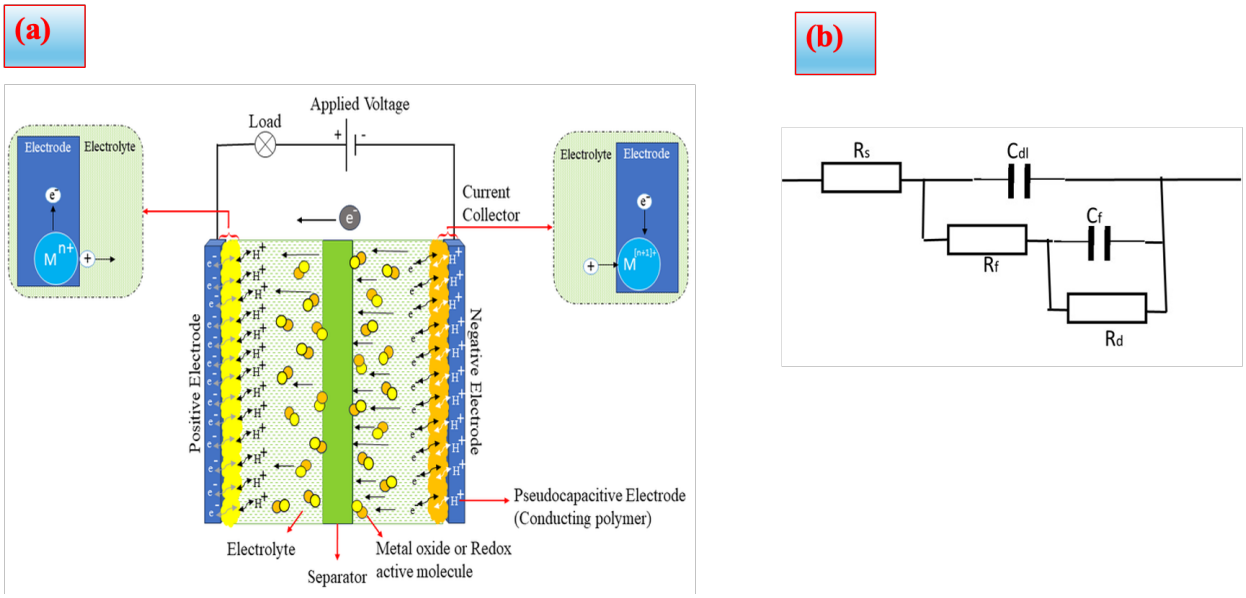


Figure 2. 6: (a) Schematic diagram of a pseudocapacitor (b) Equivalent circuit of **pseudocapacitor**[36][37]

2.3.2.1. Surface - redox Pseudocapacitors

In surface redox pseudocapacitors, charge retention primarily results from charge transferences or redox developments at the electrode surface. **Figure 2.7 (d-f)** illustrates that surface redox pseudocapacitors' CV and GCD profiles closely resemble carbon-based materials, indicating a linear affiliation in charge storage across the voltage window. This does not infer that pseudocapacitors merely store charge through the DL process. Surface redox pseudocapacitive constituents accumulate charges through both non-Faradaic and Faradaic methods. Materials that have inherent electrochemical characteristics are termed intrinsic pseudocapacitive constituents. Since 1971, numerous surface redox pseudocapacitive materials, including TMOs, have been studied. Buzzanca and Trasatti were the initial researchers to document the pseudocapacitance of Ruthenium oxide (RuO_2) in supercapacitors[39][40].

It is an inherent (redox) pseudocapacitive constituent owing to its rapid electron and proton conduction properties. Similarly, several TMOs, like Fe_3O_4 and MnO_2, also demonstrate intrinsic (redox) pseudocapacitance. Due to their various valence states, these materials facilitate rapid and bidirectional redox processes at the surface of the electrode, rendering them superior to EDLCs in terms of higher energy density at elevated discharge-charge rates. The charge retention process and electrochemical characteristics of redox-pseudocapacitors are illustrated in **Figure 2.7 (e-f)**, using MnO_2,for instance, wherein MnO_2 accumulates charge via bulk redox or surface interactions amongst the +4 and +3 oxidation states of Mn. In the reaction mechanism, as depicted in reaction **equation 2.10**[41][42]:

$$MnO_2 + xA^+ + xe \leftrightarrow A_xMnO_2 \qquad \textit{Eqn (2. 10)}$$

The representation 'A' denotes alkaline metal cation (Na^+, Li^+, K^+). Their crystallographic and crystallinity structures significantly influence the pseudocapacitive characteristics of Mn-oxides. The various physical procedures and electrode constituents account for these two unique mechanisms: pseudocapacitance and EDLC. Nonetheless, the parallels in their electrochemical monograms may be attributed to the relationship between potential and the quantity of charges generated around the electrolyte/electrode boundary or within the internal surface due to desorption/adsorption phenomena. Consequently, without specific electrochemical features, the materials cannot be classified as pseudocapacitive, rendering capacitance value calculations inappropriate. CPs and TMCs are commonly investigated as pseudo-capacitive electrode materials. These explanations concerning the pseudocapacitive characteristics of materials must apply solely to an independent electrode rather than the entire device[44][45].

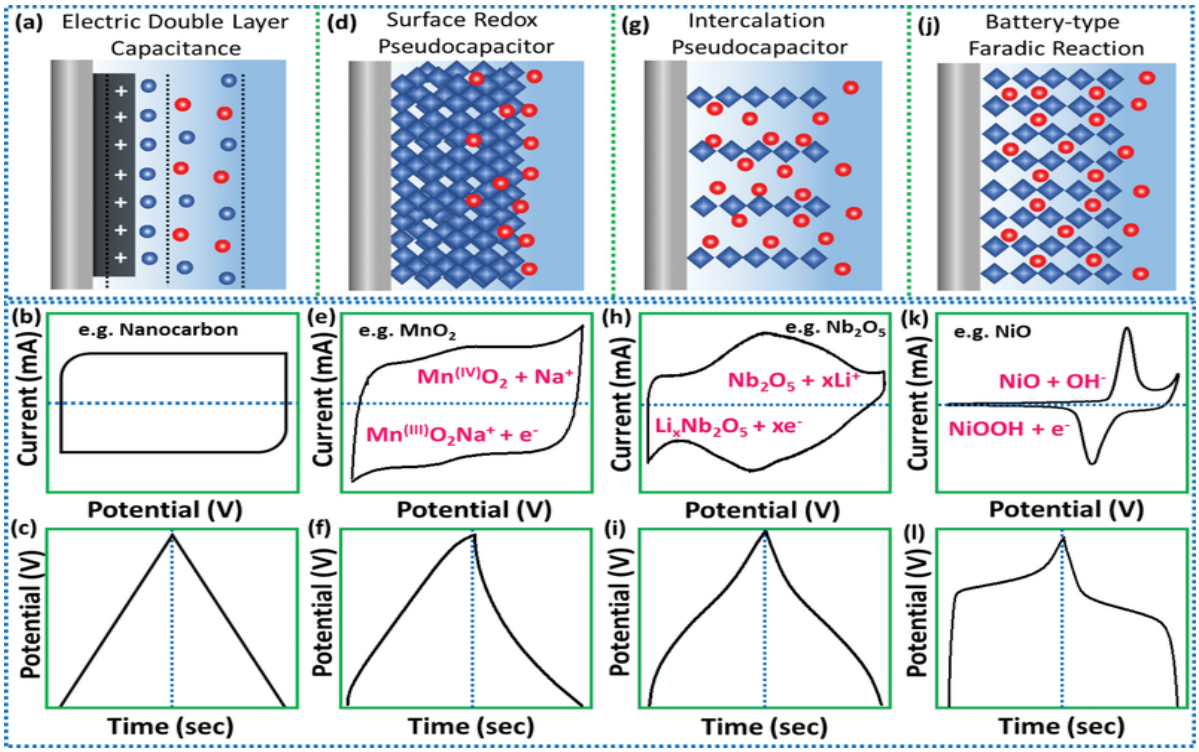


Figure 2. 7: Energy storage systems and their electrochemical characteristics: (a-c) EDLC, (d-f) surface redox pseudocapacitor, (g-i) intercalation pseudocapacitor, and (j-l) battery-type faradic reaction[43]

2.3.2.2. Intercalation Pseudocapacitors

In addition to surface redox reactions, certain layered constituents like Nb_2O_5, MoO_3,and TiO_2(B), experience Faradaic charge transference by intercalating electrolyte ions into their channels or layers without facing crystallographic phase changes. These materials demonstrate reversible and rapid charge retention rates that meet or exceed those of conventional surface-redox pseudocapacitive materials. Consequently, they cannot be explicitly classified as redox pseudocapacitors. Simon and Dunn characterize this charge retention method as intercalation pseudocapacitors, prevalent in non-aqueous electrolyte systems. A fundamental characteristic of

intercalation pseudocapacitance is that the materials do not experience phase changes throughout the intercalation process. The overarching reaction mechanism is articulated in reaction **equation 2.11** as follows[46][47]:

$$MA_y + xLi^+ + xe^- \leftrightarrow Li_xMA_y \qquad Eqn\ (2.\ 11)$$

In this mechanism, the representation MA_y denotes a metal oxide. Unlike EDLCs, the charge retention mechanism for intercalation pseudocapacitance extends beyond the surface, as portrayed in **Figure 2.7 (g-i)**, engaging the bulk of the materials for reversible Faradaic electrochemical reactions.

2.3.2.3. Battery-type energy storage Faradaic reaction

The advancement of pseudocapacitive constituents for energy-related applications has garnered significant inquisitiveness in recent years owing to their substantial energy storage capacity and high-power outputs. Nonetheless, employing nanosized operational materials in batteries results in rapid redox kinetics owing to the enhanced SA and reduced diffusion channels, altering their electrochemical characteristics from pseudocapacitive to battery-like behavior. Consequently, it turns out to be difficult to differentiate between "pseudocapacitive" and "battery" materials[48].

Such beliefs have adversely influenced the ultimate device designs. In the domain of electrochemical capacitors (ECs), generally insinuated to as supercapacitors, the term pseudocapacitance denotes the behavior of electrode materials (such as MnO_2 and RuO_2) that demonstrate the electrochemical features of a capacitive electrode, specifically a linear relationship within the relevant potential window. However, charge retention arises from electron transference

mechanisms instead of solely from the accrual of ions in the EDL, as observed in activated carbons. Furthermore, throughout the discharging and charging operation, the potential of the battery-like electrode stays stable, following the phase law and adhering to the Nernst equation[39][49].

Consequently, materials exhibiting solid-state diffusion-controlled battery reactions demonstrate distinct reduction-oxidation peaks in their cyclic voltammetry profiles and flat charge/discharge plateaus like those of batteries, as depicted in **Figure 2.7 (j-l)**. Notwithstanding these explicit definitions and attributes, numerous battery-type electrodes, such as Ni $(OH)_2$ and other materials demonstrating faradaic behavior, including those electrochemically irreversible, have been classified in the literature as pseudocapacitive materials. This misclassification engenders confusion among readers, as the concept of capacitance (F) is inapplicable solely to faradaic characteristics. In this capacity, (mAh or Coulomb C) serves as the most relevant and significant metric in these instances[50][51].

The conventional battery-like electrode materials differ from capacitor-type electrodes regarding redox processes, which are accountable for the phase transformation of the electrode constituents throughout the electrochemical process. The standard battery ingredients comprise Cu, Co, Cd, and Ni, formulated as sulfides, oxides, hydroxides, phosphates, and selenides, interacting with hydroxide ions in alkaline environments to accumulate charge[52]. For battery-like electrode constituents, it is essential to compute the specific charge (C/g) or capacity (mAh/g) from the GCD and CV profiles, as the typical (F) will not remain continual over the voltage window. These measurement systems indicate the quantity of electrons and ions received by a specific mass

typically intercalated within a crystalline solid in an electrode. The following CV and GCD curves can determine the practical capacity. Usually, cyclic voltammetry (CV) is conducted at a constant voltage rate of scanning (V/s), and the specific capacity can be calculated from the CV curves utilizing the subsequent **equation 2.12**[39]:

$$Specific\ capacity\ (A\,h/g) = \int \frac{i(V)dv(A.V)}{m(g)\vartheta(V/s)\times 3600} \qquad Eqn\ (2.\ 12)$$

Integrating the current amount across the range of voltages, the aggregate voltammetric charge is obtained, which ought to be divided by a factor of 2 in amperes. V (amperes); V signifies the scan rate, while m denotes the mass loading. The specific capacity is determined by using galvanostatic charge-discharge (CD) curves (n=1).

$$Specific\ capacity\ (A\,h/g) = \int \frac{i(A)dt(s)}{3600\times m(g)} \qquad Eqn\ (2.\ 13)$$

As per **equation 2.13**, where t represents discharge time (s), i denotes imposed current density (A), and m signifies the amount of active material (g). The electrode's specific capacity for capacitive materials may be translated into specific capacitance (F/g) using **Equation 2.14**.

$$Specific\ capacitance\ (F/g) = \frac{Specific\ capacity\ (Ah/g)\times 3600}{\Delta V(V)} \qquad Eqn\ (2.\ 14)$$

Where V represents the potential range of the isolated electrode arrangement (V).

2.3.2.4. Hybrid supercapacitors (HSCs)

Recent research has concentrated on advancing HSCs, which concurrently and asymmetrically accumulate charges by surface ion desorption/adsorption at the negative electrode and sodium/lithium de/intercalation at the positive electrode. Hybrid energy capacitors (HECs), comprising sodium-ion capacitors (NICs) and LICs, are anticipated to reconcile the disparity

between high-energy SIBs/LIBs and high-power electrochemical capacitors (ECs), emerging as the premier power basis for electric cars and (UPS) uninterruptible power systems [53].

By integrating graphene, metal oxides, and polymers, we can achieve low-cost, mechanically flexible, chemically stable, and electrically conductive hybrid electrode constituents for supercapacitors. Hybrid electrode layouts exhibit significant potential, comprising two distinct electrodes of varied materials. Composite electrodes comprise one material integrated into another within a single electrode. An important difficulty for HECs is the disparity in discharge/charge rates between the two electrodes, attributable to intrinsic variances in energy storage processes. Under standard operating circumstances of an HEC, this kinetic imbalance hinders complete energy use of the intercalation electrode. It induces a significant overpotential in the capacitive electrode, diminishing overall efficiency. Hybrids are characterized by their consistent electrical properties at high frequencies[54][55].

Hybrid capacitors amalgamate the characteristics of pseudocapacitors and EDLCs inside a single device, capable of utilizing both non-faradaic and faradaic processes. They possess superior energy and power density compared to EDLCs. These capacitors consist of non-uniform electrodes. Lithium-ion capacitors exemplify a hybrid capacitor. Numerous research studies have employed lead and nickel oxides for positively charged electrodes. Activated carbon is (AC) material is typically utilized to fabricate of cathode electrodes. The cathode carbon electrode material is broader than the anode electrode material due to the much-reduced charge storage capacity per unit volume of carbon. **Figure 2.8** illustrates the fundamental arrangement of HSCs.

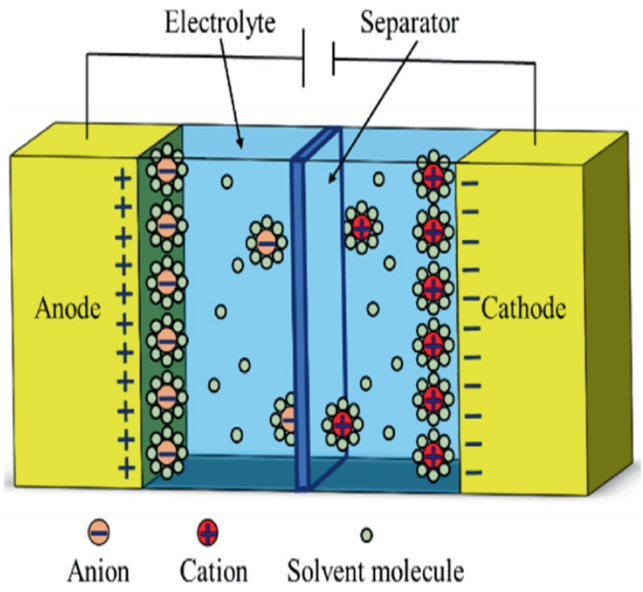


Figure 2. 8: Schematic diagram of a typical hybrid supercapacitor[56]

One battery-like accumulates energy through faradaic charge transference in the electrochemical process. In contrast, the alternative electrode maintains charge balance by electro-sorbing of visitant electrolyte ions on the functioning surface of the material, such as activated carbon[57][58].

Two separate electrochemical processes, non-Faradaic/Faradaic processes, co-occur from the same apparatus. The preceding electrode, characterized by pronounced reduction-oxidation peaks, is the source of energy supply. In contrast, the latter exhibits the absence of faradaic charge transference, with charge retention occurring solely on the surface as a double layer (DL) liable for power production. Consequently, the electrochemical retort from GCD and HSC's CV with a battery-like negative electrode and a capacitive (pseudocapacitive or EDLC) positive electrode diverges from

ultimate battery characteristics, demonstrating a more capacitive behavior, as demonstrated in **Figure 2.9**.

The elevated capacity and broad operating voltage of HSC enhance their energy retention capability; nevertheless, the battery-like electrode impedes charge kinetics owing to phase change, leading to suboptimal rate performance and reduced cycle life. Various techniques have been proposed to mitigate these difficulties, including producing nanomaterials and using conductive additives such as graphene, OLCs, AC, and CNTs[39][59].

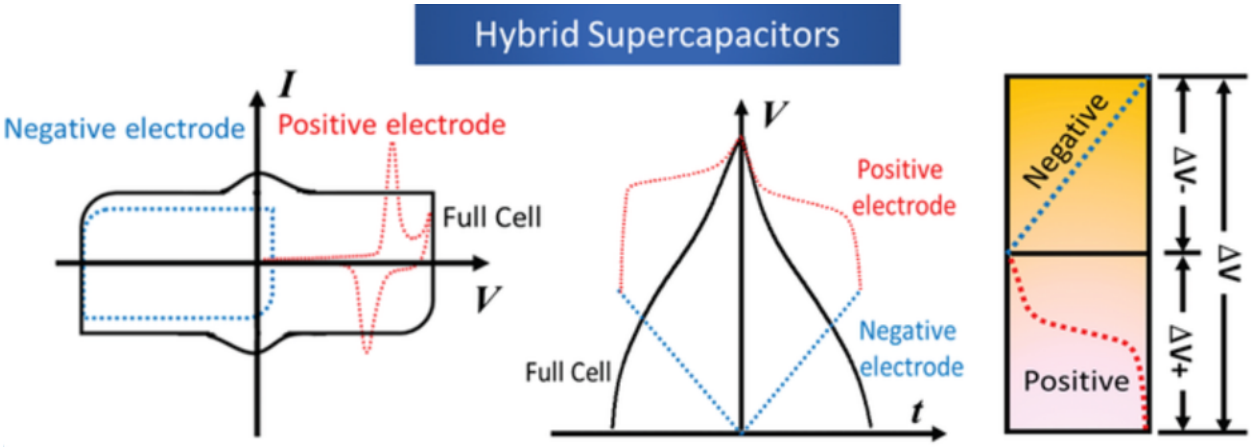


Figure 2. 9: Electrochemical monograms for a hybrid supercapacitor[39]

2.3.2.5. Asymmetric supercapacitors

Asymmetric hybrids integrate non-Faradaic and Faradaic processes by linking an electric double-layer capacitor (EDLC) electrode with a pseudocapacitive electrode. Typically, a carbon-based substance is employed as the cathode electrode, whereas pseudocapacitive materials are the positive electrode, as depicted in **Figure 2.10**. Integrating a cathode carbon electrode with a conductive polymer or metal oxide positive electrode has garnered significant attention.

Asymmetric hybrid capacitors that include these two electrodes alleviate the severity of this trade-off, resulting in superior power and energy densities compared to analogous EDLCs. Furthermore, they exhibit superior cycling stability compared to analogous symmetric pseudocapacitors[60].

Identical to asymmetric hybrids, battery-like hybrids integrate two distinct electrodes; nevertheless, they are characterized by the unique pairing of a supercapacitor electrode with a battery electrode.

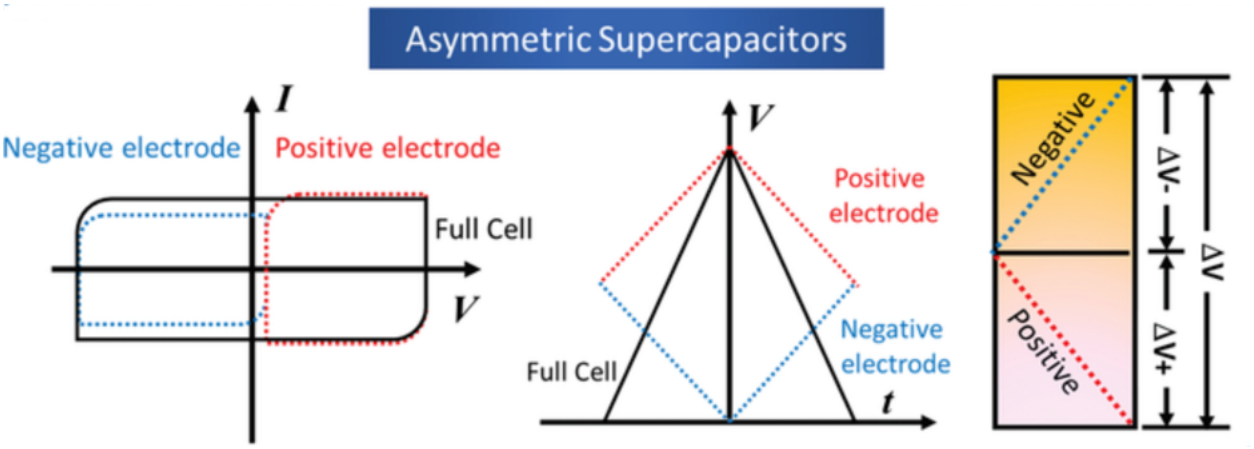


Figure 2. 10: Electrochemical signature of a typical asymmetric supercapacitor [39]

The design addresses the requirement for enhanced energy supercapacitors and high-power batteries by integrating the energy attributes of batteries with the cycle longevity, recharge durations, and power capabilities of supercapacitors. Despite the limited investigational information on battery-type hybrids compared to other supercapacitor variants, the existing data indicates that these hybrids could potentially reconcile the disparity between supercapacitors and batteries. Notwithstanding the encouraging outcomes, the prevailing agreement is that further research is essential to ascertain the complete prospective of battery-like hybrids. Composite

electrodes amalgamate carbon-based materials with either CPs or TMOs, integrating physical and chemical charge retention mechanisms inside a singular electrode. Carbon-based materials offer a double-layer capacitive charge and an extensive surface area framework that enhances the interaction between the deposited electrolyte and pseudocapacitive materials[61][62].

The pseudocapacitive materials augment the capacitance of the composite electrode via faradaic processes. To prevent ambiguity with hybrid supercapacitors, the term asymmetric should be employed when both pseudocapacitive and EDLC electrodes, or one pseudocapacitive and one EDLC electrode, are utilized in a two-electrode system, such as MnO_2 and activated carbon as depicted in **Figure 2.9 and 2.10**. To attain the optimal operating potential difference for the SCs cell, both HSCs and ASCs integrate the voltage windows of the anode and cathode electrodes. Consequently, ($q^+ = q^-$) charge balancing must be executed on either electrode to achieve optimal cell voltage and density. The optimal mass ratio of anode to cathode electrode constituents can be ascertained using equation 2.7[4][63]:

$$\frac{m^+}{m^-} = \frac{C^- \times V^-}{C^+ \times V^+} \quad or \quad \frac{m^-}{m^+} = \frac{C^+ \times V^+}{C^- \times V^-} \qquad Eqn\ (2.\ 15)$$

C^-, C^+, m^-, m^+, V^+ and V^- represent the anode and cathode materials' capacitance, masses, and potential windows. Additionally, specific power and energy densities are computed utilizing **equations 2.16 and 2.17**, which delineate the performance parameters of HSCs and ASCs.

$$E(WhKg^{-1}) = \frac{0.5 \times C \times V^2}{3.6} \qquad Eqn\ (2.\ 16)$$

$$P(WKg^{-1}) = \frac{E \times 3600}{t} \qquad Eqn\ (2.\ 17)$$

V denotes the voltage range in volts, C denotes the capacitance in farads per gram, and t indicates discharge time in seconds. Furthermore, the electrochemical kinetics of battery types, EDLC, and pseudocapacitive electrodes vary and can be differentiated utilizing the Dunn and Trasatti methodologies, which will be further discussed in the following section[64].

2.4. Distinguishing diffusion-governed processes from capacitive processes

The current advancements in intercalation pseudocapacitance have significantly expanded the array of pseudocapacitive constituents. Nonetheless, it is widely recognized that intercalation in batteries is constrained by semi-infinite effusion into the vastness of host materials, as seen by pronounced oxidation and reduction peaks in cyclic voltammetry (CV) curves. While numerous intercalation pseudocapacitive materials exhibit little redox activity in cyclic voltammetry curves, this raises the challenge of determining these diffusion processes without imposing constraints on the intrinsic kinetics. Quantifying the charge retention kinetics of these novel materials is anticipated to be a crucial approach to address this issue. In principle, redox electrode materials exhibit distinct electrochemical characteristics concerning scan speeds in cyclic voltammetry, alternating current in electrochemical impedance spectroscopy, and applied constant current in galvanostatic charge-discharge curves[39][65].

Multiple methodologies have been documented to quantify or differentiate between non-diffusion-limited and diffusion-controlled processes for electrode materials. Among them, cyclic voltammetry (CV) measurements serve as an optimal instrument, as the response current fluctuates with scanning rates based on whether the reduction-oxidation reaction is governed by ion diffusion. The aggregate charges retained in intercalation-like electrode constituents are presumed to be the

aggregate of diffusion-governed Faradaic and capacitive processes. Consequently, it is imperative to ascertain the capacitive influences and diffusion-governed Faradaic processes that affect the overall electrode material's capacity. Basic cyclic voltammetry quantifications at different scanning rates can adequately facilitate distinction since the current response to the regulated sweep rate results from an amalgamation of diffusion-controlled faradaic and surface-mediated capacitive processes[66]. At a specific potential, the correlation between the scan rate (v) and current (i) is articulated by the power rule in **equation 2.18**:

$$i = av^b \qquad \textit{Eqn (2. 18)}$$

This equation's parameter (b) can provisionally characterize the predominant charge storage mechanism. It can be ascertained from the gradient of the log-log plot of (v) and (i), as delineated in **equation 2.19**:

$$log(i) = b\, log(v) + log\ (a) \qquad \textit{Eqn (2. 19)}$$

Where (i) denotes current density, and (a) and (b) represent adjustable parameters determined by graphing log (i) against $\log(v)$. The predominant energy storage system is an adsorption-controlled, purely capacitive mechanism when $b = 1$; If $b = 0.5$, the mechanism is dictated by diffusion. When b falls between 0.5 and 1.0, the mechanism involves both capacitive and faradaic processes (EDLC + Pseudocapacitive)[4]. The power rule expression can be categorized into Faradaic and capacitive current responses with identical voltammetric principles outlined in **equations 2.20** and **2.21**. The EDLC surface-governed response is represented by[4]:

$$i \propto v \Rightarrow i = k_1 v \qquad \textit{Eqn (2. 20)}$$

While the pseudocapacitive diffusion-governed current response is expressed as:

$$i \propto v^{1/2} \Rightarrow i = k_2 v^{1/2} \qquad \textit{Eqn (2. 21)}$$

Equations 2.20 and **2.21** can be utilized to compute the aggregate current response at a specified potential, as demonstrated in **equations 2.22** and **2.23**:

$$i = k_1 v + k_2 v^{1/2} \qquad \textit{Eqn (2. 22)}$$

Where:

$$i/v^{1/2} = k_1 v^{1/2} + k_2 \qquad \textit{Eqn (2. 23)}$$

With k_2 and k_1 denoting constants that characterize the contributions of faradaic and capacitive currents, respectively. Consequently, by graphing $i/v^{1/2}$ vs $v^{1/2}$, the parameters of k_1 and k_2 can be determined. The contributions of capacitive current can be delineated from faradaic contributions by assessing the k_1 value at different scan rates and voltages[4][67].

2.5. Supercapacitor electrode materials

Selecting appropriate electrode materials and their production is indispensable for improving the capacitance performance of supercapacitors[68]. Supercapacitor electrodes must exhibit thermal stability, corrosion resistance, large surface area, adequate chemical stability, superior electrical conductance, and good wettability. They should also be ecologically benign and economical. Moreover, their capacity to transmit faradaic charge is crucial for improving capacitance performance. The specific capacitance aspect is influenced by (SA) surface area and other critical characteristics, including morphological modification, pore shape, pore size distributions, and the accessibility of pores to the electrolyte[69][70].

Consequently, two critical prerequisites for the design of a supercapacitor device are the optimization of pore morphology and dimensions, such as cylindrical, circular, spherical, and vertical rectangular shapes, and the enhancement of electrochemically functional sites by choosing electrode materials possessing significant SSA to promote the movement of electrolyte ions. The electrode material with fewer pores provides more capacitance and, thus, higher energy density. However, a more minor pore size results in a more considerable ESR, diminishing power density[71][72]. The intended use of the electrode material influences the choice of materials. Moreover, an appropriate size distribution might enhance retention capability, indicative of high-power density in a supercapacitor device. The efficient distribution of meso/micropores in the electrode material facilitates rapid ion and mass transport over a continuous channel, improving electrolyte accessibility and rendering the material appropriate for supercapacitor uses. The electrode materials are partitioned into three primary categories: conducting polymers, transition metal oxides (TMOs), and carbonaceous materials[73][74].

2.5.1. Carbon-based nano-structured materials

The capacitance of EDLC devices primarily originates from the charges accumulated at the contact between the electrolyte and the electrodes[75]. Thus, the capacitive efficiency of an EDLC unit is significantly influenced by the distribution of pores, pore dimensions, and specific surface areas of the electrode materials[76]. Carbonaceous materials are exploited as electrode materials for EDLC primarily owing to their beneficial properties, including budget-friendly, high specific surface area, ease of synthesis, and environmental sustainability[69][77]. Carbon-based materials may be utilized in diverse forms within a supercapacitor device, including fibers, foils, monoliths, and powders [78]. Numerous prevalent instances of materials composed of carbon include

activated carbon (ACs), carbon nano-onions (CNOs)/onion-like carbons (OLCs), carbon aerogels, activated carbon fibers (ACFs), graphene, carbon cloth (CC), and carbon nanotubes (CNTs), along with various carbon-based composite materials, which serve as materials for electrodes in supercapacitor (SC) devices[69][79].

2.5.1.1. Activated carbon materials (ACs)

Renewable biomass is considered a promising carbon precursor for creating sustainable products and has been thoroughly researched. A diverse array of biomass wastes is chosen for the preparation of activated carbon, including tree bark[80], lotus-flower[81], bamboo[82], walnut shells[83], marula nutshells[84], plant blossoms, and chicken bones[85], among others. Biomass is an excellent precursor for activated carbons due to its eco-friendliness, simplicity, sustainability, widespread accessibility, recyclability, and reduced environmental and biological harm. It is essential to thoroughly comprehend their features to utilize activated carbons derived from various biomasses as electrodes for supercapacitors [86][87]. Despite activated carbon offering exceptional cycle life and high-power density for EDLC, its low specific capacitance (1250-2500 S/m) and energy density significantly constrain the future applicability of activated carbon-based supercapacitors[86].

Activated carbons exhibit a complex porous architecture consisting of mesopores extending from 2-50 nm, macropores surpassing 50 nm, and micropores smaller than 2 nm, as depicted in **Figure 2.11,** resulting in a high specific surface area[87]. As previously indicated, activated carbon can be synthesized through two stages, utilizing physical or chemical activation from diverse carbon-rich organic precursors. The carbonization process entails the treatment of precursors with oxidizing

gases, including steam, carbon dioxide, and air, at elevated temperatures varying from 700-1200°C under a stable atmosphere to yield amorphous carbon. During the activation phase, the temperature applied ranges from around 400°C -700°C[72][88].

The chemical-induced activation technique transpires in the occurrence of activating chemicals such as alkalis, acids, carbonates, and chlorides, including KOH, H_3PO_4, NaOH, and $ZnCl_2$, resulting in a porous framework inside the carbon particles matrix[90]. Activated carbon exhibits numerous physicochemical features contingent upon the carbon precursors employed and the activation techniques utilized, significantly affecting its porous structure, surface area, and pore dimension spread. As said, activated carbon might be derived from numerous carbon-loaded organic materials. The activated carbon derived from coconut shells possesses more micropores than charcoal ones [91].

Research indicates that a narrower pore dimension spread may be effectively quantified for activated carbon fiber derived from activated carbon with an SA of around 2500 m^2/g. The specific capacitance parameters of electrodes for activated carbon in water-based electrolytes range from 100-300 F/g, surpassing those in organic solutions below 150 F/g due to the greater ionic size in organic electrodes[92].

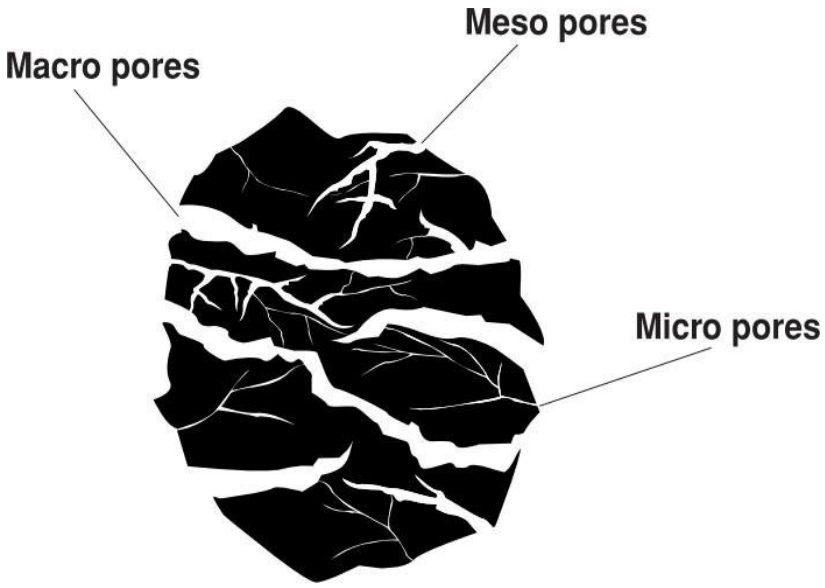


Figure 2. 11: Schematic diagram depicting the porous architecture of activated carbons[89]

A notable drawback of activated carbon lies in its poor energy density. Moreno-Fernandez et al. demonstrated that the specific capacitance parameter of 200 F/g is achievable by synthesizing activated carbon fiber monoliths, resulting in a threefold increase in density[87]. The electrochemical functionality of activated carbons can be enhanced through various strategies, including surface modification via oxidation, the fabrication of composites with activated carbon and other carbon nanomaterials, the incorporation of polymers within the carbon substrate to create composite electrodes, doping with Sulphur and oxygen functionalities, and the alteration of the Fermi level placement of activated carbons utilizing ultrasonic radiation[69][93].

2.5.1.2. Graphene materials

Graphene is a two-dimensional structure one atom thick, composed of sp^2 linked carbon atoms organized in a honeycomb crystal lattice. Since its discovery by Novoselov and Geim, graphene has been at the forefront of research across multiple scientific and technological domains, owing to its remarkable qualities[94]. It possesses exceptional chemical and thermal stability, facilitating the extended lifespan of graphene-based supercapacitors across a wide array of electrolytes, superior electrical conductivity of 200,000 cm^2/vs, and mechanical strength, which enhances electron mobility and optical transparency. Graphene exhibits adjustable structure-property correlations contingent upon its fabrication technique[95][96].

Considering energy conversion and storage demands, graphene provides a highly adjustable electrochemically active surface area (EASA) of (2630 m^2/g). It exhibits remarkable electronic conductivity owing to freely mobile high-mobility pi electrons in its orbitals, both beneath and above the graphene sheets[97][98]. Pi-orbitals' overlap strengthens C-C bonds, influencing the bonding and anti-bonding pi-orbitals' conductance and valence band states. The electronic conductivity of graphene is temperature-independent and (4.5×10^3) times greater than that of copper, resulting in a resistance of (10^{-6} Ohms cm), which is significantly lower than that of silver[99]. The electronic characteristics of graphene can be augmented through structural modifications, including functionalization, heteroatomic doping, and composite materials tailored to specific system requirements[100][101]. Graphene is a carbon allotrope consisting of a single atom in thickness, serving as the structural foundation for all other variations of carbon:(1) 0-dimensional (0D) fullerenes, formed by encapsulating graphene layers/sheets into a spherical

configuration (Buckyball), (2) 1-dimensional (1D) carbon nanotubes (CNTs), created by twirling graphene layers into a tube-shaped form, and (3) 3-dimensional (3D) graphite, constituted by stacking numerous strata of distinct graphene layers adhered by Van der Waals forces, as illustrated in **Figure 2.12**[102].

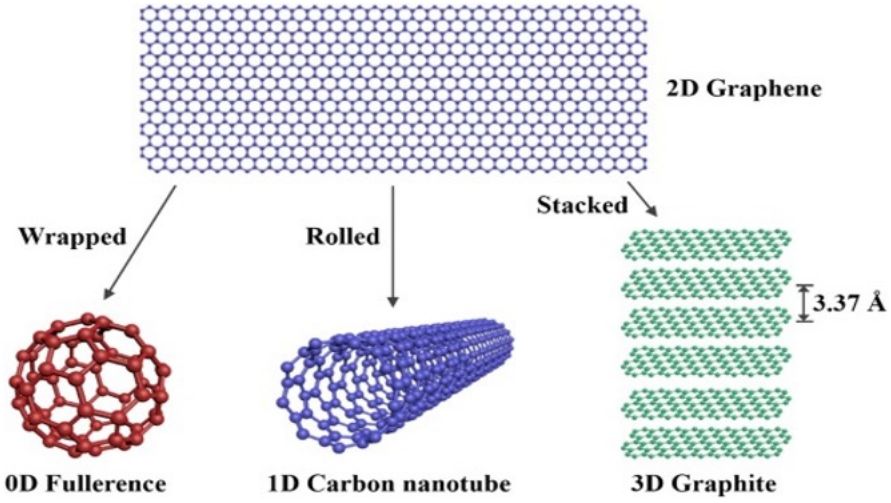


Figure 2. 12: Graphene carbon allotropes 0D fullerene,1D carbon nanotubes, and 3D graphite

Graphene, in its numerous forms, such as functionalized graphene, doped graphene with heteroatoms like iodine or nitrogen, graphene composites with polymers or transition metal oxides, and reduced graphene oxide, has been extensively developed and studied as electrodes for supercapacitors[101]. Graphene provides diverse potential for structural modification depending on the reaction procedures, making it an optimal method for designing application-specific materials. Numerous novel graphene structures have been documented, including zigzag graphene, graphene foams, pillared graphene, GNRs, graphene fibers, GQDs, and 3D-printed graphene structures, with critical applications in various energy storage systems[103][104].

Numerous processes exist for synthesizing diverse forms of graphene, including the unzipping of CNTs, CVD, micro-mechanical exfoliation, epitaxial growth, chemical and electrochemical procedures, intercalation techniques in graphite, and arc discharge methods[105]. Graphene may serve as a material for electrode in high-efficiency supercapacitors, as it is independent of spread of pores in the solid-state, unlike other carbon-containing materials, including carbon nanotubes and activated carbons. Another positive aspect of employing graphene as an electrode material is the availability of both external outer layer of the graphene layer/sheet by the electrolyte[97][106].

2.5.1.3. Onion-like carbons (OLCs)/Carbon nano onions (CNOs)

CNOs are carbonaceous nanostructures consisting of annular fullerene shells in a zero-dimensional shape and are classified as nanoparticles typically measuring less than 10 nm. It comprises several disordered and flawed shells arranged in a "Russian doll-like" configuration[107]. CNOs are a relatively recent addition to the family of carbon nanomaterials, composed of multilayer fullerene-like graphene shells[108]. The onion-like semi-spherical and multi-walled fullerene were independently described by Sumio Iijima in 1980 and Daniel Ugarte in 1992. In a 1980 publication, Lijima referred to carbon onions as 'polygonized carbon blacks,' characterized by numerous sheets of graphite organized in closed, polyhedral shells[109][110]. However, the idea does not garner as much acclaim owing to the simultaneous development of (CNTs). Before the identification of carbon nanoonions (CNOs) by Smalley, Curl, and Kroto in 1985, Lijima initially detected them in vacuum-deposited films[107][111]. Ugarte subsequently devised a technique to create carbon nanostructures by irradiating carbon soot with an electron beam[112].

In 1992, Ugarte described an unusual curling and closing of carbon nanoparticles organized inside a cage or multi-layered spherical carbon nanostructure, commonly called CNOs[113]. Its distinctive multi-layered architecture renders it a compelling enhancement to the carbon family. Carbon onions' form, size, and chemical composition can differ based on the synthesis method employed[109]. The predominant technique is graphitization, in which nanodiamonds are subjected to elevated temperatures in a vacuum or inert gas. Due to their diminutive size and superior carbon ordering, carbon onions are frequently called nanocarbon onions. Despite being a relatively diminutive nanocarbon material, its surface area can attain 600 m^2/g[114].

Currently, there is no standard for describing carbon onions, and the literature does not provide a consistent definition. Confusion over terminology is a significant issue in nanocarbons[107]. Most reports often refer to “carbon nano-onions,” “carbon onions,” or “onion-like carbon.” The authors of other studies disagree with the terminology used for the Sp^2 hybridized carbon nanostructures by Grobert, Suarez-Martinez, and Ewels, suggesting referring to these materials as multi-wall fullerenes. The unifying nomenclature of carbon onions is based on the geometrical classification of these materials. It does not consider the various characteristics of carbon ordering, such as particle size and shape[115][116].

On the other hand, the concept of fullerene may be arguable when describing large structures, such as those that are over 100 nm in size. Like other terms, the term onion-like carbon is vague when describing structures like an onion[107]. Moreover, the differentiation between multi-wall, single-wall, few-wall, and double-wall systems is not ideal for describing carbon onions since practically all are multi-walls. The distinguishing characteristics of carbon onions based on their shape, such

as their polyhedral or spherical appearance, are not practical or quantifiable. Considering the similarities of carbon nanotubes' terminology, we suggest only referring to these materials when they have at least four shells. These include those smaller than 100 nm, defective structures, and a polyhedral or spherical shape[115].

The distinguishing characteristic of carbon onions is their multi-shell structure. This is the basis of the carbon onion's terminology, which also includes hollow and carbon onions with core components, such as nanodiamonds or metal clusters[114]. As with other materials, the issues related to the classification of carbon onions are more complex than those related to molecules. According to researchers, carbon onion terminology does not apply to molecules mainly because of the materials' variable composition. Since the chemical modifications occurring in these materials are considered when describing them, using this term becomes meaningless. The term “nanodiamonds” refers to single-walled diamond structures and has been suggested due to the differentiation between these materials. However, it is impossible to define the term clearly due to the complexity of the process involved. Therefore, the structures of carbon onions must be thoroughly described to provide a scientific basis for comparison[116][117].

The structure of CNOs consists of pentagonal and hexagonal rings, with carbon atoms located at the apex points, creating delocalized pi-electron networks encompassing the entire molecule. The graphite layers associated with the CNOs are disorganized and faulty. The heptagonal and pentagonal carbon rings can be modified. It possesses several unique properties that render it suitable for various purposes. The distinctive characteristics of multi-walled fullerene enable its use across diverse applications, ranging from medicine to electronics[108][118].

They exhibit superconducting properties, effective radical scavengers (antioxidants), and feature an extended shelf life. They can be readily altered to customize qualities as derivatives, facilitating modifications to their electrical structure, solubility, and physical characteristics. **Figure 2.13** illustrates multi-walled carbon nanotubes (CNO). Owing to their diminutive diameter and low toxicity, CNOs can be utilized in both in vitro and in vivo applications[119][120].

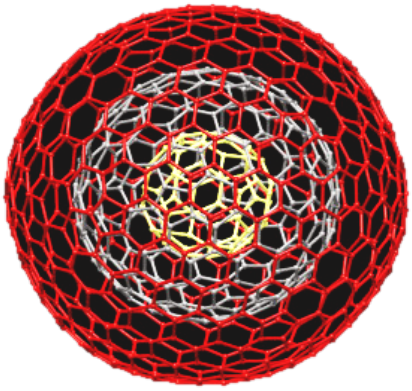


Figure 2. 13: Schematic illustration of onion-like carbon

In addition to their exceptional dielectric qualities and thermal stability, CNOs are crucial components in instruments for detecting certain medical compounds such as hormones and enzymes. One of their most attractive attributes is their capacity to accept extra electrons reversibly, coupled with a substantial surface area resulting from their spherical morphology. Nevertheless, scant assessments have been disseminated regarding the advancements of CNOs for application in supercapacitor devices[121][122].

2.5.1.3.1. Synthesis, functionalization, doping, and co-doping of onion-like carbons

Numerous studies have been conducted on fullerene's properties to understand its applications. Due to their exceptional physical characteristics, OLCs are known to be helpful in various areas, such as batteries and catalysts[112]. These multi-shelled nanostructures comprise concentric graphitic layers with SP^2 hybridization. Over the years, various techniques have been devised to enhance the OLCs' capacitance. One of these involves combining polymers and metal oxides. Another approach is incorporating porosity into the OLCs' outer shells through chemical activation. Heteroatom doping is a commonly used technique to eliminate the need for complex chemical synthesis routes[123][124].

Urgate et al. developed the initial carbon nanoonions (CNOs) by beaming carbon particles with an electron beam[114]. Subsequently, CNOs have been produced using techniques including laser ablation, electron beam irradiation, arc discharge, and flame pyrolysis. These technologies utilize various carbon-containing materials, including waste engine oil, flax seed oil, coconut oil, etc. Numerous techniques for synthesizing carbon nanoonions (CNOs) have been explored, with significant emphasis placed on the catalytic chemical vapor deposition (CCVD) technique utilizing diverse carbon precursors[125]. In conventional CCVD processes, metals like Ni and Fe are catalysts for synthesizing core-filled CNOs. Nonetheless, this approach preserves the metal nanomaterials as contaminants inside the limits of the CNO cores. The flame pyrolysis (FP) approach, described in this paper, is a substitute blueprint for the incessant synthesis of catalyst-free solid carbon nanostructures (CNOs) under ambient circumstances, as emphasized in **Chapter 3**[126].

Various studies have been conducted on the chemical functionalization of nanostructures of onion-like carbon (OLCs) to improve their solubility and control their processability. The degree to which functionalization is carried out is usually related to the size and strain of these OLCs[127].

Due to the higher curvature of small-sized OLCs (10-100nm), they are more reactive than bigger ones. This causes an increase in the C atom's pyramidalization. The functionalization of these OLCs surfaces involves the creation of functional groups that help decrease the long-range van der Waals forces[128]. These groups can also increase the OLCs' matrix or solvent attraction, resulting in a homogenous dispersion. The various functionalization methods OLCs utilize can improve their reactivity solubility and provide avenues for further modification. Exohedral covalent functionalizing involves the addition of two or more covalent bonds to serve as substitutes for the main structure. This process can also trigger secondary reactions, improving the ability of the OLCs to be used in organic and water-based applications. Introducing hydrophilic groups and water-soluble compounds onto the surface of the OLCs can improve their biocompatibility and shelf life[129][130].

The disadvantage of this process is that it mainly focuses on creating functional groups affixed to the OLCs. It can also change the hybridization between the Sp^2 and Sp^3 moieties on the graphene sheet/layer, promoting the oxidation of the OLCs. Another method is the non-covalent approach, which involves the generation of functional moieties on the surface of the OLCs without disturbing the graphene sheet's π system. The hydrophobic part of adsorbed molecules can attach to various interactions, including π-π and CH-π. On the other hand, the hydrophilic part can provide

aqueous solubility. The non-covalent approach involves the stacking of carboxylic groups through the P-P interactions. This method can create stable aqueous conditions and limit the impact of toxic substances on the surface[131][132].

The surfactant concentration and Nature affect the dispersion's stability, and the polymer wrapping around the OLC surface is solvent-dependent. Characterizing the functionalization process in the presence of other carbon allotropes is challenging. One of the most promising routes to improve the surface's stability is reducing the carbon allotrope using alkali metals. The disadvantages of this process are that the surfactant concentration and Nature affect the dispersion's strength. The polymer wrapping around the OLC surface is also solvent-dependent. Characterizing the functionalization process in the presence of other carbon allotropes is challenging. One of the most promising routes to improve the surface's stability is reducing the carbon allotrope using alkali metals[133][134].

The actions of heteroatom doping generally influence the characteristics of carbon nanomaterials. This process can broaden their potential applications by introducing new active sites. Among the elements that are commonly applied are nitrogen and boron. Boron atoms can be easily incorporated into carbon materials because of their three valence electrons. It has been demonstrated that specific carbon nanomaterials, including graphene, CNTs, and (GNRs) graphene nanoribbons, exhibited better electronic and catalytic properties when they were B-doped. The doping level of these carbon materials is a crucial parameter[135].

The boron level in the solution can affect the reactivity of specific carbon nanomaterials. B-doped onion-like carbons have not been studied extensively, suggesting that further theoretical studies

on their electronic and structural properties are needed. Doping carbon materials with nitrogen atoms has been considered as an effective approach to strengthen catalytic performance[136].

A nitrogen atom with five valence electrons can be an electron donor, creating n-type carbon materials. Adding extra electrons can enhance the selectivity and reactivity of electrocatalytic processes. It can also affect the π electron delocalization. The doping level is a vital parameter that can be used to control the different properties of a material. Significant variations in the positions of the Fermi level and the B states, along with the orbital frontier between the two systems, imply that the distribution of B dramatically affects the catalytic and electrochemical attributes of OLCs[137].

In this regard, a viable technique to augment the catalytic activity of metal-free carbon-based catalysts is the insertion of heteroatom dopants such as nitrogen, boron, Sulphur, or phosphorus. This method entails positioning atoms with differing electronegativity adjacent to carbon atoms to generate active sites[138]. Co-doping with various elements represents a viable strategy to attain synergistic effects. Co-doping with nitrogen and Sulphur has improved oxygen reduction reaction activity due to the distribution of spin density and charge density from the two dopants. N and B are a well-known pair of co-dopants that create active sites in carbon by leveraging the differing electronegativities of N, B, and C. N possesses a higher electron density ($\chi = 3.04$) relative to C ($\chi = 2.55$) whilst B exhibits more significant electron deficiency ($\chi = 2.04$)[139][140]. Boric acid and ammonia are prevalent precursors for nitrogen and boron, respectively, and these elements were incorporated simultaneously or sequentially[141].

2.5.1.4. Carbon nanotubes materials (CNTs)

Lijima initially identified MWCNTs in 1991 and subsequently announced the presence of single-walled carbon nanotubes (SWCNTs) two years thereafter[110]. The thermal conductivity of carbon nanotubes (CNTs) exceeds that of copper by over fivefold, and their tensile strength reaches 100 GPa, surpassing steel by more than one hundred times. Furthermore, carbon nanotubes possess numerous additional exceptional qualities, including low electrical resistance, robust chemical stability, excellent surface area, and low density. These outstanding features render carbon nanotubes extensively utilized in semiconductors, aircraft, renewable energy, and other domains[142][143].

The primary techniques for preparing CNTs include arc discharge, CVD, and laser ablation. CNTs synthesized using arc discharge exhibit slender tube walls and superior crystallinity, although they possess low purity and yield. Laser ablation can be conducted continuously to produce high-purity and high-quality carbon nanotubes (CNTs). Nevertheless, the yield is insufficient for industrialization. CVD is presently the predominant technique employed for the synthesis of CNTs. The reaction process is easily controllable, the reaction temperature is comparatively low, and the yield is substantial[144][145].

The primary issue with CVD is the low crystallinity of CNTs, yet their low resistance and excellent surface area render them acceptable as electrode materials for supercapacitors[146]. Like OLCs, CNTs exhibit positive curvature, enhancing their performance compared to conventional porous carbon materials, achieving a maximum energy density of 155.6 Wh/Kg, a high-power density of

263.2 W/Kg in ionic liquid, and a specific capacitance of 290.4 F/g[69]. Moreover, they have documented a noteworthy phenomenon termed electro-activation, wherein the specific capacitance of graphene and CNTs/graphene remained stable after prolonged cycling in the 1M KCL electrolyte and exhibited a significant rise. Carbon nanotubes (CNTs) can be cataloged into two types: SWCNTs and MWCNTs. The elevated conductivity of carbon nanotubes enables their dual function as electrode materials and current collectors, eliminating the need for supplementary current collectors[69][147].

This significantly decreases the resistance at the interface of the current collector and the electrode material, enhancing the power density. Simultaneously, it can diminish the overall weight of the supercapacitors, which is highly significant in the design of small supercapacitors. Furthermore, acid treatment and polyethyleneimine coating of CNTs can markedly alter the resting potential of CNT-based supercapacitors[148]. By modifying the resting potential, the operational voltage of the supercapacitors can be elevated, thus augmenting the energy density. The swift advancement of wearable electronics has garnered significant interest in flexible electrode materials. The exceptional mechanical specifications of carbon nanotubes render them one of the optimal materials for flexible electrodes. Carbon nanotubes (CNTs) may serve as electrode material in conjunction with innovative composites, transition metal oxides, and MXene materials, that are prevalent electrode materials for supercapacitors[149][150].

2.5.2. Transition metal hydroxide and oxide-based materials

TMCs are the predominant redox-active materials utilized as electrode substances in supercapacitors, particularly hybrid supercapacitors, primarily in the form of hydroxides and oxides. Transition metals (TMs) are many and mainly utilized in the composition of TM(OH)s and transition metal oxides (TMOs), including Ni, Mn, Ru, Fe, Ti, Co, Mo, Nb, and V. Transitional metal oxides serve as alternative materials for supercapacitor electrodes, offering superior power and energy due to their elevated specific capacitance and reduced resistance compared to carbon materials, in addition to their excellent conductivity[69][151].

CPs and TMOs are the predominant redox pseudocapacitive materials because they exhibit rapidly reversible redox reactions, resulting in extended operational cycles and elevated specific capacitances. Various transition metal oxides (TMOs), as defined by B.E. Conway, include Fe_3O_4, RuO_2, NiO, IrO_2, MnO_2, CuO, Co_3O_4, and V_2O_5, wherein their charge storage mechanisms are predicated on faradaic behavior. Additionally, the layered (TM (OH)s) including Co $(OH)_2$, Ni $(OH)_2$, and FeOOH with big space between the successive layers enable adequate reduction-oxidation reactions boosting the capacitance parameter of the electrodes in supercapacitors[152][153].

Nonetheless, the TM(OH)s may provide enhanced charge retention mechanisms relative to their oxide counterparts, albeit the electrical conductance of the equivalent oxides is superior. TM(OH)s have shown inferior structure resilience and, thus, diminished rate capability or cycle efficiency relative to their comparable oxides. Nonetheless, many techniques exist to mitigate this constraint

and enhance the cycling endurance of the material, including the layer-by-layer construction of TM(OH)s via cation and anion doping processes. Even though transition metal-containing materials are primarily classified as battery-related materials, they also have capacitive functionality[154][155].

2.5.2.1. Ruthenium Oxide (RuO_2)

Ruthenium oxide is extensively researched as a TMO for supercapacitor electrodes owing to its exceptional thermal and chemical stability, wide potential window (1.2 V), high metallic conductivity, prolonged cycle life, excellent rate capability, substantial theoretical capacitance (1200-2200 F/g), and highly reversible redox reactions[156]. Moreover, the exceptional characteristics of RuO_2, involving its field pollution behavior, catalytic activity, metallic conductivity, and electrochemical oxidation-reduction attributes in both crystalline and amorphous forms, render RuO_2 advantageous for a range of scientific and industrial applications, such as thin or thick resistors, electronic devices, ferroelectric films, integrated circuit development, and the latest supercapacitors. Furthermore, parameters such as annealing temperature, crystallinity, and particle size influence the pseudocapacitive performance of RuO_2[157][158].

Notably, increased crystallinity of RuO_2 correlates with reduced specific capacitances due to its dense structure, which restricts the depletion and insertion of ions and electrons, thereby enhancing electrochemical impedance. RuO_2 materials are costly, perhaps restricting their widespread usage[159]. To create affordable materials, RuO_2 hybrids are combined with other carbonaceous or pseudocapacitive substances to minimize the quantity of RuO_2 without compromising activity.

Ruthenium dioxide (RuO_2) exhibits three oxidation states: Ru^{2+}, Ru^{3+}, and Ru^{4+}. The prompt bidirectional reduction-oxidation process of RuO_2 is demonstrated by **equation 2.24**[160][161]:

$$RuO_x(OH)_y + \delta H^+ + eH^+ \rightarrow RuO_{x-\delta}(OH)_{y-\delta} \dots (0 < \delta > 2) \quad \textit{Eqn (2. 24)}$$

Synthesizing composites can enhance the efficiency of RuO_2 and decrease the expense associated with RuO_2 electrodes. The synergistic action of materials concurrently enhances the electrode's electrochemical functionality. Diverse types of RuO_2-based electrodes have been synthesized, including carbon material RuO_2, metal sulfide RuO_2 electrodes, RuO_2 electrodes adorned with carbon nanotubes, metal oxide RuO2, and carbon cloth integrated with RuO_2 nanorods by annealing and chemical vapor deposition methods[162][163].

2.5.2.2. Manganese dioxide (MnO_2)

MnO_2 is a potential electrode material for electrochemical capacitors (ECs), offering advantages such as superior electrochemical characteristics, abundant availability, environmental sustainability, and cost-effectiveness. Faraday's law indicates that the predicted specific capacitance of MnO_2 can reach approximately 1370 F/g during the Mn^{4+} to Mn^{3+} transition; nevertheless, the limited reversibility of the electrochemical redox process constrains its practical application. Furthermore, the limited conductivity of pure MnO_2 as an electrode material results in a relatively modest capacitance signal[164][165].

Recently, numerous researchers demonstrated the favorable capacitive properties of neutral aqueous electrolyte solutions across an extensive potential range, which justifies the application of MnO_2 in pseudocapacitor studies. Two charge storage processes have been proposed for the

MnO_2 electrode materials. De-intercalation/intercalation of protons (H_3O^+) or group one metal cations A^+ such as K^+, Li^+, and Na^+ into the bulk of oxide particles, accompanied by the oxidation/reduction of the Mn ion as described in **Equations 2.25** and **2.26**[164][166]:

$$MnO_2 + H^+ + e^- \leftrightarrow MnOOH^+ \quad \textit{Eqn (2. 25)}$$

$$MnO_2 + A^+ + e^- \leftrightarrow MnOOA^+ \quad \textit{Eqn (2. 26)}$$

The other aspect pertains to the desorption/adsorption process of protons and alkali metal cations in the electrolyte on the surface of the amorphous MnO_2 electrode, as depicted in **equation 2.27**:

$$MnO_{2_{surface}} + A^+ + e^- \leftrightarrow MnO_2^- A^+_{surface} \quad \textit{Eqn (2. 27)}$$

The physical and chemical surface characteristics are crucial to the electrochemical functionality of MnO_2, particularly cyclic durability, which is significantly influenced by the structure regularity of the pore-rich MnO_2. Due to their porous characteristics, the amorphous and nanocrystalline MnO_2 provide facile cation and ion diffusion. Reports indicate that α and δ exhibit the largest specific capacitances among all phases of crystalline material. Another study demonstrated that the energy retention mechanism depended on the quantity of manganese (Mn) centers as active sites. It was disclosed that an increase in the proportion of the functioning Mn centers, resulting from a reduction in crystallographic dimension, enhance specific capacitance[167][168].

Recent investigations have revealed that the configurational surface-to-bulk ratios, also known as specific surface area (SSA), significantly influence the electrochemical behavior of MnO_2. Additionally, the hydration state of MnO_2 plays a crucial role in its cyclic stability, while the specific capacitance depends on the structure of the subsequent material. Despite their beneficial

properties, supercapacitors—especially those using MnO_2-based electrodes—face challenges such as reduced specific capacitance, poor cycling stability, and high charge-discharge rates. These issues arise from factors such as MnO_2 dissolution, large band gaps, low ionic diffusion coefficients, and poor conductivity. [169][170].

2.5.2.3. Nickel Oxide (NiO)

Among many metal oxides, nickel oxide (NiO) is a viable choice for pseudocapacitors owing to its cost-effectiveness, high theoretical capacitance, excellent chemical and thermal stability, pseudocapacitive behavior, and accessibility. The essential requirements for NiO-based electrodes in supercapacitors are as follows: (i) they must exhibit a high specific surface area, (ii) the metal should exist in various oxidation numbers that coexist across a potential spectrum, (iii) electrolyte ions must be able to freely de-intercalate from the lattice upon reduction and embedded within the oxide matrix upon oxidation, (iv) the oxide must possess electrical conductivity[171][172].

The effectiveness of nickel oxide-based materials with pseudocapacitor properties is determined by the reductive-oxidative processes involving NiO or Ni $(OH)_2$ in alkaline electrolytes. This can be summarized in **equations 2.28** and **2.29**. The formation of NiO can be explained through two main propositions. The first suggests that NiO initially converts to Ni (OH)2 in an alkaline electrolyte, followed by an electrochemical reaction between NiOOH and Ni $(OH)_2$. The relationship between these two propositions can be described as follows: [173][174]:

$$NiO + OH^- \leftrightarrow 2NiOOH + e^- \qquad \textit{Eqn (2. 28)}$$

$$NiO + H_2O \leftrightarrow NiOOH + H^+ + e^- \qquad \textit{Eqn (2. 29)}$$

Transforming Ni^{2+} into NiOOH by losing electrons leads to supercapacitive mechanism within these two ideas. Most scientists favor the first preposition; however, the second theory is also pragmatic. NiO will react with OH^- in the alkaline-based electrolyte to generate Ni $(OH)_2$, contributing to a portion of the capacitance. As previously stated, in pseudocapacitive materials, the Faradaic electrochemical processes transpire only at the surface and near-surface of NiO; thus, surface features, including pore dimensional spread, surface area, and shape, are crucial to charge storage mechanisms[175][176].

Owing to the limited relationship between the electrochemical functionality of NiO and its surface area and porosity, contemporary research has predominantly focused on the investigation of morphology and synthesis methods of materials. Transition metal oxides currently represent the predominant category of electrode materials. Numerous investigations indicate that bare metal oxide electrodes can provide elevated energy densities and substantial specific capacitance at low scan rates, rendering them unsuitable for practical applications. The conductivity of metal oxides is exceedingly low. These materials' pore size distribution and surface area are challenging to regulate. NiO is frequently utilized as electrodes in faradaic rechargeable battery types[177][178].

2.5.2.4. Nickel Hydroxide

Bode et al. stated that (Ni $(OH)_2$) exhibits two polymorphic forms: β and α. β and α-Ni $(OH)_2$ possess an identical hexagonal layered structure within the brucite layers. The brucite-type structure of β-Ni $(OH)_2$ comprises of films/layers of Ni $(OH)_2$ that are free of intercalated species and precisely stacked[179]. In contrast, the α-Ni $(OH)_2$ hydrotalcite-type structure contains intercalated anions (chloride, nitrate, sulfonate, and carbonate) and water (H_2O) molecules, leading

to enhanced electrochemical activity and a more significant interlayer gap compared to β-Ni $(OH)_2$. Furthermore, Ni is found in α-Ni $(OH)_2$ with an oxidation state of +4 and a general oxidation state ranging from 3.7 to 3.3, which yields excellent electrochemical features compared to β-Ni $(OH)_2$. The robust ionic bonds among H^+, Ni^{2+}, and O_2 inside each layer, coupled with the weak interactions between neighboring layers, result in the tightly stacked structure of Ni $(OH)_2$[180][181].

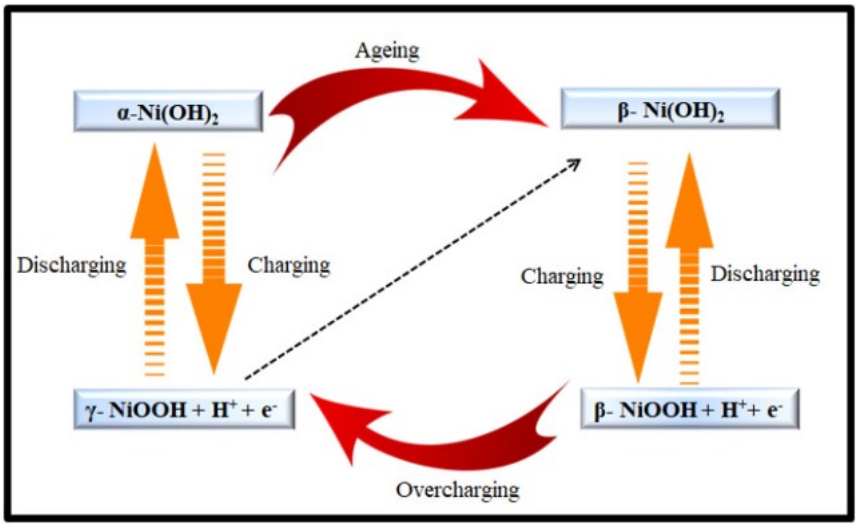


Figure 2. 14: flow diagram showing pristine Ni $(OH)_2$ phase shifts during the charge-discharge process[179]

Ni $(OH)_2$ experiences a phase shift during the discharging-charging process, as illustrated in **Figure 2.14**. the change of both β and α-Ni $(OH)_2$ phases into β and γ-NiOOH phases with states of 3.7-3.3 and 2.9 oxidation state of Ni correspondingly, during the redox process would greatly boost the specific capacitance of the electrode material. β -Ni $(OH)_2$ can be further charged to yield γ-NiOOH, which contains potassium ions and H_2O molecules from the alkaline electrolyte[182]. Concurrently, the production of Ni $(OH)_2$ occurs during discharging. α-Ni $(OH)_2$ together with $CO_3^{2-}$and water is generated when γ-NiOOH is released upon passing α-phase. Various methods

can create numerous nickel hydroxide nanostructures, including nanoplates, nanoribbons, and nanobelts. The synthetic process employed the architecture of the novel materials and their physical and chemical features, notably electrochemical properties[183][184].

2.5.3. Conducting polymers

Conducting polymers (CPs) have gained popularity in the last decade owing to their electrical and optical properties, like metals. As an inorganic material alternative, it has spurred real-world and primary research. CPs feature irregular double (Π)/single (δ) bonds and C=C conjugation, which gives them intrinsic optical, abundant electron affinities, electrochemical, electric/electronic, and low ionization properties[185]. Due to their low cost, elevated flexibility, ecological stability, and ease of synthesis, CPs are used in many versatile applications. CPs outperform inorganic materials in corrosion-free, tunable electrical conductivity, shape control, surface morphology, flexibility, and chemical variety. CPs' electric conductivity is classified by their electron (e^-) and proton (ion) conducting polymers (redox polymers and ICPs): electron delocalization through conjugated systems like polypyrrole (PPy) and polyaniline (PANI) and electron exchange reaction between the adjusting redox sites[186][187].

Chemical or electrochemical methods can synthesize CPs. Chemical methods like addition, condensation, and polymerization can synthesize CPs in many ways, but the lack of efficient n-doped conducting material and inadequate cycling stability limit pseudocapacitors' potential. CPs are usually made by direct electrochemical synthesis. Polyethylene dioxythiophene (PEDOT), Polyfuran (PF), polypyrrole (PPy)[188], Polythiophene (PTh), Polyphenylene vinylene (PPV), Polyaniline (PANI)[189], and Polyacetylene (PA)[190] derivatives are typical SC electrode CPs.

Electrochromic devices, supercapacitors, field emission displays, photovoltaic cells, sensors, and actuators use CPs[191][192].

2.5.4. Battery-type materials

Intercalation amongst support materials and foreign ions divides electrode material electrochemical mechanism processes into dual-phase transformation (Conversion-type) and de-intercalation-intercalation[193]. Guest ions of multivalent cations or alkali metal ions can be incorporated in the Van der Waals spaces or cavernous structures within matrix materials like molybdenum sulfide, lithium iron phosphate, vanadium oxide, and lithium cobaltite with slight structure variation for intercalation reactions. When reacting with guest ions, host materials, including bismuth oxide, iron oxide, and Ni-/Co-based hydroxide/oxide, will convert to new and pristine phases for phase change. Conversion-type reactions have slower electrochemical kinetics than intercalation-type reactions, but their multi-electron transfer characteristic gives them more capacity[194][195].

It is worth mentioning that such a designation strategy helps audiences understand electrode materials' electrochemical behaviors during electrochemical reactions. Still, it does not imply that a sole method can retain charge. Indeed, charge storage methods can change from intercalation to conversion as the discharge degree increases, notably for anodic materials such as molybdenum sulfide and oxide evaluated in Na^+/Li^+-containing organic electrolytes. Intercalation and two-phase processes can store energy. The choices of electrolytes (multivalence/monovalent cation, non-aqueous/aqueous, alkali/acid) and potential windows significantly affect kinetics and energy

storage. Birnessite-type MnO_2 stores Li ions capacitively in aqueous electrolytes, but H/Zn ions store energy like batteries[196][197][198].

To prevent any misunderstanding, pseudocapacitance-related contents were added to those materials. With metal hydroxyl host frameworks and charge-neutralizing anions in interlayer voids, layered transition metal hydroxides exhibit excellent energy-retention potential, driven by their redox activity and efficient ion accessibility [198]. They can also be exfoliated into 2D nanosheets to build state-of-the-art heterostructure nano-frameworks and groundbreaking nano/microdevices. Nickel hydroxide has been widely utilized as electrode material for the negative electrode in Ni-Cd alkaline-based rechargeable batteries for two decades. It has garnered attention recently due to its potential high energy density and capacity in hybrid supercapacitors[199]. Partial isomorphous replacement of Ni^{2+} by Al^{3+}, Mn^{2+}, and Co^{2+} stabilizes the α phase in strong alkaline media. Layered double hydroxides are substituted chemicals. The host layer composition is exceptionally adjustable, and LDHs like Mg-Al, Co-Mn, and Co-Al have been widely produced and studied[200][201].

2.6. Electrolytes for supercapacitors

Electrolytes significantly influence the efficiency of supercapacitors and play a crucial role in device efficacy. Although supercapacitors exhibit lower energy density than batteries, studies are actively focused on enhancing the efficiency of electrolytes and electrode materials to position supercapacitors as viable alternatives to batteries due to their ability to store significant energy over prolonged periods and their elevated power density. Energy density can be augmented by intensifying the operating voltage, represented as V, and the charge stored, designated as Q, with

Q contingent upon pore size, ion size, electrode material, and surface area. One successful technique for enhancing energy density is to be concentrating on the electrolytes[202][203].

The electrolyte's potential window is crucial for defining V and, thus, attaining elevated energy density, which exhibits a quadratic relationship with V. The selection of electrodes, in conjunction with the electrolyte, substantially influences the equivalent series resistance (ESR). Consequently, electrolytes exhibiting low ESR, indicative of robust ionic conductivity, should be used for applications that require elevated power densities. With the rising electrolyte conductivity, resistance diminishes, potentially resulting in an expanded potential window and, thus, an enhancement in energy density. Nonetheless, a contraction in the potential window will adversely affect energy density. Consequently, a tradeoff exists between energy density and conductivity[204][205].

2.6.1. Electrolyte features

The ionic size of the electrolyte is intricately linked to its capacitance. Minimizing the dimensions of electrolyte ions can markedly augment their capacity to permeate the electrode's pores and adhere to its surface, enhancing the supercapacitor's overall performance. Consequently, ionic radius and pore dimension improve charge retention performance. The efficacy of the ultracapacitor device is contingent upon the conductivity of the electrolyte; elevated conductivity facilitates a more efficient ion transport to the electrode surface. The electrolyte conductance of ions is contingent upon the valency of the ions, their ionic mobility, and the quantity of charge carriers available, as illustrated in **Figure 2.15**. An exemplary electrolyte should rapidly dissociate into free ions upon interaction with a solvent[206].

The disintegration of electrolytic ions enhances supercapacitor performance and reduces internal resistance. The electrolytes specific conductivity is influenced by the degree of dissociation (α) and the concentration of the electrolytes. α is less than 1 for weak electrolytes, whereas for high electrolytes α is approximately 1. The behavior of ions in an electric field is essential, and Stokes' law elucidates the relationship between the exterior electric field and the ionic mobility. Enhanced ion mobility may be attained at reduced viscosities. Nonetheless, this is not universally applicable, as viscosity can affect the material's dielectric constant via molecular interactions and the electric dipole moments of the solvent[207].

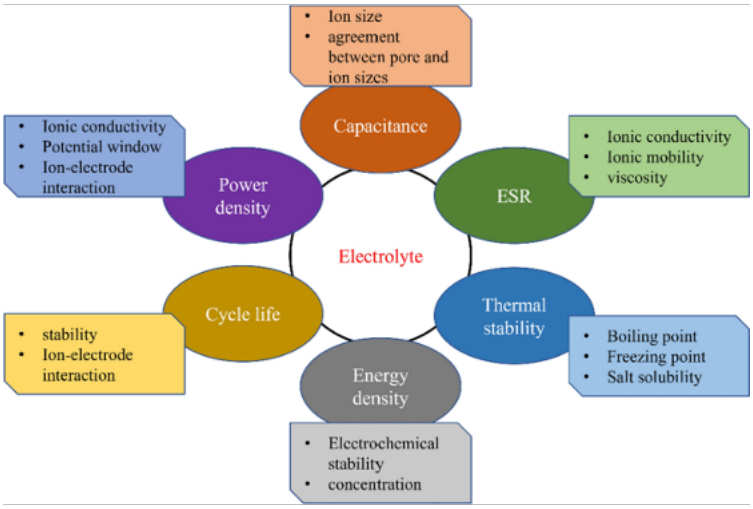


Figure 2. 15: Features affecting electrolyte characteristics[202]

The ionic velocity and the radius of solvated ions, influenced by an exterior electric field, impact ionic mobility. The relative dielectric coefficient of the solvent is utilized to examine the interaction energy between two ions. A higher dielectric constant correlates with reduced ion coupling, enhancing ionic conductivity. Nonetheless, elevated viscosity is necessary for an improved

dielectric constant, although increased viscosity diminishes ionic mobility as described by Stokes' law. Therefore, a trade-off among viscosity, ionic conductivity, and dielectric constant is necessary. Numerous more elements can influence the performance of supercapacitors[208].

Developing effective purification techniques to minimize impurities in electrolyte is essential since they can significantly elevate self-discharge and adversely affect the electrochemical stable potential window (ESPW). The organic solvent purification process can be informed by the extensive expertise accumulated in the Li-ion battery sector. Special emphasis should be given to ionic liquids (ILs) containing hydrophobic anions in the context of ionic liquid-derived electrolytes. This is beneficial for the long-duration durability of the ionic liquid. The kind of solvent and the concentration of salt in the electrolyte significantly affect the electrical conductivity of the liquid. The dissociation degree values are significantly lower in standard electrolytes[209].

Consequently, the solubility of salts in organic solvents is frequently limited, resulting in diminished ionic conductance of organic electrolytes and elevated equivalent series resistance compared to aqueous electrolytes. The electrolyte must exhibit reduced toxicity and elevated flash points for protection. Supercapacitors generally utilize one of three categories of electrolytes: quasi-solid-state, solid-state, and liquid-state electrolytes. As depicted in **Figure 2.18**, these may be additionally categorized into aqueous, ionic, and organic electrolytes for liquid electrolytes and inorganic and organic electrolytes for semi-solid and solid electrolytes[210].

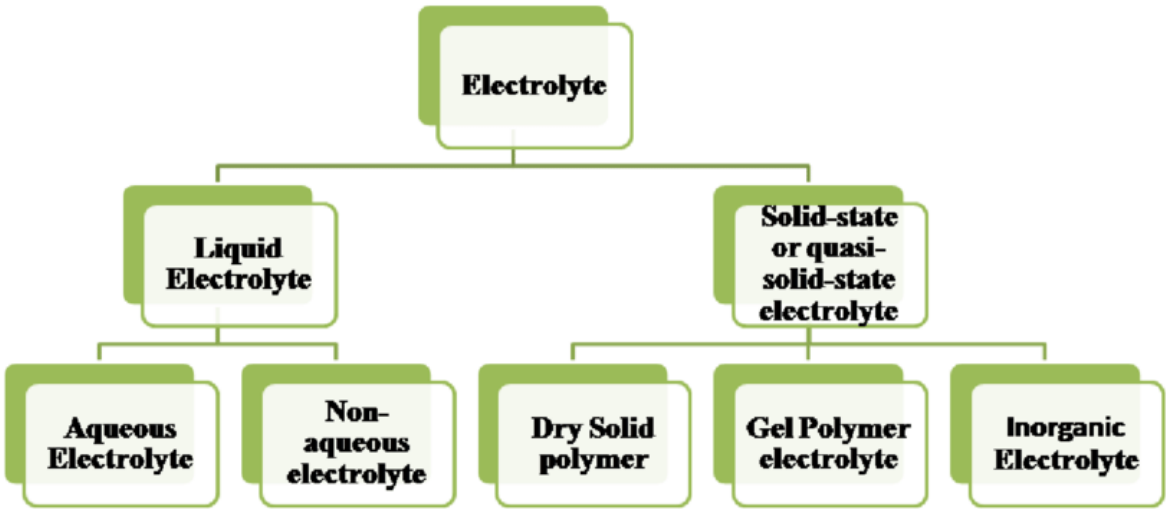


Figure 2. 16: Categorization of electrolytes[202]

2.6.1.1. Aqueous electrolyte

Aqueous electrolytes are fundamental to advancing supercapacitors owing to their intrinsic benefits, including environmental sustainability, affordability, and elevated ionic conductivity. These electrolytes primarily consist of water as the solvent, with dissolved salts that break down into ions, enabling charge transfer. The predominant varieties of aqueous electrolytes encompass sodium sulfate (Na_2SO_4), potassium hydroxide (KOH), and sulfuric acid (H_2SO_4). Each of these presents unique electrochemical characteristics. KOH is favored due to its extensive pH stability range and the creation of a quasi-solid electrolyte surface, which improves cycle longevity. Conversely, H_2SO_4 is extensively utilized owing to its minimal equivalent series resistance and elevated ionic conductivity, enhanced power performance[211].

Sodium sulfate is a feasible alternative, recognized for its non-toxic properties and safety. However, it exhibits poorer conductivity compared to the other two options. The importance of aqueous electrolytes in supercapacitors primarily arises from their ease of operation and safety in handling, rendering them appropriate for various applications. A prominent characteristic of aqueous electrolytes is their voltage window, normally restricted to 1.0-1.23V owing to the electrolysis of water[212]. This limited operational window can restrict the energy density attainable with aqueous electrolytes—application scope in advanced energy storage systems (ESS). Recent improvements have created "Water-in-salt" electrolytes, considerably broadening the voltage window to 3V, thereby improving energy density. Aqueous electrolytes: although they have a lower energy density than ionic or organic liquid electrolytes, they still have advantages[213].

They are distinguished by enhanced ion mobility and diminished viscosity, which facilitate superior charge/discharge rates and lower internal resistance. Furthermore, the aqueous electrolytes' cost-effectiveness and environmental benignity render them exceptionally appealing for sustainable supercapacitors and extensive applications[214]. Current research in this field aims to improve the stability of aqueous electrolytes and voltage range while preserving their intrinsic benefits, thereby significantly expanding the advantages of supercapacitors derived from the eco-friendliness and superior ionic conductivity of aqueous electrolytes. These attributes greatly enhance the device's overall efficacy and sustainability. Gajewska et al. demonstrated exceptional electrochemical performance in their study of the effects of electrolytes and carbon materials on the electrochemical performance of high-voltage aqueous symmetric supercapacitors[215].

In their report, Gajewska et al. examined the challenge of enhancing the working voltage of aqueous supercapacitors above the electrolyte breakdown threshold to augment the energy storage capacity of eco-friendly devices. The researchers examined the impact of textural characteristics and surface chemistry on the electrochemical performance of high-voltage aqueous supercapacitors utilizing both commercial activated carbon and synthesized P-rGO. The study examined a symmetric cell design utilizing heteroatom-rich P-rGO and extremely porous activated carbon with reduced porosity in a 2M $NaClO_4$ electrolyte. In contrast, the activated carbon-based cell was assessed in a 1M Na_2SO_4 solution. The integrated supercapacitor demonstrated an impressive power density of 30 W/kg and an energy density of 13 Wh/kg. The symmetric devices utilizing activated carbon electrodes in Na_2SO_4 exhibited exceptional charge storage characteristics, featuring an energy density of 13 Wh/kg and a maximum specific capacitance of 94 F/g at a current density of 0.2 A/g[215][216].

Recent breakthroughs in supercapacitor technology have generated significant interest in diverse aqueous electrolytes, which are widely acknowledged for their superior performance in energy storage applications. Prominent among them are electrolytes of zinc sulfate ($ZnSO_4$), potassium hydroxide (KOH), and lithium sulfate (Li_2SO_4). Recent studies have investigated novel methodologies, including water-in-salt electrolytes, wherein a high salt content in water enhances the electrochemical stability window, expanding the potential energy density of aqueous electrolytes. Utilizing hybrid aqueous electrolytes, which amalgamate several salts, has demonstrated potential in customizing electrolyte properties to align with electrode materials and

supercapacitor topologies. Such advancements are essential for high performance, environmental sustainability, and cost efficiency[213][217].

2.6.1.2. Organic electrolytes

Organic electrolytes, due to their high energy densities and extended working voltage ranges, have been important to the advancement of supercapacitor technology. These electrolytes offer a broader spectrum of electrochemical stability than their aqueous equivalents, consisting of dissolved salts and organic solvents. The predominant organic electrolytes are ethylene carbonate (EC), acetonitrile (ACN), and propylene carbonate (PC), owing to their superior voltage window (2.5-2.7 V) compared to water electrolytes. ACN is utilized due to its low viscosity and elevated dielectric constant, which optimize power density and facilitate rapid ion mobility. Solvents with elevated boiling points, such as EC and PC, improve electrolytes' thermal stability. The broader voltage range provides greater energy density than aqueous electrolytes. Acetonitrile is utilized chiefly because of its little toxicity and low ionic resistance[218][219].

Nonetheless, it presents safety issues, irreversible degradation, reduced ionic conductivity, and a propensity for rapid evaporation. In this context, organic and aqueous electrolytes possess distinct advantages and disadvantages, which determine their applicability in supercapacitors. Aqueous electrolytes exhibit elevated electrical conductivity and significant specific capacitance, yet their operational potential window is considerably limited. Organic electrolytes provide a substantial operating potential window, yet elevated costs and reduced ionic conductivity hinder them compared to aqueous electrolytes[220]. Consequently, most device constructions favor the incorporation of an aqueous electrolyte, categorized into three types based on the electrolyte's

nature: acidic (H3PO4, H2SO4), neutral (Na2SO4, NaCl, and K2SO4), and essential (KCl, KOH) electrolytes, which influence the electrochemical performance of supercapacitor electrodes[221].

Salts that dissociate into ions in a solvent to promote charge transfer are referred to as quaternary ammonium salts, including tetraethylammonium hexafluorophosphate ($TEAPF_6$) and tetraethylammonium tetrafluoroborate ($TEABF_4$). Acetonitrile is a solvent in high-performance electrolytes due to its excellent solvating properties and low boiling point, facilitating reduced internal resistance and rapid ion mobility[222]. Recent studies have focused on the formulation of mixed solvent systems, wherein salts such as lithium hexafluorophosphate ($LiPF_6$) or tetraethylammonium tetrafluoroborate ($TEABF_4$) are combined with solvents like ethylene carbonate (EC) and propylene carbonate (PC) to produce electrolytes that enhance thermal stability and operational safety. Advancements in organic electrolytes are crucial for the further evolution of supercapacitor technology, offering feasible pathways to energy storage systems that are versatile, durable, and highly efficient[223].

2.6.1.3. Ionic liquid electrolytes

Ionic liquids (IL) are salts composed of ions with a melting point beneath 100°C, facilitating their detachment into free ions in a solvent. Owing to its unique properties and structure, ionic liquid consists of an organic/inorganic anion and an asymmetric organic cation. The most notable characteristic of supercapacitors is their extensive stability range, often surpassing 4V, which substantially enhances their energy density. 1-ethyl-3-methylimidazolium tetrafluoroborate (EMIM-PF_4) and 1-butyl-3-methylimidazolium hexafluorophosphate (BMIM-PF_6) are instances of ionic liquids frequently employed[211].

Due to these ionic liquids' low volatility and exceptional thermal stability, supercapacitors exhibit enhanced reliability and stability across a broad temperature spectrum. Nevertheless, ionic liquids have low electrical conductivity, high viscosity, and elevated cost. Elevated viscosity restricts the rapid ion mobility in electrolytes and diminishes electrolyte flow to the interior of the electrode interface. Acetonitrile or propylene carbonate has been observed to enhance the conductivity of ionic liquids. As research on the material progresses, ionic liquids are increasingly significant in developing eco-friendly, reliable, and safe supercapacitors. This signifies a significant advancement in energy storage innovation[224].

2.7. Designing, assessment, and analysis of supercapacitor systems and electrodes

2.7.1. Electrode designing for supercapacitors

A supercapacitor can attain a larger specific capacitance by utilizing alternative electrode materials, enhancing pseudocapacitance, and modifying electrolytes. Supercapacitor electrodes comprise metals, carbon-based compounds, conductive polymers, and metal oxides. Metal electrodes are often covered with nanostructured modified carbon-based compounds. This enlarges the capacitor plates' surface area, substantially enhancing its capacitance. Carbon materials, conducting polymers, and inorganic materials constitute three categories of electrode nanomaterials. The electrode material is a crucial element of a SC. Several parameters, including temperature, precursor concentration, manufacturing procedure, and pH, influence the surface area of electrode material[225].

The choice of electrochemically active electrode materials is crucial for constructing high-performance supercapacitors. Consequently, after selecting the appropriate material, the electrode preparation approach is a crucial step in ensuring optimal interaction between the electrolyte and active material while preserving its inherent qualities, namely shape, structure, and electrical conductivity. Typically, in ultracapacitors, the electrodes are composed of a blend of binding material and a functional material, having or lacking a conductive admixture. The conductive supplementary, like carbon acetylene black, enhances the conductance of storage materials without compromising electrochemical retention capacity. In contrast, binders like polyvinylidene fluoride (PVDF) or polytetrafluoroethylene (PTFE) prevent functional material's dissolution when immersed in the electrolyte. These components are typically dissipated in N-methyl-2-pyrrolidone (NMP) solvent to create a slurry. The resultant paste is subsequently applied on a medium that facilitates electrical conductivity, such as nickel foam or carbon paper[4].

2.7.2. Electrode analysis for supercapacitors

Traditional three-electrode setups, consisting of reference, counter, and working electrodes, are appropriate for basic research on the functionality of a single electrode. In a three-electrode system, the working electrode functions as the main electrode where the electrochemical reaction of interest occurs (e.g., oxidation/reduction of species), reference electrodes (RE) provide a stable and known reference potential. It does not pass current, and its primary role is to allow accurate measurement of the working electrode’s potential while for the counter electrode completes the circuit by allowing current to flow. It balances the current passing through the working electrode, as illustrated in **Figure 2.17**. In acidic aqueous solutions, the counter electrode is either platinum

or carbon, the standard electrode is an Ag/AgCl or a saturated calomel electrode (SCE), and the working electrode must be titanium. In neutral aqueous solutions, a similar setup is employed; however, nickel may serve as the counter and collection electrode. In aqueous alkaline solutions, a Hg/HgO serves as the standard electrode. A case-by-case approach is necessary for non-aqueous electrolyte solutions, contingent upon the electrolyte's composition[226].

Aluminum foil is commonly utilized in laboratory tests involving normal, non-aqueous electrolytes. If the analysis is conducted over a broader potential range, alternative metals like platinum are more suitable for the electrochemical test cell. Nevertheless, platinum electrodes are unsuitable for non-aqueous solutions containing lithium ions, necessitating the use of copper or nickel, as in lithium-ion batteries. The widely utilized reference electrode is Li (Li/Li+), with silver (Ag/Ag+) also employed. Carbon is a more adaptable material for use as a counter electrode. Relevant references must be reviewed to establish experimental setups for non-aqueous solutions. The selection of counter-collector metals and the reference electrode may be influenced by factors including as cost, availability, and stability within a cell[227].

For the assessment of cell performance akin to that of a conventional capacitor, two-electrode cells are advised. This mechanism is crucial for assessing the cell's power density, cycle life, and energy density. Typically, two identical working electrodes are positioned on the opposite sides of a separator, with the voltage between them being regulated and observed, as depicted in **Figure 2.17**. The working electrode functions similarly to the three-electrode system, whereas the counter electrode acts as both the reference and counter electrode. It completes the circuit and serves as

the potential reference, but this makes potential control less precise than in the three-electrode system. In an entirely symmetric two-electrode cell, considering the charge numbers and sizes of the solvate anion and cation, the cell capacitance in F/g is theoretically one-fourth of the single-electrode capacitance recorded in a three-electrode cell [228]. It is important to recognize that the capacitance should be determined by the aggregate of active materials in both electrodes. The capacitance parameters in numerous literatures are ambiguous about whether they pertain to single-electrode capacitance or cell capacitance.

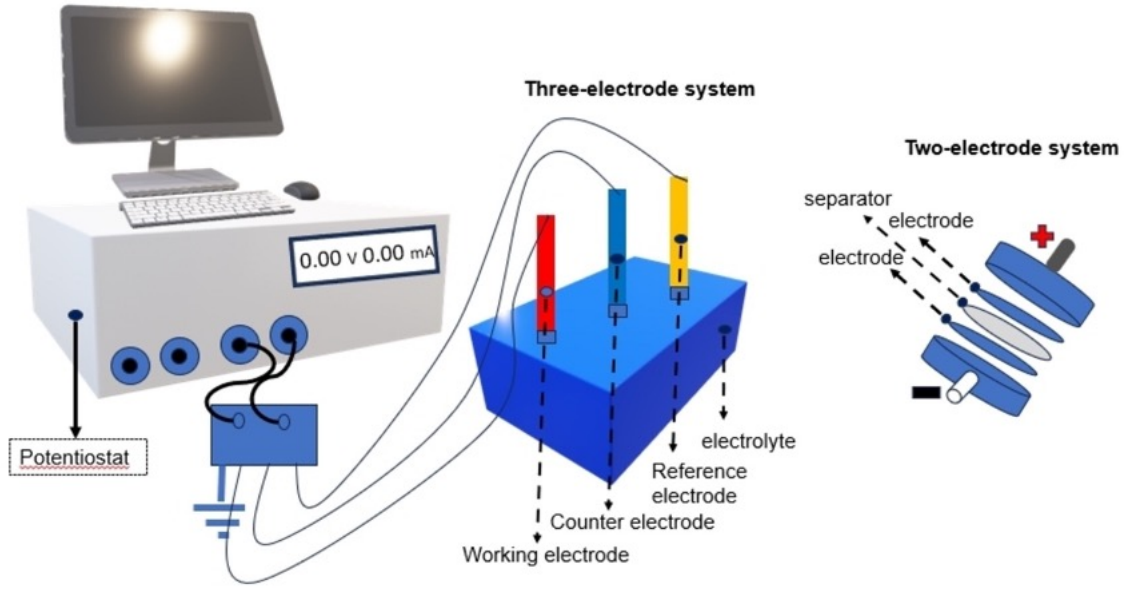


Figure 2. 17: Schematic depiction of a three-electrode and two-electrodes utilizing a battery-type Swagelok cell[229]

For a two-electrode setup, the capacitance of one electrode does not correspond to that observed in a three-electrode setup due to several factors, including the disparate potential variations of the cathode and anode electrodes during discharge and charge measurements, the size differences between solvate anions and cations, among others. The gap becomes more evident when

pseudocapacitance is established, as the pseudocapacitances of the anode and cathode electrodes typically differ significantly[230].

2.8. Electrochemical techniques

2.8.1. Cyclic voltammetry (CV)

Cyclic voltammetry (CV) is a prevalent electrochemical technique for assessing the electrochemical characteristics of materials, predominantly in ultracapacitor studies. In CV, the potential of the working electrode is gradually adjusted linearly in a time-dependent cyclic manner, and the subsequent current is acquired. This technique produces a current-voltage map, termed a voltammogram, which yields significant findings regarding the electrochemical properties of the electrode material. CV assists in assessing the electrochemical characteristics of electrode materials utilized in supercapacitors [211].

It offers insights into the charge retention mechanism, the reversibility of electrode reactions, and the capacitive characteristics of the electrode material. CV may differentiate between pseudocapacitive (Faradaic) and capacitive (non-Faradaic) charge retention methods. In a pseudocapacitance process, the current response has redox peaks, but in a capacitive process, the current response is rectangular[231][232]. CV elucidates the kinetics of electrochemical reactions at the electrolyte/electrode interface, encompassing the kinetics of electron transfer reactions and charge separation, potential-dependent capacitance variations, and redox thermodynamics. The cyclic voltammetry (CV) method can ascertain a material's specific capacitance by integrating of the area beneath the CV curve, as illustrated in **equations 2.30** and **2.31**.

$$C_{sp} = \frac{\Delta Q}{m \times \Delta V} = \frac{\int_0^{2V_{0/v}} |i| dt}{m \times 2V_0} \quad \text{Eqn (2. 30)}$$

Equation 2.31 is employed to transform the current response-derived data of the CV into specific capacitance:

$$C_{sp}\left[\frac{F}{g}\right] = \frac{I[mA]}{v[mV/s] \times m[g]} \quad \text{Eqn (2. 31)}$$

While **equation 2.32** applies to three-electrode systems, it is utilized for calculating specific capacitance, C_{sp} (F/cm^3, F/cm^2, and F/g), which correspond to volumetric, areal, and gravimetric capacitances, respectively.

$$C_{sp} = \frac{C}{S} \quad \text{Eqn (2. 32)}$$

Where S is the effective mass (g), area (cm^2), or volume (cm^3) of the electrode In a two-electrode setup, in which both the counter and working electrodes are indistinguishable, **equation 2.27** is employed to determine the specific capacitance, C_{sp}, per electrode (F/cm^3, F/cm^2, and F/g) for volumetric, geometric, and gravimetric specific capacitances, respectively.

$$C_{sp} = \frac{4C}{S} \quad \text{Eqn (2. 33)}$$

Where *S* denotes the mass (g), geometric area (cm^2), or volume (cm^3) of the functioning material in both electrodes, In EDLCs, the CV curve is generally rectangular, signifying optimal capacitive characteristics with limited faradaic reactions. Simultaneously, pseudocapacitors have unique redox peaks in the CV curve, signifying faradaic processes that enhance capacitance, as demonstrated in **Figure 2.18**.

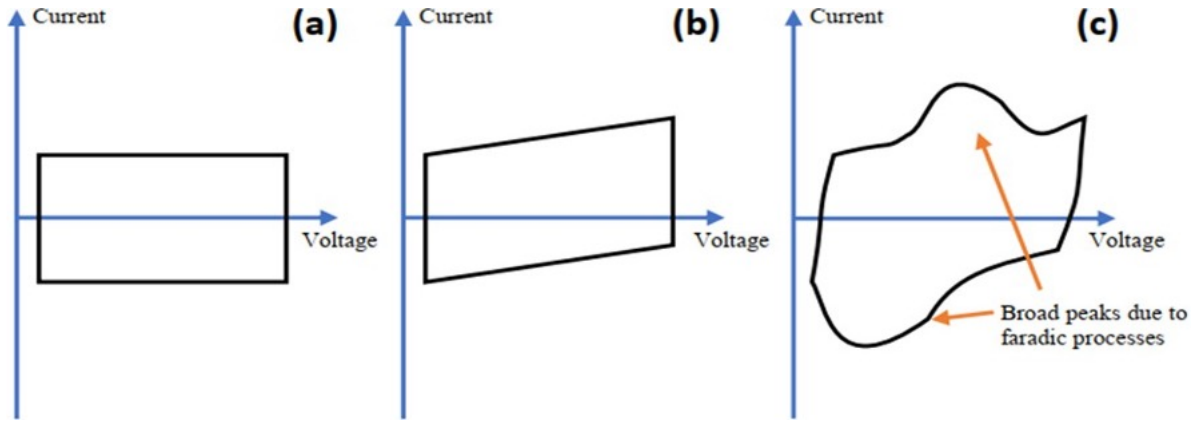


Figure 2. 18: An illustration of cyclic voltammograms of (a) ideal capacitor (b) capacitor with resistivity (c) pseudocapacitor[4]

An optimal potential range guarantees optimum capacitance while preventing electrolyte breakdown and electrode material deterioration. For aqueous electrolytes, the voltage range is typically constrained to (1.0-1.23V) owing to the limitations imposed by water electrolysis. A broader potential window of up to (2.5-2.7V) is applicable for ionic and organic electrolytes. The scan rate in cyclic voltammetry influences the morphology of the voltammogram. An increased scan rate results more prominent peaks and elevated current responses, signifying constraints and comparisons. Determining an appropriate electrochemical window in cyclic voltammetry experiments is essential to prevent irreparable reactions that may harm the electrolyte and electrode. CV can also furnish data regarding the supercapacitor's electrochemical durability and leakage current throughout multiple discharge and charge cycles[4][233].

2.8.2. Galvanostatic charge-discharge (GCD)

GCD is a crucial electrochemical technique applied to assess the performance of supercapacitors. In GCD analysis, a steady current drains and subsequently charges the ultracapacitor, while the potential across the supercapacitor is documented with time. This results in a discharge/charge curve, essential for assessing key operational parameters of SCs, including power density, specific capacitance, and energy density. The GCD is employed to determine the specific capacitance, which quantifies power and energy densities, offering a thorough insight into supercapacitor performance [234].

Repeated GCD cycles are employed to evaluate the lifespan and cycle durability of the supercapacitor, which is essential for real-world applications. In the charging phase, the voltage ascends linearly until a predetermined voltage is attained. During discharge, the voltage diminishes linearly[235]. As depicted in **Figure 2.19**, an abrupt decline in voltage, referred to as the IR drop, is noted at the commencement of the discharge phase.

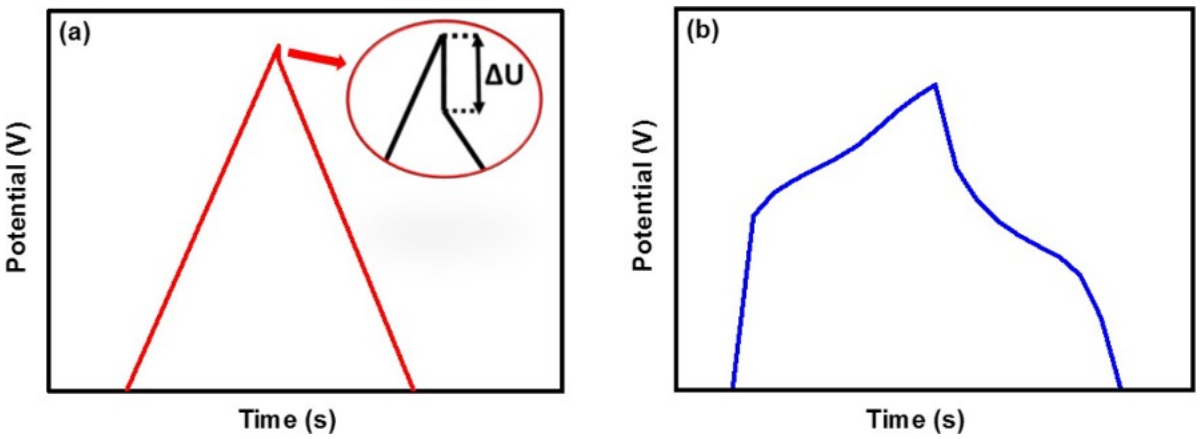


Figure 2. 19: GCD graph of (a) EDLC depicting IR drop (b) Redox pseudocapacitor or faradaic[4]

It signifies the intrinsic resistance of the ultracapacitor. The symmetry and linearity of the charge and discharge curves are utilized to assess the features of the supercapacitor electrodes, including power density, optimal power density, specific capacitance, and energy density. The capacitance $C(F)$ of a ultracapacitor is defined by the **equation 2.34**:

$$C = \frac{I\Delta t}{\Delta V} \qquad \textit{Eqn (2. 34)}$$

where $I(A)$ denotes current, $\Delta V(V)$ signifies the voltage interval throughout discharge, omits the IR drop, and $\Delta t(s)$ indicates the discharge duration. The energy density, maximum power density, and power density for supercapacitors are derived using galvanostatic charge-discharge findings. Power density P_{sp} (W/Kg) and gravimetric energy density E_{sp} (Wh/Kg) computations are performed using **equations 2.36** and **2.35**:

$$E_{sp} = \frac{CV^2}{2m} \times \frac{1000}{3600} \qquad \textit{Eqn (2. 35)}$$

$$P_{sp} = \frac{E_{sp} \times 3600}{\Delta t} \qquad \textit{Eqn (2. 36)}$$

Where $\Delta V(V)$ represents the most significant voltage applied, $m(Kg)$ denotes the mass of the operational material in each electrode, and $\Delta t(s)$ indicates the discharge duration. The optimal power is determined using **equation 2.37**:

$$P_{max} = \frac{\Delta V^2 \times 1000}{4m \times ESR} \qquad \textit{Eqn (2. 37)}$$

Where ΔV represents the applied maximum voltage window, $m(Kg)$ denotes the mass of effective material in each electrode. The ESR for the system is ascertained from the initial voltage drop on

the discharge curve of the GCD curves and may be computed using **equation 2.38**:

$$ESR = \frac{\Delta V_{iR\ drop}}{2I} \qquad Eqn\ (2.\ 38)$$

Finally, capacity retention (%) and coulombic efficiency (η %) for supercapacitors are determined using **equations 2.40** and **2.39**.

$$\eta\ (\%) = \frac{t_d}{t_c} \times 100\% \qquad Eqn\ (2.\ 39)$$

Where t_d represents discharge time and t_c represents charging time. Capacity retention is calculated as:

$$Capacity\ retention = \frac{C_{p_{final}}}{C_{p_{initial}}} \times 100\% \qquad Eqn\ (2.\ 40)$$

Where C_p final represents the final capacitance, and C_p initial denotes the beginning capacitance. Long-term GCD cycling tests are essential for assessing the endurance and stability of the supercapacitor over prolonged durations[4][236].

2.8.3. Electrochemical impedance spectroscopy (EIS)

EIS is a robust and highly sensitive approach employed to analyze supercapacitors' electrochemical and electrical characteristics. Electrochemical Impedance Spectroscopy (EIS) is often implemented as a transfer function measurement technique to explore linear time-invariant systems. In an electrochemical system, the primary challenge is maintaining a steady condition during the measuring process[237]. EIS employs a continuous periodic perturbation or minor amplitude potential to stimulate the electrochemical system across various frequencies, as depicted in **Figure 2.20**. The correlation between voltage and current is markedly nonlinear In a

ultracapacitor device. Nevertheless, when only a limited segment of the I-V curve is taken into account, Pseudo-linearity may be presumed, the impedance Z' is computed by implementing a small amplitude interchanging excitation voltage, E, and measuring the phase shift, (ϕ), in the resultant current. This phase transition is influenced by the resistance to electron transport induced by electrode kinetics, chemical processes, the electrolyte, and diffusion within the cell. The impedance Z (Ω) is formally represented as a multifaceted quantity consisting of real impedance designated as Z' and orthogonal reactance denoted as Z'' [238].

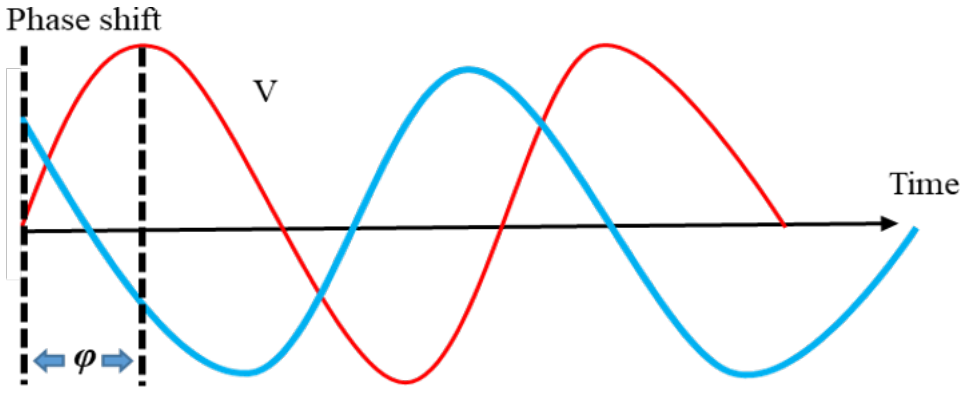


Figure 2. 20: Phase change ϕ in the current (I) due to a sinusoidal fluctuation's voltage (V) in a pseudo-linear circuit[4]

The resistance constitutes the actual component of the multifaceted value and is a framework characteristic that remains unaffected by the applied AC. The imaginary component, known as reactance, varies with frequency and becomes apparent in conductors and capacitors when subjected to an incident alternating current frequency. The excitation potential, V(V), is a time-dependent function in **equation 2.41**, In contrast, the output signal, I(A), is similarly time-dependent but includes a phase shift (ϕ) (rad) as shown in **equation 2.42**:

$$V_t = V_0 sin\omega t \qquad Eqn\ (2.41)$$

$$I_t = I_0 sin\,(\omega t - \phi) \qquad \text{Eqn (2. 42)}$$

Where $V_t(V)$ represents the voltage at the time, $t(s)$, $V_0(V)$ denotes the amplitude of the voltage signal at, $t = 0$, $I_t(A)$ indicates the current response signal at, $t = 0$, and $\omega(\text{rad.s}^{-1})$ signifies the angular frequency, with $\omega = 2\pi f$ and $f(\text{Hz})$ representing the frequency.

EIS data can be utilized to design the ultracapacitor through an equivalent electrical circuit, which enhances the understanding and refinement of its effectiveness. A key result of EIS is the Nyquist plot, which depicts the orthogonal component of impedance (Z'') vs the actual component (Z') across various frequencies. EIS is frequently employed to determine the specific capacitance of two- and three-electrode setups by analyzing the total resistance at the electrolyte/electrode charge collection interface (ESR) and charge transfer resistance R_{ct}. The EIS curve comprises two distinct segments: a linear portion at low frequency attributed to various electrochemical events during measurement, and a semicircular loop at high frequency exceeding (10^4 Hz), as captured in **Figure 2.21**[211][239].

Conversely, EIS data can be represented in an alternative format for analytical reasons. One such graphical representation is the Bode plot, showing both the phase shift $\phi(\omega)$ and resistance magnitude $|Z(\omega)|$ against the logarithm of frequency (log f). This graph categorizes the materials' electrical response into three distinct zones: Charge transfer, diffusion-controlled processes, and low-frequency may induce electrical relaxation. Relaxations at intermediate frequencies are linked to long-range conduction and ion propagation within the electrolyte's bulk, while elevated frequencies correlate with short-distance ion migrations[240].

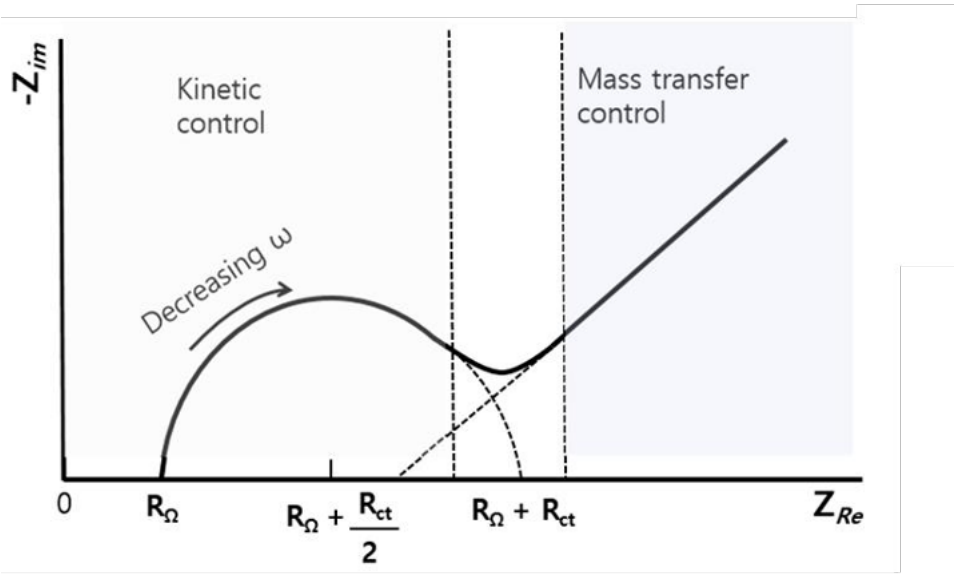


Figure 2. 21: Nyquist plot with R_{Ω} and R_{ct} [4]

Furthermore, the EIS data is modeled using an EEC (electric equivalent circuit) that illustrates the different units of the system, such as inductors, resistors, and capacitors, and their respective parameters can be enhanced. Potential components encompass solution resistance, influenced by ionic concentration, ion type, temperature, and the conductance area, and double-layer capacitance at the electrolyte-electrode boundary. The resistance is contingent upon ionic concentration, ion types, surface irregularity of the electrode, temperature, and more factors. Polarization resistance is governed by the reactant's diffusion and reaction kinetics at the electrolyte/electrode interface[240].

Charge transfer resistance, arising from a singular kinetically governed electrochemical reaction, is contingent upon reaction kinetics, concentrations of reactants and products, and diffusion, resulting in an impedance known as Warburg impedance, which is frequency contingent. The inclined line representing Warburg impedance exhibits 45° slope in a Nyquist plot. At the same

time, the (CPE) constant-phase element is a construct devised to characterize a non-ideal capacitor, therefore regarded as empirical. Ascribed to this impedance element are inhomogeneous current dissemination, surface roughness, or alternative considerations. Impedance associated with this parameter is determined using **equation 2.43**[240].

$$Z_{CPE} = \frac{1}{[Q(j2\pi f)^n]} \qquad \textit{Eqn (2. 43)}$$

Q represents a frequency-invariant parameter associated with interfacial properties, while n is obtained from the gradient of the log Z(ω) versus log f, constrained within the interval $-1 \leq n \leq 1$. When $0.5 < n < 1$, the exhibits capacitive characteristics. At $n = 0$, its behavior corresponds to that of a resistor, whereas for $n=0.5$, its impedance aligns with Warburg resistance. when $n= -1$, the response is analogous to an inductor[241].

2.8.4. An overview of the literature review

Energy storage systems are crucial for transitioning to sustainable energy technologies as they maintain equilibrium between supply and demand, ensuring constant energy availability. Supercapacitors have garnered significant attention due to their remarkable attributes, including high power density, extended cycle life, rapid charge and discharge rates, and environmental sustainability. This chapter discusses the categorization of supercapacitors according to their charge storage mechanisms (i.e., electric double-layer capacitors (EDLCs), pseudocapacitors, and battery-type capacitors) and the nanostructured electrode materials such as carbon-based (i.e., activated carbon, graphene, CNTs, and OLCs), transition metal (hydro)oxide-based (i.e., RuO_2, MnO_2, NiO, and $Ni(OH)_2$) and conducting polymers to illustrate their effect on the supercapacitor storage mechanism. Followed by the provision of a literature background on the electrochemical techniques (i.e., CV, GCD, and EIS) that are essential in understanding the electrochemical behavior of the electrode materials developed for supercapacitors. The key findings in this chapter displayed the role conventional carbon materials play in the supercapacitor performance due to their high rate capacity derived from their high conductivities and low energy densities derived from the absence of Faradaic contributions as compared to metal oxides and conducting polymers. Another key point was to demonstrate alternative strategies such as exploring heteroatom doping (i.e., nitrogen, boron, and boron-nitrogen), functionalization, and chemical activation to enhance surface reactivity and wettability that leads to improved supercapacitive performance. The provided literature in this chapter pointed towards the choice of electrode materials and the electrochemical techniques employed in this study.

3.0. References

[1] J. P. Cheng, J. Zhang, and F. Liu, "Recent development of metal hydroxides as electrode material of electrochemical capacitors," *RSC Advances*, 4, no. 73, pp. 38893–38917, 2014. [Online]. Available: https://doi.org/10.1039/C4RA06738J. Accessed: Jan 2024.

[2] C. Lewiner, *World Energy Markets Observatory 2024 | 26th Edition*, Capgemini, Oct. 2024. [Online]. Available: https://www.capgemini.com/wp-content/uploads/2024/10/World-Energy-Markets-Observatory-2024_26th-Edition.pdf. Accessed: Jan. 15, 2025.

[3] Department of Mineral Resources and Energy, *South African Energy Price Report 2024*, Pretoria, South Africa, 2024.[Online].Available: https://www.dmre.gov.za/Portals/0/Energy%20Resources/Energy%20Sector%20Reports/Energy-Price-Report-2024.pdf. Accessed: Feb. 15, 2025.

[4] T. P. Mofokeng, *Hierarchical Nitrogen-Doped Carbon Nanotube-Carbon Nanofiber-Based Networks for Electrochemical Capacitors*, M.Sc. thesis, Univ. of the Witwatersrand, Johannesburg, South Africa, 2021. [Online]. Available: https://wiredspace.wits.ac.za/items/dd0657a2-7aaf-4378-b62b-2c438e625e23. Accessed: Jan 15, 2025.

[5] J. Mitali, S. Dhinakaran, and A. A. Mohamad, "Energy storage systems: a review," *Energy Storage and Saving*, 1, pp. 166–216, Sep. 2022, doi: 10.1016/j.enss.2022.07.002.

[6] H. Adam, S. C. B. Gopinath, T. Adam, M. A. Fakhri, E. T. Salim, and S. Subramaniam, "Exploring faradaic and non-faradaic electrochemical impedance spectroscopy approaches in Parkinson's disease diagnosis," *Heliyon*, 10, Article e27433, Mar. 2024, doi: 10.1016/j.heliyon.2024.e27433.

[7] C. Lu, W. Wu, L. Wang, R. Tian, and F. Du, "Thick electrode for energy storage systems: A facile strategy towards high energy density Li-ion batteries," *Next Materials*, 4, Art. no. 100170, Jul. 2024, doi: 10.1016/j.nxmate.2024.100170.

[8] D. Cericola and R. Kötz, "Hybridization of rechargeable batteries and electrochemical capacitors: Principles and limits," *Electrochim Acta*, 72, pp. 1–17, Jun. 2012, doi: 10.1016/j.electacta.2012.03.151.

[9] B. Guo, F. Jin, L. Li, Z. Z. Pan, X. W. Xu, and H. Wang, "Design strategies of high-performance lead-free electroceramics for energy storage applications," *J. Mater. Sci. Mater. Electron.*, 35, Art. no. 2452, Mar. 2024, doi: 10.1007/s12598-023-02452-4.

[10] W. Liu, X. Sun, X. Yan, Y. Gao, X. Zhang, K. Wang, and Y. Ma, "Review of Energy Storage Capacitor Technology," *Batteries*, 10, Art. no. 271, Aug. 2024, doi: 10.3390/batteries10080271.

[11] M. Sayed and M. Farag, "Lithium-Ion Batteries: Modelling and State of Charge Estimation."

[12] M. Libale, *Metal oxide modified functionalized onion proposal*, M.Sc. proposal, University of the Witwatersrand, Johannesburg, South Africa, Aug. 19, 2022.

[13] S. J. Uke, S. P. Mardikar, A. Kumar, Y. Kumar, M. Gupta, and Y. Kumar, "A review of π-conjugated polymer-based nanocomposites for metal-ion batteries and supercapacitors," *Royal Soc. Open Sci.*, 8, Art. no. 210567, Oct. 2021, doi: 10.1098/rsos.210567.

[14] R. Kahwaji, "Supercapacitors: A short literature review," *ResearchGate*, Jan. 2019. [Online].Available: https://www.researchgate.net/publication/331471216_Supercapacitors_A_Short_Litterature_Review. [Accessed: 3-Feb-2025].

[15] K. Malaie and M. R. Ganjali, "Ferrite nanoflowers," in *Ferrite Nanostructured Magnetic Materials: Technologies and Applications*, J. P. Singh, K. H. Chae, R. C. Srivastava, and O. F. Caltun, Eds. Woodhead Publishing Series in Electronic and Optical Materials. Elsevier, 2023, pp. 351–374. doi: 10.1016/B978-0-12-823717-5.00019-X.

[16] S. Biswas and A. Chowdhury, "Organic supercapacitors as the next generation energy storage device: Emergence, opportunity, and challenges," *ChemPhysChem*, 24, no. 3, Art. no. e202200567, Feb. 2023, doi: 10.1002/cphc.202200567.

[17] P. Le, "The silent power of supercapacitors," *Embedded Computing Design*, Feb. 13, 2019. [Online]. Available: https://embeddedcomputing.com/technology/analog-and-power/the-silent-power-of-supercapacitors. Accessed: Feb. 15, 2025.

[18] N. Zhou, T. Liu, B. Wen, C. Gong, G. Wei, and Z. Su, "Recent advances in the construction of flexible sensors for biomedical applications," *Biotechnol. J.*, 15, no. 12, Art. no. e2000094, Dec. 2020, doi: 10.1002/biot.202000094.

[19] U. Gulzar *et al.*, "Next-generation textiles: from embedded supercapacitors to lithium ion batteries," *J Mater Chem A Mater*, 4, no. 43, pp. 16771–16800, 2016, doi: 10.1039/C6TA06437J.

[20] V. V. Jadhav, R. S. Mane, and P. V. Shinde, "Electrochemical supercapacitors: History, types, designing processes, operation mechanisms, and advantages and disadvantages," in *Electrochemical Supercapacitors: Materials, Systems, and Applications*, S. M. Islam and M. R. K. Mollah, Eds. Springer, 2020, pp. 11–36. doi: 10.1007/978-3-030-16718-9_2.

[21] V. V. Jadhav, R. S. Mane, and P. V. Shinde, "Electrochemical supercapacitors: History, types, designing processes, operation mechanisms, and advantages and disadvantages," in *Electrochemical Supercapacitors: Materials, Systems, and Applications*, S. M. Islam and M. R. K. Mollah, Eds. Springer, 2020, pp. 11–36. doi: 10.1007/978-3-030-16718-9_2.

[22] Q. Navid, M. Taali, M. Khosravy, and M. S. S. Danish, "Recent advances in bio-based electrode materials in supercapacitor applications: Energy storage materials and technologies," *Journal of Sustainable Energy Revolution*, 3, no. 1, pp. 1–13, Jun. 2022, doi: 10.37357/1068/jser/3.1.01.

[23] Z. S. Iro, C. Subramani, and S. S. Dash, "A Brief Review on Electrode Materials for Supercapacitor," *Int J Electrochem Sci*, 11, pp. 10628–10643, Dec. 2016, doi: 10.20964/2016.12.50.

[24] R. P. Deshpande, "What is electric double layer capacitor (EDLC)?," *Capacitor Connect*, Mar. 13, 2024. [Online]. Available: https://www.capacitorconnect.com/what-is-electric-double-layer-capacitor-edlc/. Accessed: Jan. 29, 2025.

[25] W. Chen, C. Hu, Y. Yang, J. Cui, and Y. Liu, "Rapid synthesis of carbon dots by hydrothermal treatment of lignin," *Materials*, 9, no. 3, Art. no. 184, Mar. 2016, doi: 10.3390/ma9030184

[26] P. Saha and M. Khanra, "Equivalent circuit model of supercapacitor for self-discharge analysis – A comparative study," in *Proc. Int. Conf. Signal Process., Commun., Power Embedded Syst. (SCOPES)*, 2016, pp. 1381–1386, doi: 10.1109/SCOPES.2016.7955667.

[27] A. M. Bond and K. B. Oldham, "Effect of heterogeneity on the DC and AC voltammetry of the $[Fe(CN)_6]^{3-/4-}$ solution-phase process at a highly heterogeneous electrode," *Anal. Chem.*, 80, pp. 4132–4139, Jun. 2008, doi: 10.1021/ac800421r.

[28] L. G. H. Staaf, P. Lundgren, and P. Enoksson, "Present and future supercapacitor carbon electrode materials for improved energy storage used in intelligent wireless sensor systems," *Nano Energy*, 10, pp. 1–12, Oct. 2014, doi: 10.1016/j.nanoen.2014.06.028.

[29] K. B. Oldham, "Effect of Diffusion Coefficient Diversity on Steady-State Voltammetry When Homogeneous Equilibria and Migration Are Encountered," *Anal Chem*, 68, pp. 4173–4179, Dec. 1996, doi: 10.1021/ac9601730.

[30] T. P. Mofokeng, Z. N. Tetana, and K. I. Ozoemena, "Defective 3D nitrogen-doped carbon nanotube-carbon fibre networks for high-performance supercapacitor: Transformative role of nitrogen-doping from surface-confined to diffusive kinetics," *Carbon N Y*, 169, pp. 312–326, Nov. 2020, doi: 10.1016/j.carbon.2020.07.049.

[31] A. Tyagi, K. Mishra, and V. K. Shukla, "Structural and Electrochemical Properties of KOH-Activated Carbon Soot Derived from Sinapis alba (Yellow Mustard Oil) for EDLC Application," *J Electron Mater*, 51, no. 10, pp. 5670–5685, Oct. 2022, doi: 10.1007/s11664-022-09832-z.

[32] P. Bhojane, "Recent advances and fundamentals of pseudocapacitors: Materials, mechanism, and its understanding," *J. Energy Storage*, 45, Art. no. 103654, Jan. 2022, doi: 10.1016/j.est.2021.103654.

[33] P. Bhojane, "Recent advances and fundamentals of Pseudocapacitors: Materials, mechanism, and its understanding," *J Energy Storage*, 45, Art. no. 103654, Jan. 2022, doi: 10.1016/j.est.2021.103654.

[34] A. Venkataraman, "Pseudocapacitors for energy storage," M.S. thesis, Dept. Physics, Portland State Univ., Portland, OR, USA, 2015. [Online]. Available: https://doi.org/10.15760/etd.2483.

[35] T. Brousse, D. Bélanger, and J. W. Long, "To Be or Not To Be Pseudocapacitive?," *J Electrochem Soc*,162, no. 5, pp. A5185–A5189, 2015, doi: 10.1149/2.0201505jes.

[36] P. Mehra, S. Saxena, and S. Bhullar, "A comprehensive analysis of supercapacitors and their equivalent circuits—A review," *World Electr. Veh. J.*, 15, Art. no. 332, Aug. 2024, doi: 10.3390/wevj15080332.

[37] R. P. Deshpande, "What is a Pseudocapacitor?," *Capacitor Connect*, Apr. 20, 2024. [Online]. Available: https://www.capacitorconnect.com/what-is-a-pseudocapacitor/. Accessed: Mar. 1, 2025.

[38] C. Costentin and J. M. Savéant, "Energy storage: Pseudocapacitance in prospect," *Chem. Sci.*, vol. 10, pp. 5656–5666, 2019, doi: 10.1039/C9SC01662G.

[39] N. R. Chodankar et al., "True meaning of pseudocapacitors and their performance metrics: Asymmetric versus hybrid supercapacitors," *Small*, 16, Art. no. 2002806, Sep. 2020, doi: 10.1002/smll.202002806.

[40] S. S. Djokić, Ed., *Electrodeposition and Surface Finishing: Fundamentals and Applications*, 57, Modern Aspects of Electrochemistry. New York, NY, USA: Springer, 2014. [Online]. Available: https://doi.org/10.1007/978-1-4939-0289-7.

[41] M. Huang, F. Li, F. Dong, Y. X. Zhang, and L. L. Zhang, "MnO_2 -based nanostructures for high-performance supercapacitors," *J Mater Chem A Mater*, 3, pp. 21380–21423, 2015, doi: 10.1039/C5TA05523G.

[42] K. Zhang, X. Han, Z. Hu, X. Zhang, Z. Tao, and J. Chen, "Nanostructured Mn-based oxides for electrochemical energy storage and conversion," *Chem Soc Rev*, 44, pp. 699–728, 2015, doi: 10.1039/C4CS00218K.

[43] N. K. Pavithra Siddu, S. M. Jeong, and C. S. Rout, "MXene–carbon based hybrid materials for supercapacitor applications," *Energy Adv.*, 3, pp. 341–365, Jan. 2024, doi: 10.1039/D3YA00502J.

[44] H. T. Tan, W. Sun, L. Wang, and Q. Yan, "2D Transition Metal Oxides/Hydroxides for Energy-Storage Applications," *ChemNanoMat*, 2, pp. 562–577, Jul. 2016, doi: 10.1002/cnma.201500177.

[45] S. Devaraj and N. Munichandraiah, "Effect of Crystallographic Structure of MnO_2 on Its Electrochemical Capacitance Properties," *The Journal of Physical Chemistry C*, 112, pp. 4406–4417, Mar. 2008, doi: 10.1021/jp7108785.

[46] V. Augustyn *et al.*, "High-rate electrochemical energy storage through Li+ intercalation pseudocapacitance," *Nat Mater*, 12, pp. 518–522, Jun. 2013, doi: 10.1038/nmat3601.

[47] T. Brezesinski, J. Wang, S. H. Tolbert, and B. Dunn, "Ordered mesoporous α-MoO3 with iso-oriented nanocrystalline walls for thin-film pseudocapacitors," *Nat Mater*, 9, pp. 146–151, Feb. 2010, doi: 10.1038/nmat2612.

[48] J. Ban *et al.*, "In-plane grain boundary induced defect state in hierarchical NiCo-LDH and effect on battery-type charge storage," *Nano Res*, 16, pp. 4908–4916, Apr. 2023, doi: 10.1007/s12274-022-4485-1.

[49] S. Deebansok et al., "A novel approach for classifying battery and pseudocapacitor materials using capacitive tendency and supervised machine learning," *Research Square*, May 29, 2023. [Online]. Available: https://doi.org/10.21203/rs.3.rs-2930525/v1.

[50] S. S. Djokić, Ed., *Electrodeposition and Surface Finishing: Fundamentals and Applications*, vol. 57, Modern Aspects of Electrochemistry. New York, NY, USA: Springer, 2014. [Online]. Available: https://doi.org/10.1007/978-1-4939-0289-7.

[51] M. Liang, L. Wang, V. Presser, X. Dai, F. Yu, and J. Ma, "Combining Battery-Type and Pseudocapacitive Charge Storage in Ag/Ti3C2Tx MXene Electrode for Capturing Chloride Ions with High Capacitance and Fast Ion Transport," *Advanced Science*, 7, Sep. 2020, doi: 10.1002/advs.202000621.

[52] C. Arbizzani et al., "Good practice guide for papers on supercapacitors and related hybrid capacitors for the Journal of Power Sources," *J. Power Sources*, 450, Art. no. 227636, Feb. 2020, doi: 10.1016/j.jpowsour.2019.227636.

[53] A. Afif, S. M. Rahman, A. T. Azad, J. Zaini, M. A. Islam, and A. K. Azad, "Advanced materials and technologies for hybrid supercapacitors for energy storage – A review," *J. Energy Storage*, 25, Art. no. 100852, Oct. 2019, doi: 10.1016/j.est.2019.100852.

[54] Y. Cai, B. Zhao, J. Wang, and Z. Shao, "Non-aqueous hybrid supercapacitors fabricated with mesoporous TiO2 microspheres and activated carbon electrodes with superior performance," *J Power Sources*, 253, pp. 80–89, May 2014, doi: 10.1016/j.jpowsour.2013.11.097.

[55] R. Kötz and M. Carlen, "Principles and applications of electrochemical capacitors," *Electrochim Acta*, 45, pp. 2483–2498, May 2000, doi: 10.1016/S0013-4686(00)00354-6.

[56] S. Q. Liew and H. K. Jun, "Fundamentals, mechanism, and materials for hybrid supercapacitors," in *Advances in Material Research and Applications*, S. K. Gupta, S. K. Saha, and S. K. Pal, Eds., Springer, 2022, pp. 71–100, doi: 10.1007/978-3-030-99302-3_4.

[57] E. Lim *et al.*, "High-Performance Sodium-Ion Hybrid Supercapacitor Based on Nb_2O_5@Carbon Core–Shell Nanoparticles and Reduced Graphene Oxide Nanocomposites," *Adv Funct Mater*, 26, pp. 3711–3719, Jun. 2016, doi: 10.1002/adfm.201505548.

[58] X. Yun, J. Li, Z. Luo, J. Tang, and Y. Zhu, "Advanced aqueous energy storage devices based on flower-like nanosheets-assembled Ni0.85Se microspheres and porous Fe2O3 nanospheres," *Electrochim Acta*, 302, pp. 449–458, Apr. 2019, doi: 10.1016/j.electacta.2019.02.038.

[59] V. M. A. S. I. Varakin, "Journal of Power," W097/075/8, Aug. 14, 1995. [Online]. Available: [URL]. Accessed: Mar. 10, 2025.

[60] T. Ramachandran, S. S. Sana, K. D. Kumar, Y. A. Kumar, H. H. Hegazy, and S. C. Kim, "Asymmetric supercapacitors: Unlocking the energy storage revolution," *J. Energy Storage*, vol. 73, Art. no. 109096, Dec. 2023, doi: 10.1016/j.est.2023.109096.

[61] Y.-R. Wang et al., "Superhydrophilic nickel hydroxide ultrathin nanosheets enable high-performance asymmetric supercapacitors," *Rare Metals*, 43, pp. 138–147, Nov. 2023, doi: 10.1007/s12598-023-02386-x.

[62] D. W. Wang, F. Li, and H. M. Cheng, "Hierarchical porous nickel oxide and carbon as electrode materials for asymmetric supercapacitor," *J Power Sources*, 185, pp. 1563–1568, Dec. 2008, doi: 10.1016/J.JPOWSOUR.2008.08.032.

[63] M. S. Halper and J. C. Ellenbogen, "Supercapacitors: A brief overview," MITRE Corporation, McLean, VA, Tech. Rep. MP 05W0000272, Mar. 2006. [Online]. Available: https://www.mitre.org/sites/default/files/pdf/06_0667.pdf. [Accessed: Feb. 18, 2025].

[64] A. Muzaffar, M. B. Ahamed, K. Deshmukh, and J. Thirumalai, "A review on recent advances in hybrid supercapacitors: Design, fabrication and applications," *Renewable and Sustainable Energy Reviews*,101, pp. 123–145, Mar. 2019, doi: 10.1016/j.rser.2018.10.026.

[65] J. S. Ko, C.-H. Lai, J. W. Long, D. R. Rolison, B. Dunn, and J. Nelson Weker, "Differentiating Double-Layer, Psuedocapacitance, and Battery-like Mechanisms by Analyzing Impedance Measurements in Three Dimensions," *ACS Appl Mater Interfaces*, 12, pp. 14071–14078, Mar. 2020, doi: 10.1021/acsami.0c02020.

[66] H. Shao, Z. Lin, K. Xu, P. L. Taberna, and P. Simon, "Electrochemical study of pseudocapacitive behavior of Ti3C2Tx MXene material in aqueous electrolytes," *Energy Storage Mater*, 18, pp. 456–461, Mar. 2019, doi: 10.1016/J.ENSM.2018.12.017.

[67] T. -C. Liu, W. G. Pell, B. E. Conway, and S. L. Roberson, "Behavior of Molybdenum Nitrides as Materials for Electrochemical Capacitors: Comparison with Ruthenium Oxide," *J Electrochem Soc*, 145, pp. 1882–1888, Jun. 1998, doi: 10.1149/1.1838571.

[68] L. Lai *et al.*, "Preparation of Supercapacitor Electrodes through Selection of Graphene Surface Functionalities," *ACS Nano*, 6, pp. 5941–5951, Jul. 2012, doi: 10.1021/nn3008096.

[69] P. Forouzandeh, V. Kumaravel, and S. C. Pillai, "Electrode materials for supercapacitors: A review of recent advances," *Catalysts*, 10, Art. no. 969, Aug. 2020, doi: 10.3390/catal10090969.

[70] L. Xie *et al.*, "Hierarchical porous carbon microtubes derived from willow catkins for supercapacitor applications," *J Mater Chem A Mater*, 4, pp. 1637–1646, 2016, doi: 10.1039/C5TA09043A.

[71] E. Frackowiak and F. Béguin, "Carbon materials for the electrochemical storage of energy in capacitors," *Carbon N Y*, 39, pp. 937–950, May 2001, doi: 10.1016/S0008-6223(00)00183-4.

[72] L. L. Zhang and X. S. Zhao, "Carbon-based materials as supercapacitor electrodes," *Chem Soc Rev*, 38, Art no. 2520, 2009, doi: 10.1039/b813846j.

[73] M. Vangari, T. Pryor, and L. Jiang, "Supercapacitors: Review of Materials and Fabrication Methods," *Journal of Energy Engineering*, 139, pp. 72–79, Jun. 2013, doi: 10.1061/(ASCE)EY.1943-7897.0000102.

[74] L.-F. Chen *et al.*, "Synthesis of Nitrogen-Doped Porous Carbon Nanofibers as an Efficient Electrode Material for Supercapacitors," *ACS Nano*, 6, pp. 7092–7102, Aug. 2012, doi: 10.1021/nn302147s.

[75] F. Qi *et al.*, "Graphitization induced by KOH etching for the fabrication of hierarchical porous graphitic carbon sheets for high performance supercapacitors," *J Mater Chem A Mater*, 6, pp. 14170–14177, 2018, doi: 10.1039/C8TA01186A.

[76] X. He, H. Ma, J. Wang, Y. Xie, N. Xiao, and J. Qiu, "Porous carbon nanosheets from coal tar for high-performance supercapacitors," *J Power Sources*, 357, pp. 41–46, Jul. 2017, doi: 10.1016/J.JPOWSOUR.2017.04.108.

[77] Z. S. Iro, C. Subramani, and S. S. Dash, "A Brief Review on Electrode Materials for Supercapacitor," *Int J Electrochem Sci*, 11, pp. 10628–10643, Dec. 2016, doi: 10.20964/2016.12.50.

[78] H. Yang, S. Kannappan, A. S. Pandian, J.-H. Jang, Y. S. Lee, and W. Lu, "Graphene supercapacitor with both high power and energy density," *Nanotechnology*, 28, p. 445401, Nov. 2017, doi: 10.1088/1361-6528/aa8948.

[79] R. Sahoo, T. H. Lee, D. T. Pham, T. H. T. Luu, and Y. H. Lee, "Fast-Charging High-Energy Battery–Supercapacitor Hybrid: Anodic Reduced Graphene Oxide–Vanadium(IV) Oxide Sheet-on-Sheet Heterostructure," *ACS Nano*, 13, pp. 10776–10786, Sep. 2019, doi: 10.1021/acsnano.9b05605.

[80] L. Luo, Y. Zhou, W. Yan, X. Wu, S. Wang, and W. Zhao, "Two-step synthesis of B and N co-doped porous carbon composites by microwave-assisted hydrothermal and pyrolysis process for supercapacitor application," *Electrochim Acta*, 360, Art no. 137010, Nov. 2020, doi: 10.1016/j.electacta.2020.137010.

[81] L.-H. Zheng, M.-H. Chen, S.-X. Liang, and Q.-F. Lü, "Oxygen-rich hierarchical porous carbon derived from biomass waste-kapok flower for supercapacitor electrode," *Diam Relat Mater*, 113, Art no. 108267, Mar. 2021, doi: 10.1016/j.diamond.2021.108267.

[82] L. Luo, T. Chen, W. Zhao, and M. Fan, "Hydrothermal doping of nitrogen in bamboo-based super activated carbon for hydrogen storage," *BioResources*, 12, pp. 6237–6250, Jul. 2017. [Online]. Available: https://bioresources.cnr.ncsu.edu/resources/hydrothermal-doping-of-nitrogen-in-bamboo-based-super-activated-carbon-for-hydrogen-storag/. [Accessed: Feb. 18, 2025].

[83] H. Fu *et al.*, "Walnut shell-derived hierarchical porous carbon with high performances for electrocatalytic hydrogen evolution and symmetry supercapacitors," *Int J Hydrogen Energy*, 45, pp. 443–451, Jan. 2020, doi: 10.1016/j.ijhydene.2019.10.159.

[84] B. Shaku, T. P. Mofokeng, N. J. Coville, K. I. Ozoemena, and M. S. Maubane-Nkadimeng, "Biomass valorisation of marula nutshell waste into nitrogen-doped activated carbon for use in high performance supercapacitors," *Electrochim Acta*, 442, Feb. 2023, doi: 10.1016/j.electacta.2023.141828.

[85] D. J. Tarimo, K. O. Oyedotun, N. F. Sylla, A. A. Mirghni, N. M. Ndiaye, and N. Manyala, "Waste chicken bone-derived porous carbon materials as high performance electrode for supercapacitor applications," *J Energy Storage*, 51, Art no. 104378, Jul. 2022, doi: 10.1016/j.est.2022.104378.

[86] W. Yuan, J. Liu, W. Yi, L. Liang, Y. Zhu, and X. Chen, "Boron and nitrogen co-doped double-layered mesopore-rich hollow carbon microspheres as high-performance electrodes for supercapacitors," *J Colloid Interface Sci*, 573, pp. 232–240, Aug. 2020, doi: 10.1016/j.jcis.2020.03.126.

[87] G. Moreno-Fernandez, J. Ibañez, J. M. Rojo, and M. Kunowsky, "Activated Carbon Fiber Monoliths as Supercapacitor Electrodes," *Advances in Materials Science and Engineering*, 2017, pp. 1–8, 2017, doi: 10.1155/2017/3625414.

[88] C. Arbizzani, M. Mastragostino, and F. Soavi, "New trends in electrochemical supercapacitors," *J Power Sources*, 100, pp. 164–170, Nov. 2001, doi: 10.1016/S0378-7753(01)00892-8.

[89] M. S. Reza, A. K. Hasan, S. Afroze, M. S. A. Bakar, J. Taweekun, and A. K. Azad, "Analysis on preparation, application, and recycling of activated carbon to aid in COVID-19 protection," *International Journal of Integrated Engineering*, 12, pp. 233–244, 2020, doi: 10.30880/ijie.2020.12.05.029.

[90] "The Electrochemical Society Interface • Spring 2008," *Interface*, 17, pp. 1–2, Spring 2008. [Online]. Available: https://www.electrochem.org/dl/interface/if_curr_iss.htm. Accessed: Mar. 10, 2025.

[91] A. G. Pandolfo and A. F. Hollenkamp, "Carbon properties and their role in supercapacitors," *J Power Sources*, 157, pp. 11–27, Jun. 2006, doi: 10.1016/J.JPOWSOUR.2006.02.065.

[92] J. Yan, Q. Wang, T. Wei, and Z. Fan, "Recent Advances in Design and Fabrication of Electrochemical Supercapacitors with High Energy Densities," *Adv Energy Mater*, 4, Mar. 2014, doi: 10.1002/aenm.201300816.

[93] N. Choudhary *et al.*, "Asymmetric Supercapacitor Electrodes and Devices," *Advanced Materials*, 29, Jun. 2017, doi: 10.1002/adma.201605336.

[94] A. K. Geim and K. S. Novoselov, "The rise of graphene," *Nat Mater*, 6, pp. 183–191, Mar. 2007, doi: 10.1038/nmat1849.

[95] A. A. Balandin, "Thermal properties of graphene and nanostructured carbon materials," *Nat Mater*, 10, pp. 569–581, Aug. 2011, doi: 10.1038/nmat3064.

[96] E. Pop, V. Varshney, and A. K. Roy, "Thermal properties of graphene: Fundamentals and applications," *MRS Bull*, 37, pp. 1273–1281, Dec. 2012, doi: 10.1557/mrs.2012.203.

[97] Q. Tang, Z. Zhou, and Z. Chen, "Graphene-related nanomaterials: tuning properties by functionalization," *Nanoscale*, 5, p. 4541, 2013, doi: 10.1039/c3nr33218g.

[98] D. G. Papageorgiou, I. A. Kinloch, and R. J. Young, "Mechanical properties of graphene and graphene-based nanocomposites," *Prog Mater Sci*, 90, pp. 75–127, Oct. 2017, doi: 10.1016/j.pmatsci.2017.07.004.

[99] R. Prasher, "Graphene Spreads the Heat," *Science (1979)*, 328, Art no. 5975, pp. 185–186, Apr. 2010, doi: 10.1126/science.1188998.

[100] J. Duan, S. Chen, M. Jaroniec, and S. Z. Qiao, "Heteroatom-Doped Graphene-Based Materials for Energy-Relevant Electrocatalytic Processes," *ACS Catal*, 5, pp. 5207–5234, Sep. 2015, doi: 10.1021/acscatal.5b00991.

[101] L. R. Radovic, C. V. Mora-Vilches, A. J. A. Salgado-Casanova, and A. Buljan, "Graphene functionalization: Mechanism of carboxyl group formation," *Carbon N Y*, 130, pp. 340–349, Apr. 2018, doi: 10.1016/j.carbon.2017.12.112.

[102] S. Y. Yip and W. Andreoni, Eds., *Handbook of Materials Modeling*, 2nd ed., Springer, Cham, 2020. [Online]. Available: https://link.springer.com/referenceworkentry/10.1007%2F978-3-319-50256-0_38-1. Accessed: Mar. 11, 2025.

[103] S. Mao, G. Lu, and J. Chen, "Three-dimensional graphene-based composites for energy applications," *Nanoscale*, 7, pp. 6924–6943, 2015, doi: 10.1039/C4NR06609J.

[104] D. Akinwande *et al.*, "A review on mechanics and mechanical properties of 2D materials—Graphene and beyond," *Extreme Mech Lett*, 13, pp. 42–77, May 2017, doi: 10.1016/j.eml.2017.01.008.

[105] S. W. Bokhari *et al.*, "Advances in graphene-based supercapacitor electrodes," *Energy Reports*, 6, pp. 2768–2784, Nov. 2020, doi: 10.1016/j.egyr.2020.10.001.

[106] M. S. Fuhrer, C. N. Lau, and A. H. MacDonald, "Graphene: Materially Better Carbon," *MRS Bull*, 35, pp. 289–295, Apr. 2010, doi: 10.1557/mrs2010.551.

[107] M. Zeiger, N. Jäckel, V. N. Mochalin, and V. Presser, "Review: Carbon onions for electrochemical energy storage," *J. Mater. Chem. A*, 4, pp. 3172–3196, 2016, doi: 10.1039/c5ta08295a.

[108] S. Kaur, A. Krishnan, and S. Chakraborty, "Recent advances and challenges of carbon nano onions (CNOs) for application in supercapacitor devices (SCDs)," *Energy Storage and Technology*, Elsevier Ltd., Nov. 2023. [Online].
Available: https://doi.org/10.1016/j.est.2023.107928. [Accessed: Jan. 18, 2025].

[109] D. Ugarte, "Curling and closure of graphitic networks under electron-beam irradiation," *Nature*, 359, pp. 707–709, Oct. 1992, doi: 10.1038/359707a0.

[110] S. Iijima, "Helical microtubules of graphitic carbon," *Nature*, 354, pp. 56–58, Nov. 1991, doi: 10.1038/354056a0.

[111] G. Speranza, "Carbon nanomaterials: Synthesis, functionalization and sensing applications," *Nanomaterials*, 11, Art. no. 967, Apr. 2021, doi: 10.3390/nano11040967.

[112] J. Goclon, B. Bankiewicz, P. Kolek, and K. Winkler, "Role of nitrogen doping in stoichiometric and defective carbon nano-onions: Structural diversity from DFT calculations," *Carbon N Y*, 176, pp. 198–208, May 2021, doi: 10.1016/J.CARBON.2021.01.131.

[113] J. Xiao, G. Ouyang, P. Liu, C. X. Wang, and G. W. Yang, "Reversible Nanodiamond-Carbon Onion Phase Transformations," *Nano Lett*, 14, pp. 3645–3652, Jun. 2014, doi: 10.1021/nl5014234.

[114] S. Iijima, "Direct observation of the tetrahedral bonding in graphitized carbon black by high-resolution electron microscopy," *J. Cryst. Growth*, 50, pp. 675–683, Nov. 1980. [Online]. Available: https://ui.adsabs.harvard.edu/abs/1980JCrGr..50..675I.

[115] "Fullerenes," in *The IUPAC Compendium of Chemical Terminology*, 2nd ed., Research Triangle Park, NC: International Union of Pure and Applied Chemistry (IUPAC), 2014. [Online]. Available: https://doi.org/10.1351/goldbook.F02547. [Accessed: Feb. 18, 2025].

[116] A. Bianco, H.-M. Cheng, M. Enoki, M. S. Dresselhaus, M. Loiseau, J. Ma, P. M. Ajayan, M. Terrones, and M. S. Strano, "All in the graphene family – A recommended nomenclature for two-dimensional carbon materials," *Carbon*, 65, pp. 1–6, Dec. 2013. [Online]. Available: https://www.sciencedirect.com/science/article/pii/S0008622313008002.

[117] M. Zeiger, N. Jäckel, M. Aslan, D. Weingarth, and V. Presser, "Understanding structure and porosity of nanodiamond-derived carbon onions," *Carbon N Y*, 84, pp. 584–598, 2015, doi: 10.1016/j.carbon.2014.12.050.

[118] O. O. Ayeleru et al., "Innovative approaches in characterization of carbon nanotube," in *Handbook of Carbon Nanotubes*, J. Abraham et al., Eds., Springer International Publishing, 2022, pp. 109–129, doi: 10.1007/978-3-030-91346-5_55.

[119] O. Mykhailiv, H. Zubyk, and M. E. Plonska-Brzezinska, "Carbon nano-onions: Unique carbon nanostructures with fascinating properties and their potential applications," *Inorganica Chim Acta*, 468, pp. 49–66, Nov. 2017, doi: 10.1016/j.ica.2017.07.021.

[120] Y. Hu, *Carbon and Metal Oxides Based Nanomaterials for Flexible High Performance Asymmetric Supercapacitors*, Springer Theses, Springer Singapore, 2018. [Online]. Available: https://doi.org/10.1007/978-981-10-8342-6. [Accessed: Mar. 12, 2025].

[121] S. Sek, J. Breczko, M. E. Plonska-Brzezinska, A. Z. Wilczewska, and L. Echegoyen, "STM-Based Molecular Junction of Carbon Nano-Onion," *ChemPhysChem*, 14, pp. 96–100, Jan. 2013, doi: 10.1002/cphc.201200624.

[122] M. H. Ghanbari and Z. Norouzi, "A new nanostructure consisting of nitrogen-doped carbon nanoonions for an electrochemical sensor to the determination of doxorubicin," *Microchemical Journal*, vol. 157, Art no. 105098, Sep. 2020, doi: 10.1016/j.microc.2020.105098.

[123] J. Guo, X. Wang, and B. Xu, "One-step synthesis of carbon-onion-supported platinum nanoparticles by arc discharge in an aqueous solution," *Mater Chem Phys*, 113, pp. 179–182, Jan. 2009, doi: 10.1016/j.matchemphys.2008.07.039.

[124] C. Zhang *et al.*, "The efficient synthesis of carbon nano-onions using chemical vapor deposition on an unsupported Ni-Fe alloy catalyst," *Carbon N Y*, 49, pp. 1151–1158, Apr. 2011, doi: 10.1016/j.carbon.2010.11.030.

[125] T. H. Mongwe, *Synthesis of Chain-like Carbon Nano-Onions for Application in Room Temperature Volatile Organic Chemical Gas Sensors*, Ph.D. dissertation, University of the Witwatersrand, Johannesburg, South Africa, 2021. [Online]. Available: https://wiredspace.wits.ac.za/items/57d17f63-6fd1-45a2-8c1d-cbe0f74580ad. Accessed: Mar. 12, 2025.

[126] T.H. Mongwe, N.J. Coville, and M.S. Maubane-Nkadimeng, "Synthesis of onion-like carbon nanoparticles by flame pyrolysis," in *Nanoscience*, 8, pp. 198–220, The Royal Society of Chemistry, 2022, doi: 10.1039/9781839167218-00198.

[127] S. Merum, J. B. Veluru, and R. Seeram, "Functionalized carbon nanotubes in bio-world: Applications, limitations and future directions," *Mater. Sci. Eng. B*, 229, pp. 198–220, Sep. 2017, doi: 10.1016/j.mseb.2017.06.002.

[128] R. Dubey, D. Dutta, A. Sarkar, and P. Chattopadhyay, "Functionalized carbon nanotubes: synthesis, properties and applications in water purification, drug delivery, and material and biomedical sciences," *Nanoscale Adv.*, 3, pp. 5722–5744, 2021, doi: 10.1039/d1na00293g.

[129] C. A. Dyke and J. M. Tour, "Overcoming the insolubility of carbon nanotubes through high degrees of sidewall functionalization," *Chem. Eur. J.*, 10, pp. 1101–1111, Feb. 2004, doi: 10.1002/chem.200305534.

[130] J. Zhu, J. D. Kim, H. Peng, J. L. Margrave, V. N. Khabashesku, and E. V. Barrera, "Improving the dispersion and integration of single-walled carbon nanotubes in epoxy composites through functionalization," *Nano Lett*, 3, pp. 1107–1113, Aug. 2003, doi: 10.1021/nl0342489.

[131] M. Noordadi, F. Mehrnejad, R. H. Sajedi, M. Jafari, and B. Ranjbar, "The potential impact of carboxylic-functionalized multi-walled carbon nanotubes on trypsin: A Comprehensive spectroscopic and molecular dynamics simulation study," *PLoS One*, 13, Art no. e0198519, Jun. 2018, doi: 10.1371/journal.pone.0198519.

[132] P. Wolski, K. Nieszporek, and T. Panczyk, "Pegylated and folic acid functionalized carbon nanotubes as pH controlled carriers of doxorubicin. Molecular dynamics analysis of the stability and drug release mechanism," *Physical Chemistry Chemical Physics*, 19, pp. 9300–9312, 2017, doi: 10.1039/c7cp00702g.

[133] P. J. Boul, J. M. Bonard, and L. Forró, "Reversible sidewall functionalization of buckytubes," *Chem. Phys. Lett.*, 314, pp. 485–490, 1999. [Online]. Available: https://www.sciencedirect.com/science/article/pii/S0009261499007137.

[134] B.V. Basheer, J.J. George, S. Siengchin, and J. Parameswaranpillai, "Polymer grafted carbon nanotubes—Synthesis, properties, and applications: A review," *Nano-Struct. Nano-Objects*, 22, Art. no. 100429, Apr. 2020, doi: 10.1016/j.nanoso.2020.100429.

[135] J. Goclon, "Manipulation of structural and electronic properties of B-doped carbon nano–onions based on DFT modelling," *Appl Surf Sci*, 532, Art no. 147267, Dec. 2020, doi: 10.1016/J.APSUSC.2020.147267.

[136] L. Bai, Y. Ge, and L. Bai, "Boron and nitrogen co-doped porous carbons synthesized from polybenzoxazines for high-performance supercapacitors," *Coatings*, 9, Oct. 2019, doi: 10.3390/COATINGS9100657.

[137] E. Y. Choi and C. K. Kim, "Fabrication of nitrogen-doped nano-onions and their electrocatalytic activity toward the oxygen reduction reaction," *Sci Rep*, 7, Dec. 2017, doi: 10.1038/s41598-017-04597-6.

[138] R. Qiao, A. P. Roberts, A. S. Mount, S. J. Klaine, and P. C. Ke, "Translocation of C_{60} and Its Derivatives Across a Lipid Bilayer," *Nano Lett*, 7, pp. 614–619, Mar. 2007, doi: 10.1021/nl062515f.

[139] M. P. Thomas, N. Wanninayake, M. De Alwis Goonatilleke, D. Y. Kim, and B. S. Guiton, "Direct imaging of heteroatom dopants in catalytic carbon nano-onions," *Nanoscale*, 12, pp. 6144–6152, 2020, doi: 10.1039/D0NR00335B.

[140] J. Jin *et al.*, "Catalyst-Free Synthesis of Crumpled Boron and Nitrogen Co-Doped Graphite Layers with Tunable Bond Structure for Oxygen Reduction Reaction," *ACS Nano*, 8, pp. 3313–3321, Apr. 2014, doi: 10.1021/nn404927n.

[141] U. S. Kodithuwakku, N. Wanninayake, M. P. Thomas, B. S. Guiton, and D. Y. Kim, "Unlocking efficiency in oxygen reduction reaction: Synergistic edge dopants of nitrogen and boron in carbon nano onions," *Electrochim. Acta*,471, Art. no. 143365, Dec. 2023, doi: 10.1016/j.electacta.2023.143365.

[142] Z. Zhai et al., "A review of carbon materials for supercapacitors," *Mater. Des.*, 222, Art. no. 111017, Sep. 2022, doi: 10.1016/j.matdes.2022.111017.

[143] S. Iijima and T. Ichihashi, "Single-shell carbon nanotubes of 1-nm diameter," *Nature*, 363, pp. 603–605, Jun. 1993, doi: 10.1038/363603a0.

[144] Q. Wang, Z. H. Wen, and J. H. Li, "A Hybrid Supercapacitor Fabricated with a Carbon Nanotube Cathode and a TiO_2 –B Nanowire Anode," *Adv Funct Mater*,16, pp. 2141–2146, Oct. 2006, doi: 10.1002/adfm.200500937.

[145] M. Hashida, S. Shimizu, and S. Sakabe, "Carbon-nanotube cathode modified by femtosecond laser ablation," *J Phys Conf Ser*, 59, pp. 487–491, Apr. 2007, doi: 10.1088/1742-6596/59/1/105.

[146] J. Ye, H. F. Cui, X. Liu, T. M. Lim, W. Zhang, and F. Sheu, "Preparation and Characterization of Aligned Carbon Nanotube–Ruthenium Oxide Nanocomposites for Supercapacitors," *Small*, 1, pp. 560–565, May 2005, doi: 10.1002/smll.200400137.

[147] Q. Cheng, J. Tang, J. Ma, H. Zhang, N. Shinya, and L.-C. Qin, "Graphene and carbon nanotube composite electrodes for supercapacitors with ultra-high energy density," *Physical Chemistry Chemical Physics*, 13, Art no. 17615, 2011, doi: 10.1039/c1cp21910c.

[148] X. Li, J. Rong, and B. Wei, "Electrochemical Behavior of Single-Walled Carbon Nanotube Supercapacitors under Compressive Stress," *ACS Nano*, 4, pp. 6039–6049, Oct. 2010, doi: 10.1021/nn101595y.

[149] A. C. Dillon, "Carbon Nanotubes for Photoconversion and Electrical Energy Storage," *Chem Rev*, 110, pp. 6856–6872, Nov. 2010, doi: 10.1021/cr9003314.

[150] Q. Liu *et al.*, "Fabrication of a fibrous MnO2@MXene/CNT electrode for high-performance flexible supercapacitor," *Ceram Int*, 46, pp. 11874–11881, Jun. 2020, doi: 10.1016/J.CERAMINT.2020.01.222.

[151] T. Nguyen and M. F. Montemor, "Redox active materials for metal compound based hybrid electrochemical energy storage: a perspective view," *Appl Surf Sci*, 422, pp. 492–497, Nov. 2017, doi: 10.1016/J.APSUSC.2017.06.008.

[152] B. E. Conway, "Transition from 'Supercapacitor' to 'Battery' Behavior in Electrochemical Energy Storage," *J Electrochem Soc*, 138, pp. 1539–1548, Jun. 1991, doi: 10.1149/1.2085829.

[153] P. E. Lokhande, U. S. Chavan, and A. Pandey, "Materials and Fabrication Methods for Electrochemical Supercapacitors: Overview," *Electrochemical Energy Reviews*, 3, pp. 155–186, Mar. 2020, doi: 10.1007/s41918-019-00057-z.

[154] R. Liang *et al.*, "Transition Metal Oxide Electrode Materials for Supercapacitors: A Review of Recent Developments," *Nanomaterials*, vol. 11, Art no. 1248, May 2021, doi: 10.3390/nano11051248.

[155] Y. Zhang *et al.*, "Effects of microstructure and electrochemical properties of Ti/IrO2–SnO2–Ta2O5 as anodes on binder-free asymmetric supercapacitors with Ti/RuO2–NiO as cathodes," *Ceram Int*, 46, pp. 17640–17650, Aug. 2020, doi: 10.1016/J.CERAMINT.2020.04.066.

[156] V. C. Lokhande, A. C. Lokhande, C. D. Lokhande, J. H. Kim, and T. Ji, "Supercapacitive composite metal oxide electrodes formed with carbon, metal oxides and conducting polymers," *J Alloys Compd*, 682, pp. 381–403, Oct. 2016, doi: 10.1016/J.JALLCOM.2016.04.242.

[157] C. Zhao and W. Zheng, "A review for aqueous electrochemical supercapacitors," *Front. Energy Res.*, 3, Art. no. 23, May 2015, doi: 10.3389/fenrg.2015.00023.

[158] C. Peng, J. Jin, and G. Z. Chen, "A comparative study on electrochemical co-deposition and capacitance of composite films of conducting polymers and carbon nanotubes," *Electrochim Acta*, 53, pp. 525–537, Dec. 2007, doi: 10.1016/J.ELECTACTA.2007.07.004.

[159] J. P. Zheng, P. J. Cygan, and T. R. Jow, "Hydrous Ruthenium Oxide as an Electrode Material for Electrochemical Capacitors," *J Electrochem Soc*, 142, pp. 2699–2703, Aug. 1995, doi: 10.1149/1.2050077.

[160] H. Wang, D. Zhang, T. Yan, X. Wen, L. Shi, and J. Zhang, "Graphene prepared via a novel pyridine–thermal strategy for capacitive deionization," *J Mater Chem*, 22, p. 23745, 2012, doi: 10.1039/c2jm35340g.

[161] J. W. Long, K. E. Swider, C. I. Merzbacher, and D. R. Rolison, "Voltammetric Characterization of Ruthenium Oxide-Based Aerogels and Other RuO_2 Solids: The Nature of Capacitance in Nanostructured Materials," *Langmuir*,15, pp. 780–785, Feb. 1999, doi: 10.1021/la980785a.

[162] Y. Xie and C. Yao, "Electrochemical performance of RuO_2 -TiO_2 nanotube hybrid electrode material," *Mater Res Express*, 6, p. 125550, Jan. 2020, doi: 10.1088/2053-1591/ab69c9.

[163] C. W. Kuo, J. C. Chang, B. W. Wu, and T. Y. Wu, "Electrochemical characterization of RuO2-Ta2O5/polyaniline composites as potential redox electrodes for supercapacitors and hydrogen evolution reaction," *Int J Hydrogen Energy*, 45, pp. 22223–22231, Aug. 2020, doi: 10.1016/J.IJHYDENE.2019.08.059.

[164] S. H. Li, Q. H. Liu, L. Qi, L. H. Lu, and H. Y. Wang, "Progress in Research on Manganese Dioxide Electrode Materials for Electrochemical Capacitors," *Chinese Journal of Analytical Chemistry*, 40, pp. 339–346, Mar. 2012, doi: 10.1016/S1872-2040(11)60534-3.

[165] C. P. Yi and S. R. Majid, "The electrochemical performance of deposited manganese oxide-based film as electrode material for electrochemical capacitor application," in *Semiconductors – Growth and Characterization*, InTech, 2018, doi: 10.5772/intechopen.71957.

[166] M. Toupin, T. Brousse, and D. Bélanger, "Charge Storage Mechanism of MnO_2 Electrode Used in Aqueous Electrochemical Capacitor," *Chemistry of Materials*, 16, pp. 3184–3190, Aug. 2004, doi: 10.1021/cm049649j.

[167] J. H. Chae, K. C. Ng, and G. Z. Chen, "Nanostructured materials for the construction of asymmetrical supercapacitors," *Proceedings of the Institution of Mechanical Engineers, Part A: Journal of Power and Energy*, 224, pp. 479–503, Jun. 2010, doi: 10.1243/09576509JPE861.

[168] S. Devaraj and N. Munichandraiah, "Effect of Crystallographic Structure of MnO_2 on Its Electrochemical Capacitance Properties," *The Journal of Physical Chemistry C*, 112, pp. 4406–4417, Mar. 2008, doi: 10.1021/jp7108785.

[169] C. Sun, Y. Zhang, S. Song, and D. Xue, "Tunnel-dependent supercapacitance of MnO_2: effects of crystal structure," *J Appl Crystallogr*, 46, pp. 1128–1135, Aug. 2013, doi: 10.1107/S0021889813015999.

[170] O. Ghodbane, J.-L. Pascal, and F. Favier, "Microstructural Effects on Charge-Storage Properties in MnO_2 -Based Electrochemical Supercapacitors," *ACS Appl Mater Interfaces*, vol. 1, no. 5, pp. 1130–1139, May 2009, doi: 10.1021/am900094e.

[171] J. Huang, K. Wang, and Z. Wei, "Conducting polymernanowire arrays with enhanced electrochemical performance," *J. Mater. Chem.*, vol. 20, no. 6, pp. 1117–1121, 2010, doi: 10.1039/B919928D.

[172] Y. Zhang *et al.*, "Progress of electrochemical capacitor electrode materials: A review," *Int J Hydrogen Energy*, 34, pp. 4889–4899, Jun. 2009, doi: 10.1016/j.ijhydene.2009.04.005.

[173] R. S. Kate, S. A. Khalate, and R. J. Deokate, "Overview of nanostructured metal oxides and pure nickel oxide (NiO) electrodes for supercapacitors: A review," *J Alloys Compd*, 734, pp. 89–111, Feb. 2018, doi: 10.1016/j.jallcom.2017.10.262.

[174] B.E. Conway, *Electrochemical Supercapacitors: Scientific Fundamentals and Technological Applications*, Springer US, 1999. [Online]. Available: https://doi.org/10.1007/978-1-4757-3058-6.

[175] Y. Q. Zhang *et al.*, "Self-assembled synthesis of hierarchically porous NiO film and its application for electrochemical capacitors," *J Power Sources*, 199, pp. 413–417, Feb. 2012, doi: 10.1016/J.JPOWSOUR.2011.10.065.

[176] X. Xia *et al.*, "Graphene Sheet/Porous NiO Hybrid Film for Supercapacitor Applications," *Chemistry – A European Journal*, 17, pp. 10898–10905, Sep. 2011, doi: 10.1002/chem.201100727.

[177] J. W. Lee, T. Ahn, D. Soundararajan, J. M. Ko, and J.-D. Kim, "Non-aqueous approach to the preparation of reduced graphene oxide/α-Ni(OH)2 hybrid composites and their high capacitance behavior," *Chemical Communications*, 47, Art no. 6305, 2011, doi: 10.1039/c1cc11566a.

[178] S. K. Meher, P. Justin, and G. Ranga Rao, "Microwave-Mediated Synthesis for Improved Morphology and Pseudocapacitance Performance of Nickel Oxide," *ACS Appl Mater Interfaces*, 3, pp. 2063–2073, Jun. 2011, doi: 10.1021/am200294k.

[179] S. Sharma, P. Kadyan, R. K. Sharma, N. Kumar, and S. Grover, "Progressive updates on nickel hydroxide and its nanocomposite for electrochemical electrode material in asymmetric supercapacitor device," *J Energy Storage*, 87, Art no. 111368, May 2024, doi: 10.1016/J.EST.2024.111368.

[180] P. Jeevanandam, Yu. Koltypin, and A. Gedanken, "Synthesis of Nanosized α-Nickel Hydroxide by a Sonochemical Method," *Nano Lett*, 1, pp. 263–266, May 2001, doi: 10.1021/nl010003p.

[181] G.-X. Tong, F.-T. Liu, W.-H. Wu, J.-P. Shen, X. Hu, and Y. Liang, "Polymorphous α- and β-Ni(OH)2 complex architectures: morphological and phasal evolution mechanisms and enhanced catalytic activity as non-enzymatic glucose sensors," *CrystEngComm*, 14, Art no. 5963, 2012, doi: 10.1039/c2ce25622c.

[182] D. Yang, R. Wang, M. He, J. Zhang, and Z. Liu, "Ribbon- and Boardlike Nanostructures of Nickel Hydroxide: Synthesis, Characterization, and Electrochemical Properties," *J Phys Chem B*, 109, pp. 7654–7658, Apr. 2005, doi: 10.1021/jp050083b.

[183] D. A. Corrigan and S. L. Knight, "Electrochemical and Spectroscopic Evidence on the Participation of Quadrivalent Nickel in the Nickel Hydroxide Redox Reaction," *J Electrochem Soc*, vol. 136, pp. 613–619, Mar. 1989, doi: 10.1149/1.2096697.

[184] K.-H. Young *et al.*, "Fabrications of High-Capacity Alpha-Ni(OH)2," *Batteries*, 3, Art no. 6, Mar. 2017, doi: 10.3390/batteries3010006.

[185] E. Dhandapani, S. Thangarasu, S. Ramesh, K. Ramesh, R. Vasudevan, and N. Duraisamy, "Recent development and prospective of carbonaceous material, conducting polymer and their

composite electrode materials for supercapacitor — A review," *J Energy Storage*, 52, Art no. 104937, Aug. 2022, doi: 10.1016/J.EST.2022.104937.

[186] D. Chaudhuri and D. D. Sarma, "BF3-doped polyaniline: A novel conducting polymer," *Pramana*, 67, pp. 135–139, Jul. 2006, doi: 10.1007/s12043-006-0044-7.

[187] M. Gerard, A. Chaubey, and B. D. Malhotra, "Application of conducting polymers to biosensors," *Biosens Bioelectron*, 17, pp. 345–359, May 2002, doi: 10.1016/S0956-5663(01)00312-8.

[188] S. Hashmi, "Polypyrrole and poly(3-methyl thiophene)-based solid state redox supercapacitors using ion conducting polymer electrolyte," *Solid State Ion*, 152–153, pp. 883–889, Dec. 2002, doi: 10.1016/S0167-2738(02)00390-9.

[189] Q. Wu, Y. Xu, Z. Yao, A. Liu, and G. Shi, "Supercapacitors Based on Flexible Graphene/Polyaniline Nanofiber Composite Films," *ACS Nano*, 4, pp. 1963–1970, Apr. 2010, doi: 10.1021/nn1000035.

[190] T. Luo, X. Xu, M. Jiang, Y. Lu, H. Meng, and C. Li, "Polyacetylene carbon materials: facile preparation using $AlCl_3$ catalyst and excellent electrochemical performance for supercapacitors," *RSC Adv*, 9, pp. 11986–11995, 2019, doi: 10.1039/C9RA01205B.

[191] S. Huang, L. Ren, J. Guo, H. Zhu, C. Zhang, and T. Liu, "The preparation of graphene hybrid films decorated with poly[2-methoxy-5-(2′-ethyl-hexyloxy)-1,4-phenylene vinylene] particles prepared by non-solvent induced precipitation," *Carbon N Y*, 50, pp. 216–224, Jan. 2012, doi: 10.1016/j.carbon.2011.08.038.

[192] M. Tomczykowa and M. Plonska-Brzezinska, "Conducting Polymers, Hydrogels and Their Composites: Preparation, Properties and Bioapplications," *Polymers (Basel)*, 11, Art no. 350, Feb. 2019, doi: 10.3390/polym11020350.

[193] H. Liu, X. Liu, S. Wang, H. K. Liu, and L. Li, "Transition metal based battery-type electrodes in hybrid supercapacitors: A review," *Energy Storage Mater*, 28, pp. 122–145, Jun. 2020, doi: 10.1016/J.ENSM.2020.03.003.

[194] D.-Y. Feng, Z. Sun, Z.-H. Huang, X. Cai, Y. Song, and X.-X. Liu, "Highly loaded manganese oxide with high rate capability for capacitive applications," *J Power Sources*, 396, pp. 238–245, Aug. 2018, doi: 10.1016/j.jpowsour.2018.06.026.

[195] Y. Zhang et al., "Defect promoted capacity and durability of N-MnO_{2-x} branch arrays via low-temperature NH_3 treatment for advanced aqueous zinc ion batteries," *Small*, vol. 15, Art. no. 1905452, Nov. 2019, doi: 10.1002/smll.201905452.

[196] M. Song, H. Tan, D. Chao, and H. J. Fan, "Recent advances in Zn-ion batteries," *Adv. Funct. Mater.*, vol. 28, Art. no. 1802564, Oct. 2018, doi: 10.1002/adfm.201802564.

[197] X. Liu, R. Ma, Y. Bando, and T. Sasaki, "A General Strategy to Layered Transition-Metal Hydroxide Nanocones: Tuning the Composition for High Electrochemical Performance," *Advanced Materials*, 24, pp. 2148–2153, Apr. 2012, doi: 10.1002/adma.201104753.

[198] M. Morishita *et al.*, "Structural Analysis by Synchrotron XRD and XAFS for Manganese-Substituted α- and β-Type Nickel Hydroxide Electrode," *J Electrochem Soc*, 155, Art no. A936, 2008, doi: 10.1149/1.2987947.

[199] C. Wang, X. Zhang, Z. Xu, X. Sun, and Y. Ma, "Ethylene Glycol Intercalated Cobalt/Nickel Layered Double Hydroxide Nanosheet Assemblies with Ultrahigh Specific Capacitance: Structural Design and Green Synthesis for Advanced Electrochemical Storage," *ACS Appl Mater Interfaces*, 7, pp. 19601–19610, Sep. 2015, doi: 10.1021/acsami.5b03176.

[200] L. J. Yang, X. P. Gao, Q. D. Wu, H. Y. Zhu, and G. L. Pan, "Phase Distribution and Electrochemical Properties of Al-Substituted Nickel Hydroxides," *The Journal of Physical Chemistry C*, 111, pp. 4614–4619, Mar. 2007, doi: 10.1021/jp0655468.

[201] Q. Wang and D. O'Hare, "Recent Advances in the Synthesis and Application of Layered Double Hydroxide (LDH) Nanosheets," *Chem Rev*, 112, pp. 4124–4155, Jul. 2012, doi: 10.1021/cr200434v.

[202] A. Mendhe and H. S. Panda, "A review on electrolytes for supercapacitor device," *Discover Mater.*, vol. 3, Art. no. 29, Dec. 2023, doi: 10.1007/s43939-023-00065-3.

[203] C. Zhong, Y. Deng, W. Hu, J. Qiao, L. Zhang, and J. Zhang, "A review of electrolyte materials and compositions for electrochemical supercapacitors," *Chem Soc Rev*, 44, pp. 7484–7539, 2015, doi: 10.1039/C5CS00303B.

[204] B.E. Conway, *Electrochemical Supercapacitors: Scientific Fundamentals and Technological Applications*, Springer US, 1999. [Online]. Available: https://doi.org/10.1007/978-1-4757-3058-6. [Accessed: Jan. 18, 2025].

[205] O. IBUKUN and H. K. JEONG*, "Effects of Aqueous Electrolytes in Supercapacitors," *New Physics: Sae Mulli*, 69, pp. 154–158, Feb. 2019, doi: 10.3938/NPSM.69.154.

[206] F. Béguin, V. Presser, A. Balducci, and E. Frackowiak, "Carbons and Electrolytes for Advanced Supercapacitors," *Advanced Materials*, 26, pp. 2219–2251, Apr. 2014, doi: 10.1002/adma.201304137.

[207] B. Pal, S. Yang, S. Ramesh, V. Thangadurai, and R. Jose, "Electrolyte selection for supercapacitive devices: a critical review," *Nanoscale Adv*, 1, pp. 3807–3835, 2019, doi: 10.1039/C9NA00374F.

[208] A. Lewandowski, A. Olejniczak, M. Galinski, and I. Stepniak, "Performance of carbon–carbon supercapacitors based on organic, aqueous and ionic liquid electrolytes," *J Power Sources*, 195, pp. 5814–5819, Sep. 2010, doi: 10.1016/j.jpowsour.2010.03.082.

[209] J. N. Ramavath, M. Raja, S. Kumar, and R. Kothandaraman, "Mild acidic mixed electrolyte for high-performance electrical double layer capacitor," *Appl Surf Sci*, 489, pp. 867–874, Sep. 2019, doi: 10.1016/j.apsusc.2019.05.343.

[210] N. Kanaujiya, N. Kumar, Y. Sharma, and G. D. Varma, "Probing the Electrochemical Properties of Flower Like Mesoporous MoS2 in Different Aqueous Electrolytes," *J Electron Mater*, 48, pp. 904–915, Feb. 2019, doi: 10.1007/s11664-018-6801-9.

[211] S. S. Shah and Md. A. Aziz, "Properties of electrode materials and electrolytes in supercapacitor technology," *J. Chem. Environ.*, 3, pp. 1–45, Feb. 2024, doi: 10.56946/jce.v3i1.309.

[212] W. G. Nunes, B. G. A. Freitas, R. M. Beraldo, R. M. Filho, L. M. Da Silva, and H. Zanin, "A rational experimental approach to identify correctly the working voltage window of aqueous-based supercapacitors," *Sci Rep*,10, Art no. 19195, Nov. 2020, doi: 10.1038/s41598-020-75851-7.

[213] D. A. C. da Silva *et al.*, "Effect of conductivity, viscosity, and density of water-in-salt electrolytes on the electrochemical behavior of supercapacitors: molecular dynamics simulations and *in situ* characterization studies," *Mater Adv*, 3, pp. 611–623, 2022, doi: 10.1039/D1MA00890K.

[214] T. S. Bhat, P. S. Patil, and R. B. Rakhi, "Recent trends in electrolytes for supercapacitors," *J. Energy Storage*, 50, Art. no. 104222, Jun. 2022, doi: 10.1016/j.est.2022.104222.

[215] K. Gajewska, A. Moyseowicz, D. Minta, and G. Gryglewicz, "Effect of electrolyte and carbon material on the electrochemical performance of high-voltage aqueous symmetric supercapacitors," *J Mater Sci*, 58, pp. 1721–1738, Jan. 2023, doi: 10.1007/s10853-023-08148-5.

[216] K. Gajewska, A. Moyseowicz, D. Minta, and G. Gryglewicz, "Effect of electrolyte and carbon material on the electrochemical performance of high-voltage aqueous symmetric supercapacitors," *J Mater Sci*, 58, pp. 1721–1738, Jan. 2023, doi: 10.1007/s10853-023-08148-5.

[217] C. Zhao and W. Zheng, "A review for aqueous electrochemical supercapacitors," *Front. Energy Res.*, vol. 3, Art. no. 23, May 2015, doi: 10.3389/fenrg.2015.00023.

[218] X. Wang, Y. Li, F. Lou, M. E. Melandsø Buan, E. Sheridan, and D. Chen, "Enhancing capacitance of supercapacitor with both organic electrolyte and ionic liquid electrolyte on a biomass-derived carbon," *RSC Adv*, 7, pp. 23859–23865, 2017, doi: 10.1039/C7RA01630A.

[219] S. Ahmed, A. Ahmed, and M. Rafat, "Supercapacitor performance of activated carbon derived from rotten carrot in aqueous, organic and ionic liquid based electrolytes," *Journal of Saudi Chemical Society*, 22, pp. 993–1002, Dec. 2018, doi: 10.1016/j.jscs.2018.03.002.

[220] D. Jiang, Z. Jin, D. Henderson, and J. Wu, "Solvent Effect on the Pore-Size Dependence of an Organic Electrolyte Supercapacitor," *J Phys Chem Lett*, 3, pp. 1727–1731, Jul. 2012, doi: 10.1021/jz3004624.

[221] X. Tian, Q. Zhu, and B. Xu, "'Water-in-Salt' Electrolytes for Supercapacitors: A Review," *ChemSusChem*, 14, pp. 2501–2515, Jun. 2021, doi: 10.1002/cssc.202100230.

[222] S. Li *et al.*, "An intrinsically non-flammable organic electrolyte for wide temperature range supercapacitors," *Chemical Engineering Journal*, 457, Art no. 141265, Feb. 2023, doi: 10.1016/j.cej.2022.141265.

[223] S. Islam, S. M. A. Nayem, A. Anjum, S. Shaheen Shah, A. J. S. Ahammad, and Md. A. Aziz, "A mechanistic overview of the current status and future challenges in air cathode for aluminum air batteries," *Chem. Rec.*, vol. 24, no. 1, Art. no. e202300017, Jan. 2024, doi: 10.1002/tcr.202300017.

[224] L. Miao, Z. Song, D. Zhu, L. Li, L. Gan, and M. Liu, "Ionic Liquids for Supercapacitive Energy Storage: A Mini-Review," *Energy & Fuels*, 35, pp. 8443–8455, May 2021, doi: 10.1021/acs.energyfuels.1c00321.

[225] P. Mone, S. Deore, S. Balgude, and V. Pandit, "Fabrication, design and performance evaluation of supercapacitors review," *Mater. Today Proc.*, vol. 53, pp. 130–133, 2022, doi: 10.1016/j.matpr.2021.12.427.

[226] M. Inagaki, H. Konno, and O. Tanaike, "Carbon materials for electrochemical capacitors," *J Power Sources*, 195, pp. 7880–7903, Dec. 2010, doi: 10.1016/J.JPOWSOUR.2010.06.036.

[227] S. Shiraishi, "Characterization of activated carbons for electric double layer capacitors," *TANSO*, 2007, pp. 195–199, Jun. 2007, doi: 10.7209/tanso.2007.195.

[228] M. D. Stoller and R. S. Ruoff, "Best practice methods for determining an electrode material's performance for ultracapacitors," *Energy Environ Sci*, 3, Art no. 1294, 2010, doi: 10.1039/c0ee00074d.

[229] M. Y. Perdana, B. A. Johan, M. Abdallah, M. E. Hossain, M. A. Aziz, T. N. Baroud, and Q. A. Drmosh, "Understanding the behavior of supercapacitor materials via electrochemical impedance spectroscopy: A review," *Chem. Rec.*, vol. 24, no. 5, Art. no. e202400007, May 2024, doi: 10.1002/tcr.202400007.

[230] D. Weingarth, A. Foelske-Schmitz, A. Wokaun, and R. Kötz, "PTFE Bound Activated Carbon - A Quasi Reference Electrode for Ionic Liquids and Its Application," *ECS Trans*, vol. 50, pp. 111–117, Mar. 2013, doi: 10.1149/05011.0111ecst.

[231] M. J. Bleda-Martínez, J. A. Maciá-Agulló, D. Lozano-Castelló, E. Morallón, D. Cazorla-Amorós, and A. Linares-Solano, "Role of surface chemistry on electric double layer capacitance of carbon materials," *Carbon N Y*, 43, pp. 2677–2684, Nov. 2005, doi: 10.1016/j.carbon.2005.05.027.

[232] S. S. Shah, Md. A. Aziz, W. Mahfoz, and Md. Akhtaruzzaman, "Types of supercapacitors," in *Biomass-Based Supercapacitors*, Wiley, 2023, pp. 93–104, doi: 10.1002/9781119866435.ch6.

[233] E. Frackowiak and F. Béguin, "Carbon materials for the electrochemical storage of energy in capacitors," *Carbon N Y*, 39, pp. 937–950, May 2001, doi: 10.1016/S0008-6223(00)00183-4.

[234] S. M. Abu Nayem, A. Ahmad, S. Shaheen Shah, A. S. Alzahrani, A. J. S. Ahammad, and M. A. Aziz, "Cover picture: High performance and long-cycle life rechargeable aluminum ion battery: Recent progress, perspectives and challenges," *Chem. Rec.*, 22, Art. no. e202281201, Dec. 2022, doi: 10.1002/tcr.202281201.

[235] S. M. Abu Nayem, A. Ahmad, S. Shaheen Shah, A. S. Alzahrani, A. J. S. Ahammad, and M. A. Aziz, "Cover picture: High performance and long-cycle life rechargeable aluminum ion battery: Recent progress, perspectives and challenges," *Chem. Rec.*, 22, Art. no. e202281201, Dec. 2022, doi: 10.1002/tcr.202281201.

[236] B. A. Johan, S. Ali, A. D. Shuaibu, S. S. Shah, A. S. Alzahrani, and Md. A. Aziz, "Metal negatrode supercapatteries: Advancements, challenges, and future perspectives for high-performance energy storage," *Chem. Rec.*, 24, Art. no. e202300239, Jan. 2024, doi: 10.1002/tcr.202300239.

[237] S. Wang, J. Zhang, O. Gharbi, V. Vivier, M. Gao, and M. E. Orazem, "Electrochemical impedance spectroscopy," *Nat. Rev. Methods Primers*, 1, Art. no. 41, Jun. 2021, doi: 10.1038/s43586-021-00039-w.

[238] A. I. Zia and S. C. Mukhopadhyay, *Electrochemical Sensing: Carcinogens in Beverages*, Springer International Publishing, 2016, pp. 21–67, doi: 10.1007/978-3-319-32655-9.

[239] J. Joe, H. Yang, C. Bae, and H. Shin, "Metal Chalcogenides on Silicon Photocathodes for Efficient Water Splitting: A Mini Overview," *Catalysts*, 9, Art no. 149, Feb. 2019, doi: 10.3390/catal9020149.

[240] J. B. Jorcin, M. E. Orazem, N. Pébère, and B. Tribollet, "CPE analysis by local electrochemical impedance spectroscopy," *Electrochim Acta*, 51, pp. 1473–1479, Jan. 2006, doi: 10.1016/J.ELECTACTA.2005.02.128.

[241] F. Béguin and E. Frąckowiak, Eds., *Supercapacitors: Materials, Systems, and Applications*, Wiley-VCH, 2013, pp. 21–67, doi: 10.1002/9783527646661.

Chapter 3

Synthesis of Onion-like carbon by flame pyrolysis method, experimental methods and characterization techniques

3.0. Introduction

Spherical carbon nano-structured materials (SCNMs) have consistently garnered substantial interest within the scientific community. The SCNMs are generated by carbon spheres, carbon dots, and fullerene-like CNOs[1]. From fullerenes to carbon nanotubes and, most recently, to graphene, carbon nanomaterials have been extensively researched and employed in several fields, such as electronics, interfacial science, and energy storage[2]. Nevertheless, two carbon materials identified before as fullerenes and nanotubes have long been overshadowed by more widely recognized and extensively studied nanocarbons. Nonetheless, both have been subject to growing research efforts in recent years[3]. Carbon nano-onions (CNOs) are constituted by closed spherical carbon shells that derive their name from the concentric layered structure that closely resembles that often seen in onions. CNOs are sporadically termed as (OLC) onion-like carbon[4].

The above designations encompass a wide range of coaxial shells, ranging from concentric fullerenes to tiny (less than 100 nm) polyhedral nanostructures[5]. Two forms of onion-like carbons (OLCs) may be identified: hollow onion-like carbon (H-OLCs) with polyhedral-shaped shells and solid onion-like carbon (S-OLCs) with a fullerene concentric spherical core-shell morphology[3][6]. The initial documentation of CNOs was published by Lijima in 1980 when

COs were seen as a side product through the production of CNTs[7]. Urgate produced the initial carbon nano onion subjecting, and carbon soot was applied to electron beam irradiation. Afterwards, CNTs were synthesized using laser ablation, arc discharge, flame pyrolysis, and electron beam injection[8][9]. Recently, onion-like Carbons have garnered noteworthy interest due to their distinctive characteristics that set them apart from other carbon nanomaterials[8].

The synthesis of OLCs is crucial for their wide-ranging uses. Nowadays, the synthesis of OLCs has been achieved using various techniques. The initial technique documented by Sumio Lijima was the identification of spherical CNOs as a secondary result of the synthesized carbon black produced in a vacuum using a transmission electron microscope (TEM) in 1980[5].

Through direct observation, Daniel Urgate conducted a comprehensive reexamination of this process in 1992 and successfully identified a formation mechanism for generating spherical graphitic structures. Curling and closure are straightforward methods for obtaining OLCs wrapped with catalytic particles as efficient catalysts[10]. They have synthesized OLCs by arc discharge between two graphite rods immersed in deionized water without needing metallic catalysts. Nevertheless, the resulting products consisted of a combination of contaminants, such as amorphous carbon, bits of graphite, and carbon nanotubes[11].

While the purifying process was intricate, applying functionalization to the OLCs was straightforward[12]. The thermal annealing of the nanodiamond resulted in the synthesis of significant quantities of CNOs. Nevertheless, it appeared demanding to isolate them from the

initial diamond origin. Detonation synthesis of CNOs by liquid carbon condensation has also been recorded[13]. Overall, most of the techniques, as mentioned earlier, demand significant energy consumption and have a meager yield of OLCs with sophisticated Purification treatment procedures.

Furthermore, several synthetic methods can generate CNOs with distinct architectures and characteristics. The intended use of OLCs should determine the optimal selection of an application technique. Due to its prospective applications, it is crucial to establish an intuitive and cost-effective approach for the industrial-scale fabrication of refined OLCs. Therefore, researchers have started investigating novel procedures for synthesizing OLCs[14].

Thus, the mass manufacture of OLCs necessitates a cost-effective and user-friendly manufacturing technique. The flame synthesis process is a prospective technique for industrial-scale production of OLCs due to its cost-effectiveness, user-friendly nature, and absence of byproducts. OLCs can be manufactured on a massive scale without a sophisticated vacuum chamber apparatus. The flame pyrolysis method, also known as the open flame-aided synthesis methodology, is an alternative approach for continuously manufacturing catalyst-free solid OLCs at ambient conditions[15][16]. During this method, the carbon precursor is broken down into radical or atomic fragments, which then react to produce aggregates of OLCs with the fundamental nucleation sites where they can subsequently form agglomerates. OLC layers are formed mainly from the interior to the exterior of the carbon particle-nodules formed due to the automatic curling mechanism [17][18].

Flame pyrolysis is a process that utilizes easily accessible carbon-containing liquids and oils such as flax seed oil, paraffin oil, and naphthalene. OLCs are produced using the flame pyrolysis method, which employs waste diesel engine oil as a carbon source. The combustion process in a diesel engine closely resembles that of normal hydrocarbon flames[19][20].

A flame pyrolysis process yields onion-like carbon-free from contamination by other types of carbon. Therefore, the use of highly corrosive agents for the elimination of undesired substances is unnecessary. The choice of precursor significantly influences the wettability of OLCs, particularly in electrochemical energy storage applications. This is crucial since it enhances the adsorption of ions in the transport of electrolytes and facilitates electron transport at the boundary of the electrolyte-electrode[21]. Electroconductive material with a significant surface area are necessary for energy retention in supercapacitors. The introduction of dopants can enhance the conductivity of untreated soot. Given their similar atomic weights to carbon, both boron and nitrogen can readily substitute carbon in a carbon network. Substituting nitrogen and boron in a carbon matrix can modify the Fermi level, enhancing the material's conductivity[22][23].

In this study, flame pyrolysis produced onion-like carbon that underwent functionalization using hydrogen peroxide and was individually and concurrently doped with nitrogen and boron using Chemical vapor decomposition. The characteristics of these OLCs were then investigated using different characterization techniques such as SEM, TEM, XRD, XPS, Raman,TGA, and BET. The selection of waste engine oil as a carbon source ,was based on its extended carbon chains, which can be broken down into Onion-like carbons.

3.1. Reagents and materials

Table 3. 1: Materials and reagents used in this research

Reagents and materials	Speciation and purity	Supplier
Waste engine Oil	-	Total energies
Nitric acid, HNO_3	≥ 55%	Ace
Hydrogen peroxide, H_2O_2	≥ 50%	Merck
Boric acid, H_3BO_3	≥ 99.5%	Sigma-Aldrich
Melamine, $C_3H_6N_6$	≥ 99%	Sigma-Aldrich
Ammonium pentaborate tetrahydrate, $NH_4B_5O_8.4H_2O$	≥ 99%	Sigma-Aldrich
Nitrogen gas, $N_{2(g)}$	≥ 99%	Afrox
Argon gas, $Ar_{(g)}$	≥ 99%	Afrox
4-dimethylamino pyridine	≥ 99%	Ace
Ammonium hydroxide solution	≥ 25%	Ace
Nickel (II) nitrate hexahydrate	≥ 99.99%	Merck

3.2. Flow diagram of synthesis and characterization of onion-like carbon

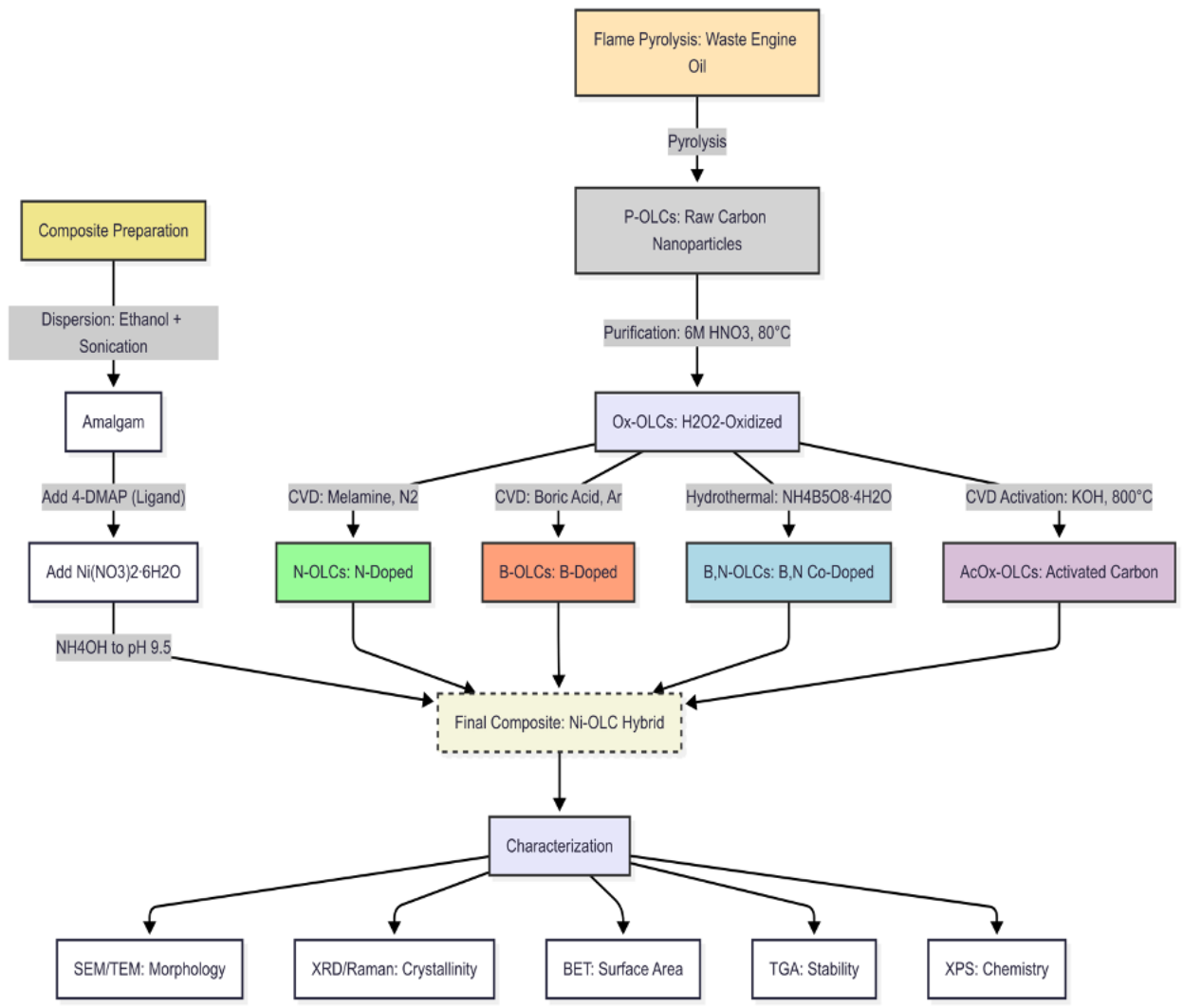


Figure 3. 1: Flow diagram of the synthesis process and characterization techniques.

3.3. Synthesis methods used in the preparation of the samples

3.3.1. Synthesis of OLCs using flame pyrolysis

Flame pyrolysis was employed to transform waste engine oil into onion-like carbons. A wick was submerged in 45 ml of used engine oil, and then the wick was ignited to produce a flame. The oil was replenished four times, resulting in a total of 180 ml used. The resulting black, powdery byproduct from the combustion was collected on a brass plate for two hours. The pitch-black carbon, weighing 2.7755 g, was then categorized as P-OLCs [8], as shown in **Figure 3.2.**

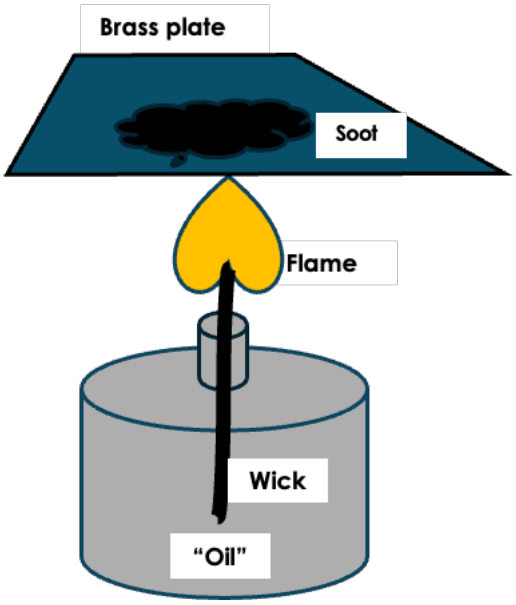


Figure 3. 2: The synthesis of OLCs using the flame pyrolysis technique.

3.3.2. Functionalization of Pristine OLCs (P-OLCs)

The P-OLCs were purified using 2M nitric acid (HNO_3) and oxidation with 50% hydrogen peroxide (H_2O_2). Initially, 2g of P-OLCs was transferred into a round-bottom flask, adding 50 ml of 2M HNO_3. The concoction was refluxed at 80°C for six hours. After refluxing, the acidified P-OLC mixture was vacuum filtered, rinsed several times with distilled water, and dried overnight at 80°C. The sediment from P-OLCs was treated with 20% hydrogen peroxide to incorporate carboxylic (-COO) functional groups. To achieve this, 20 ml of 50% hydrogen peroxide was mixed with distilled water in a 1:2 ratio before adding it to the washed acidified P-OLCs. This mixture was stirred and refluxed at 100°C for another 6 hours. Following this process, oxidized P-OLCs were obtained. The oxidized P-OLCs were first filtered, then washed multiple times with distilled water, and then dried overnight in an oven at 100 ° C. The final product was labeled as Ox-OLCs, as depicted in **Figure 3.3** [24].

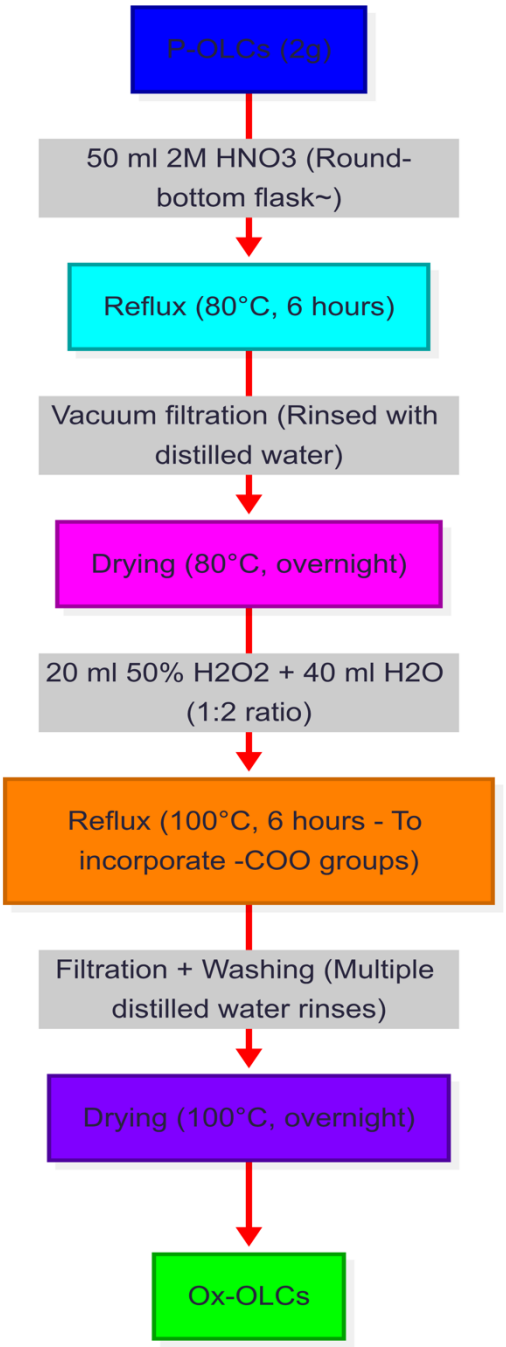


Figure 3. 3: Step by step flow diagram of P-OLCs Functionalization

3.3.3. Ex-situ nitrogen doping of Ox-OLCs

Ex-situ doping was performed by mixing 0.5g Ox-OLCs with 1.5g of melamine in a 1:3 ratio.20 mL of distilled water was added to this mixture. The mixture was stirred for two hours at room temperature and then dried overnight at 80°C. Following this, the dried mixture was subjected to CVD by heating it to 800°C for 2hrs, with a heating rate of 5°C per minute. During this process, nitrogen gas flowed through the mixture in a quartz boat at 150 ml/min. After heating, the sample was washed with distilled water, as depicted in **Figure 3.4**. The finished residue produced from this process was labeled as N-OLCs [25].

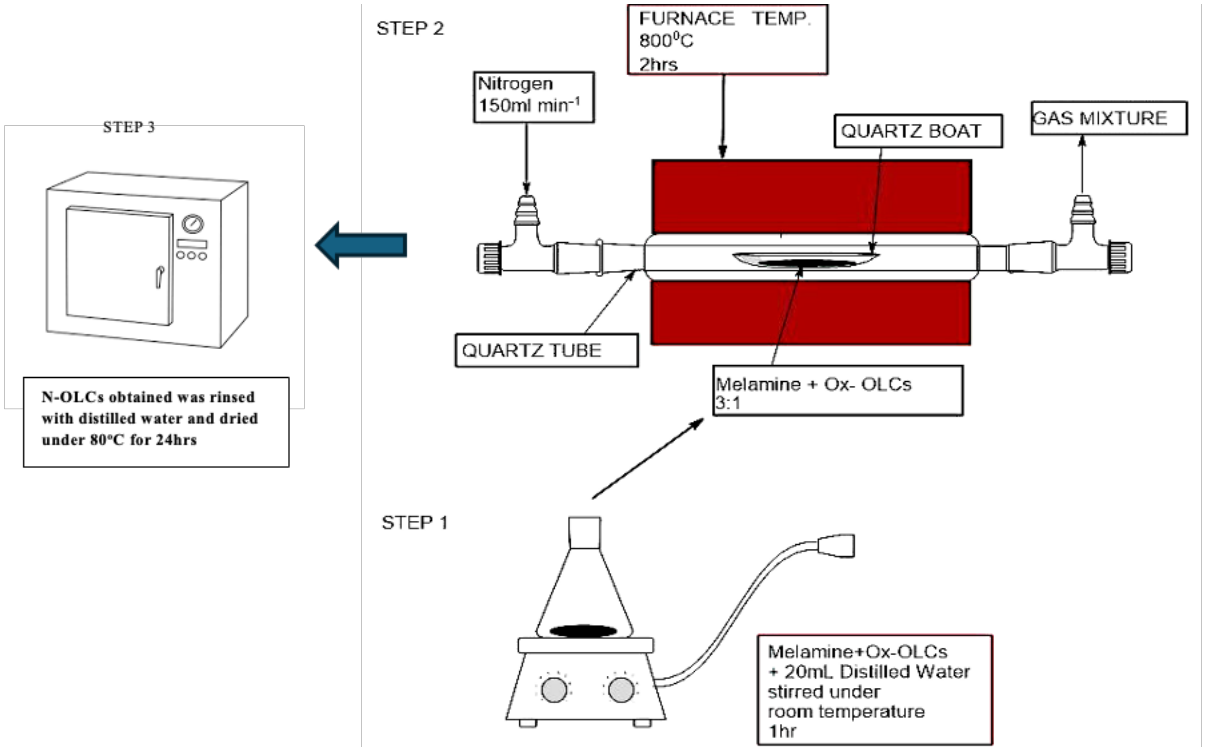


Figure 3. 4: Schematic diagram depicting doping of Ox-OLCs with nitrogen

3.3.4. Boron doping

The formation of B-OLCs was achieved using a CVD technique, with boric acid being utilized as the boron precursor and argon being employed as the carrier gas. The reaction was conducted in a (1:5) ratio. For 1 hour, 0.5g of Ox-OLCs and 0.1g of boric acid were manually blended with a mortar and pestle. The prepared mixture was transferred into a quartz boat and placed within a chemical vapor deposition (CVD) chamber. The furnace was ramped from 50 -100°C at a rate of 1.0 K/min and held at 100°C for 1 hour. The mixture was then heated in the furnace at 10 K /min to 900°C, with 150 ml/min of argon gas flowing through it. The mixture was maintained at 900°C for 2 hours and cooled gradually to room temperature. A product was secured after the reaction had been allowed to cool to room temperature. The specimen was refluxed in deionized water for 3 hours at 110 °C to have residual boron oxide removed through vacuum filtration, rinsed multiple times with distilled water, and then dried in an oven for 24 hours at 100 °C, as shown in **Figure 3.5**. These were B-OLC samples [26] [27].

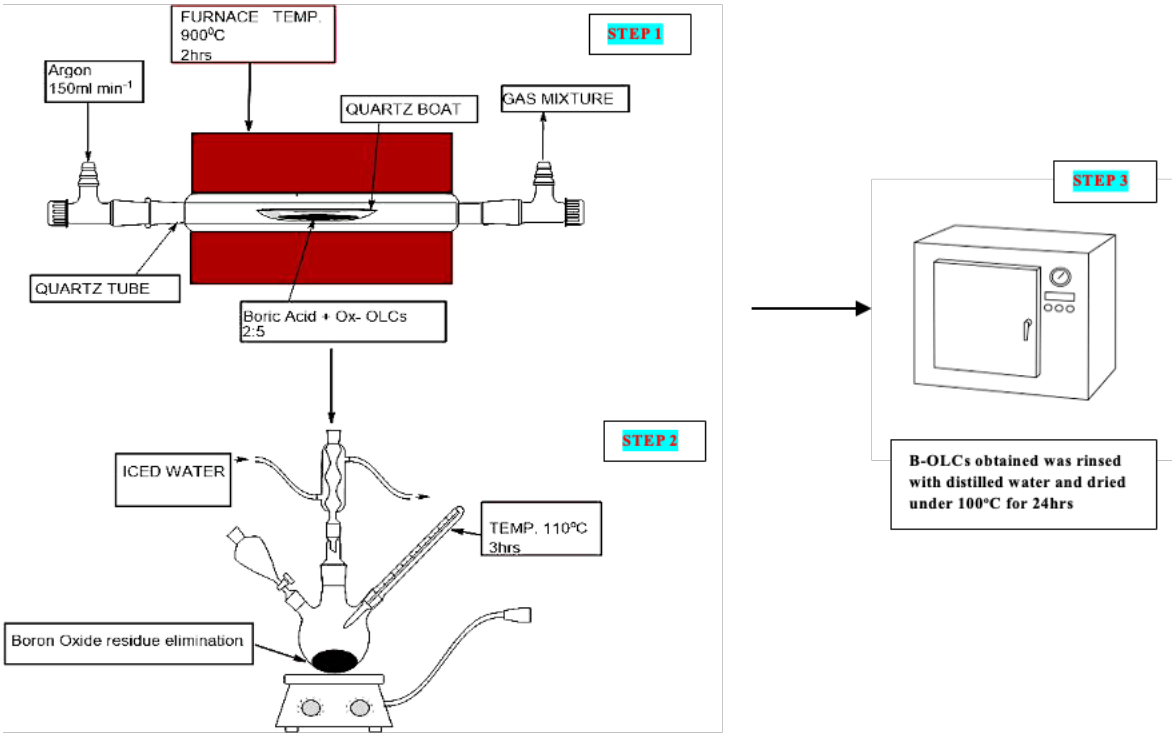


Figure 3. 5: Schematic diagram depicting doping of Ox-OLCs with boron.

3.3.5. Boron and nitrogen co-doped Ox-OLCs preparation

A hydrothermal process prepared co-doped onion-like carbon (N and B). In a container with 45 ml of deionized water, a mixture was created using 0.5 g of oxidized onion-like carbon (Ox-OLCs) and ammonium pentaborate tetrahydrate ($NH_4B_5O_8 \cdot 4H_2O$) in a 1:4 ratio, with vigorous stirring. This homogeneous mixture was transferred into 50 ml stainless-steel autoclaves lined with Teflon and heated to 190°C for 30 hours. After heating, the substance was extracted and washed repeatedly until the pH reached neutral after cooling to room temperature. The co-doped onion-like carbon materials containing both boron and nitrogen were collected and labeled as B, N-OLCs. They were dried overnight at 80°C, as shown in **Figure 3.6** [28].

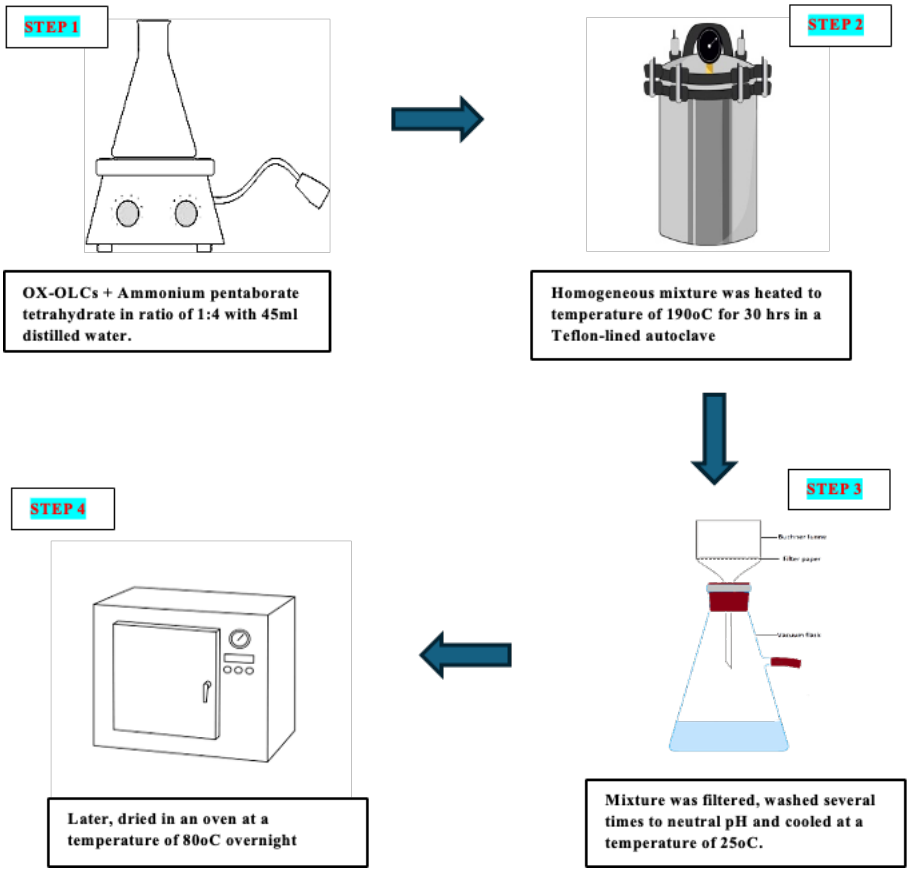


Figure 3. 6: Schematic diagram depicting co-doping of Ox-OLCs with boron and nitrogen

3.3.6. Preparation of the OLCs/Ni $(OH)_2$ composites with the mass ratio of (1:4)

A mixture was prepared by dispersing 250 milligrams of OX-OLCs, N-OLCs, B-OLCs, and B, N-OLCs in 25 mL of anhydrous ethanol. The amalgam was then subjected to sonication for 30 minutes. The resulting suspension was then combined with 25 mL of an aqueous solution containing (4-dimethylamino) pyridine at a concentration of 20 mM and stirred. Subsequently, equal amounts of nickel (II) nitrate hexahydrate (1:4) were introduced into each sample; then, a

5% ammonium hydroxide solution was added to the precipitated mixture of samples until the pH level reached 9.5.

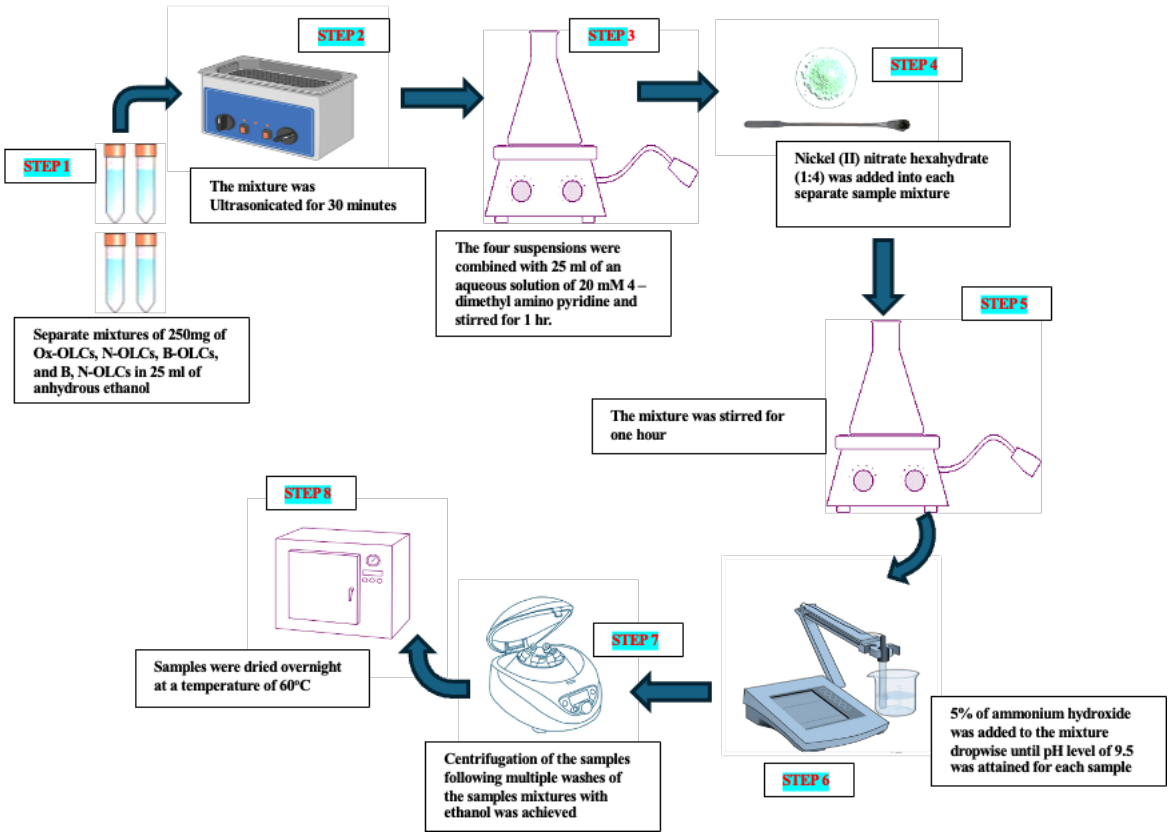


Figure 3. 7: schematic diagram depicting decoration of Ox-OLCs, N-OLCs, B-OLCs and B, N-OLCs.

The composite material was acquired through centrifugation, following multiple washes of the sample mixtures with ethanol, followed by overnight drying at a temperature of 60°C in an oven. The composites were prepared with mass ratios of Ox-OLCs to Ni $(OH)_2$ of approximately 1:4, as shown in **Figure 3.7**, consisting of P-OLCs/Ni $(OH)_2$ OX-OLCs/Ni $(OH)_2$, N-OLCs/Ni $(OH)_2$, B-OLCs/Ni $(OH)_2$, and B, N- OLCs/Ni $(OH)_2$ [29].

3.3.7. Preparation of activated carbon with the mass ratio of (1:3)

The synthesis of activated carbon involved the addition of 0.7g of the Ox-OLCs sample to potassium hydroxide in a 1:3 mass ratio in 50 ml of distilled water. The amalgam was mixed for 24 hours at ambient temperature and then dried overnight at 80°C. The resulting blend was transferred to a quartz boat and heated in a furnace at 800°C for 2 hours, with a heating amount of 5°C/min, under a nitrogen gush of 150 ml/min. Afterwards, the material was washed with 1.0M HCl and distilled water until a neutral pH was reached, as shown in **Figure 3.8**. The final sample was labeled as AcOx-OLCs[25].

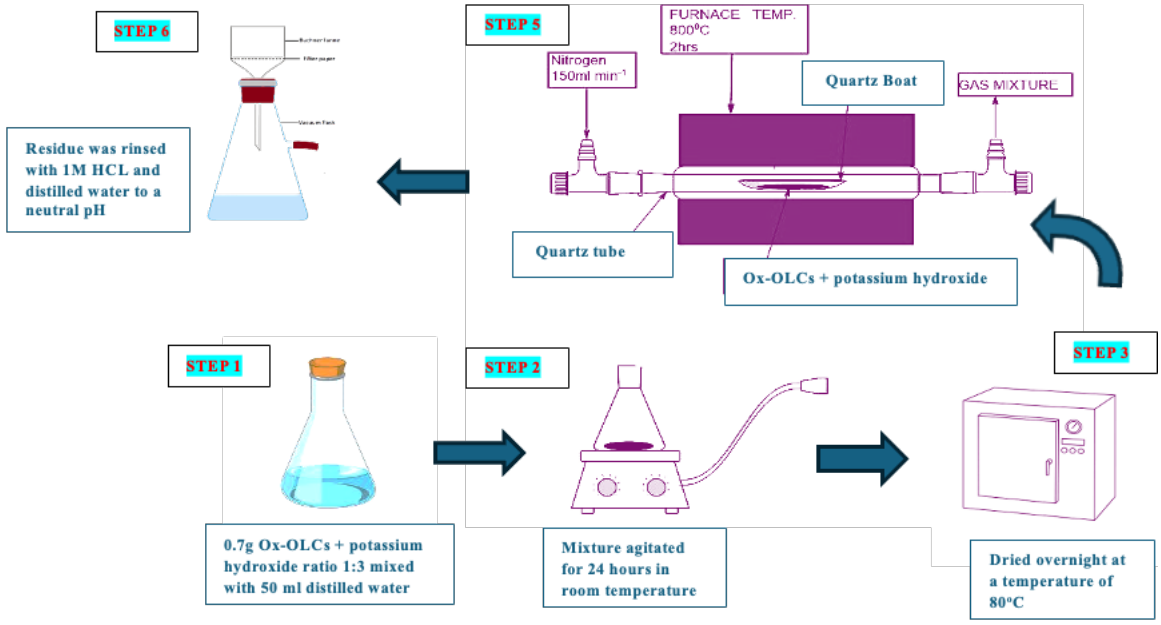


Figure 3. 8: Schematic representation depicting active theation process of Ox-OLCs.

3.4. A concise summary of various characterization techniques

3.4.1. Scanning Electron Microscope (SEM)

SEM is a rapid and forthright method for sample examination in materials engineering and science. The SEM offers high-resolution examination and several analytical modes, each revealing distinct information regarding the surface characteristics of materials. SEM is an advanced technology utilized to analyze the surface of a substance. In SEM, an electron beam accelerated to up to 30 kV voltages is concentrated on the sample[30].

The interactions between the sample and the electron beam generate signals, which are subsequently collected by detectors. The captured signals are amalgamated to create a picture. The principal components of the SEM are an electron lens system, an electron cannon, several electron detectors, electron-beam deflection coils, and recording and display systems[31], as depicted in **Figure 3.9 (a)**. The resolution limit is the lowest distance by which two structures can be separated and still be perceived as two discrete entities. Ernst Abbe demonstrated that the resolution limit is contingent upon the wavelength of the illuminating source. The enlarged image becomes indistinct when resolution is beyond the threshold at some wavelength. Due to interference and diffraction, a light point cannot be concentrated into a faultless dot[32].

Conversely, the image will exhibit a bigger diameter than the source, comprising a disc formed of concentric rings with decreasing intensity. Creating images in the SEM relies on the signals fashioned by the contacts between the sample and the electron beam. These contacts can be

classified into two primary categories: elastic and inelastic. The predominant signal generated by the interaction of the principal electron beam through the sample is the subsequent electron emission signal[33]. **Figure 3.9(b)** depicts another effective technique for generating images in scanning electron microscopy: uncovering of backscattered electrons (BSE), which yield structural and compositional information. A BSE is characterized as one that has experienced one or more scattering events and exits the surface with an energy over 50 eV. A distinct category of signals generated by the contact of the principal electron beam with the sample is distinctive X-rays[34].

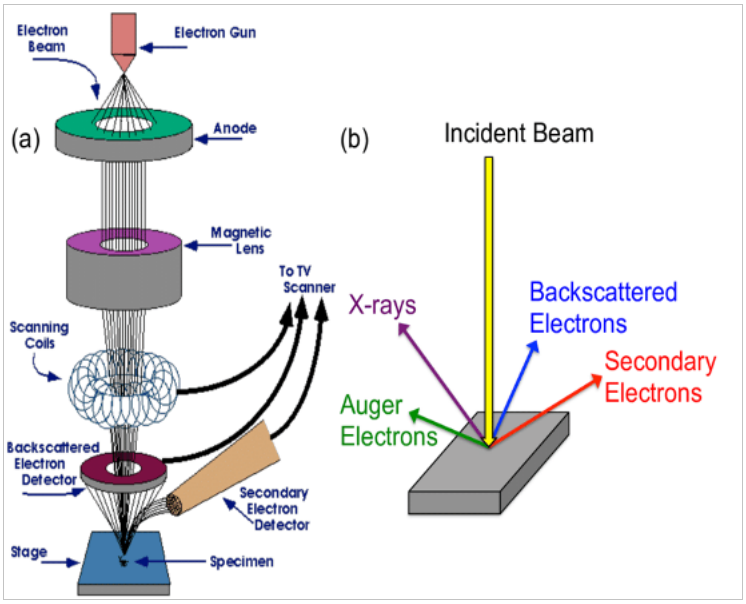


Figure 3. 9: (a) schematic representation depicting Scanning electron microscope (b) depicts how a beam act on the sample[35].

Examining distinctive X-rays for chemical information is the predominant microanalytical approach in scanning electron microscopy. Alongside the most frequently utilized signals like backscattered electrons, characteristic X-rays, and secondary electrons, various other types of signals are produced during the contact of the electron beam with the material, which may be employed for microstructure research. They are cathodoluminescence-transmitted electrons,

Auger electrons, and sample (or absorbed) current. All samples in this dissertation displayed electrical conductivity; therefore, they were plated with gold/palladium on carbon tape via drop coating to prevent the formation of electrostatic charge on their surfaces[36][37].

SEM parameters employed in this analysis

The scanning electron microscopy (SEM) analysis utilized a Zeiss sigma high-resolution field emission SEM (FE-SEM), model Sigma-0339, produced by Carl Zeiss, Oberkochen, Germany. Imaging was performed using SmartSEM software version 6.05, employing secondary electron and InLens detectors. The acceleration voltage was established at 3kV, accompanied by an aperture size of 30 µm. Energy dispersive X-ray spectroscopy (EDS) results were obtained at an acceleration voltage of 20 kV, utilizing a working distance of 12.5 mm. The EDS detector utilized was an Oxford Xplore30 AztecLiveLite layered probe detector, managed using Aztec software. Samples were affixed to Carbon tape and later coated with a thin layer of gold-palladium. The objective of this analysis within the the Thesis report was to evaluate the surface morphology, particle size distribution, and structural integrity of onion-like carbon materials, adhering to standard protocols for carbon nanostructure analysis, with the the aim of enhancing the conductivity of carbon electrode materials.

3.4.2. Transmission Electron Microscope (TEM)

While most periodic table elements were previously identified, the interior structure of materials remained undiscovered. Appropriate experimental procedures were developed that enabled structural study of the interior of materials. Shortly thereafter, the transmission electron microscope was invented, providing a depth of field that surpassed that of optical microscopes. The continuous advancement of transmission electron microscopes has finally achieved atomic

resolution. In addition to a prolonged lifespan, the electron source necessitates excellent brightness and little dispersion of kinetic electron energy. Contemporary transmission electron microscopes (TEMs) are outfitted with either lanthanum hexaboride (LaB_6) or field emission guns (FEGs)[38].

LaB_6 filaments provide an intense current, yet their brilliance is three orders of magnitude inferior to that of FEGs. The elevated current is particularly advantageous for energy-filtering transmission electron microscopy (EFTEM). Due to their electric charge, electrons can be redirected by magnetic or electric forces. Contemporary electron microscopes include circular magnetic lenses, as shown in **Figure 3.10**. In typical TEMs, the sample is lit by a practically parallel electron beam. The objective lens creates a magnified secondary picture of the lighted region, which is subsequently enlarged by post-sample lenses onto the image detector[39][40].

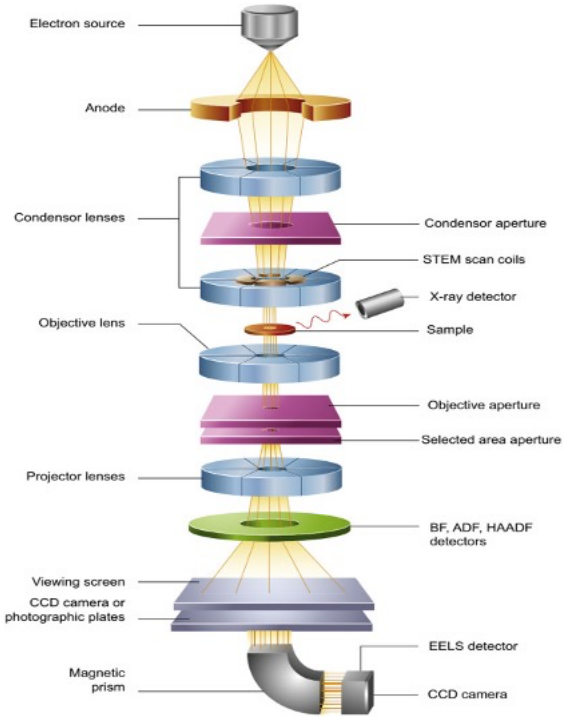


Figure 3. 10: Schematic representation depicting Transmission electron microscope[41]

Contemporary FEG-TEMs frequently incorporate scanning coils, enabling the microscopes to operate in an alternative imaging mode known as scanning mode. The fundamental type of electron spectrometer is a prism. Electrons are refracted approximately 90^{o} in a perpendicular stationary magnetic field[42]. The energy filter aims to create images from electrons that have experienced a particular energy loss. Energy-dispersive semiconductor detectors are employed to detect distinctive X-rays. Despite their inadequate energy resolution, their detection effectiveness surpasses wavelength-dispersive detectors, a crucial need in transmission electron microscopy due to the low count rate. The contact of electrons with matter is significantly more intense than X-rays with matter[43][44].

This is a natural result of electrical charge, and this robust interaction facilitates the investigation of small material volumes, underpinning elevated spatial resolution. While the overall potential of an atom, produced by the charged nucleus and the electron cloud, governs the scattering process, one can identify specific scenarios where the scattering center is attributed to a singular electron, a single nucleus, or a combination of both[45][46].

TEM parameters employed in this study analysis

High-resolution imaging of interior structures was conducted using an FEI Tecnai T12 Spirit transmission electron microscope at an accelerating voltage of 120 kV. Samples were suspended in ethanol, drop-cast onto carbon-coated copper grids, and subsequently dried before imaging. The TEM examination was utilized to directly examine the nanoscale stacking characteristics of graphitic layers in onion-like carbons. This method was employed to visualize the concentric

graphitic layers and evaluate the crystallinity, therefore validating the successful development of the onion-like carbon structure.

3.4.3. Raman Spectroscopy

The primary spectroscopies utilized to identify molecular vibrations are founded on Raman scattering and infrared absorption processes. They are extensively used to convey information on physical forms and chemical configurations, identify compounds by distinctive spectrum trends, and quantitatively and partially quantitatively ascertain the quantity of the material in a sample. Raman dispersion is less commonly employed than infrared incorporation due to sample deterioration and fluorescence issues. Nevertheless, recent advancements in equipment technology have streamlined the devices and significantly mitigated the problems [47].

The advancements, coupled with Raman spectroscopy's capability to analyze water-based solutions, samples within glass containers, and unprepared samples, have resulted in a swift expansion of the technique's applications. In practice, contemporary Raman spectroscopy is straightforward[48]. Scattering is a regularly employed technique. For instance, it is extensively utilized for quantifying particle dimension and dispersion down to dimensions below 1μm. The primary scattering approach employed for molecule identification is Raman scattering, as depicted in **Figure 3.11(b)**. The absorption mechanism is engaged in several spectroscopic techniques. For instance, it is utilized in acoustic spectroscopy, where there exists a minimal energy disparity between the excited and ground states, and in X-ray absorption spectroscopy, when there is a substantial difference[49].

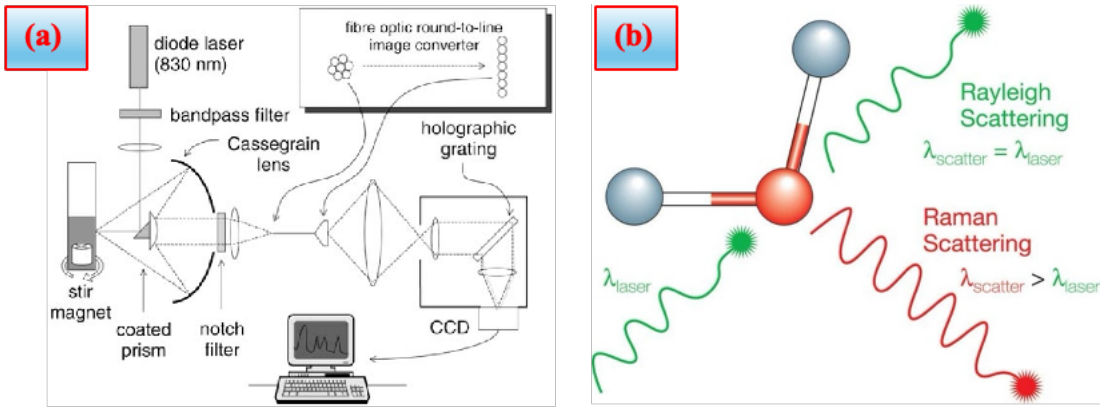


Figure 3. 11: (a) Schematic representation of Raman instrument (b) Schematic diagram of Raman Principle[50][51].

Among these extremes lie several prevalent techniques, including EPR, NMR, electronic absorption, infrared absorption, vacuum UV Spectroscopy, and fluorescence emission. Radiation is frequently defined by its wavelength. Nonetheless, spectroscopy focuses on the interference of radiation with the molecular states under examination, typically expressed as a form of energy. Consequently, utilizing wavenumber scales or frequency is generally advantageous, as they are linearly correlated with energy. In Raman dispersion, light interrelates with the molecule, distorting the electron cloud surrounding the nuclei to create a transient condition known as a 'virtual phase.' This state lacks stability, resulting in the rapid re-radiation of the photon, as illustrated in **Figure 3.11(a)**[52][53].

The energy alterations observed in vibrational spectroscopy are those necessary to induce nuclear motion. If just electron cloud displacement contributes to scattering, the photons will experience little frequency alterations due to the relatively low mass of the electrons. This scattering phenomenon is classified as elastic scattering and is the predominant mechanism. For molecules, this phenomenon is referred to as Rayleigh scattering, as depicted in **Figure 3.11(b)**. When the

nuclear signal is triggered during the dispersion phase, an energy exchange occurs between the incident photon and the molecule, either absorbing or emitting energy. This results in an inelastic process where the scattered photon possesses an energy shift equivalent to one vibrational quantum relative to the incident photon. This occurrence is termed Raman scattering [54][55].

Raman parameters employed in this study analysis

Raman spectroscopy of the onion-like carbons (OLCs) was conducted utilizing a Bruker Senterra Raman microscope. The measurements were conducted using a 532 nm excitation laser at a power of 5–10 mW to reduce sample heating and prevent damage. Spectra were obtained throughout the range of 800–2000 cm^{-1}, encompassing the typical D-band (~1350 cm^{-1}) and G-band (~1580–1605 cm^{-1}) linked to disorder and graphitic structures, respectively. A 50× objective lens was employed to concentrate on representative areas of the OLC sample, with accumulation times of 10–30 seconds each scan utilized to improve the signal-to-noise ratio. The ID/IG ratios were determined using the integrated areas of the D- and G-bands to assess the extent of faults and graphitization in the OLCs.

3.4.4. X-ray diffraction (XRD)

Powder XRD is a sophisticated, compact instrument. It possesses several prominent characteristics and novel accessories, such as a temperature-controlled component and humidity compartment, which can broaden the scope of its uses by offering analytical perspectives on the influence of temperature and humidity on material properties. When X-rays interact with a crystal, they diffract in a manner specific to its framework. In powder XRD, the scattering configuration is derived from a powder sample of the material instead of a singular crystal, as illustrated in **Figure 3.12(a)**.

Powder diffraction is frequently more uncomplicated and practical than one-crystalline diffraction, as it functions without requiring distinct crystals[56].

A diffraction pattern graphs intensity versus the angle of the detector, 2θ. The outcome is a diffractogram, as **Figure 3.12(b)** illustrates. In a diffraction configuration, the position of the peaks is contingent upon the wavelength. Absolute intensity may fluctuate based on experimental and instrumental conditions. Diffractometers can function in both reflection and transmission settings[57]. The reflective variant is more prevalent. The interrelation of the incident X-ray beam with the sample generates powerful reflected X-rays by positive interference when Bragg's law is satisfied. This formula delineates the fundamental link among the wavelength of the incident rays, the angle of incidence of the beam, and the interplanar spacing of the atomic crystal lattice. Constructive interference transpires when the variations in the travel route of the incident X-rays correspond to an integer multiple of the wavelength[58].

$$n\lambda = 2d\ sin\theta \qquad eqn\ (3.\ 1)$$

In this context, n represents integers (1, 2, 3, ...), λ denotes the wavelength of the incoming X-ray, d signifies the spacing among the diffracting planes, and θ indicates the angle of incidence. The angle separating the X-ray source, and the detector is 2θ, as depicted in **Equation 3.1**[61].

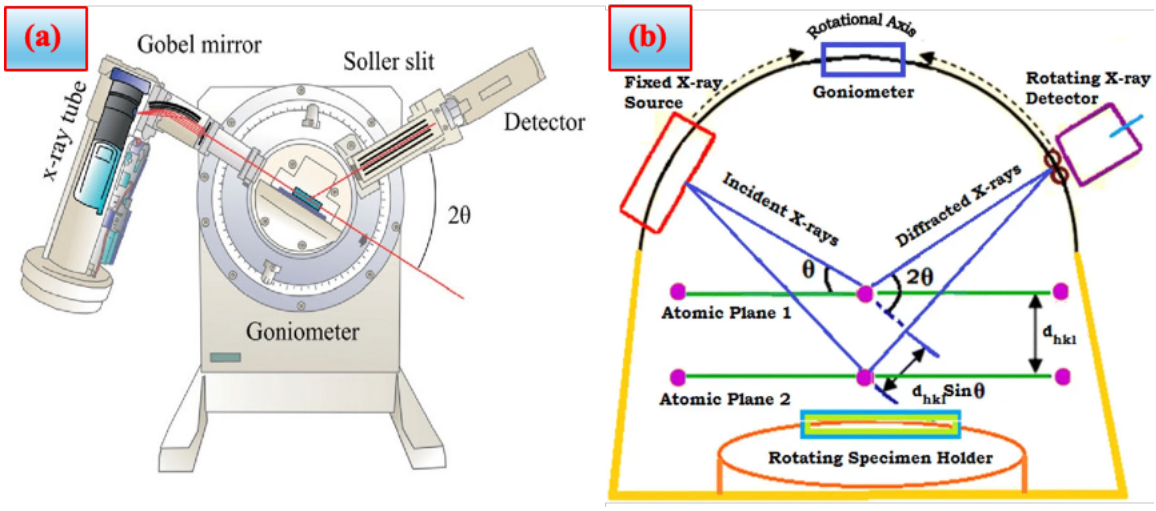


Figure 3. 12: (a) Schematic diagram of X-ray diffraction (b) Schematic representation of Bragg Bonteno configuration[59][60].

XRD parameters employed in this study

X-ray diffraction (XRD) observations were conducted utilising a Bruker D2 Phaser diffractometer, which employed Cu Kα radiation (λ = 1.5405 Å), operating at 30 kV and 10 mA. Data were acquired throughout a 2θ range of 10° to 90°, utilising a step size of 0.02° and a counting duration of 1 second each step. This investigation was utilised to identify the crystalline phases, ascertain the interlayer spacing, and assess the degree of graphitisation by scrutinising the typical diffraction peaks of carbon materials, specifically the (002) reflection, as documented in prior research.

3.4.5. X-ray photoelectron spectroscopy (XPS)

One of the most prevalent surface-sensitive methods is XPS. Recent papers have recorded the prevalent misapprehension of materials science representation data in the literature. Materials techniques for analysis, such as XPS, have grown increasingly accessible and user-friendly, although the figure of genuine specialists in these methods has not risen. Consequently, numerous

beginner users of a technology like XPS endeavor to independently interpret data, frequently resulting in inaccuracies[62].

XPS is a surface-sensitive investigative method wherein X-rays strike a material's surface, and the kinetic energy of the released electrons is quantified, as depicted in **Figure 3.13(a)**. The two primary attributes of this method that enhance its efficacy as an investigative method are its surface sensitivity and its capacity to disclose chemical state details of the elements within the sample. All elements, save hydrogen and helium, are detectable. XPS has been employed to investigate the surfaces of various materials, including plastics, textiles, dirt, and semiconductors. In XPS, the specimen is exposed to mild X-rays, and the kinetic energy of the released electrons is examined. The released photoelectron results from the total transfer of X-ray energy to a core-level electron, as shown in **Figure 3.13(a)**[63][64].

The photoelectron peaks are labeled according to the component and the orbital from which they were emitted. Electrons with a binding energy less than that of the X-ray source are ejected from the material and detected via the XPS technique. The binding energy is a distinction of the material itself and does not change with the choice of X-ray source used for ejection, as depicted in Figure 3.12(b). While the binding energy of photoelectrons remains unchanged across different X-ray

sources, the kinetic energy of the emitted photoelectrons will differ due to processes such as X-ray fluorescence or Auger electron radiation[65].

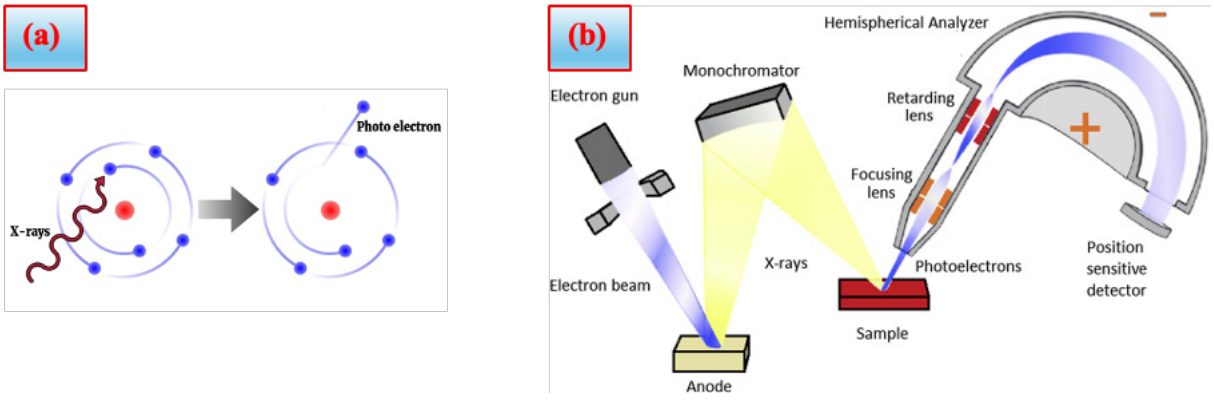


Figure 3. 13: (a) Schematic representation of XPS principle (b) depiction of X-ray photoelectron spectroscopy[66][67]

X-ray fluorescence is absent in the electron spectrum. Auger electrons produced by the procedure will be recognized and are frequently utilized in XPS for qualitative analysis. A significant advantage of XPS compared to other techniques is its capacity to ascertain the chemical surroundings of atoms within a sample, facilitating diverse levels of spectral comprehension, encompassing fundamental elemental analysis, in-depth evaluations of chemical shifts and bonding characteristics in the surface area, as well as relaxation structures or various loss that yield further insights into the chemical makeup of the surface[67].

XPS parameters employed in this study analysis

The surface composition of the four synthesized OLCs composites was analyzed using X-ray Photoelectron Spectroscopy (XPS) following the MAT-XPS-0008 analysis procedure. Measurements were performed on a Thermo ESCAlab 250xi instrument equipped with a

monochromatic Al Kα X-ray source (1486.7 eV) operating at 300 W, with a spot size of 900 µm. Survey spectra were acquired at a pass energy of 100 eV, while high-resolution spectra were recorded at 20 eV, under an ultra-high vacuum with a pressure below 1×10^{-8} mbar. This setup enabled accurate determination of elemental composition and chemical states on the sample surfaces.

3.4.6. Brunauer – Emmet – Teller (BET)

Gas adsorption is a widely employed instrumental method for characterizing mesoporous and micro materials, including a broad range of pore sizes. Substantial advancements have occurred in gas adsorption in recent years. Consequently, there is an enhanced comprehension of the actual capabilities of gas adsorption and its constraints. The utilization of N_2 in the BET ideal is commonly practiced; nonetheless, this methodology has certain drawbacks[68].

The BET technique comprises two stages, as **Figure 3.14(b)** shows. The physisorption isotherm must be converted into a BET graph to determine the monolayer capacity in the initial step, as depicted in **Figure 3.14(a)**. In the second stage, the surface area is computed. This computation employs the empirically established monolayer capacity alongside the hypothesized cross-sectional area of N_2, as illustrated in **Figure 3.14(b)**. The standard value for the cross-sectional area of N_2, commonly established as the default value in commercial programs, is an average of 0.162 nm^2/molecule[69]. Emmett and Brunauer obtained this quantity. Presuming the N_2 molecule is sphere-shaped in a close-packed liquid form at the adsorption temperature, computations using

the latest dimension of liquid density for N_2 demonstrate excellent concordance with the original value[69].

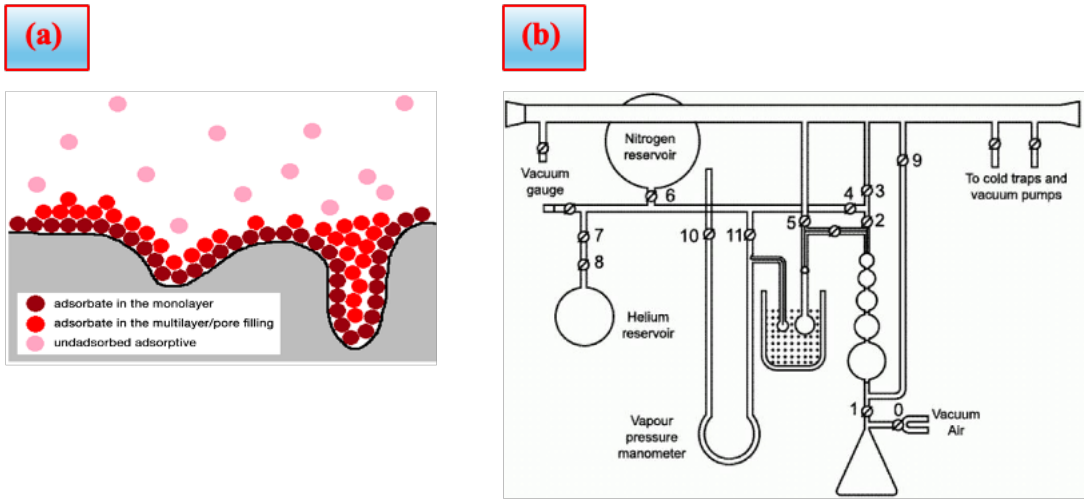


Figure 3. 14: (a) Representation of monolayer formation (b) depiction of Brunauer-Emmet-Teller surface area instrument[70][71].

BET parameters employed in this study analysis

The specific surface area and porosity of the onion-like carbon (OLC) samples were quantified with a Micromeritics TriStar II Plus surface area and porosity analyser (Version 3.03). Nitrogen adsorption–desorption isotherms were obtained at –195.85 °C (77 K). Approximately 0.0795 g of the sample was introduced into Port 2, and the free volume was ascertained using helium displacement (ambient free volume: 7.3837 cm^3; analytical free volume: 20.7985 cm^3). An equilibration interval of 10 seconds was implemented for each relative pressure point. The 0.05–0.30 P/P_0 range was employed for BET surface area assessment, whereas the complete isotherm was analysed for pore volume and pore size distribution. No automatic degassing was utilised; rather, samples were manually pre-treated using recognised protocols for carbon material preparation. The objective of this technique was to measure the specific surface area and pore

structural attributes, which are essential for the electrochemical performance of OLCs. The methodology followed the ISO 9277 standard for BET surface area measurement.

3.4.7. Thermogravimetric analysis (TGA)

According to the International Confederation for Thermal Analysis and Calorimetry (ICTAC), thermal evaluation is a series of methods to observe modifications in a sample's chemical or physical properties over time under a temperature regimen. TGA monitors and records the sample's mass, temperature, and time. The temperature program can involve heating, isothermal periods, cooling, or a mixture of these. The setup features a highly accurate microbalance linked to a sample pan within the furnace, with a temperature programmer and thermobalance control. The microbalance measures the sample within the enclosed furnace[72].

The sample temperature is measured by a thermocouple positioned near the pan. A protective tube separates the cooling coils and heating elements from the pan. A continuous flow of purge gas, ranging from 20-200 ml/min, passes over the sample. In a lower-loading TGA setup, the sample pan is suspended beneath the balance using a hook, while the purge gas passes through a capillary tube on one side and is expelled from the opposite flank of the pan. For upper-loading TGA configurations, a support rod secures the sample pan and thermocouple overhead the balance.

In this setup, the purge gas usually flows in from the bottom of the pan and out through the top[73][74]. The furnace and sample support are positioned horizontally in a side-loading design, with purge gas flowing over the pan's surface. The stove layout, gas entry, sample holder, and exit points mitigate turbulence intensity close to the sample pan and reduce interference in the mass

flow signal. In the top-side loading systems, the cooling coils and heating elements are orientated parallel to the flow stream[76].

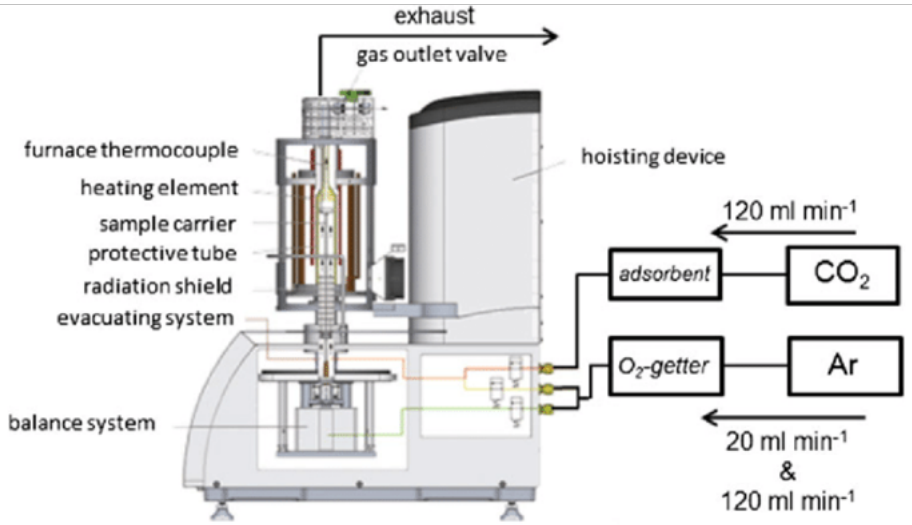


Figure 3. 15: Representation of Thermogravimetric analysis instruments set-up[75]

TGA parameters employed in this study analysis

Thermal stability and compositional analysis were conducted utilising a PerkinElmer TGA 4000 simultaneous thermal analysis system. Approximately 8 mg of the material was measured and transferred to an alumina crucible. The temperature was elevated from 35 °C to 900 °C at a heating rate of 10 °C min^{-1} in a nitrogen environment (20 mL min^{-1}, 3.5 pressure), subsequently followed by an oxidative phase in air (20 mL min^{-1}, 3.6 bar) to assess the oxidative behaviour. The analysis was conducted at atmospheric total pressure, with the specified inlet gas pressures aligning with system supply circumstances. This approach was utilised to acquire mass loss profiles related to the emission of volatile components, the disintegration of surface functional groups, and the thermal degradation of the carbonaceous structure under both inert and oxidative circumstances. All parameters were chosen in compliance with ASTM E1131 standards for the thermal examination of carbonaceous materials.

3.4. References

[1] T. H. Mongwe, B. J. Matsoso, B. K. Mutuma, N. J. Coville, and M. S. Maubane, "Synthesis of chain-like carbon nano-onions by a flame assisted pyrolysis technique using different collecting plates," *Diam Relat Mater*, vol. 90, pp. 135–143, Nov. 2018, doi: 10.1016/j.diamond.2018.10.002.

[2] V. N. Mochalin, O. Shenderova, D. Ho, and Y. Gogotsi, "The properties and applications of nanodiamonds," *Nature Nanotechnology*, 7, pp. 11–23, Dec. 2011, doi: 10.1038/nnano.2011.209.

[3] J. K. McDonough and Y. Gogotsi, "Carbon onions: Synthesis and electrochemical applications," *Electrochemical Society Interface*, 22, pp. 61–66, 2013, doi: 10.1149/2.F05133if.

[4] Y. V. Butenko, L. Šiller, and M. R. C. Hunt, "Carbon Onions," in *Handbook of Nanophysics: Clusters and Fullerenes*, K. D. Sattler, Ed., CRC Press, 2010, pp. 1–18, doi: 10.1201/9781420075557-39.

[5] S. Iijima, "Direct observation of the tetrahedral bonding in graphitized carbon black by high-resolution electron microscopy," *J. Cryst. Growth*, 50, pp. 675–683, Nov. 1980. [Online]. Available: https://doi.org/10.1016/0022-0248(80)90013-5.

[6] D. Ugarte, "Curling and closure of graphitic networks under electron-beam irradiation," *Nature*, 359, pp. 707–709, Oct. 1992, doi: 10.1038/359707a0.

[7] S. Iijima, "High resolution electron microscopy of some carbonaceous materials," *J Microsc*, 119, pp. 99–111, May 1980, doi: 10.1111/j.1365-2818.1980.tb04081.x.

[8] T. H. Mongwe, B. J. Matsoso, B. K. Mutuma, N. J. Coville, and M. S. Maubane, "Synthesis of chain-like carbon nano-onions by a flame assisted pyrolysis technique using different collecting plates," *Diam Relat Mater*, 90, pp. 135–143, Nov. 2018, doi: 10.1016/j.diamond.2018.10.002.

[9] K. Bogdanov *et al.*, "Annealing-induced structural changes of carbon onions: High-resolution transmission electron microscopy and Raman studies," *Carbon N Y*, 73, pp. 78–86, 2014, doi: 10.1016/j.carbon.2014.02.041.

[10] D. Ugarte, "Curling and closure of graphitic networks under electron-beam irradiation," *Nature*, 359, pp. 707–709, Oct. 1992, doi: 10.1038/359707a0.

[11] N. Sano *et al.*, "Properties of carbon onions produced by an arc discharge in water," *J Appl Phys*, vol. 92, pp. 2783–2788, Sep. 2002, doi: 10.1063/1.1498884.

[12] A. S. Rettenbacher, B. Elliott, J. S. Hudson, A. Amirkhanian, and L. Echegoyen, "Preparation and functionalization of multilayer fullerenes (carbon nano-onions)," *Chemistry - A European Journal*, vol. 12, pp. 376–387, Dec. 2005, doi: 10.1002/chem.200500517.

[13] M. Bagge-Hansen et al., "Detonation synthesis of carbon nano-onions via liquid carbon condensation," *Nat. Commun.*, 10, Dec. 2019, doi: 10.1038/s41467-019-11666-z.

[14] Y. Bian, L. Liu, D. Liu, Z. Zhu, Y. Shao, and M. Li, "Electrochemical synthesis of carbon nano onions," *Inorg Chem Front*, 7, pp. 4404–4411, Nov. 2020, doi: 10.1039/d0qi00950d.

[15] S. S. Hou, W. C. Huang, and T. H. Lin, "Flame synthesis of carbon nanostructures using mixed fuel in oxygen-enriched environment," *J. Nanopart. Res.*, vol. 14, no. 11, Art no. 1243, Nov. 2012, doi: 10.1007/s11051-012-1243-4.

[16] R. Serrano-Bayona, C. Chu, P. Liu, and W. L. Roberts, "Flame synthesis of carbon and metal-oxide nanoparticles: Flame types, effects of combustion parameters on properties and measurement methods," *Materials*, 16, art. no. 1192, Feb. 2023, doi: 10.3390/ma16031192.

[17] V. Dhand, J. S. Prasad, M. V. Rao, S. Bharadwaj, Y. Anjaneyulu, and P. K. Jain, "Flame synthesis of carbon nano onions using liquefied petroleum gas without catalyst," *Materials Science and Engineering C*, 33, pp. 758–762, Mar. 2013, doi: 10.1016/j.msec.2012.10.029.

[18] L. Levy, I. S. Chaudhuri, N. Krueger, and R. J. McCunney, "Does carbon black disaggregate in lung fluid? A critical assessment," *Chem. Res. Toxicol.*, 25, pp. 2001–2006, Oct. 2012, doi: 10.1021/tx300160z.

[19] J. Mohapatra *et al.*, "Enzymatic and non-enzymatic electrochemical glucose sensor based on carbon nano-onions," *Appl Surf Sci*, 442, pp. 332–341, Jun. 2018, doi: 10.1016/j.apsusc.2018.02.124.

[20] K. M. Tripathi, A. Singh, A. Bhati, S. Sarkar, and S. K. Sonkar, "Sustainable Feasibility of the Environmental Pollutant Soot to Few-Layer Photoluminescent Graphene Nanosheets for Multifunctional Applications," *ACS Sustain Chem Eng*, 4, pp. 6399–6408, Dec. 2016, doi: 10.1021/acssuschemeng.6b01045.

[21] S. Bokome, *Synthesis and Application of Boron-Nitrogen Doped Carbon Nano-Onions in Supercapacitors*, MSc dissertation, University of the Witwatersrand, Johannesburg, South Africa, Jan. 28, 2020. [Online]. Available: https://wiredspace.wits.ac.za/items/57d17f63-6fd1-45a2-8c1d-cbe0f74580ad. Accessed: Dec. 2024.

[22] P. Rani and V. K. Jindal, "Designing band gap of graphene by B and N dopant atoms," *RSC Adv*, 3, pp. 802–812, Jan. 2013, doi: 10.1039/c2ra22664b.

[23] L. S. Panchakarla *et al.*, "Synthesis, structure, and properties of boron- and nitrogen-doped graphene," *Advanced Materials*, 21, pp. 4726–4730, Dec. 2009, doi: 10.1002/adma.200901285.

[24] L. L. Sikeyi *et al.*, "Microwave assisted synthesis of nitrogen doped and oxygen functionalized carbon nano onions supported palladium nanoparticles as hybrid anodic electrocatalysts for direct alkaline ethanol fuel cells," *Int J Hydrogen Energy*, 46, pp. 10862–10875, Mar. 2021, doi: 10.1016/j.ijhydene.2020.12.154.

[25] B. Shaku, T. P. Mofokeng, N. J. Coville, K. I. Ozoemena, and M. S. Maubane-Nkadimeng, "Biomass valorisation of marula nutshell waste into nitrogen-doped activated carbon for use in high performance supercapacitors," *Electrochim Acta*, 442, Feb. 2023, doi: 10.1016/j.electacta.2023.141828.

[26] Y. Lin, Y. Zhu, B. Zhang, Y. A. Kim, M. Endo, and D. S. Su, "Boron-doped onion-like carbon with enriched substitutional boron: The relationship between electronic properties and catalytic performance," *J Mater Chem A Mater*, 3, pp. 21805–21814, 2015, doi: 10.1039/c5ta03141a.

[27] L. L. Sikeyi, T. D. Ntuli, T. H. Mongwe, N. W. Maxakato, N. J. Coville, and M. S. Maubane-Nkadimeng, "Platinum nanoparticles loaded on pristine and boron oxide modified carbon nano-onions for enhanced ammonia electrooxidation in alkaline direct ammonia fuel cells," *Catal. Today*, 383, pp. 55–62, Jan. 2022. [Online]. Available: https://www.sciencedirect.com/science/article/pii/S1572665722004039. Accessed: Mar. 12, 2025.

[28] L. Luo *et al.*, "High performance supercapacitor electrodes based on B/N Co-doped biomass porous carbon materials by KOH activation and hydrothermal treatment," *Int J Hydrogen Energy*, 46, pp. 31927–31937, Sep. 2021, doi: 10.1016/j.ijhydene.2021.06.211.

[29] D. M. Bobrowska, K. Brzezinski, L. Echegoyen, and M. E. Plonska-Brzezinska, "A new perspective on carbon nano-onion/nickel hydroxide/oxide composites: Physicochemical properties and application in hybrid electrochemical systems," *Fullerenes, Nanotubes and Carbon Nanostructures*, 25, pp. 193–203, Mar. 2017, doi: 10.1080/1536383X.2016.1267151.

[30] T. P. Mofokeng, *Hierarchical Nitrogen-Doped Carbon Nanotube–Carbon Nanofiber-Based Networks for Electrochemical Capacitors*, MSc dissertation, University of the

Witwatersrand, Johannesburg, South Africa, 2021. [Online]. Available: https://wiredspace.wits.ac.za/items/dd0657a2-7aaf-4378-b62b-2c438e625e23. Accessed: Dec. 2024.

[31] W. Zhou, R. P. Apkarian, Z. L. Wang, and D. Joy, "Fundamentals of scanning electron microscopy," in *Scanning Microscopy for Nanotechnology*, Springer, 2007, pp. 1–40. [Online]. Available: https://www.springer.com/gp/book/9780387497624. Accessed: Mar. 15, 2025.

[32] J. I. Goldstein, D. E. Newbury, P. Echlin, D. C. Joy, C. E. Lyman, and E. Lifshin, "Special topics in scanning electron microscopy," in *Scanning Electron Microscopy and X-ray Microanalysis*, 3rd ed., Springer, 2003, pp. 195–270, doi: 10.1007/978-1-4615-0215-9_5.

[33] A. Mohammed and A. Abdullah, "Scanning electron microscopy (SEM): A review," *Proc. 2018 Int. Conf. Hydraulics Pneumatics*, Baile Govora, Romania, Nov. 7–9, 2018, pp. 77–85. [Online]. Available: https://fluidas.ro/hervex/proceedings2018/77-85.pdf. Accessed: Mar. 2, 2025.

[34] O. C. Wells, *Scanning Electron Microscopy*, McGraw-Hill, 1974. [Online]. Available: https://archive.org/details/scanningelectron00well. Accessed: Mar. 25, 2025.

[35] M. J. Walock, "Nanocomposite coatings based on quaternary metal-nitrogen and Nanocomposite coatings based on quaternary metal-nitrogen and nanocarbon systems nanocarbon systems." [Online]. Available: https://digitalcommons.library.uab.edu/etd-collection/3246

[36] J. I. Goldstein, D. E. Newbury, P. Echlin, D. C. Joy, C. E. Lyman, and E. Lifshin, *Scanning Electron Microscopy and X-ray Microanalysis*, 3rd ed. Boston, MA: Springer US, 2003. doi: 10.1007/978-1-4615-0215-9.

[37] A. Ali, N. Zhang, and R. M. Santos, "Mineral Characterization Using Scanning Electron Microscopy (SEM): A Review of the Fundamentals, Advancements, and Research Directions," *Applied Sciences*, 13, Art. no. 12600, Nov. 2023, doi: 10.3390/app132312600

[38] W. Sigle, "Analytical transmission electron microscopy," *Annu. Rev. Mater. Res.*, 35, pp. 239–314, 2005, doi: 10.1146/annurev.matsci.35.102303.091623.

[39] W. Bollmann, "Interference Effects in the Electron Microscopy of Thin Crystal Foils," *Philosophical Magazine*,86, pp. 4573–4574, Oct. 2006, doi: 10.1080/14786430600779524.

[40] H. Rose, "Prospects for realizing a sub-Å sub-eV resolution EFTEM," *Ultramicroscopy*, 78, pp. 13–25, Jun. 1999, doi: 10.1016/S0304-3991(99)00025-X.

[41] L. Hu, D. Hach, D. Chaumont, C. H. Brachais, and J. P. Couvercelle, "One step grafting of monomethoxy poly(ethylene glycol) during synthesis of maghemite nanoparticles in aqueous medium," *Colloids Surf A Physicochem Eng Asp*, 330, pp. 1–7, Nov. 2008, doi: 10.1016/J.COLSURFA.2008.07.044.

[42] L. Reimer, *Energy-Filtering Transmission Electron Microscopy*, Springer Series in Optical Sciences, 71. Berlin, Heidelberg: Springer Berlin Heidelberg, 1995, pp. XIII + 425, doi: 10.1007/978-3-540-48995-5.

[43] M. Haider, S. Uhlemann, and J. Zach, "Upper limits for the residual aberrations of a high-resolution aberration-corrected STEM," *Ultramicroscopy*, 81, pp. 163–175, Apr. 2000, doi: 10.1016/S0304-3991(99)00194-1.

[44] J. M. Ede, "Deep learning in electron microscopy," *Mach. Learn.: Sci. Technol.*, 2, Art. no. 011004, Mar. 2021, doi: 10.1088/2632-2153/ABD614.

[45] U. Dahmen, R. Erni, V. Radmilovic, C. Ksielowski, M.-D. Rossell, and P. Denes, "Background, status and future of the Transmission Electron Aberration-corrected Microscope project," *Philosophical Transactions of the Royal Society A: Mathematical, Physical and Engineering Sciences*, 367, pp. 3795–3808, Sep. 2009, doi: 10.1098/rsta.2009.0094.

[46] J. Ximen, "The electron optical imaging system and its aberrations," *Advances in Imaging and Electron Physics*, 226, pp. 1–88, Jan. 2023, doi: 10.1016/bs.aiep.2023.03.003.

[47] E. Smith and G. Dent, *Modern Raman Spectroscopy: A Practical Approach*, John Wiley & Sons, 2005. [Online]. Available: https://onlinelibrary.wiley.com/doi/book/10.1002/0470011831. Accessed: Mar. 4, 2025.

[48] J. M. Ede, "Deep learning in electron microscopy," *Mach. Learn.: Sci. Technol.*, 2, Art. no. 011004, Mar. 2021, doi: 10.1088/2632-2153/ABD614.

[49] A. Kudelski, "Analytical applications of Raman spectroscopy," *Talanta*, 76, pp. 1–8, Jun. 2008, doi: 10.1016/J.TALANTA.2008.02.042.

[50] N. Li *et al.*, "Guidelines for Raman spectroscopy and imaging techniques in food safety analysis," *Food Safety and Health*, 2, pp. 221–237, Apr. 2024, doi: 10.1002/fsh3.12040.

[51] E. Cordero, "In-vivo Raman spectroscopy: from basics to applications," *J Biomed Opt*, 23, Art no. 1, Jun. 2018, doi: 10.1117/1.JBO.23.7.071210.

[52] J. R. Ferraro, K. Nakamoto, and C. W. Brown, *Introductory Raman Spectroscopy*, 2nd ed., Academic Press, 2003. [Online]. Available: https://www.sciencedirect.com/book/9780122541056/introductory-raman-spectroscopy. Accessed: Mar. 5, 2025.

[53] H. Mi, Z. Ma, and J. P. Blanchard, "Raman spectroscopy for monitoring strain on graphene and oxidation corrosion on nuclear claddings," in Raman Spectroscopy and Applications, InTech, 2017. doi: 10.5772/65111.

[54] R. Bands, "Raman data and analysis: Raman spectroscopy for analysis and monitoring," *Jobin Yvon*, [Online]. Available: https://www.jobinyvon.fr. [Accessed: Mar. 25, 2025].

[55] P. Rostron, S. Gaber, and D. Gaber, "Raman spectroscopy, review," *Int. J. Eng. Technol. Res.*, 6, pp. 50–64, May 2017. [Online]. Available: https://www.erpublication.org/page/view_issue/volume6-issue1.

[56] F. Adams, "X-Ray absorption and diffraction – Overview," in *Encyclopedia of Analytical Science*, 2nd ed., vol. 9, P. J. Worsfold, A. Townshend, and C. F. Poole, Eds. Oxford: Elsevier, Jan. 2004, pp. 365–377, doi: 10.1016/B0-12-369397-7/00668-3.

[57] A. Chauhan, "Powder XRD Technique and its Applications in Science and Technology," *J Anal Bioanal Tech*, 5, 2014, doi: 10.4172/2155-9872.1000212.

[58] J. A. BEARDEN, "X-Ray Wavelengths," *Rev Mod Phys*, 39, pp. 78–124, Jan. 1967, doi: 10.1103/RevModPhys.39.78.

[59] B. Stefanov, *Photocatalytic TiO_2 Thin Films for Air Cleaning: Effect of Facet Orientation, Chemical Functionalization, and Reaction Conditions*, 1307, Acta Universitatis Upsaliensis, 2015, pp. 1–148. [Online]. Available: http://urn.kb.se/resolve?urn=urn:nbn:se:uu:diva-265056. [Accessed: Feb. 18, 2025].

[60] G. R. Khan, "Crystallographic, structural and compositional parameters of Cu–ZnO nanocrystallites," *Appl Phys A Mater Sci Process*, 126, Apr. 2020, doi: 10.1007/s00339-020-03480-y.

[61] M. Hušák *et al.*, "Metergoline II: structure solution from powder diffraction data with preferred orientation and from microcrystal," *Struct Chem*, 19, pp. 517–525, Jun. 2008, doi: 10.1007/s11224-008-9312-0.

[62] F. A. Stevie and C. L. Donley, "Introduction to x-ray photoelectron spectroscopy," *Journal of Vacuum Science & Technology A: Vacuum, Surfaces, and Films*, 38, Dec. 2020, doi: 10.1116/6.0000412.

[63] J. Matthew, "Surface analysis by Auger and x-ray photoelectron spectroscopy. D. Briggs and J. T. Grant (eds). IMPublications, Chichester, UK and SurfaceSpectra, Manchester, UK, 2003. 900 pp., ISBN 1-901019-04-7, 900 pp," *Surface and Interface Analysis*, 36, pp. 1647–1647, Jan. 2004, doi: 10.1002/sia.2005.

[64] P. E. Batson, "Aberration correction results in the IBM STEM instrument," *Ultramicroscopy*, 96, pp. 239–249, Sep. 2003, doi: 10.1016/S0304-3991(03)00091-3.

[65] C. J. Powell, D. R. Baer, K. Artyushkova, C. R. Brundle, J. E. Castle, M. H. Engelhard, K. J. Gaskell, J. T. Grant, R. T. Haasch, M. R. Linford, A. G. Shard, P. M. A. Sherwood, and V. S. Smentkowski, "Practical guides for x-ray photoelectron spectroscopy: First steps in planning, conducting, and reporting XPS measurements," *J. Vac. Sci. Technol. A*, 37, Art. no. 031401, May 2019. [Online]. Available: https://doi.org/10.1116/1.5065501

[66] L. T. Gibson, "Archaeometry and antique analysis: (b) metallic and ceramic objects," in *Encyclopedia of Analytical Science*, P. J. Worsfold, A. Townshend, and C. F. Poole, Eds., Oxford, UK: Elsevier Limited, 2004, pp. 117–123.

[67] Diamond Light Source, "How XPS works," *Diamond Light Source*, [Online]. Available: https://www.diamond.ac.uk/industry/Techniques-Available/Spectroscopy/X-ray-Photoelectron-Spectroscopy-XPS/How-XPS-works.html. [Accessed: Mar. 25, 2025].

[68] L. López-Pérez, V. Zarubina, and I. Melián-Cabrera, "The Brunauer–Emmett–Teller model on alumino-silicate mesoporous materials. How far is it from the true surface area?," *Microporous and Mesoporous Materials*, 319, Art no. 111065, May 2021, doi: 10.1016/J.MICROMESO.2021.111065.

[69] V. B. Mohan, K. Jayaraman, and D. Bhattacharyya, "Brunauer–Emmett–Teller (BET) specific surface area analysis of different graphene materials: A comparison to their structural regularity and electrical properties," *Solid State Commun*, 320, Art no. 114004, Oct. 2020, doi: 10.1016/J.SSC.2020.114004.

[70] Anton Paar, "BET theory," *Anton Paar Wiki*, [Online]. Available: https://wiki.anton-paar.com/en/bet-theory/. [Accessed: Mar. 5, 2025].

[71] V. N. J. Venkatesha, "Pore architecture modulated clays and zeolites as solid acid catalysts for selected organic reactions," Ph.D. dissertation, Dept. Chem., Bangalore Inst. Technol., Bangalore, India, Dec. 2015. Available: https://www.researchgate.net/publication/326041035_Pore_architecture_modulated_clays_and_zeolites_as_solid_acid_catalysts_for_selected_organic_reactions. [Accessed: Mar. 15, 2025].

[72] N. Saadatkhah et al., "Experimental methods in chemical engineering: Thermogravimetric analysis—TGA," *Can. J. Chem. Eng.*, 2020. [Online]. Available: https://doi.org/10.1002/cjce.23673

[73] S. Vyazovkin, A. K. Burnham, J. M. Criado, L. A. Pérez-Maqueda, C. Popescu, and N. Sbirrazzuoli, "ICTAC Kinetics Committee recommendations for performing kinetic computations on thermal analysis data," *Thermochim Acta*, 520, pp. 1–19, Jun. 2011, doi: 10.1016/j.tca.2011.03.034.

[74] L. Liu, B. Kong, Q. Jiao, J. Yang, Q. Liu, and X. Liu, "Structure Characterization and CO_2 Gasification Kinetics of Tri-High Coal-Chars Derived from High-Temperature Pyrolysis," *ACS Omega*, 4, pp. 19030–19036, Nov. 2019, doi: 10.1021/acsomega.9b02024.

[75] K. M. Allen, E. N. Coker, N. Auyeung, and J. F. Klausner, "Cobalt Ferrite in YSZ for Use as Reactive Material in Solar Thermochemical Water and Carbon Dioxide Splitting, Part I: Material Characterization," *JOM*, 65, pp. 1670–1681, Dec. 2013, doi: 10.1007/s11837-013-0704-2.

[76] J. D. Menczel, "Thermogravimetric analysis (TGA)," in *Thermal Analysis of Polymers: Fundamentals and Applications*, J. D. Menczel, Ed., Hoboken, NJ, USA: John Wiley & Sons, Inc., 2009, pp. 1–6. [Online]. Available: https://www.researchgate.net/publication/285356048_Introduction. [Accessed: Mar. 15, 2025].

Chapter 4

Physicochemical and structural characterization of synthesized materials

4.1. Results and Discussion

4.1.1. Scanning Electron Microscopy (SEM) imaging, Energy Dispersive Spectroscopy (EDS) and elemental EDS mapping of pristine, oxidized, and doped onion-like carbon.

All the synthesized OLCs (i.e., pristine:P-OLCs, functionalized: Ox-OLCs, nitrogen doped: N-OLCs, boron doped: B-OLCs, activated functionalized:Ac-OLCs, and boron-nitrogen co-doped: BN-OLCs) displayed distinct variations in morphology, characterized by porous structures that contained multiple outcroppings and channels [1]. All samples consisted of nanoparticle aggregates. The images in **Figures 4.1a-e** and **4.2a-f** depict a quasi-spherical morphology produced by the pyrolysis process. Notably, the sample in **Figure 4.1a** exhibit substantial alterations in particle sizes and shapes compared to **Figures 4.1 (b-e)** and **4.2 (a-f).** Additionally, OLCs, when subjected to hydrogen peroxide, experiences oxidation. This oxidation incorporates functional groups that have oxygen in them, including hydroxyl (-OH), carboxyl (-COOH), and carbonyl (C=O) groups, onto the exterior of the carbon nanostructures. The morphological alterations resulting from this oxidation activity are chiefly associated with incorporating these functional groups, as depicted in **Figures 4.1(b-e)** and **4.2 (a-f)**. The morphological modifications

from this oxidation activity are principally related to integrating these functional groups. The surfaces of these samples exhibit a porous nature, as represented in **Figures 4.1 (b-e) and 4.2 (a-f)**, a distinctive feature of carbon nanostructures. These facilitate the transportation of ions in the electrodes/electrolytes, resulting in high-performance supercapacitors [2].

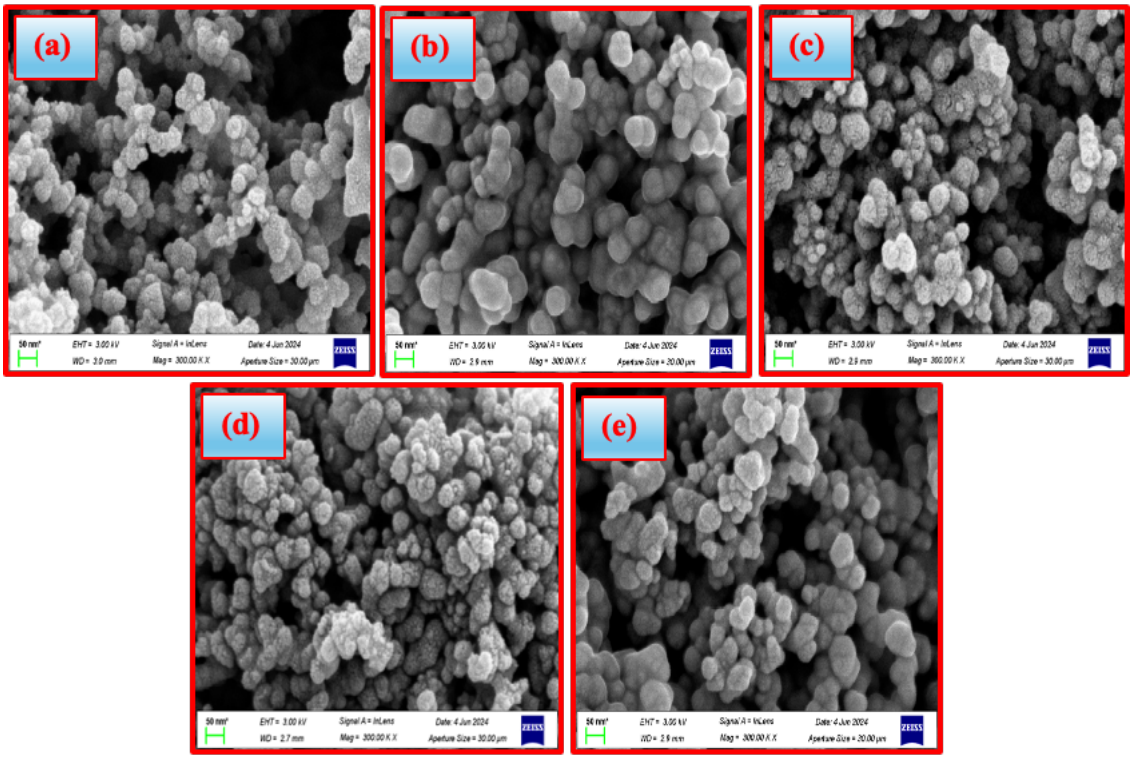


Figure 4. 1: SEM images of (a) P-OLCs (b) Ox-OLCs (c) N-OLCs (d) B-OLCs (e) B, N-OLCs

The introduction of nitrogen atoms into carbon materials alters their hydrophilicity and wettability, thereby influencing their ability to disperse in polar solvents. The relationship between the variables is depicted in **Figures 4.1c, 4.1e, 4.2c, and 4.1e** [3]. The textural properties of OLCs structures were modified by nitrogen doping, boron doping, and co-doping, which aligns with the results obtained from TEM and gas adsorption measurements [4]. The B, N-OLCs/Ni $(OH)_2$ in **Figure 4.2e** exhibits a highly aggregated, overlapping structure, irregular presence of cavities, and

a thin wall. This morphology may be attributed to the B and N heteroatoms found on the surface of the OLCs. These heteroatoms provide ample opportunities for enhancing the transport properties of Ni $(OH)_2$.

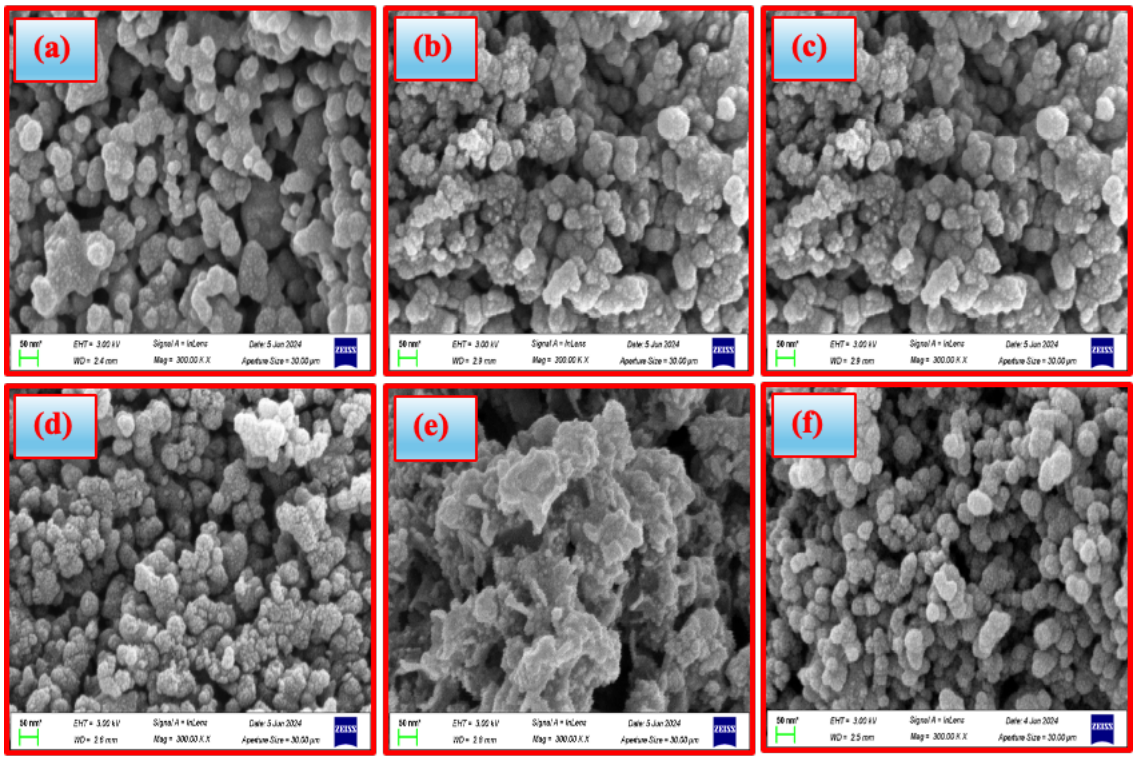


Figure 4. 2: SEM images of composites and activated functionalized onion-like carbon (a) P-OLCs/Ni $(OH)_2$ (b) Ox-OLCs/Ni $(OH)_2$ (c) N-OLCs/Ni $(OH)_2$ (d) B-OLCs/Ni $(OH)_2$ (e) B, N-OLCs/Ni $(OH)_2$ (f) AcOx-OLCs

The presence of boron and nitrogen on the surface of the OLC structure can be inferred from the EDS mapping of B, N-OLCs/Ni $(OH)_2$, shown in **Figure 4.6a**. SEM and EDS were utilized, as shown in **Figure 4.3,** to analyze the distribution of carbon (C) atoms, oxygen (O) atoms, and nickel atoms (Ni). **Figure 4.3a** shows that the carbon, oxygen and Ni atoms were evenly distributed in Ox-OLCs/Ni $(OH)_2$. **Table 4.1** illustrates the atomic percentages of C, O, Ni as 89.62%, 8.57%, and 1.27% respectively. Au and Pd presence in the sample resulted from materials used for coating

and silicon presence due to glass cheaps released from silica boat. Peaks of C, O, and Ni were observed in **Figure 4.3b,** proving the existence of elements on the material's of the surface.

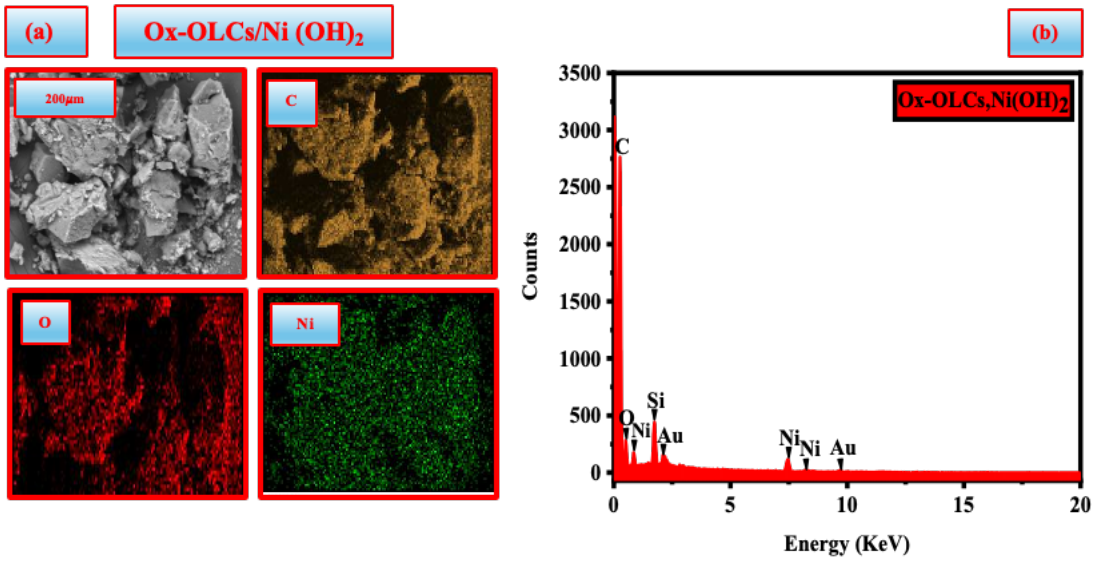


Figure 4. 3: EDS mapping and Elemental EDS analysis for Ox-OLCs/Ni (OH)₂ (a) EDS mapping (b) Elemental EDS analysis

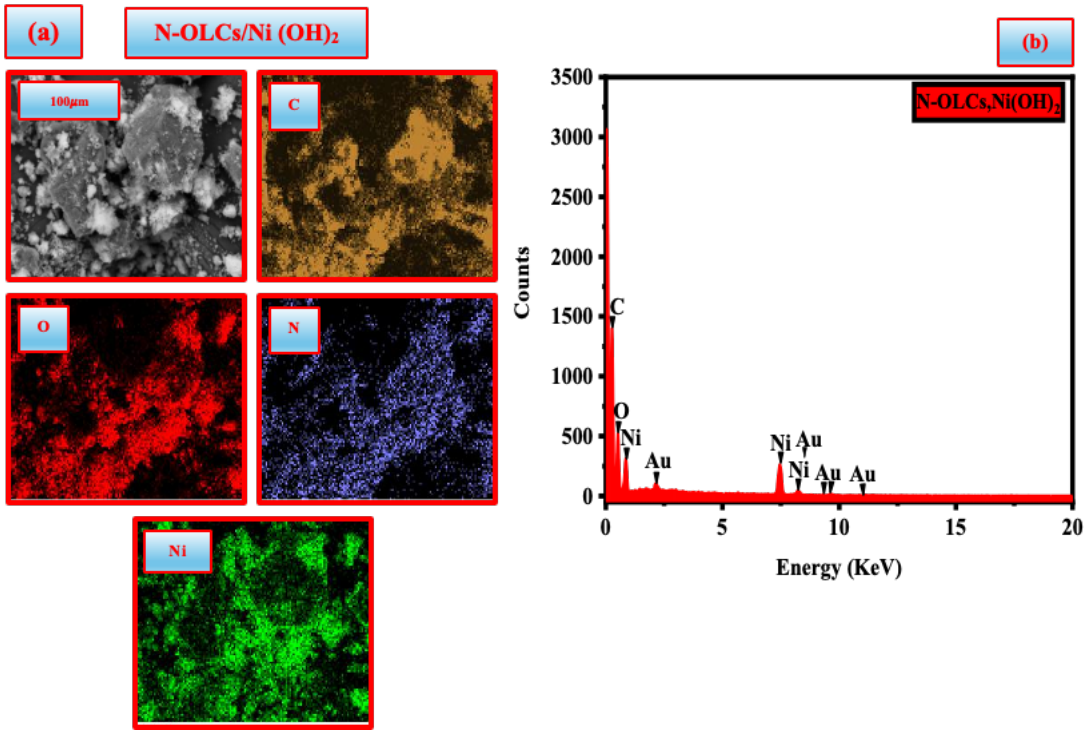


Figure 4. 4: (a) EDS mapped area of N-OLCs/Ni (OH)₂ (b) Elemental analysis for N-OLCs/Ni (OH)₂

The EDS mapping of N-OLCs/Ni(OH)$_2$ in **Figure 4.4a** demonstrates a homogeneous distribution of the components C, O, and N over the surface of N-OLCs/Ni(OH)$_2$. The Ni element similarly demonstrates an equal distribution **(Figure 4.4a)**. The EDS examination revealed the following atomic percentages of the elements: C (67.56%), O (26.94%), and Ni (5.36%), as depicted in **Table 4.1**. The presence of Au resulted from the coating of N-OLCs/Ni (OH)$_2$. **Figure 4.4b** shows the occurrence of C, O, and nickel on the sample's surface. **Figure 4.6a** delineates elements C, O, B, and Ni in B, N-OLCs/Ni (OH)$_2$, evidenced by the peaks analogous to C, O, B, and Ni depicted in **Figure 4.6b**. Furthermore, the spread of these elements within the sample is uniform, as illustrated in **Figure 4.6a**. EDS specifies the atomic percentages as follows: C (65.90%), O (14.37%), B (17.38%), and Ni (2.27%), as shown in **Table 4.1**. The presence of Au is a result of the coating applied to the samples.

Table 4. 1: Atomic percentages of different atoms in OLCs materials

Elements	Atomic Percentages of elements				
	Ox-OLCs/Ni (OH)$_2$	N-OLCs/Ni (OH)$_2$	B-OLCs/Ni (OH)$_2$	B, N-OLCs/Ni (OH)$_2$	AcOx-OLCs
B	-	-	13.95	17.38	-
C	89.62	67.56	77.31	65.90	92.07
O	8.57	26.94	7.75	14.37	6.78
Ni	1.27	5.36	0.92	2.27	-
Au	0.24	0.14	0.07	0.08	0.28
Pd	0.13	-	-	-	-
Si	0.17	-	-	-	-
K	-	-	-	-	0.18
Totals	**100**	**100**	**100**	**100**	**100**

EDS mapping and elemental examination of AcOx-OLCs in **Figures 4.5a and 4.5b** revealed the presence of C, O, and K in the produced sample, with atomic percentages of around 92.07% for C and 6.78% for O and 0.18% for K. The existence of the K element may be ascribed to inadequate sample washing or an ineffective washing process that fails to remove the element entirely —the presence of Au results from the coating.

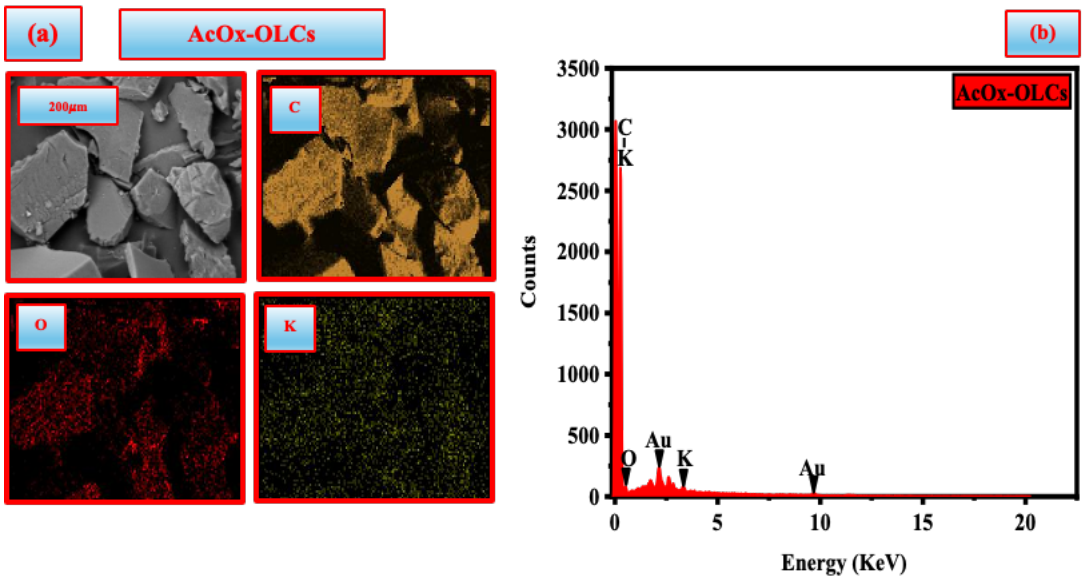


Figure 4. 5: (a) EDS mapped area for AcOx-OLCs (b) EDS elemental analysis for AcOx-OLCs

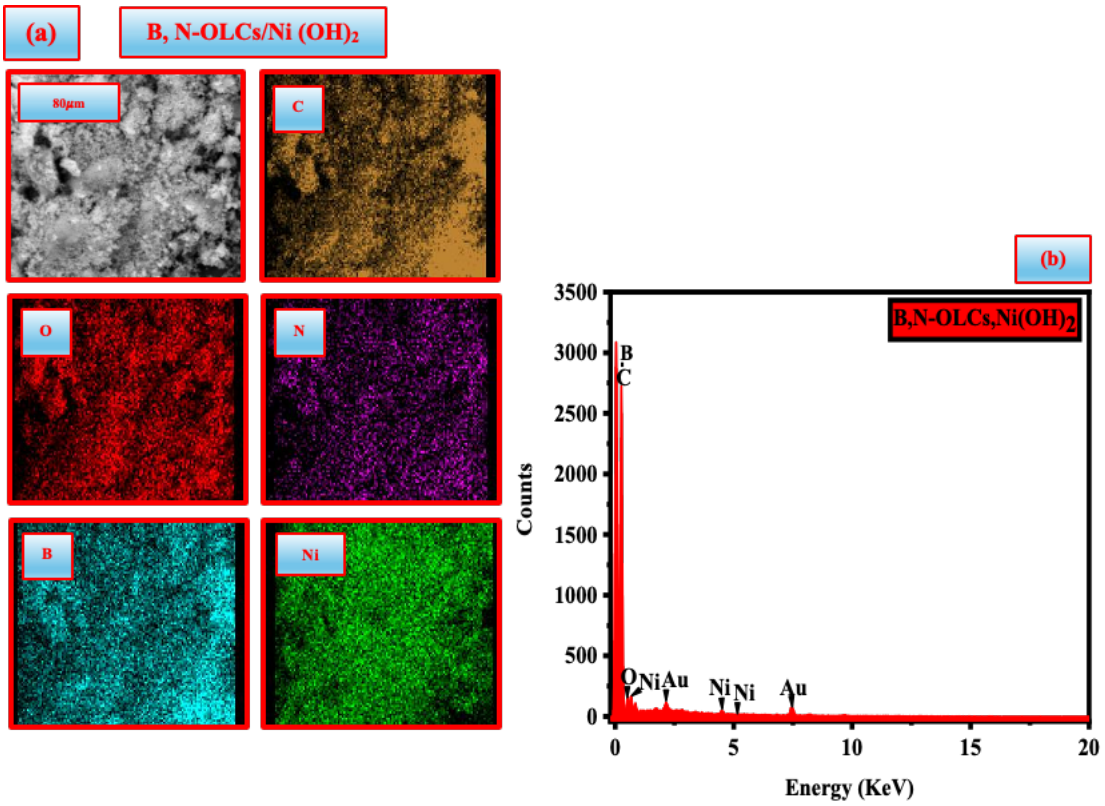


Figure 4. 6: (a) EDS mapped area for B, N-OLCs/Ni (OH)₂ (b) Elemental analysis for B, N-OLCs/Ni (OH)₂

4.1.2. TEM analysis and particle distribution graphs for onion-like carbon samples

Figure 4.7 TEM analysis (shown in **Figure 4.7**) reveals the existence of carbon nodules averaging 35.78 nm in diameter, exhibiting a turbostatic morphology with a minimal amount of graphitization, interconnected to form a porous architecture[5]. No lattice borders are visible; it is evident that the OLCs consist of multilayer nanosheets layered onto one another at the edges **Figure 4.7a-f**. The OLCs consisted of dualistic regions: the internal short-distance ordered ringed solid center and the external unstructured or amorphous carbon area, as depicted in **Figures 4.7a, 4.7d, and 4.7e** by the arrows. The inner core displayed concentric layers with a mean interplanar

spacing of 0.36 nm calculated with XRD data using Bragg's law. Following the functionalization as depicted in **Figure 4.7c** and doping in **(Figure 4.7c, 4.7d, 4.7e)** of the pristine OLCs (P-OLCs), an alteration or restructuring of the carbon concentric multilayers and the amorphous area was seen, as indicated by the arrows in **Figure 4.7c, 4.7e and 4.7f**.

This phenomenon can be ascribed to the structural modifications of the carbon lattice resulting from exposure to elevated temperatures of 800-900°C, particularly during the doping and co-doping processes, which transform Sp^2 to Sp^3 deficient carbon atoms[6]. No lattice fringes are visible in all the images shown in **Figure 4.7a-4.7g**; it is evident that the OLCs consist of multilayer nanosheets layered onto one another at the edges, as shown in **Figures 4.7c, 4.7d, and 4.7e** by the arrows. These may arise from lattice distortion and expansion caused by an increased presence of nitrogen and boron atoms. Excessive nitrogen and boron atoms disrupt the concentric layer structure and increase the interconnection of aromatic rings. Multiple potential causes exist for the emergence of individual imperfections in onions. For instance, they may be induced by impurity atoms confined within the carbon sphere[7].

These can initiate new atomic bonds, disrupt the spherical carbon layer, or cause other structural alterations in the onion, as depicted in **Figure 4.7c**. The identified single-point imperfections in onions contrast with the point faults in actual crystals, such as self-interstitial atoms, interstitial or substitutional impurity atoms, and vacancies [8]. In the context of onions, a point defect refers to a flaw created by the interaction and subsequent reconstruction of two adjacent onion layers. This flaw indeed encompasses many atoms. It is widely recognized that carbon atoms can organize into

various configurations of graphitic carbon rings. The planar graphitic layer consists of carbon atoms organized in hexagonal arrangements[9].

The configuration of pentagonal and heptagonal carbon rings induces the network to curve upward and downward, respectively, which suggests a defective of disordered onion-like carbon structure. The creation of heptagonal and pentagonal atomic rings causes the bending and closing of carbon nano onions, as shown in **Figures 4.7b-4.7g** [10]. Pentagonal atomic rings constitute the foundation for constructing the ideal bulky-ball C60[11]. However, synthesizing heptagonal carbon rings will result in a wrinkled carbon sheet. In such instances, carbon nanostructures display disjointed lines in the TEM pictures[12]. **Figures 4.8** and **4.9** show a histogram of particle sizes obtained from imageJ.Js, which consists of approximately 100 particles. This histogram (particle sizes ranging from (42.52±0.92nm, 34.98±3.44 nm, 37.42±1.42nm, 32.58±0.91 nm, 32.62±1.72, 35.01±2.02 and 35.19±3.16 nm) as shown in **Figures 4.8** and **4.9**, Pristine OLCs (P-OLCs) have the largest particle size since they remain unmodified and retain their original structure, as shown in **Figure 4.8a**. In contrast, P-OLCs decorated with Ni $(OH)_2$, depicted in **Figure 4.8b**, suffer a decrease in size due to the partial collapse of the graphitic layers, the introduction of defects, and altered surface energy. Oxidized OLCs (Ox-OLCs), shown in **Figure 4.8c**, experience a moderate size reduction because of mild etching and restructuring from oxygen functional groups[13]. Nitrogen-doped OLCs (N-OLCs) in **Figure 4.8d** also shrink in size due to structural distortions and increased defect density[14]. **Figures 4.9a** and **4.9b** illustrate that boron-nitrogen co-doping (B, N-OLCs) increases lattice strain and defects, leading to further shrinkage. Conversely, boron-doped OLCs (B-OLCs) are slightly larger than N-OLCs due to structural stability. Finally, **Figure**

4.9c shows that Ni $(OH)_2$ on boron-doped OLCs (BOLCs/Ni $(OH)_2$) may stabilize or slightly increase particle size, countering typical reductions[15]. Exploring microstructure necessitates interaction with covalent metal hydroxide/OLCs, maximizing the accessible electroactive surface area [16].

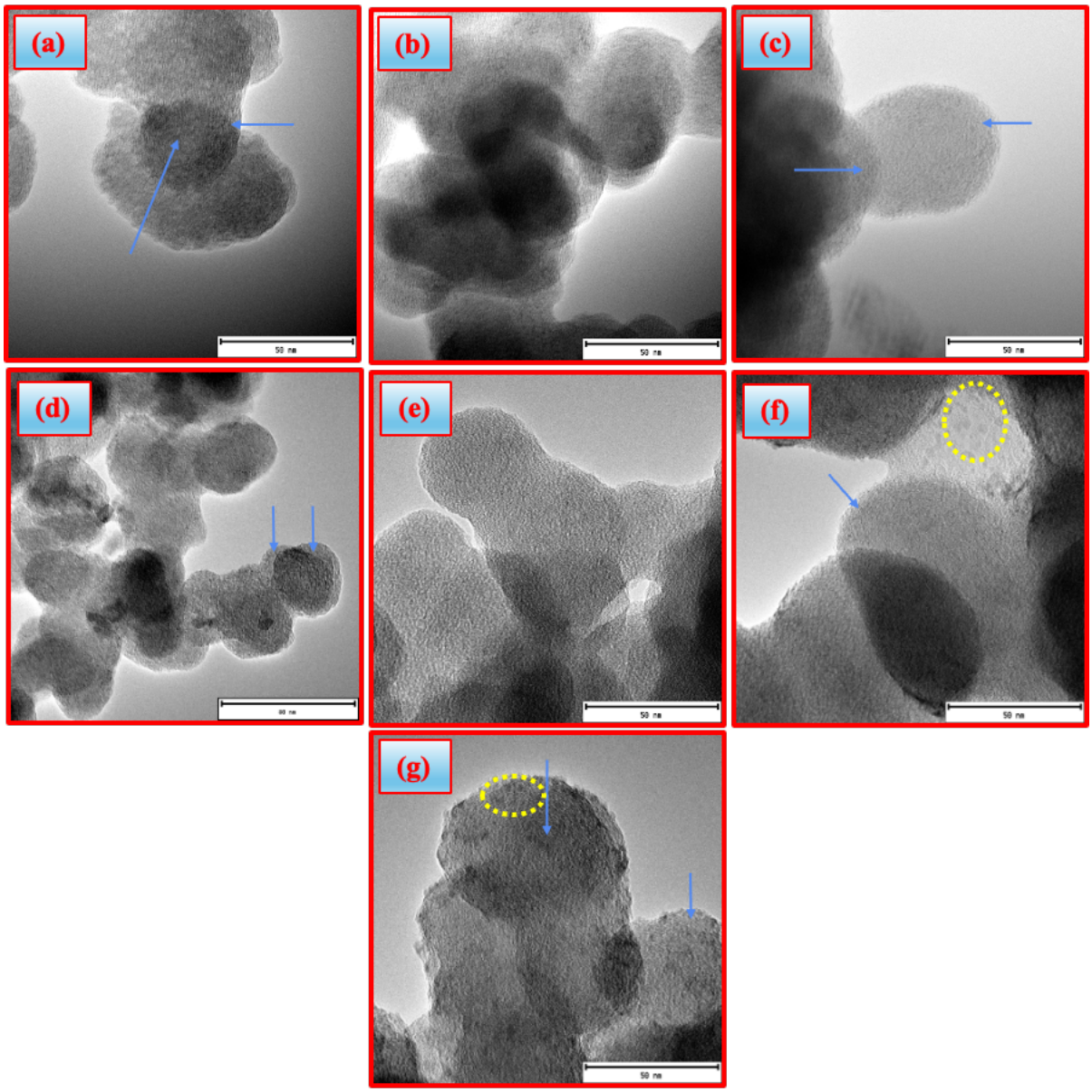


Figure 4. 7: TEM images for (a) P-OLCs (b) Ox-OLCs (c) N-OLCs (d) B-OLCs (e) B, N-OLCs (f) P-OLCs/Ni $(OH)_2$ (g) B-OLCs/Ni $(OH)_2$

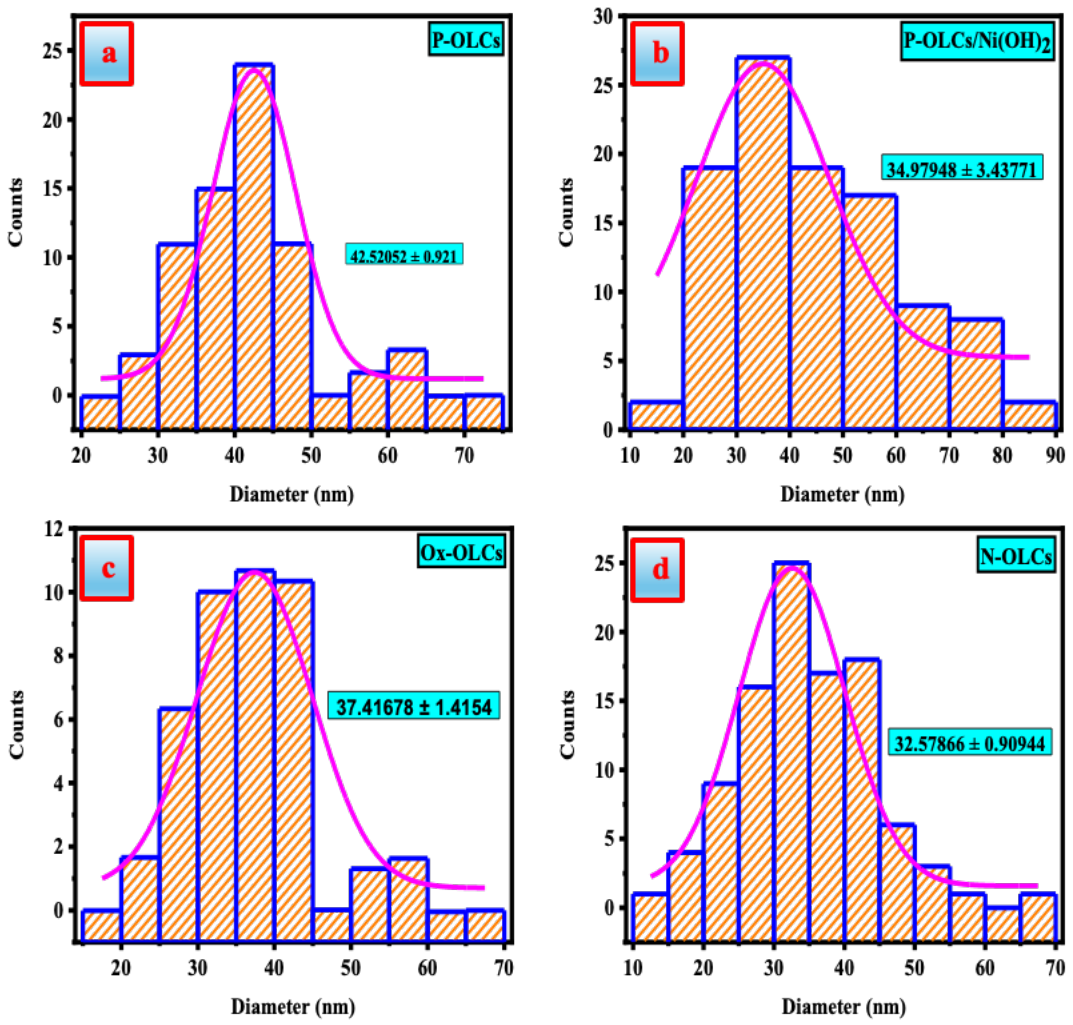


Figure 4. 8: Histograms plots of particle distribution for (a) P-OLCs (b) P-OLCs/Ni (OH)$_2$ (c) Ox-OLCs (d) N-OLCs

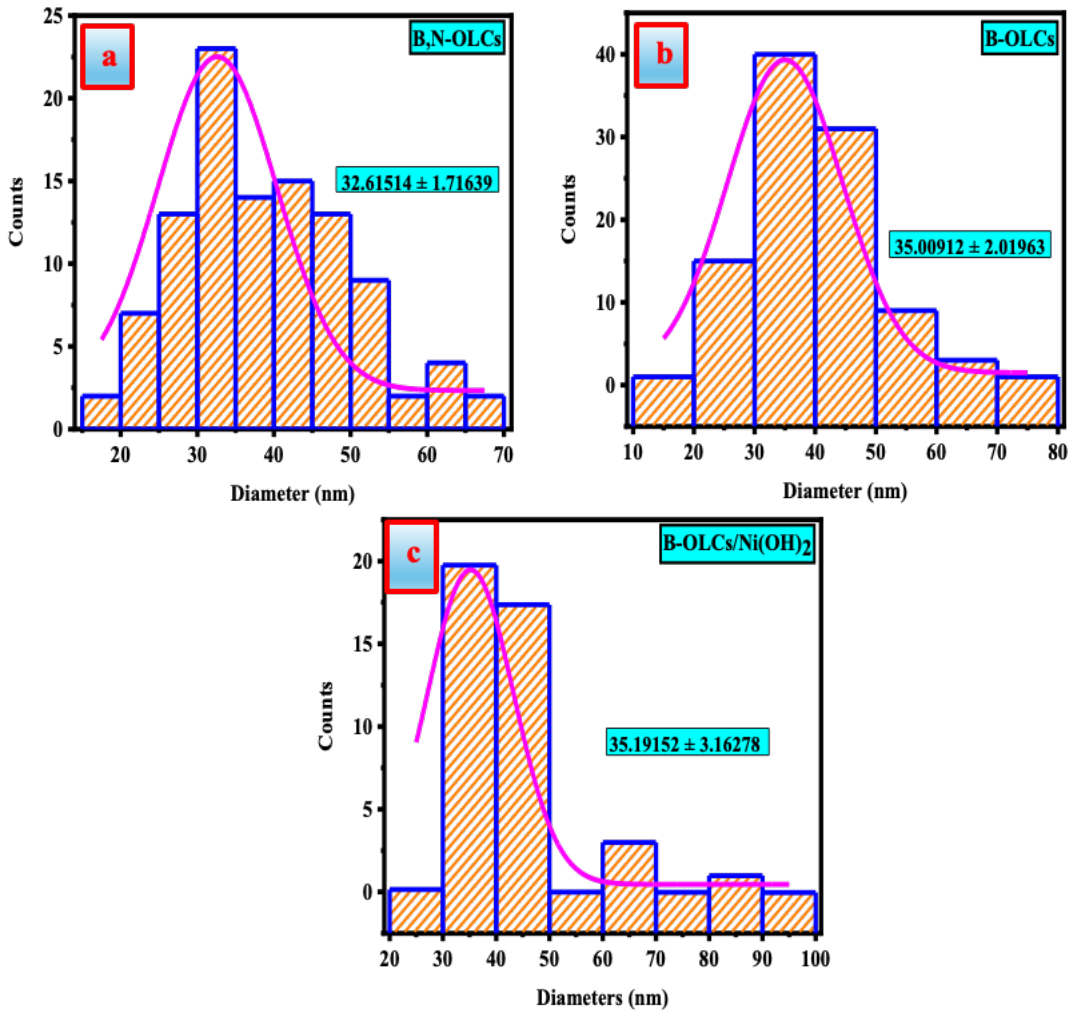


Figure 4. 9: Histogram plots for (a) B, N-OLCs (b) B-OLCs (c) B-OLCs/ Ni (OH)₂

4.1.3. BET surface area analysis

Analyzing the N_2 adsorption–desorption isotherms enables a detailed evaluation of the BET surface area of the OLCs. The electrochemical characteristics of the synthesized OLC-based/Ni $(OH)_2$ composites can be inferred through an assessment of their surface area, pore structure, defect density, and heteroatom contents[17]. BET analysis reveals that AcOx-OLCs possess a substantial

surface area of 507 m^2/g, characterized by predominantly microporous channels measuring 2.3 nm, alongside a pore volume of 0.62 cm^3/g, as depicted in **Table 4.2**. This suggests a significant abundance of accessible active sites and minimized ion diffusion pathways [18]. In contrast, N-OLCs/Ni $(OH)_2$, while exhibiting a reduced surface area of 260 m^2/g and an increased mesopore size of 6.6 nm alongside a pore volume of 0.76 cm^3/g, is anticipated to gain from improved electrolyte infiltration and accelerated ion transport. This agrees with earlier findings by Fan et al. [19], where mesoporous CNFs@Ni $(OH)_2$/NiO-250 composites with a surface area of 49.3 m^2/g, pore size 7.21 nm, and pore volume 0.116 cm^3/g showed enhanced rate capability due to improved ion accessibility. Raman analysis **(Figure 4.13)** suggests that N-OLCs/Ni $(OH)_2$ maintains a significant defect density, while XPS **(Figure 4.15)** confirms nitrogen functionalities, potentially enhancing surface polarity and promoting interfacial charge transfer.

Table 4. 2: BET surface area for pristine, functionalized, doped, co-doped and composites of OLCs

Samples	Surface area (m^2g^{-1})	Pore volume (cm^3g^{-1})	Pore size (nm)
P-OLCs	58	0,19	1,5
Ox-OLCs	52	0,55	4,7
N-OLCs	254	0,58	2,4
B-OLCs	348	0,74	3,6
B, N-OLCs	72	0.78	8,6
AcOx-OLCs	507	0,62	2,3
P-OLC/Ni $(OH)_2$	75	0,45	7,1
Ox-OLC/Ni $(OH)_2$	72	0,44	6,8
N-OLC/Ni $(OH)_2$	260	0,76	6,6
B-OLC/Ni $(OH)_2$	207	0,65	5,0
B, N-OLC/Ni $(OH)_2$	146	0,59	8,1

The synergistic properties indicate that N-OLCs/Ni $(OH)_2$ may achieve an advantageous balance between conductivity and the availability of electroactive sites, potentially surpassing materials with excessively small pores, restricted surface area, or diminished defect densities[20]. Conversely, **Table 4.2** presents BET analysis for, B-OLCs/Ni $(OH)_2$ (207 m^2/g, 0.65 cm^3/g, 5.0 nm) and B, N-OLCs/Ni $(OH)_2$ (146 m^2/g, 0.59 cm^3/g, 8.1 nm) demonstrate intermediate textural characteristics, indicating moderate ion accessibility and defect-mediated redox activity [21][22]. Ox-OLCs/Ni $(OH)_2$, characterized by the lowest surface area (72 m^2/g) and pore volume (0.44 cm^3/g), as presented in **Table 4.2**, appears to be limited by a scarcity of active sites and diminished wettability, potentially impeding its electrochemical performance[18][23].

When compared to their parent OLCs, most composites display marked increases in surface area and pore volume. For instance, P-OLCs (58 m^2/g, 0.19 cm^3/g, 1.5 nm) and Ox-OLCs (52 m^2/g, 0.55 cm^3/g, 4.7 nm) exhibit substantially lower values than their composite forms. Similarly, N-OLCs (254 m^2/g, 0.58 cm^3/g, 2.4 nm), B-OLCs (348 m^2/g, 0.74 cm^3/g, 3.6 nm), and B, N-OLCs (72 m^2/g, 0.78 cm^3/g, 8.6 nm), as presented in **Table 4.2**, each undergo notable structural alterations post Ni $(OH)_2$ incorporation, generally enhancing mesoporosity, which facilitates ion transport[24][25]. All materials, including OLCs and composites, exhibit Type IV isotherms with H3 hysteresis loops, indicating slit-shaped mesopores from the aggregation of plate-like particles. The steep desorption drop at low relative pressures suggests cavitation phenomena, where tensile strength effects cause rapid evaporation of condensed nitrogen in mesopores[26][27].

In conclusion, Ni $(OH)_2$ integration into heteroatom-doped OLCs—particularly N-OLCs—optimizes the interplay between ion transport, electroactive site density, and conductivity. These

results, consistent with literature values, position N-OLCs/Ni $(OH)_2$ as a highly promising candidate for high-rate supercapacitor applications.

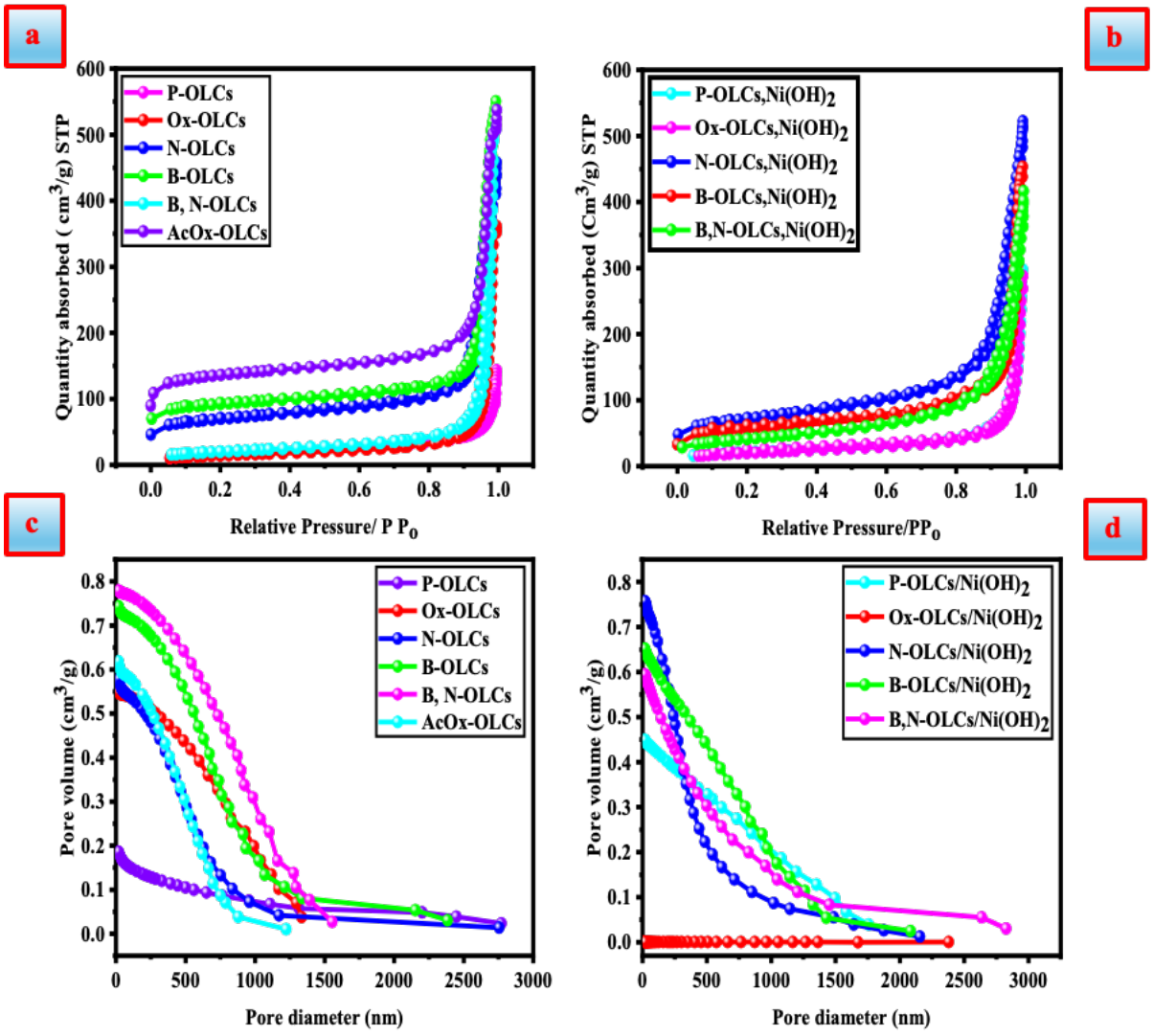


Figure 4. 10: N_2 adsorption and desorption isotherms (a) comparison of different OLCs samples (b) comparison of different OLCs/Ni $(OH)_2$ (c) comparison of pore size distribution of OLC sample (d) pore size distribution of OLC/Ni $(OH)_2$

4.1.4. TGA and DTGA analysis of pristine, functionalized, and doped OLCs

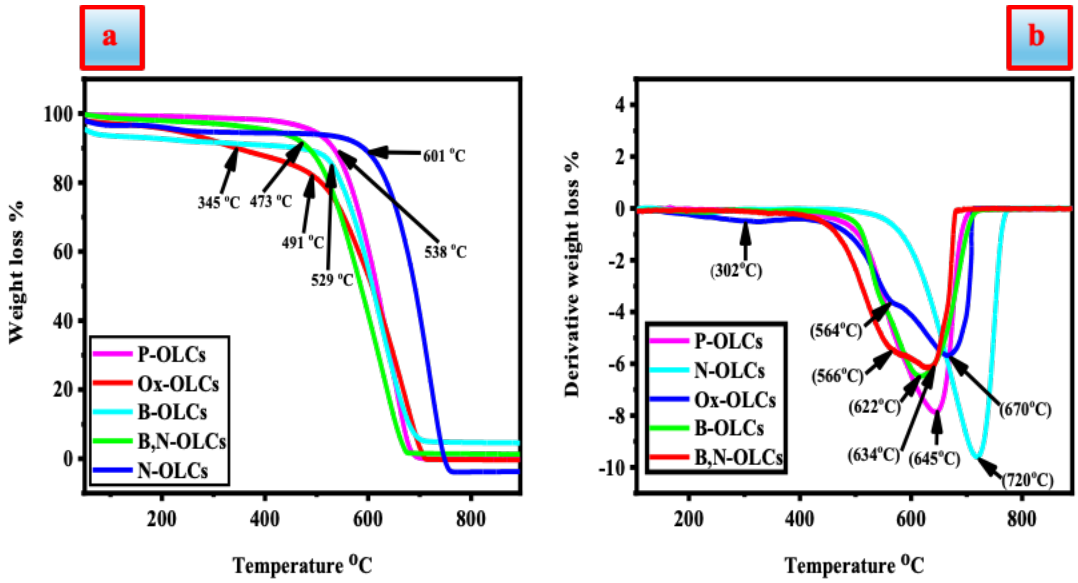


Figure 4. 11: Thermogravimetric analysis graph for OLCs (b) Differential-thermogravimetric graph for OLC samples

The TGA and DTG techniques were employed to evaluate the samples' thermal stability and weight loss. The study's findings indicated the presence of two distinct phases of weight reduction at temperatures of 345°C and 601°C. P-OLCs experienced a decrease in weight at a temperature of 538°C, N-OLCs at 601°C, B-OLCs at 529°C, and B, N-OLCs at 473°C. As mentioned above, the outcomes are demonstrated in **Figure 4.11a**. **Figure 4.11a** depicts the observed reduction in weight of Ox-OLCs at a temperature of 345°C. It is worth noting that weight loss may transpire during this phase if the material retains water or water-based constituents, as they can be removed [28]. The weight reduction observed at the higher temperatures of 345 °C and 491 °C may be ascribed to the breakdown of carboxylic functional groups [29].

P-OLCs and Ox-OLCs exhibited thermal stability at 645°C and 670°C, respectively. As shown in **Figure 4.11b**, the lack of oxidation-induced residue supports this observation. The N-OLCs demonstrated superior thermal stability at a temperature of 720°C compared to other OLCs, as illustrated in **Figure 4.11b**. The increased durability of N-OLCs can be ascribed to the heightened carbon content arising from the breakdown of melamine [30]. Carbon atoms can also undergo loss at a temperature of 720°C due to degradation induced by combustible carbon gas emissions. Nitrogen atom incorporation into the carbon framework is evident in nitrogen-substituted organic light-emitting compounds. Gaseous compounds containing Nitrogen, such as nitrogen oxides (NOx) or ammonia (NH_3), can be emitted at elevated temperatures [31].

The liberation of nitrogen atoms results in a decrease in weight, as shown in **Figure 4.11b**. The stability of the network in B-OLCs can be influenced by the interaction between boron atoms and the carbon lattice structure at temperatures of 622°C, as depicted in **Figure 4.11b**. This influence is particularly pronounced at the elevated temperature of 622°C. The potential weight loss of B-OLCs may be influenced by the presence of boron, which can impact their thermal stability. The observed outcome depends on implementing the boron doping method and the specific amount of boric acid (H_3BO_3) used [32]. At a temperature of 622°C, the carbon structure experiences decomposition, releasing volatile compounds.

Carbon atoms can be lost due to degradation induced by carbon-containing combustible gases. Can emit boron atoms in the form of boron-containing gases or compounds, such as borate, in the case of B-OLCs. The bonding configuration of boron within the lattice structure determines the

specific emission mechanism. The liberation of boron decreases mass, as depicted in **Figure 4.11b**. However, it can be observed from **Figure 4.11a** that the material does not undergo complete decomposition due to the existence of specific compounds that contain boron, such as borate [33]. As depicted in **Figure 4.11a,** nitrogen-doped OLCs (N-OLCs) experienced a percentage of weight loss below zero percent, which may be attributed to the TGA instrument experiencing calibration issues, resulting in inaccurate weight measurements. These may lead to a perceived reduction in weight.

Variations in the buoyancy of the sample, influenced by the surrounding gas atmosphere, can lead to apparent weight increases, particularly when the gas density experiences substantial changes with temperature. The sample may adsorb atmospheric gases during heating, resulting in weight gain. This is especially pertinent when the sample exhibits a high surface area and significant porosity. Volatile and reactive decomposition products of melamine or N-OLCs may interact with the atmosphere. The sample holder, resulting in complex weight variations in the experimental setup, including the type of gas employed (e.g., nitrogen, air), the flow rate, and the heating rate, can significantly affect the TGA results. The distinct characteristics of nitrogen-doped carbon materials, such as their elevated reactivity and ability to form stable intermediates, may influence a typical TGA behavior[34][35].

4.1.5. XRD analysis

The structural parameters were determined by analyzing the (002) peaks of the X-ray diffraction patterns. The XRD diffraction characteristic of the OLCs samples is portrayed in **Figure 4.12a**. This pattern exhibited a significantly elevated baseline and a broad peak width. The known diffraction angle 2θ of the (002) peak in crystalline graphite is 26.56º[36]. However, in **Figure 4.12a**, the (002) peak is observed at approximately 24.7º for P-OLCs, 25.5º for OX-OLCs, 25.1º for N-OLCs, 25.7º for B-OLCs, and 25.3º for B, N-OLCs as presented in **Table 4.3**. These findings suggest that this material's micro-crystallites are distinct from graphite's. **Figures 4.12a and 4.12c** illustrate the presence of a prominent peak (101) at 2θ angles of 42.3º for P-OLCs, OX-OLCs (43.7º), N-OLCs (43.4º), B-OLCs (43.9º), AcOx-OLCs (43.8º), and B, N-OLCs (43.3º) as shown in **Table 4.3**.

A single peak in the broad 101 peaks can be attributed to the lack of clear separation between the 100 and 101 peaks, collectively forming the 101 peaks. This suggests an incomplete stacking of carbon atom layers within the structure. The findings validate that the onion-like carbon consisted predominantly of "turbostatic" structures, as indicated in TEM images in **Figure 4.7** [37]. The materials depicted in **Figure 4.12a** exhibit broad peaks, indicating a higher concentration of OLCs nanoparticles with a well-organized structure [38]. However, the peaks of OX-OLCs at 2θ (43.7º) degrees, which correspond to the (101) planes, were no longer observed. The absence of narrow peaks observed in the OLCs samples depicted in **Figure 4.12a** and their composites illustrated in **Figure 4.12b** attributed to the reflections occurring on the onion-like carbons.

The broad (002) graphite peaks exhibited nearly identical shapes across all samples, as illustrated in **Figure 4.12a**. The positions of the (002) peaks at 24.7º, 25.5º, 25.1º, 25.7º, 25.4º, and 25.3º for

P-OLCs, OX-OLCs, N-OLCs, B-OLCs, AcOx-OLCs and B, N-OLCs, respectively, correspond to a mean interlayer spacing of 0.36 nm between the nano graphitic shells, as depicted in **Table 4.3**.The experimental observation of an interlayer spacing of 0.36 nm calculate using Bragg's equation indicates the absence of three-dimensional (3D) ordering and the presence of a "turbostatic" nature in the quasi-spherical and polyhedral (OLCs) with parallel imperfect graphitic sheets that were randomly translated [39]. The reflections (002) and (101) indicate the presence of amorphous suggesting disordered carbon structure. The peak angles of diffraction in OLCs/$Ni(OH)_2$ composites appear at the 2θ values of 11.5º, 25.0º, 33.4º, 59.9º for N-OLCs/$Ni(OH)_2$ corresponding to *hkl* planes 001, 002, 110, 300, for B-OLCs/$Ni(OH)_2$ 2θ values were 24.8º, 33.1º, 59.1º equivalent to *hkl* planes 002,110,300 respectively, and B, N-OLCs/$Ni(OH)_2$ 2θ values was 24.8º, 33.2º, 59.7º linked to *hkl* planes 002, 110, and 300 subsequently as shown in **Table 4.3** and **Figure 4.12b**. The diffraction peaks obtained closely correspond to the information reported in the literature for the hexagonal $\propto -Ni\ (OH)_2$ nanostructure (**JCPDS card no. 22-0444**) [40].

In contrast, the N-OLCs/Ni $(OH)_2$ sample exhibits a greater abundance of diffraction peaks, particularly the prominent peak (001) observed at the 2θ =11.5º, which corresponds to the hexagonal alpha structure of nickel hydroxide, as illustrated in **Figure 4.12b**. There was no observation of this diffraction peak in the B-OLCs/Ni $(OH)_2$ and B, N-OLCs/Ni $(OH)_2$ samples. The decrease in the size of the crystallites of the onion-like carbons (OLCs) potentially causes the lack of a peak observed in samples B-OLCs/Ni $(OH)_2$ and B, N-OLCs/Ni $(OH)_2$[41].

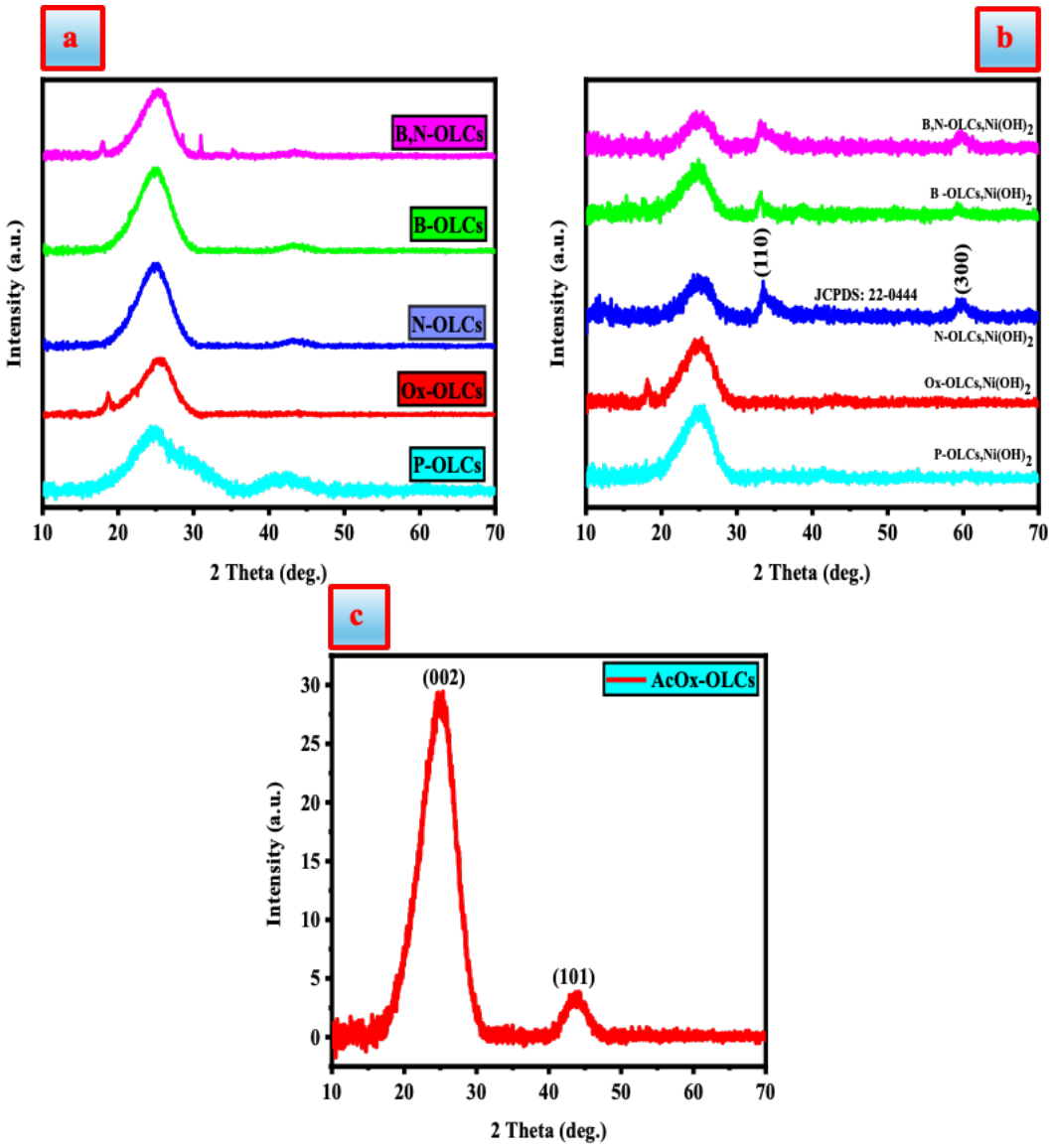


Figure 4. 12: X-ray diffraction (XRD) patterns of different OLCs sample (a) OLCs samples pristine, functionalized, doped and co-doped (b) OLCs/Ni $(OH)_2$ composites (c) Activated functionalized onion-like carbon (AcOx-OLCs).

The increase in ammonium molarity in the existing analysis leads to an enhancement in the pH value of the resulting solution. The elevation of pH in the reacting solution reduces the size of the crystallites in the synthesized materials [42] [43]. **Figure 4.12c** illustrates the XRD pattern of activated functionalized onion-like carbon (AcOx-OLCs). The broad (002) diffraction peak (2θ = 24.5) is attributable to amorphous carbon structures. The faint and broad diffraction peak (2θ = 46.5) is attributable to the orientation of the graphitic structure. One can infer that nearly all the materials in **Figure 4.12** exhibit amorphous solid characteristics, possessing substantial internal surface area and pore volume, particularly for activated carbon (AcOx-OLCs), B-OLCs, and N-OLCs, as indicated in **Table 4.2** of the BET data. All the OLC materials in **Figure 4.12** had a highly disordered microcrystalline structure characterized by randomly orientated graphitic microcrystals. The results indicate that the samples are semicrystalline or amorphous[44].

The two feeble diffraction maxima suggested the minimal proportion of the ordered crystalline phase in samples N-OLCs/Ni $(OH)_2$, B-OLCs/Ni $(OH)_2$, and B, N-OLCs/Ni $(OH)_2$ as depicted in **Figure 4.12b**. XRD spectra for each onion-like carbon exhibited a form characteristic of amorphous carbon, displaying prominent asymmetric peaks corresponding to 2 Theta values of around 25.4^0 and 45^0 [45]. This assumption aligns with the SEM pictures of the OLCs presented in **Figures 4.1** and **4.2**. The Scherrer equation was used to determine the average crystallite sizes from XRD data. Distinct variations in crystallite size across the various OLC materials, indicating disparities in graphitization degree and defect density, both of which affect electrode performance in supercapacitors [46]. The crystallite size within the pure OLCs set rose sequentially from P-OLCs (1.270 nm) to Ox-OLCs (1.352 nm), AcOx-OLCs (1.939 nm), N-OLCs and B-OLCs (both

2.048 nm), and B, N-OLCs (2.628 nm), as shown in **Table 4.3**. This development indicates a heightened level of graphitization, commonly linked to higher electrical conductivity resulting from diminished interlayer defects and improved π- electron delocalization. An increased level of graphitization reduces the equivalent series resistance (ESR), thereby improving power density [47] [48].

Moreover, alterations to surface chemistry such as activation in AcOx-OLCs and heteroatom doping in N-, B-, and B, N-OLCs can improve ion accessibility and wettability, hence promoting efficient transport of electrolyte ions. The almalgamation of these structural and chemical parameters indicates that the trend in crystallite size corroborates a forecasted hierarchy of power density performance for the undoped materials as follows: B, N-OLCs are greater than or equal to N-OLCs, which are approximately equal to B-OLCs, followed by AcOx-OLCs, Ox-OLCs, and finally P-OLCs [49][50]. B, N-OLCs $\geq$ N-OLCs$\approx$B-OLCs >AcOx-OLCs >Ox-OLCs > P-OLCs. This rating can be further validated through Raman spectrosctopy as shown in **Figure 4.13**. Following the decorating with Ni $(OH)_2$, the apparent crystallite sizes exhibited a substantial increase across all samples, particularly in P-OLCs/Ni $(OH)_2$ (4.707 nm) and B-OLCs/Ni $(OH)_2$ and B-OLCs/Ni $(OH)_2$ (4.460nm) [44][51].

Larger crystallite size along c- axis values signify improved graphitization; However, effect on power density is contigent upon three competing factors: (i) Carbon domain graphitization (promoted by larger crystallite sizes along c-axis), (ii) the thickness coverage of the Ni $(OH)_2$ layer (excess coverage may impede ion transport), and (iii) interfacial charge transfer between OLCs

Table 4. 3 XRD data analysis for OLCs and the composites OLCs/Ni (OH)₂

Sample name	(hkl) peaks	2θ degrees	d spacing (nm)	Crystal size (nm)
P-OLCs	(002)	24.7	0.36	1.270
	(101)	42.3		
Ox-OLCs	(002)	25.5	0.35	1.352
	(101)	43.7		
N-OLCs	(002)	25.1	0.35	2.048
	(101)	43.4		
B-OLCs	(002)	25.7	0.35	2.048
	(101)	43.9		
B, N-OLCs	(002)	25.3	0.36	2.628
	(101)	43.3		
AcOx-OLCs	(002)	25.4	0.36	1.939
	(101)	43.8		
P-OLCs/Ni (OH)₂	(002)	25.3	0.34	4.707
Ox-OLCs/Ni (OH)₂	(001)	12.4	0.35	1.971
	(002)	25.2		
N-OLCs/Ni (OH)₂	(001)	11.5	0.36	3.350
	(002)	25.0		
	(110)	33.4		
	(300)	59.9		
B-OLCs/Ni (OH)₂	(002)	24.8	0.36	4.460
	(110)	33.1		
	(300)	59.1		
B, N- OLCs/Ni (OH)₂	(002)	24.8	0.36	3.430
	(110)	33.2		
	(300)	59.7		

and Ni $(OH)_2$ (augmented by heteroatom doping, especially in N- and B, N- doped systems). According to XRD – derived crystallite size analysis, the composites with the highest power capacity are anticipated to be B-OLCs/Ni $(OH)_2$ and B, N-OLCs/Ni $(OH)_2$, due to their substantial crystallite sizes along c-axis values and advantageous interfacial chemistry. N-OLCs/Ni $(OH)_2$ are closely followed, whereas P-OLCs/Ni (OH)2 benefits from enhanced crystallite sizes but lacks interfacial enhancements generated by heteroatoms. [52][53].

4.1.6. Raman Spectroscopy

Figure 4.13 juxtaposes the first-order Raman response of pristine OLCs (P-OLCs), oxygen-functionalized OLCs (Ox-OLCs), and the heteroatom-modified derivatives derived from Ox-OLCs. In P-OLCs, the D and G bands are situated at approximately 1330.62 cm^{-1} and 1586.44 cm^{-1}, respectively, aligning with the D band of curved sp^2 carbons. Following oxygen functionalization (Ox-OLCs), both bands demonstrate distinct upshifts: D → 1337.62 cm^{-1} (+7.00 cm^{-1} upshift) and G → 1593.52 cm^{-1} (+7.08 cm^{-1} upshift) in comparison to P-OLCs, as depicted in **Table 4.4**. The D band (defect-activated breathing mode of six-atom rings near K, stimulated by intervalley double resonance) indicates variations in defect density and curvature, whereas the G band is responsive to doping and strain in sp^2 networks [54][55].

The simultaneous increase of D and G in **Figure 4.13** aligns with oxygen groups creating sp^3 defects (qualitatively elevating I_D) and inducing p-type charge withdrawal/strain that enhances the E_2g phonon (resulting in a blue shift of G)[56][57]. In comparison to Ox-OLCs, the activated sample (AcOx-OLCs) seen in **Figure 4.13** exhibits a downshift of D to 1325.12 cm^{-1} (−12.50 cm^{-1}) alongside an upshift of G to 1598.82 cm^{-1} (+5.30 cm^{-1}), as shown in **Table 4.4**. This

divergence—D softening while G stiffens—frequently coincides with (i) pore opening and localized relaxing of highly curved or strained rings that diminish the D-mode frequency, alongside (ii) partial removal or reconfiguration of oxygen moieties and charge redistribution that enhance the stiffness of the E_2g mode[56][58].

Numerous carbon materials exhibit a reduction or reorganization of D-related disorder signatures following thermal or chemical activation or reduction, whereas charge transfer and residual strain preserve or elevate the G-band position[58][59]. AcOx-OLCs generally maintain adequate defects for redox/ion adsorption while providing a marginally more conductive graphitic framework than Ox-OLCs; this is expected to result in a moderately reduced or rebalanced I_D/I_G ratio relative to Ox-OLCs, as depicted in **Figure 4.13**[60][61].

In boron-doped OLCs (B-OLCs) generated from Ox-OLCs, **Figure 4.13** demonstrates a downshift in D to 1328.79 cm^{-1} (−8.83 cm^{-1} compared to Ox-OLCs) and an upshift in G to 1597.05 cm^{-1} (+3.53 cm^{-1}), as illustrated in **Table 4.4**. Substitutional B serves as a traditional p-dopant in sp^2 carbon; p-type charge transfer enhances the G phonon through non-adiabatic Kohn-anomaly suppression, resulting in an upshift, while the softening of the D-mode aligns with a nuanced relaxation of local curvature/strain and a redistribution of defects [55][62].

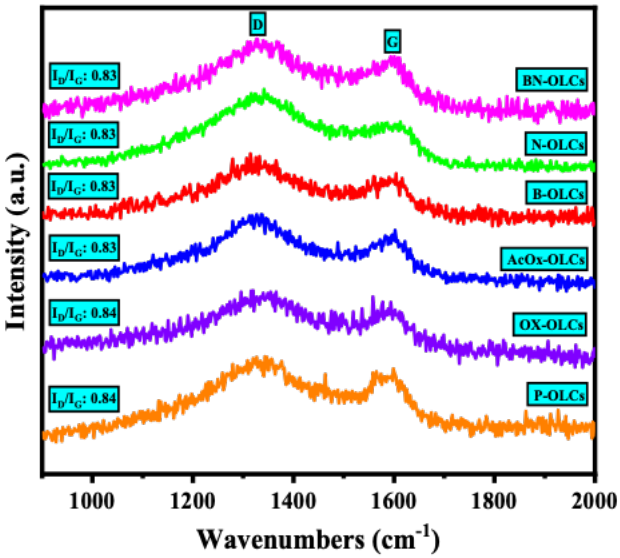


Figure 4. 13: Raman spectroscopy graph of different OLCs samples

In OLCs, the net G shift with B can be minor due to p-type stiffening being partially mitigated by tensile strain from elongated B–C bonds; studies on B-OLCs indicate slight yet discernible G upshifts at elevated B concentrations, consistent with the G upshift +3.53 cm^{-1} trend [62].

In **Figure 4.13**, the N-OLCs, illustrates D at 1341.62 cm^{-1} (+4.00 cm^{-1}; upshift) and a notable G at 1614.77 cm^{-1} (+21.25 cm^{-1}; upshift) in comparison to Ox-OLCs, as depicted in **Table 4.4**. The significant G-band blue shift is indicative of pronounced charge doping: both n- and p-type doping result in G-mode stiffening and narrowing due to the attenuation of the Kohn anomaly at gamma; the observed shift magnitude (approximately +21.25 cm^{-1}) is typical of elevated carrier densities and/or the synergistic effects of charge and compressive strain in curved shells[63][64].

In nitrogen-doped carbons, graphitic-N (quaternary N) significantly enhances electron density and conductivity while elevating G; pyridinic/pyrrolic-N further augments defectiveness (frequently increasing I_D) and contributes to catalytically active regions[65][66]. Be aware that in significantly defective carbons, a shoulder of about 1610–1620 cm^{-1} (sometimes referred to as D′) may overlap with the G band; however, in this analysis, as shown in **Figure 4.13**, it remains consistent with the predominant G-mode stiffening characteristic of charged or strained sp^2 shells[55][56].

In B,N co-doped OLCs (B,N-OLCs), **Figure 4.13** indicates that the D band is located at 1336.39 cm^{-1} (a downshift of −1.23 cm^{-1} compared to Ox-OLCs) and the G band at 1603.74 cm^{-1} (an upshift of +10.22 cm^{-1}) as shown in **Table 4.4**. The intermediate G position between B-OLCs and N-OLCs is physically plausible: co-doping introduces donor (N) and acceptor (B) species that can partially offset each other's Fermi-level shifts while concurrently augmenting local polarization and defect chemistry at edges and curvature sites [62][67]. In CNO/OLC literature, co-doping with boron and nitrogen frequently optimizes the density of heteroatom-polarized sites while maintaining satisfactory conductivity; G locations within the ~1596–1606 cm^{-1} range are typical for these materials, corresponding to your measurement of 1603.74 cm^{-1} [67][68].

The N-OLCs attain the peak G value (1614.77 cm^{-1}) due to electron donation from graphitic-N and potential compressive microstrain in nested shells, which significantly stiffens the E_2g phonon by suppressing the Kohn anomaly at gamma. Gate-doping investigations in graphene and intercalation analysis in charged graphites demonstrate that both n- and p-doping can induce a blue

shift in G by 10–25 cm^{-1} at elevated carrier density, consistent with the spectrum as shown in **Figure 4.13** [63][69].

Table 4. 4: Representation of Raman Spectroscopy data for onion-like carbon, doped, co-doped and activated functionalized onion- like carbon.

Samples	I_D/I_G	Type of bands		Shift types in D band		Shift types in G band	
		D-band (~cm^{-1})	G-band (~cm^{-1})	D-band Upshifts (~cm^{-1})	D-band Downshift (~cm^{-1})	G-band Upshifts (~cm^{-1})	G-band Downshift (~cm^{-1})
P-OLCs	4.73	~ 1330.62	~ 1586.44	-	-		-
Ox-OLCs	4.66	~ 1337.62	~ 1593.52	~ 7.00	-	~7.08	-
N-OLCs	4.83	~ 1341.62	~ 1614.77	~ 4.00	-	~21.25	-
B-OLCs	3.89	~ 1328.79	~ 1597.05	-	~ 8.83	~3.53	-
B, N-OLCs	4.55	~ 1336.39	~ 1603.74	-	~1.23	~10.22	-
AcOx-OLCs	3.41	~ 1325.12	~ 1598.82	-	~ 12.5	~5.3	-

In contrast, B,N-OLCs exhibit a more moderate G (1603.74 cm^{-1}) due to the opposing charge shifts induced by B (the acceptor) and N (the donor), resulting in a smaller net Fermi-level displacement and non-adiabatic stiffening compared to pure N-doping; nonetheless, local bond polarization and curvature maintain a G exceeding 1600 cm^{-1}[62][69].

According to **Figure 4.13**, the spectral signature that aligns most closely with optimal electrochemical performance, integrating conductivity and a high density of redox/adsorption sites, is N-OLCs. The significant G band upshift (+21.25 cm^{-1} compared to Ox-OLCs) indicates the highest carrier density and phonon stiffening within the dataset, suggesting minimal charge-

transfer resistance and enhanced electronic pathways through the onion shells[55][70]. Concurrently, the D band upshift implies that defects are sufficiently prevalent to accommodate active sites (e.g., pyridinic/pyrrolic nitrogen) and to promote ion accessibility across curved, turbostatic layers [56][66].

In supercapacitive regimes, the combination of a conductive graphitic backbone and heteroatom or defect-assisted adsorption generally results in enhanced rate capability and usable capacitance; similarly, in catalysis (e.g., ORR/OER), nitrogen-doped carbons often surpass undoped or exclusively oxygen-functionalized counterparts for the same rationale[71]. Nonetheless, B,N-OLCs need acknowledgement: Literature frequently indicates that synergistic B–N co-doping enhances catalytic performance through the polarization of neighboring C sites and dual-site mechanisms, even when the G shift is less pronounced than in N-only materials. Therefore, if the objective is specifically the ORR in alkaline media, B, N-OLCs can compete with or exceed N-OLCs despite the reduced G upshift [68][72]. Based on **Figure 4.13**, N-OLCs are the most probable top performers in general electrochemistry, as they exhibit the most distinct spectroscopic indicator of superior electrical quality (most G stiffening) while maintaining defect-derived functionality.

4.1.7. X-ray Photoelectron Spectroscopy (XPS)

Elemental analysis and X-ray photoelectron spectroscopy (XPS) were utilized to demonstrate the chemical alterations in the materials. **Table 4.5** presents the elemental composition of carbonized materials infused with several elements, specifically boron and nitrogen, adorned with nickel hydroxide. The results indicate a reduction in carbon content relative to the pure Ox-OLCs, which are doped with boron and Nitrogen, co-doped with both B and N and adorned with nickel hydroxide. The atomic percentage of oxygen concentration in boron-doped OLC (B-OLCs/Ni $(OH)_2$) declined from 17.16% to 15.84%, whereas in nitrogen-doped OLC (N-OLCs/Ni $(OH)_2$) it climbed from 17.16% to 30.33%, and in boron and nitrogen co-doped OLC (B, N-OLCs/Ni $(OH)_2$) it rose from 17.16% to 42.07% as shown in **Table 4.5**. As measured by XPS, the oxygen concentration changes in doped OLCs depend on the dopant type. In boron-doped OLCs (B-OLCs/Ni $(OH)_2$), oxygen decreases slightly from 17.16% to 15.84%, likely due to boron's lower electronegativity reducing oxygen affinity and stabilizing the structure with Ni $(OH)_2$ [73]. In nitrogen-doped OLCs (N-OLCs/Ni $(OH)_2$), oxygen rises from 17.16% to 30.33%, as nitrogen's higher electronegativity boosts surface reactivity, promoting oxygen-containing groups, aided by Ni $(OH)_2$. In boron and nitrogen co-doped OLCs (B, N-OLCs/Ni $(OH)_2$), oxygen increases significantly to 42.07%, attributed to a synergistic effect increasing defect sites and surface polarity, enhanced by Ni $(OH)_2$ interactions[74][75].

Nitrogen content increased from 2.21% to 4.25% for both N-OLCs/Ni $(OH)_2$ and B, N-OLCs/Ni $(OH)_2$, but for B-OLCs/Ni $(OH)_2$, it decreased from 2.21% to 1.73%. The nickel hydroxide content in N-OLCs/Ni $(OH)_2$ exhibited the highest atomic percentage at 17.61%, followed by B, N-

OLCs/Ni $(OH)_2$ at 16.35%, and B-OLCs/Ni $(OH)_2$ at 2.78% as shown in **Table 4.5**. As previously noted, the reduction in carbon content can be ascribed to the incorporation of heteroatoms; when Ox-OLCs are doped with Nitrogen or boron, these heteroatoms substitute certain carbon atoms within the structure. This substitution effectively diminishes the atomic fraction of carbon. Nitrogen doping introduces nitrogen atoms into the carbon lattice, resulting in C-N bonds, which reduces the overall carbon content observed by XPS in the sample, as depicted in **Figure 4.16**. Moreover, incorporating Nitrogen and boron, along with the decoration of nickel hydroxide, establishes novel chemical bonds and functional groups, as illustrated in **Figures 4.18** and **4.19c** [76].

The newly created bonds may include C-N, C-B, and Ni-O, which modify the surface chemistry of the OLC. Including these other elements and their corresponding bonds significantly diminishes the atomic proportion of carbon, as depicted in **Figures 4.18** and **4.19c**. When nickel hydroxide is applied to the OLCs, it accumulates nickel hydroxide on the surface of the OLCs. This process indicate that nickel is present on the surface, likely as part of the Ni $(OH)_2$ structure. The exact positions and shapes of these peaks can also hint at nickel's chemical state—here, it's typically in the +2-oxidation state (Ni^{2+}), as expected in nickel hydroxide. So, seeing Ni2p3/2 and Ni2p1/2 just means nickel from Ni $(OH)_2$ is part of the material and detectable on the OLCs surface[73][77]. The elevated presence of nickel and oxygen from nickel hydroxide significantly reduces the observed carbon content, as demonstrated in **Table 4.5** for N/OLCs/Ni $(OH)_2$ and B, N-OLCs/Ni $(OH)_2$ [78]. The presence of nickel on the surface may create a composite material in which the

nickel partially obscures the carbon atoms, as depicted in **Figures 4.19(a-c)**. The synergistic action of boron and Nitrogen co-doping significantly diminishes the carbon concentration[77].

The co-doping of boron and nitrogen incorporates additional heteroatoms into the carbon lattice, resulting in a more pronounced decrease in the atomic percentage of carbon content. Furthermore, the interplay of boron, nitrogen, and nickel hydroxide can generate intricate structures that conceal carbon atoms, as shown in **Figures 4.18** and **4.19c** [79]. This discovery is anticipated as incorporating heteroatoms into the structure reduces graphitic carbonaceous materials. This leads to the diminished prevalence of C-H, C-C, and C=C bonds, as illustrated in **Figures 4.13** of the Raman spectroscopy analysis. The XPS scan of the produced material revealed three peaks for Ox-OLCs, as depicted in **Figures 4.15 (a-c)**: C1s at 285.2 eV, O1s at 533.2 eV, and N1s at 406.2 eV. For N-OLCs/Ni $(OH)_2$ shown in **Figures 4.16 (a-d)** and **Figure 4.19a**, four peaks were identified: C1s (285.8 eV), O1s (532.5 eV), N1s (407.7 eV), and Ni2p (858.8 eV). For B-OLCs/Ni $(OH)_2$ shown in **Figures 4.17(a-d)** and **Figure 4.19b**, five peaks were discerned: C1s (284.8 eV), O1s (532.2 eV), N1s (399.6 eV), B1s (191.0 eV), and Ni2p (856.4 eV). In contrast, B, N-OLCs/Ni $(OH)_2$ depicted in **Figure 4.18 (a-c) and Figure 4.19c** exhibited four peaks. C1s (285.2 eV), O1s (532.1 eV), N1s (407.1 eV), and Ni2p (857.5 eV).

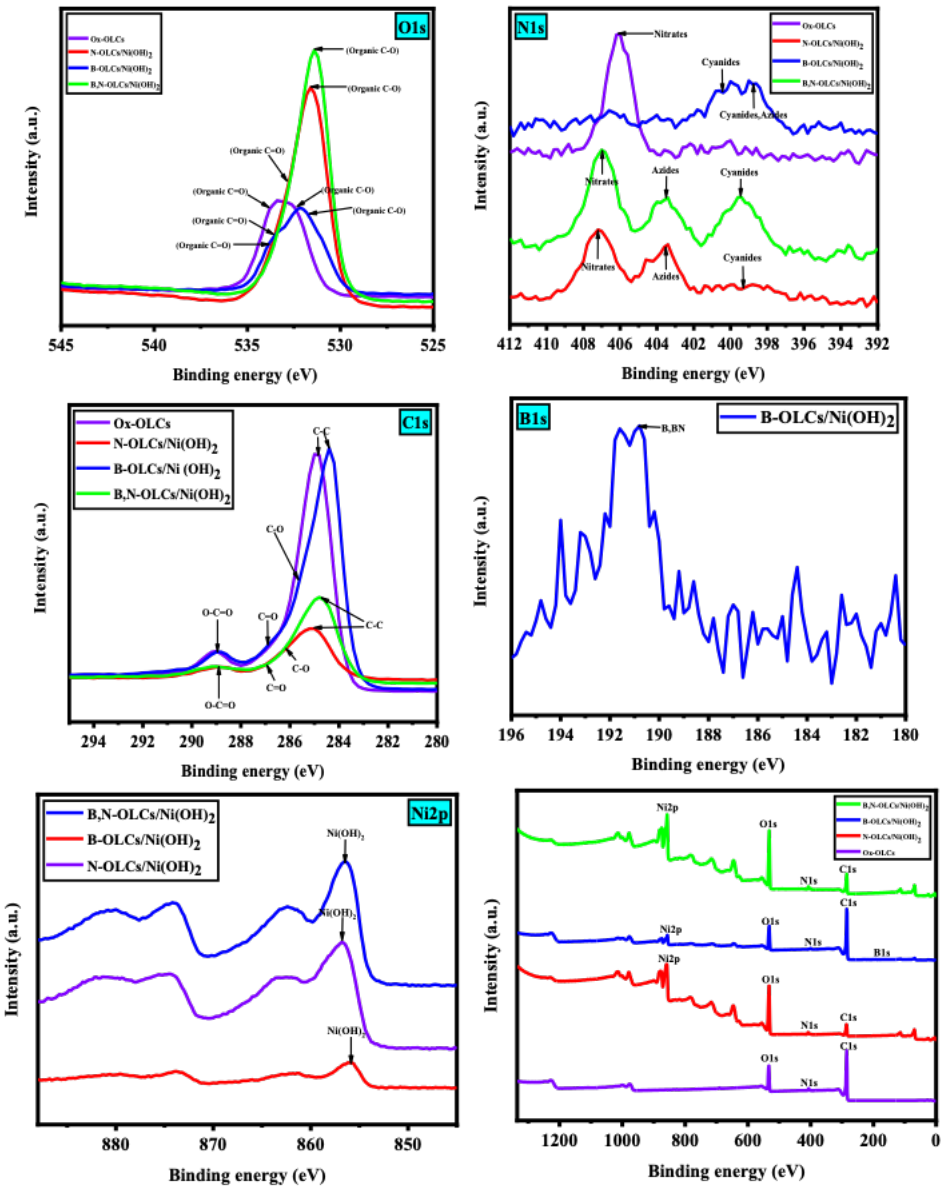


Figure 4. 14 : Comparison of experimental XPS spectra for O 1s, N 1s, C 1s, B 1s, Ni2p, and survey data of Ox-OLCs, N-OLCs/Ni(OH)$_2$, B-OLCs/Ni(OH)$_2$, and B,N-OLCs/Ni(OH)$_2$.

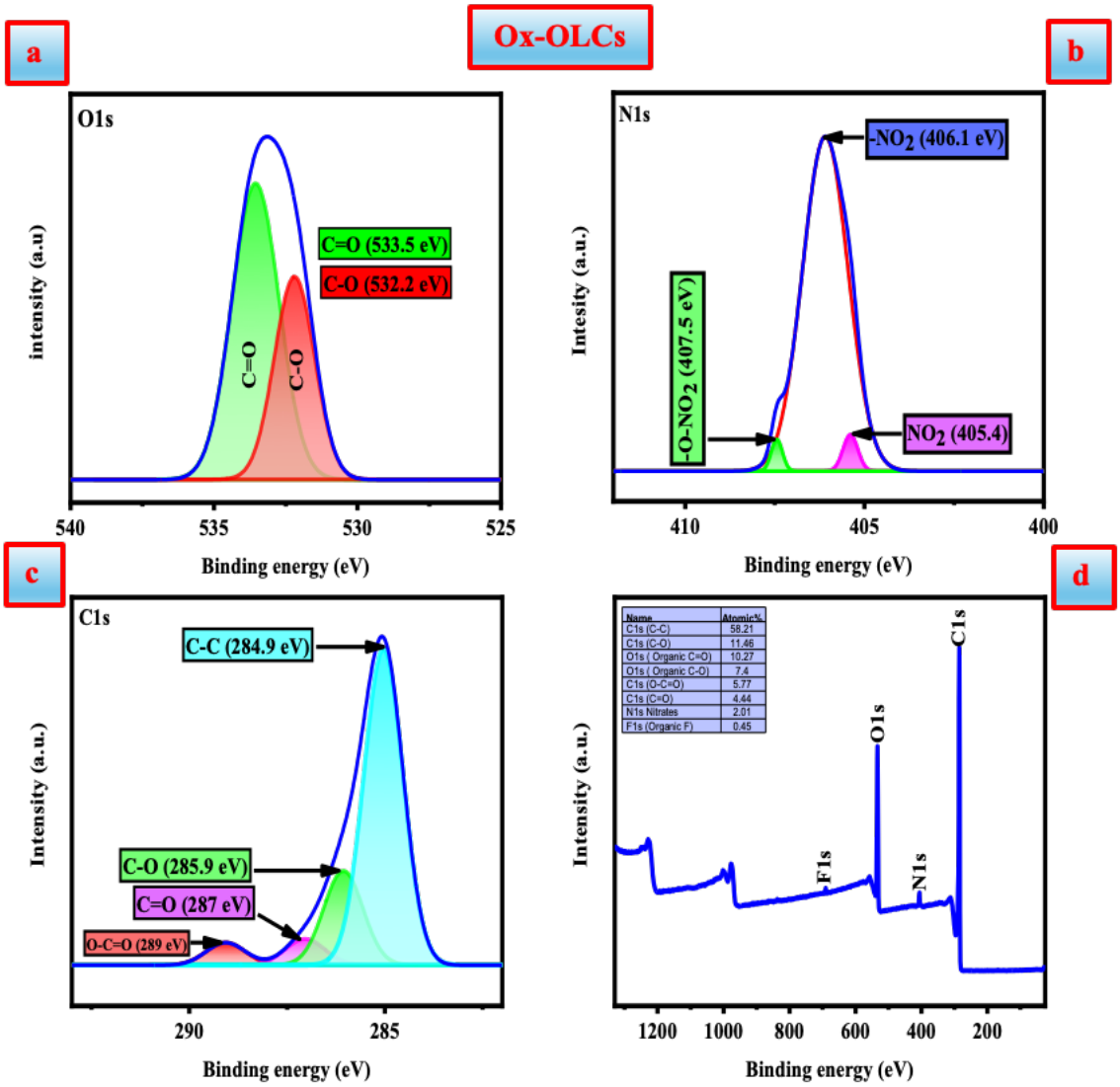


Figure 4. 15 : X-ray photoelectron spectroscopy data for Ox-OLCs (a), (b), (c) and (d) depicts deconvoluted spectra O1s, N1s, Cs and survey data respectively.

Nitrogen, boron, and nickel were identified in the materials, as illustrated in **Figures 4.20 (a-c)**. Spectra of Nitrogen, carbon, oxygen, boron, and nickel were acquired to ascertain the elemental variations and quantify them at the material surfaces.

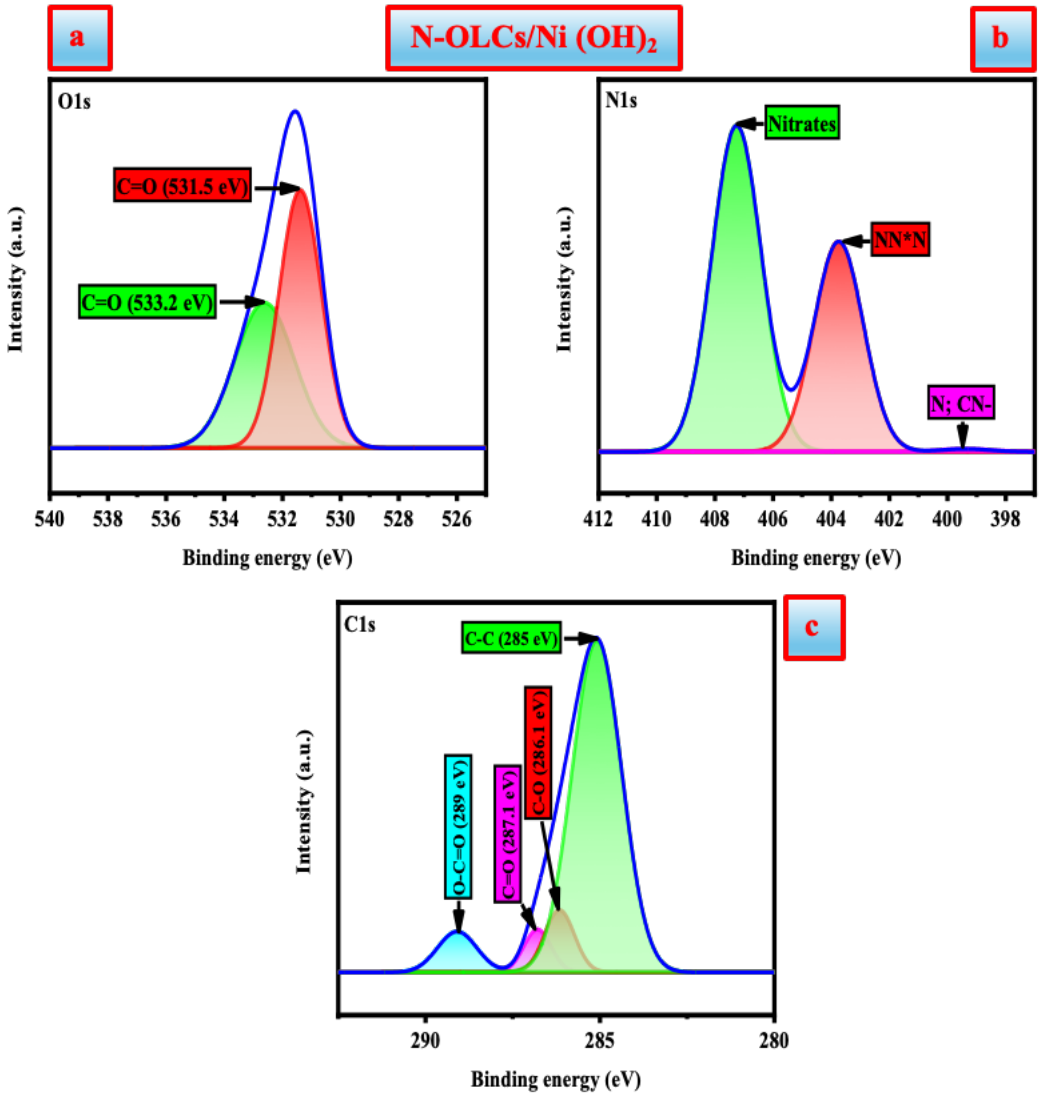


Figure 4. 16 : X-ray photoelectron spectroscopy data for N-OLCs/Ni (OH)₂ (a), (b), (c) depict deconvoluted spectra O1s, N1s and C1s respectively.

Figure 4.15a illustrates the spectra of Ox-OLCs: O1s; C=O (533.5 eV) and C-O (532.2 eV), N1s; -O-NO_2 (407.5 eV), NO_2 (406.1 eV), and (405.4 eV) **Figure 4.15b**, while for C1s; C-C (284.9

eV), C-O (285.9 eV), C=O (287.0 eV), and O-C=O (289.0 eV) for Ox-OLCs/Ni $(OH)_2$ shown in **Figure 4.15c**.

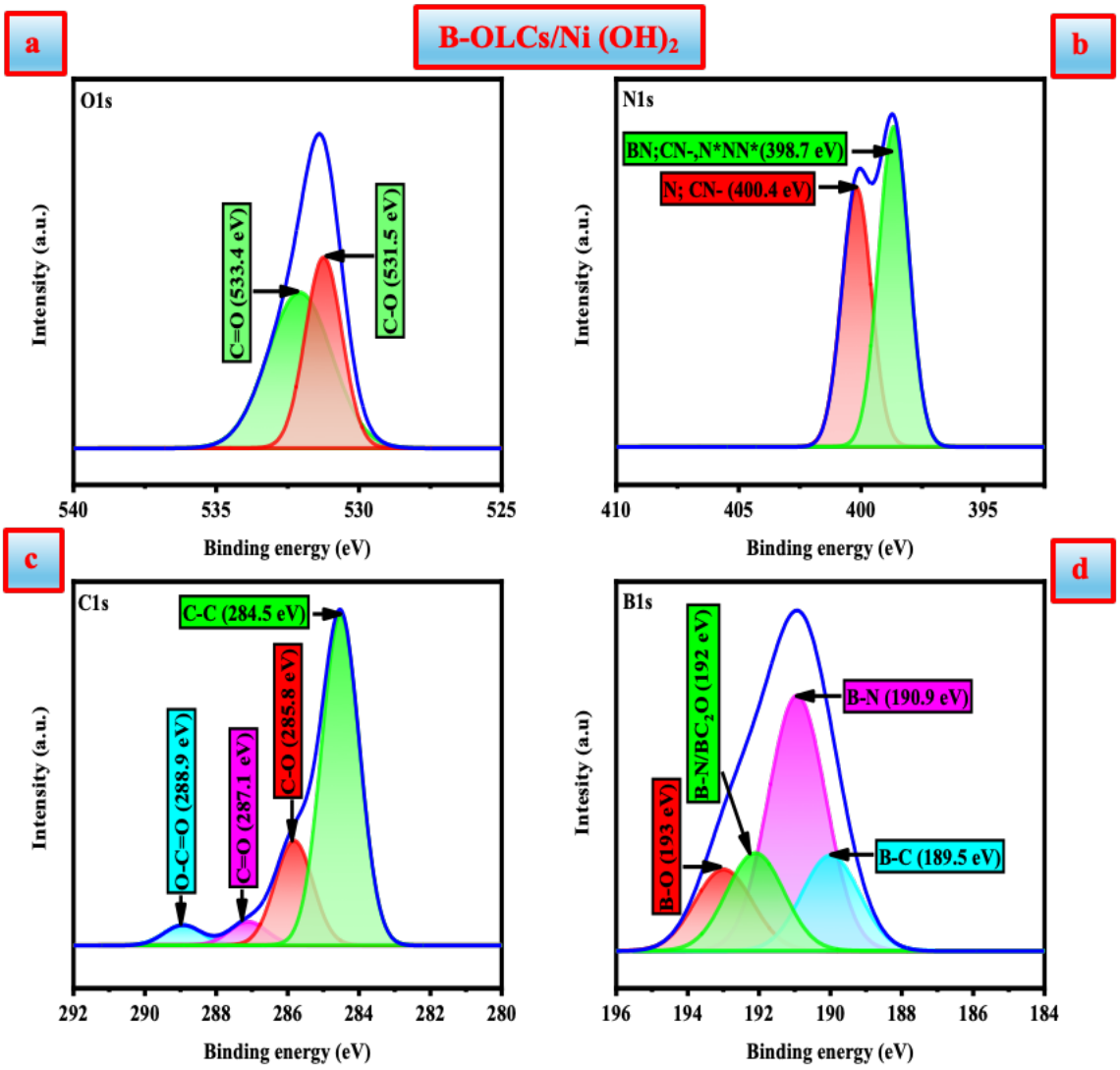


Figure 4. 17: X-ray photoelectron spectroscopy data for B-OLCs/Ni $(OH)_2$, (a), (b), (c) and (d) depicts deconvoluted spectra of O1s, N1s, C1s and B1s respectively.

The observable spectra included O1s; C=O (531.5 eV) and C-O (533.2 eV) depicted in **Figure 4.16a**, N1s; nitrates (407.2 eV), azide NN*N (403.7 eV), and cyanides; organic N (N; CN-)(399.3

eV) shown in **Figure 4.16b and Table 4.5**, as well as C1s; C-C (285.0 eV), C-O (286.1 eV), C=O (287.1 eV), and O-C=O (289.0 eV) illustrated in **Figure 4.16c**.

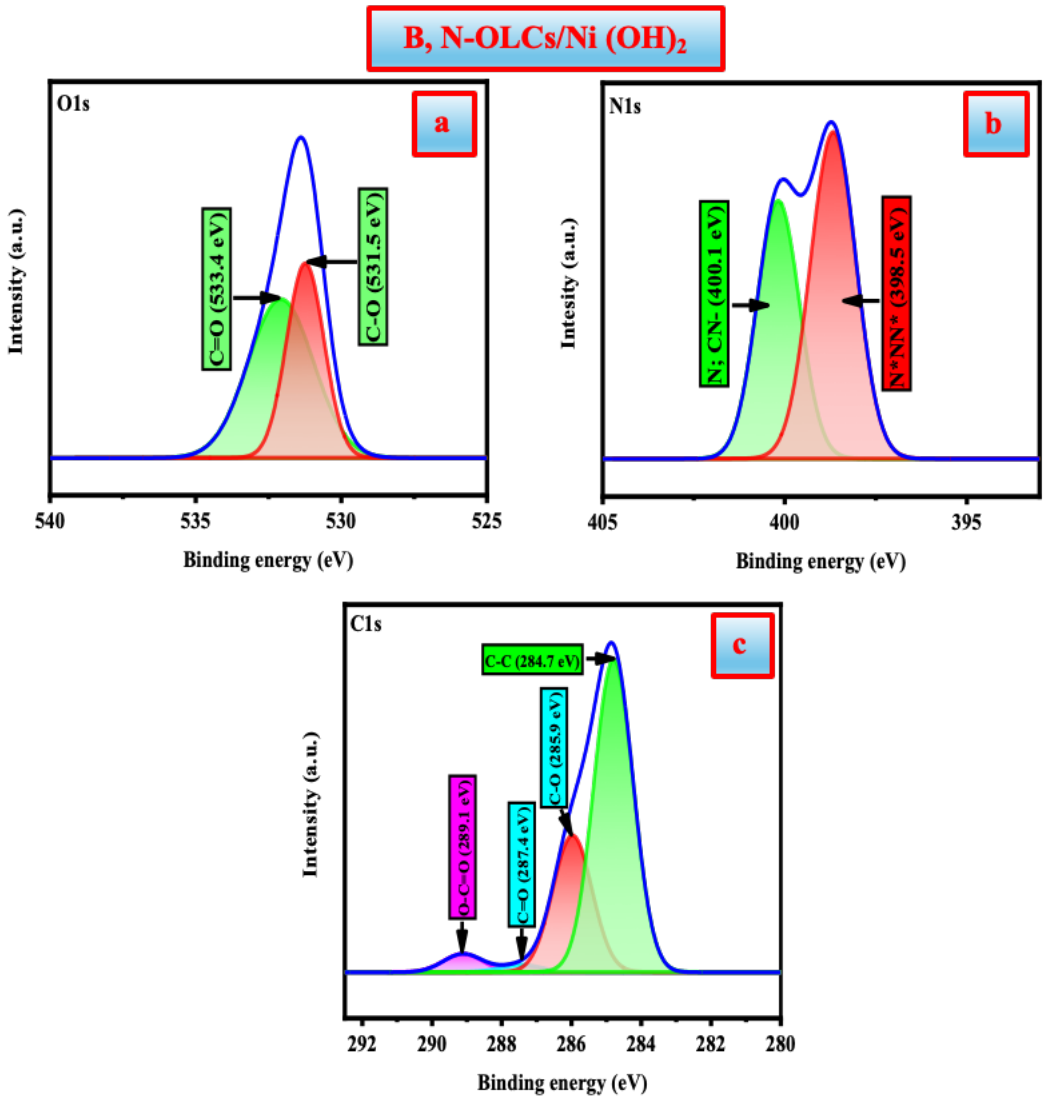


Figure 4. 18: X-ray photoelectron spectroscopy data for B, N-OLCs/Ni (OH)$_2$, (a), (b), and (c) depicts deconvoluted spectra of O1s, N1s, C1s respectively.

The Ni2p emission spectrum displayed two shake-up satellites, depicted in **Figure 4.19(a) and Table 4.5**. The peaks at 857.0 eV and 874.6 eV correspond to Ni^{2+}, whereas those at 863.5 eV and 881.9 eV are attributed to Ni^{3+}.

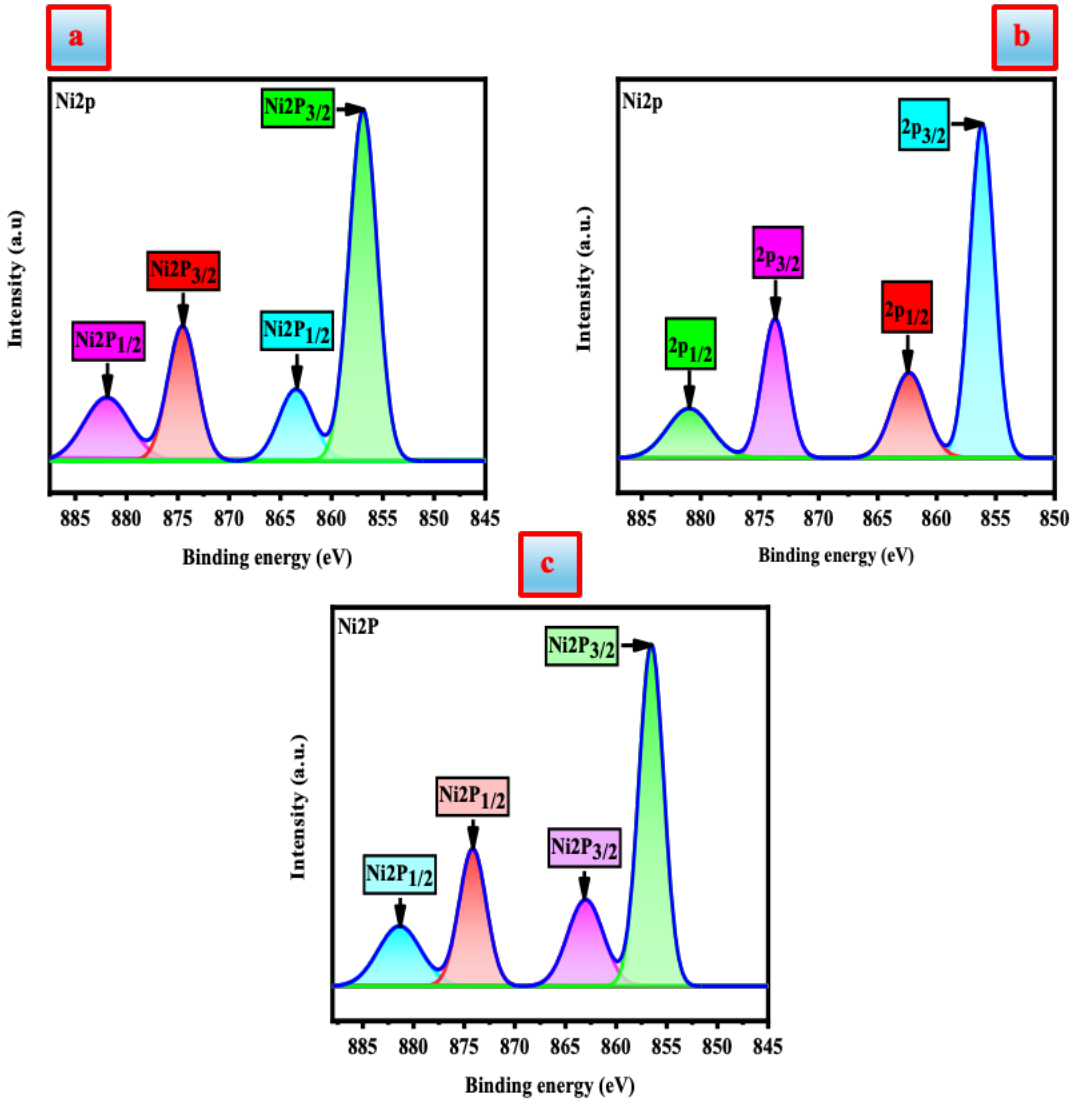


Figure 4. 19: X-ray photoelectron spectroscopy data for (a) N-OLCs/Ni $(OH)_2$ (b) B-OLCs/Ni $(OH)_2$, and (c) B, N-OLCs/Ni $(OH)_2$ depicts deconvoluted spectra of Ni2p respectively.

For B-OLCs/Ni(OH)$_2$ shown in **Figure 4.17**, the elemental identification and quantification are as follows: O1s; C=O (533.4 eV) and C-O (285.8 eV) illustrated in **Figure 4.17a**, N1s; BN; CN-, N*NN* (398.7 eV) and N; CN- (400.4 eV) depicted in **Figure 4.17b**, C1s; C-C (284.5 eV), C-O

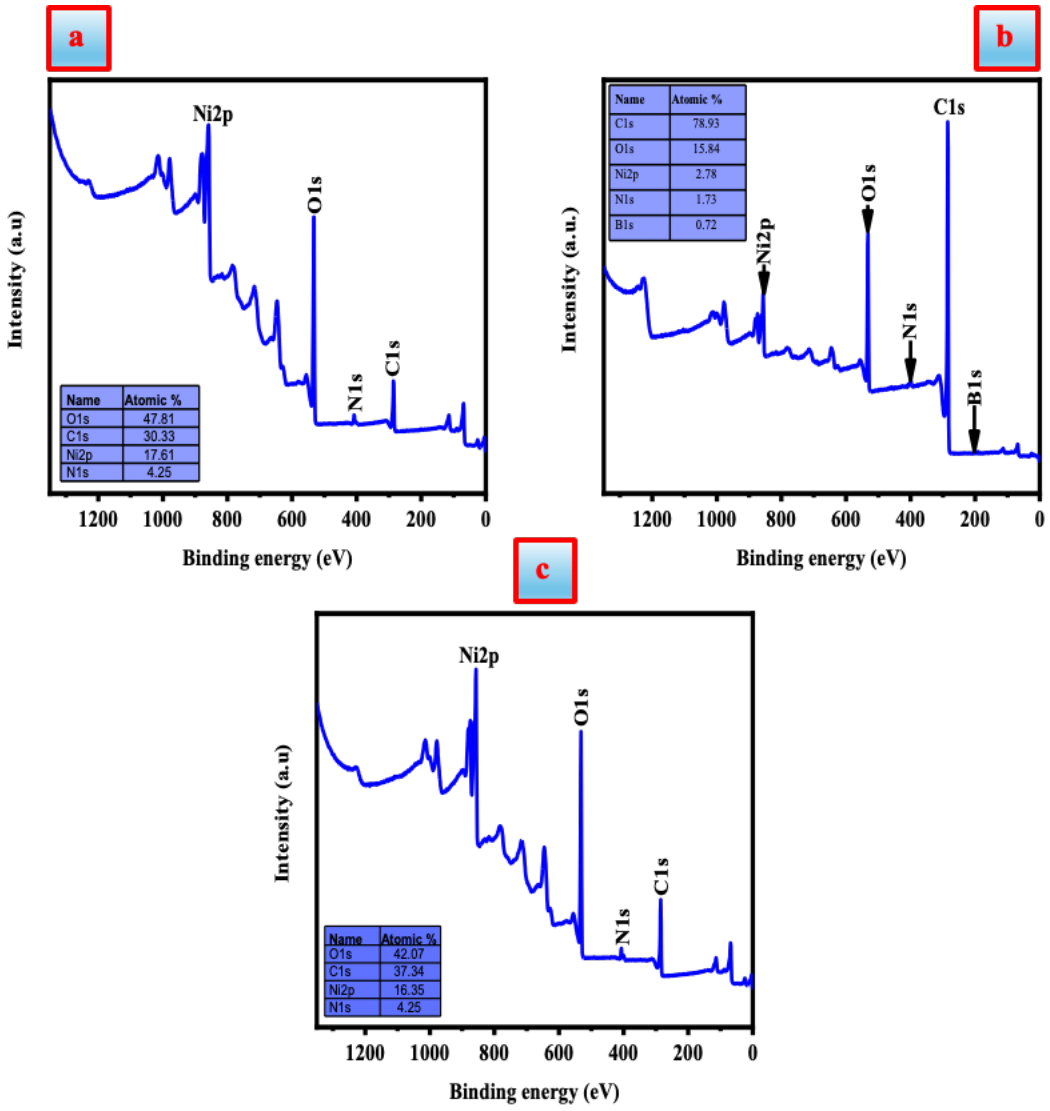


Figure 4. 20: X-ray photoelectron spectroscopy data for (a) N-OLCs/Ni (OH)$_2$ (b) B-OLCs/Ni (OH)$_2$ and (c) B, N-OLCs/Ni (OH)$_2$ depicts survey spectra respectively.

(285.8 eV), C=O (287.1 eV), and O-C=O (288.9 eV) shown in **Figure 4.17c**, B1s; B-C (189.5 eV), B-N (190.9 eV), B-N/BC_2O (192.0 eV), and B-O (193 eV) shown in **Figure 4.17d**.

Table 4. 5: **Representation of X-ray photoelectron spectroscopy data of onion-like carbon, doped co-doped and decorated with nickel hydroxide.**

Binding energy (eV)					
Sample	C	O	N	B	Ni
Ox-OLCs	285.2	533.2	406.2	-	-
N-OLCs/Ni $(OH)_2$	285.8	532.5	407.7	-	858.8
B-OLCs/Ni $(OH)_2$	284.8	532.2	399.6	191.0	856.4
B, N-OLCs/Ni $(OH)_2$	285.2	532.1	407.1	-	857.5
Elemental analysis (wt.%)					
	C	O	N	B	Ni
Ox-OLCs	80.29	17.16	2.21	-	-
N-OLCs/Ni $(OH)_2$	47.81	30.33	4.25	-	17.61
B-OLCs/Ni $(OH)_2$	78.93	15.84	1.73	0.72	2.78
B, N-OLCs/Ni $(OH)_2$	37.34	42.07	4.25	-	16.35
FWHM (eV)					
	C	O	N	B	Ni
Ox-OLCs	3.2	3.7	3.1	-	3.1
N-OLCs/Ni $(OH)_2$	3.9	4.1	3.9	-	9.0
B-OLCs/Ni $(OH)_2$	3.4	3.9	4.4	3.2	4.3
B, N-OLCs/Ni $(OH)_2$	3.4	3.6	3.2	-	3.9

The Ni2p spectrum displays two satellite peaks at (856.1 eV) and (873.7 eV) corresponding to Ni^{2+}, while the peaks at (862.4 eV) and (881.0 eV) are attributed to Ni^{3+}, as illustrated in **Figure 4.18b and Table 4.5**. For B, N-OLCs depicted in **Figure 4.18**, the O1s spectrum exhibited C=O

at 533.4 eV and C-O at 531.5 eV shown in **Figure 4.18a**; the N1s spectrum revealed N; CN at 400.1 eV and N*NN* at 398.5 eV shown in **Figure 4.18b**; the C1s spectrum displayed C-C at 284.7 eV, C-O at 285.9 eV, C=O at 287.4 eV, and O-C=O at 289.1 eV as shown in **Figure 4.18c**. In the Ni2p spectrum, two prominent satellite peaks at 856.5 eV and 874.2 eV corresponded to Ni^{2+}, while 863.0 eV and 881.3 eV corresponded to Ni^{3+}, as depicted in **Figure 4.19c and Table 4.5**.

Oxygen vacancies in the functionalized and doped OLCs decorated with Ni $(OH)_2$ were assessed through the XPS data, focusing on the O1s, C1s, and Ni2p spectra. The presence and extent of oxygen vacancies were inferred from shifts in binding energies and relative peak intensities, which were influenced by the surface's chemical environment and defect states. These findings were then correlated with the BET surface areas to explore their relationship [73].

Oxygen vacancies in the functionalized and doped OLCs decorated with Ni $(OH)_2$ were assessed through the XPS data, focusing on the O1s, C1s, and Ni2p spectra. The presence and extent of oxygen vacancies were inferred from shifts in binding energies and relative peak intensities, which were influenced by the surface's chemical environment and defect states. These findings were then correlated with the BET surface areas to explore their relationship [80].

For Ox-OLCs/Ni $(OH)_2$, O1s peaks were observed at 533.5 eV (C=O) and 532.2 eV (C-O) as depicted in **Figure 4.15a**, with C1s peaks at 284.9 eV (C-C), 285.9 eV (C-O), 287 eV (C=O), and 289 eV (O-C=O), shown in **Figure 4.15c** . The relatively high intensity of oxygen-related peaks

(C-O, C=O) and moderate BET surface area (72 m^2/g), depicted in **Table 4.2**, suggest that oxygen vacancies were limited, as oxygen functional groups were abundant on the surface. The lower surface area indicates fewer exposed defect sites, implying that oxygen was retained rather than lost as vacancies [81] [82].

In N-OLCs/Ni $(OH)_2$, O1s peaks were detected at 531.5 eV (C-O) and 533.2 eV (C=O), as depicted in **Figure 4.16a**, with C1s at 285 eV (C-C), 286.1 eV (C-O), 287.1 eV (C=O), and 289 eV (O-C=O), as illustrated in **Figure 4.16c**. Ni2p showed Ni^{2+} (857 eV, 874.6 eV) and Ni^{3+} (863.5 eV, 881.9 eV), as shown in **Figure 4.19a**. The shift of C-O to a lower binding energy (531.5 eV) and the highest BET surface area (260 m^2/g), as illustrated in **Table 4.2**, suggest that oxygen vacancies were less prevalent, as nitrogen doping enhanced surface reactivity, promoting oxygen incorporation. The presence of Ni^{3+} indicates partial oxidation of Ni $(OH)_2$, further supporting oxygen retention rather than vacancy formation [73][75].

For B-OLCs/Ni $(OH)_2$, O1s peaks were recorded at 533.4 eV (C=O) and 531.5 eV (C-O), as shown in **Figure 4.17a**, with C1s at 284.5 eV (C-C), 285.8 eV (C-O), 287.1 eV (C=O), and 288.9 eV (O-C=O), as represented in **Figure 4.17c**. Ni2p peaks were at Ni^{2+} (856.1 eV, 873.7 eV) and Ni^{3+} (862.4 eV, 881.0 eV), as depicted in **Figure 4.19b**. The lower C-C binding energy (284.5 eV) and a BET surface area of 207 m^2/g, as shown in **Table 4.2**, suggest that boron doping introduced some oxygen vacancies, reducing oxygen-containing groups. The lower Ni^{2+} binding energy and Ni^{3+} presence indicate a modified Ni $(OH)_2$ environment, potentially linked to oxygen defects [83].

In B, N-OLCs/Ni $(OH)_2$, O1s peaks were found at 531.5 eV (C-O) and 533.4 eV (C=O), as depicted in **Figure 4.18a**, with C1s at 284.7 eV (C-C), 285.9 eV (C-O), 287.4 eV (C=O), and 289.1 eV (O-C=O), as illustrated in **Figure 4.19c**. Ni2p peaks were observed at Ni^{2+} (856.5 eV, 874.2 eV) and Ni^{3+} (863.0 eV, 881.3 eV), as shown in **Figure 4.19c**. The moderate BET surface area (146 m^2/g), shown in **Table 4.2**, and balanced oxygen-related peaks suggest that co-doping increased defect density. However, oxygen vacancies were not as pronounced as in B-OLCs, likely due to nitrogen's stabilizing effect on oxygen. The Ni^{2+} and Ni^{3+} peaks indicate a mixed oxidation state, possibly reflecting a balance between oxygen retention and vacancy formation [84].

The BET surface areas (Ox-OLCs: 72 m^2/g, N-OLCs: 260 m^2/g, B-OLCs: 207 m^2/g, B, N-OLCs: 146 m^2/g), depicted in **Table 4.2**, were linked to oxygen vacancies as follows: higher surface areas (e.g., N-OLCs) were associated with more oxygen retention due to increased sites for functional groups, while moderate-to-high areas with doping (e.g., B-OLCs) suggested more vacancies due to heteroatom-induced defects. Lower surface areas (e.g., Ox-OLCs) implied fewer vacancies, as oxygen was more uniformly bonded [85].

The observed peaks at O1s (533 eV) typically indicate low-oxygen ordered defect sites and surface-adsorbed oxygen species[86]. Furthermore, the peak at 533 eV is generally attributed to the abundance of physisorbed and chemisorbed water near the material's interface. Ox-OLCs exhibited the existence of oxidized nitrogen species, with bonding energies ranging from 403 to 407.5 eV. N-OLCs/Ni $(OH)_2$ contained pyridinic Nitrogen at 398.5 to 400 eV, graphitic or quaternary Nitrogen at 401 to 403 eV and oxidized nitrogen species at 403 to 407.5 eV. The B-

OLCs/Ni $(OH)_2$ exhibited pyridinic nitrogen species, potentially manifesting within the energy range of 398.5 to 400 eV. In the case of B, N-OLCs/Ni $(OH)_2$, pyridinic nitrogen species were also present, with binding energies of 398.5-400 eV [76].

The local chemical environment and additional functional groups or flaws within the carbon structure can also affect the precise binding energy. Surface effects and interactions with other elements, such as nickel hydroxide in decorated OLCs, may further alter the binding energies. Including pyrrolic and pyridinic species, chemically functioning nitrogen bonding structures enhance the material's conductivity, which is crucial for boosting capacitance[87]. Nitrogen and oxygen are expected to augment the wettability of carbon materials, hence increasing the accessibility of the electrode surface for improved capacitive performance. The presence of pyrrolic and pyridinic Nitrogen enhances performance by potentially offering additional reversible faradaic capacity in an alkaline aqueous solution [30].

Pyrrolic and pyridinic structures incorporate two and three sp^2 carbon atoms, each contributing a pair of electrons. This structure can enhance electron transport and conductivity. The augmentation of the Full Width at Half Maximum (FWHM) of the C1s peak in XPS for functionalized OLC when doped with Nitrogen and adorned with nickel hydroxide, as well as when doped with boron and Nitrogen, can be ascribed to various factors associated with the chemical and structural alterations induced by these processes as depicted in **Table 4.5** [88]. Introducing Nitrogen into the carbon lattice generates many nitrogen functions, including pyridinic, pyrrolic, and graphitic Nitrogen. The diverse bonding environments lead to peak broadening in the C1s spectrum owing

to the fluctuations in the chemical surroundings of the atoms. Boron doping incorporates boron atoms into the carbon lattice, forming B-C bonds[89].

The presence of boron atoms results in several chemical states, broadening the C1s, N1s, and B1s peaks, as illustrated in **Table 4.5**. Modifying OLC with nickel hydroxide introduces extra elements (nickel and oxygen) and forms new chemical bonds, namely C-O and C-Ni. The formation of these new bonds and the interaction between nickel hydroxide and the carbon surface result in the broadening of the C1s, N1s, and Ni2p peaks[90]. The presence of nickel hydroxide can also create stress and imperfections in the carbon lattice. The synergistic influence of boron and nitrogen heteroatoms results in a more intricate chemical milieu. The existence of various dopants and their interactions with carbon atoms leads to an expanded dispersion of binding energies, hence augmenting the FWHM, as depicted in **Table 4.5** [91]. The doping and decorating processes may induce structural flaws and disorder within the carbon lattice. [1]Flaws disturb the carbon lattice's regularity, resulting in a broader spectrum of detectable binding energies [92].

4.2. Synthesis technique of OLCs produced via flame pyrolysis

The synthesis of OLCs via flame pyrolysis is posited to occur through a bottom-up strategy. During this process, the carbon supply is broken into atomic or radical fragments, which then react to create OLC aggregates with primary nucleation sites, forming agglomerates. The development of OLC layers commences internally and progresses outwardly, mainly from the carbon particle nodules, following the auto-curling cycle. Larger OLCs are generated from the aggregation of multi-layered OLCs that arise when carbon lattices produce polycyclic aromatic hydrocarbons (PAH), as depicted in **Figure 4.21** [6][93].

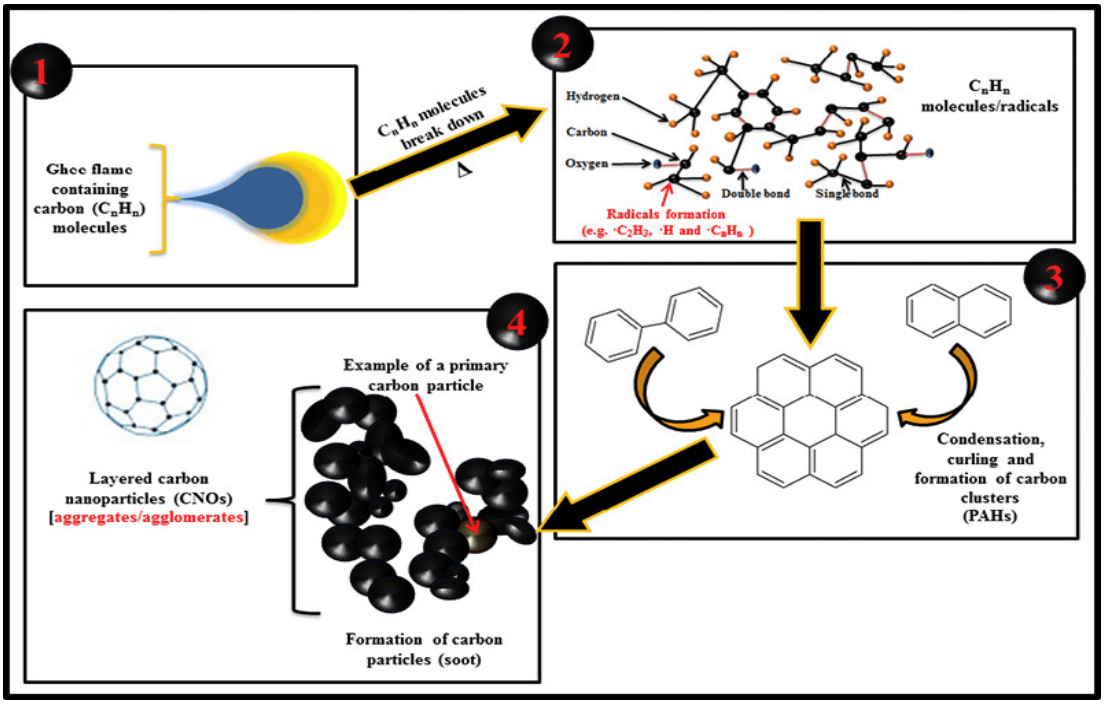


Figure 4. 21: Schematic diagram of the mechanism of synthesis of onion-like carbon by flame pyrolysis[73]

4.3. Conclusion

The flame pyrolysis technique has effectively facilitated the synthesis of OLC nanoparticles with waste engine oil as a carbon precursor. Their onion-like structure had an average particle size of 35.73 nm, as verified by TEM examinations. The TGA data corroborates that the OLC is devoid of contamination from other carbon forms. The TGA results validated functionalization. The functionalization, nitrogen, boron doping, co-doping, and decorating with nickel hydroxide do not modify the structure of OLCs, as evidenced by the TEM pictures. Raman and XRD analyses revealed the existence of flaws in the OLC materials. which can function as reactive sites for electrolyte adsorption in energy storage applications. The XPS data indicates that nitrogen and

boron doping, and co-doping successfully facilitated the deposition of nickel hydroxide on the surface of the OLC matrix. The doping of OLCs influenced their microporosity and mesoporosity, as evidenced by the BET data. In summary, the physicochemical properties of OLCs are impacted by functionalization, doping, and co-doping.

4.4. References

[1] O. Mykhailiv *et al.*, "Boron-Doped Polygonal Carbon Nano-Onions: Synthesis and Applications in Electrochemical Energy Storage," *Chemistry - A European Journal*, 23, pp. 7132–7141, May 2017, doi: 10.1002/chem.201700914.

[2] G. Siemiaszko *et al.*, "Composites containing resins and carbon nano-onions as efficient porous carbon materials for supercapacitors," *Sci Rep*, 13, Dec. 2023, doi: 10.1038/s41598-023-33874-w.

[3] O. Mykhailiv *et al.*, "Improvement of the Structural and Chemical Properties of Carbon Nano-onions for Electrocatalysis," *ChemNanoMat*, 3, pp. 583–590, Aug. 2017, doi: 10.1002/cnma.201700161.

[4] D. Govindarajan *et al.*, "In-situ growth of binder-free Cr/NiO thin film electrodes via co-sputtering for asymmetric supercapacitors," *Appl Surf Sci*, 630, Sep. 2023, doi: 10.1016/j.apsusc.2023.157475.

[5] C. Duong-Viet et al., "Magnetic induction assisted pyrolysis of plastic waste to liquid hydrocarbons on carbon catalyst," *Mater. Today Catal.*, 3, pp. 246–257, Nov. 2023. [Online]. Available: https://doi.org/10.1016/j.mtcata.2023.100028

[6] T. H. Mongwe, B. J. Matsoso, B. K. Mutuma, N. J. Coville, and M. S. Maubane, "Synthesis of chain-like carbon nano-onions by a flame assisted pyrolysis technique using different collecting plates," *Diam Relat Mater*, 90, pp. 135–143, Nov. 2018, doi: 10.1016/j.diamond.2018.10.002.

[7] P. Fraundorf, W. Qin, P. Moeck, and E. Mandell, "Making sense of nanocrystal lattice fringes," *J. Appl. Phys.*, 98, p. 113701, 2005. [Online]. Available: https://doi.org/10.1063/1.2135414

[8] M. Ozawa, H. Goto, M. Kusunoki, and E. Osawa, "Continuously growing spiral carbon nanoparticles as the intermediates in the formation of fullerenes and nanoonions," *Journal of Physical Chemistry B*, 106, pp. 7135–7138, Jul. 2002, doi: 10.1021/jp025639z.

[9] M. Ghosh, S. K. Sonkar, M. Saxena, and S. Sarkar, "Carbon nano-onions for imaging the life cycle of Drosophila melanogaster," *Small*, 7, pp. 3170–3177, Nov. 2011, doi: 10.1002/smll.201101158.

[10] B. I. Dunlap, "Relating carbon tubules," *Phys. Rev. B*, 49, pp. [page 1-8], Feb. 15, 1994. [Accessed: Mar. 9, 2025].

[11] N. Revaprasadu and M. D. Khan, Eds., *Nanoscience*, vol. 8, Cambridge, UK: Royal Society of Chemistry, 2022. [Online]. Available: https://doi.org/10.1039/9781839167218

[12] S. Ihara, S. Itoh, K. Akagi, R. Tamura, and M. Tsukada, "Structure of polygonal defects in graphitic carbon sheets," *Phys. Rev. B*, 54, pp. 14713–14719, Nov. 1996, doi: 10.1103/PhysRevB.54.14713.

[13] Z. Z. Liu et al., "Facile synthesis of $Ni(OH)_2$ through low-temperature N-doping for efficient hydrogen evolution," *Catalysts*, 14, Art. no. 534, Aug. 2024. [Online]. Available: https://doi.org/10.3390/catal14080534

[14] Y. Liu *et al.*, "Understanding the enhancement effect of boron doping on the electrochemical performance of single-crystalline Ni-rich cathode materials," *J Colloid Interface Sci*, 604, pp. 776–784, Dec. 2021, doi: 10.1016/J.JCIS.2021.07.027.

[15] S. Ramesh et al., "$Ni(OH)_2$-decorated nitrogen-doped MWCNT nanosheets as an efficient electrode for high-performance supercapacitors," *Sci. Rep.*, 9, Art. no. 6034, Dec. 2019. [Online]. Available: https://doi.org/10.1038/s41598-019-42281-z

[16] D. Mohapatra, S. Badrayyana, and S. Parida, "Facile wick-and-oil flame synthesis of high-quality hydrophilic onion-like carbon nanoparticles," *Mater Chem Phys*, 174, pp. 112–119, May 2016, doi: 10.1016/J.MATCHEMPHYS.2016.02.057.

[17] M. Yaseen *et al.*, "A Review of Supercapacitors: Materials Design, Modification, and Applications," *Energies (Basel)*, 14, , Art no. 7779, Nov. 2021, doi: 10.3390/en14227779.

[18] X. Du, Z. Lin, X. Wang, K. Zhang, H. Hu, and S. Dai, "Electrode Materials, Structural Design, and Storage Mechanisms in Hybrid Supercapacitors," *Molecules*, 28, Art no. 6432, Sep. 2023, doi: 10.3390/molecules28176432.

[19] P. Fan and L. Xu, "Core-shell carbon nanofibers@$Ni(OH)_2$/NiO composites for high-performance asymmetric supercapacitors," *Materials*, 15, Art. no. 8377, Dec. 2022. [Online]. Available: https://doi.org/10.3390/ma15238377

[20] H. M. Jeong *et al.*, "Nitrogen-Doped Graphene for High-Performance Ultracapacitors and the Importance of Nitrogen-Doped Sites at Basal Planes," *Nano Lett*, 11, pp. 2472–2477, Jun. 2011, doi: 10.1021/nl2009058.

[21] J.-H. Yang *et al.*, "Boron-doped α-Ni(OH)2 nanoflowers with high specific surface area as electrochemical capacitor materials," *Mater Lett*, 128, pp. 380–383, Aug. 2014, doi: 10.1016/j.matlet.2014.04.170.

[22] Z. Shang *et al.*, "Design of B/N Co-doped micro/meso porous carbon electrodes from CNF/BNNS/ZIF-8 nanocomposites for advanced supercapacitors," *Journal of Bioresources and Bioproducts*, 8, pp. 292–305, Aug. 2023, doi: 10.1016/j.jobab.2023.05.002.

[23] P. Sirisinudomkit, P. Iamprasertkun, A. Krittayavathananon, T. Pettong, P. Dittanet, and M. Sawangphruk, "Hybrid Energy Storage of Ni(OH)2-coated N-doped Graphene Aerogel//N-doped Graphene Aerogel for the Replacement of NiCd and NiMH Batteries," *Sci Rep*, 7, Art no. 1124, Apr. 2017, doi: 10.1038/s41598-017-01191-8.

[24] A. Fallah, "Boron-doped sucrose carbons for supercapacitor electrode: Artificial neural network-based modelling approach," *Sci. Rep.*, 13, Art. no. 12040, Jul. 2023, doi: 10.1038/s41598-023-39240-0.

[25] Y. Song, X. Zhang, P. A. A. Klusener, and P. Nockemann, "Advancing mesoporous carbon synthesis for supercapacitors: a systematic investigation of cross-linking agent effects on pore structure and functionality," *Nanoscale*, 15, pp. 19658–19670, 2023, doi: 10.1039/D3NR03244B.

[26] M. Thommes *et al.*, "Physisorption of gases, with special reference to the evaluation of surface area and pore size distribution (IUPAC Technical Report)," *Pure and Applied Chemistry*, 87, pp. 1051–1069, Oct. 2015, doi: 10.1515/pac-2014-1117.

[27] S. Álvarez, M. C. Blanco-López, A. J. Miranda-Ordieres, A. B. Fuertes, and T. A. Centeno, "Electrochemical capacitor performance of mesoporous carbons obtained by templating technique," *Carbon N Y*, 43, pp. 866–870, 2005, doi: 10.1016/j.carbon.2004.10.044.

[28] S. S. Rekhviashvili and M. M. Bukhurova, "Stability of a Carbon Nano-Onion in Contact with a Graphite Substrate," *Technical Physics Letters*, 45, pp. 591–593, Jun. 2019, doi: 10.1134/S1063785019060294.

[29] M. M. Safaee, M. Gravely, A. Lamothe, M. McSweeney, and D. Roxbury, "Enhancing the Thermal Stability of Carbon Nanomaterials with DNA," *Sci Rep*, 9, 1, Dec. 2019, doi: 10.1038/s41598-019-48449-x.

[30] B. Shaku, T. P. Mofokeng, N. J. Coville, K. I. Ozoemena, and M. S. Maubane-Nkadimeng, "Biomass valorisation of marula nutshell waste into nitrogen-doped activated carbon for use in high-performance supercapacitors," *Electrochimica Acta*, 442, Art. no. 141828, Feb. 2023. [Online]. Available: https://doi.org/10.1016/j.electacta.2023.141828

[31] E. Y. Choi and C. K. Kim, "Fabrication of nitrogen-doped nano-onions and their electrocatalytic activity toward the oxygen reduction reaction," *Sci. Rep.*, 7, Art. no. 4597, Dec. 2017. [Online]. Available: https://doi.org/10.1038/s41598-017-04597-6

[32] L. L. Sikeyi, T. D. Ntuli, T. H. Mongwe, N. W. Maxakato, N. J. Coville, and M. S. Maubane-Nkadimeng, "Platinum nanoparticles loaded on pristine and boron oxide modified carbon nano-onions for enhanced ammonia electrooxidation in alkaline direct ammonia fuel cells," *Appl. Catal. B Environ.*, 302, Art. no. 120812, 2022. [Online]. Available: https://doi.org/10.1016/j.apcatb.2022.120812

[33] O. Mykhailiv *et al.*, "Boron-Doped Polygonal Carbon Nano-Onions: Synthesis and Applications in Electrochemical Energy Storage," *Chemistry - A European Journal*, vol. 23, pp. 7132–7141, May 2017, doi: 10.1002/chem.201700914.

[34] A. M. Thamizhchelvan and N. Lien, "Unique nanostructures of carbon nano onions," in *Handbook of Functionalized Carbon Nanostructures*, A. Barhoum and K. Deshmukh, Eds., Cham: Springer International Publishing, 2024, pp. 181–228. [Online]. Available: https://doi.org/10.1007/978-3-031-32150-4_5

[35] R. J. Krupadam and S. S. Rayalu, "Melamine-based resins and their carbons for CO_2 capture: a review," *Emergent Mater.*, 4, pp. 545–563, 2021. [Online]. Available: https://doi.org/10.1007/s42247-020-00157-3

[36] J. B. Aladekomo and R. H. Bragg, "Structural transformations induced in graphite by grinding: Analysis of 002 X-ray diffraction line profiles," *Carbon*, 28, pp. 897–906, 1990. [Online]. Available: https://doi.org/10.1016/0008-6223(90)90338-Y

[37] S. M. Lee, S. H. Lee, and J. S. Roh, "Analysis of activation process of carbon black based on structural parameters obtained by XRD analysis," *Crystals (Basel)*, 11, pp. 1–11, Feb. 2021, doi: 10.3390/cryst11020153.

[38] M. Zhao, H. Song, X. Chen, and W. Lian, "Large-scale synthesis of onion-like carbon nanoparticles by carbonization of phenolic resin," *Acta Mater*, 55, pp. 6144–6150, Oct. 2007, doi: 10.1016/j.actamat.2007.07.013.

[39] Q. Zou, Y. G. Li, B. Lv, M. Z. Wang, L. H. Zou, and Y. C. Zhao, "Transformation of onion-like carbon from nanodiamond by annealing," *Inorganic Materials*, 46, pp. 127–131, Feb. 2010, doi: 10.1134/S002016851002007X.

[40] P. Kumar, A. Soni, V. Kumar, J. S. Gwag, R. Singhal, and A. K. Mukhopadhyay, "pH dependent microstructural changes of α-Ni(OH)2 hollow-sphere nanostructure thin films," *Journal of Materials Science: Materials in Electronics*, 35, Mar. 2024, doi: 10.1007/s10854-024-12129-y.

[41] D. S. Kang, S. M. Lee, S. H. Lee, and J. S. Roh, "X-ray diffraction analysis of the crystallinity of phenolic res-in-derived carbon as a function of the heating rate during the carbonization process," *Carbon Letters*, 27, pp. 108–111, Jul. 2018, doi: 10.5714/CL.2018.27.108.

[42] A. K. Mondal, D. Su, S. Chen, B. Sun, K. Li, and G. Wang, "A simple approach to prepare nickel hydroxide nanosheets for enhanced pseudocapacitive performance," *RSC Adv*, 4, pp. 19476–19481, 2014, doi: 10.1039/c4ra01719f.

[43] W. Sun, X. Rui, M. Ulaganathan, S. Madhavi, and Q. Yan, "Few-layered Ni(OH)2 nanosheets for high-performance supercapacitors," *J Power Sources*, 295, pp. 323–328, Jul. 2015, doi: 10.1016/j.jpowsour.2015.07.024.

[44] X. Y. Liu *et al.*, "Preparation of a carbon-based solid acid catalyst by sulfonating activated carbon in a chemical reduction process," *Molecules*, 15, pp. 7188–7196, Oct. 2010, doi: 10.3390/molecules15107188.

[45] A. K. Kercher and D. C. Nagle, "Microstructural evolution during charcoal carbonization by X-ray diffraction analysis," *Carbon*, 41, pp. 15-27, Jan. 2003, doi: 10.1016/S0008-6223(02)00261-4. [Accessed: Mar. 9, 2025].

[46] N. E. Sorokina and N. V. Maksimova, "Anodic oxidation of graphite in 10 to 98% HNO_3," *Russ. J. Electrochem.*, 37, pp. 441–447, Apr. 2001, doi: 10.1023/A:1016677705364.

[47] M. J. Climent, A. Corma, S. Iborra, and A. Velty, "Carbohydrates as green raw materials for the chemical industry: Conversion of sugar derivatives into liquid hydrocarbon fuels," *Nature*, 438, pp. 178-181, Nov. 2005, doi: 10.1038/nature04077.

[48] L. Lu, V. Sahajwalla, C. Kong, and D. Harris, "Quantitative X-ray diffraction analysis and its application to various coals," *Carbon*, 39, pp. 1821–1833, Oct. 2001. [Online]. Available: https://doi.org/10.1016/S0008-6223(00)00318-3

[49] J. Biscoe and B. E. Warren, "An X-Ray Study of Carbon Black," *J Appl Phys*, 13, pp. 364–371, Jun. 1942, doi: 10.1063/1.1714879.

[50] M. Okamura *et al.*, "Acid-catalyzed reactions on flexible polycyclic aromatic carbon in amorphous carbon," *Chemistry of Materials*, 18, pp. 3039–3045, Jun. 2006, doi: 10.1021/cm0605623.

[51] G. S. Szymanski *et al.*, "Linking the Defective Structure of Boron-Doped Carbon Nano-Onions with Their Catalytic Properties: Experimental and Theoretical Studies," *ACS Appl Mater Interfaces*, 13, pp. 51628–51642, Nov. 2021, doi: 10.1021/acsami.1c12126.

[52] B. Manoj and A. G. Kunjomana, "Study of stacking structure of amorphous carbon by X-ray diffraction technique," *Int. J. Electrochem. Sci.*, 7, pp. 3127-3134, 2012. [Online]. Available: http://www.electrochemsci.org/papers/vol7/7043127.pdf.

[53] G. S. Szymanski *et al.*, "Linking the Defective Structure of Boron-Doped Carbon Nano-Onions with Their Catalytic Properties: Experimental and Theoretical Studies," *ACS Appl Mater Interfaces*, 13, pp. 51628–51642, Nov. 2021, doi: 10.1021/acsami.1c12126.

[54] TUINSTRA F and KOENIG JL, "RAMAN SPECTRUM OF GRAPHITE," *Journal of Chemical Physics*, 53, pp. 1126–1130, 1970, doi: 10.1063/1.1674108.

[55] A. C. Ferrari and D. M. Basko, "Raman spectroscopy as a versatile tool for studying the properties of graphene," *Nat Nanotechnol*, 8, pp. 235–246, Apr. 2013, doi: 10.1038/nnano.2013.46.

[56] J.-B. Wu, M.-L. Lin, X. Cong, H.-N. Liu, and P.-H. Tan, "Raman spectroscopy of graphene-based materials and its applications in related devices," *Chem Soc Rev*, 47, pp. 1822–1873, 2018, doi: 10.1039/C6CS00915H.

[57] W. Liu and G. Speranza, "Tuning the Oxygen Content of Reduced Graphene Oxide and Effects on Its Properties," *ACS Omega*, 6, pp. 6195–6205, Mar. 2021, doi: 10.1021/acsomega.0c05578.

[58] Z. Li, L. Deng, I. A. Kinloch, and R. J. Young, "Raman spectroscopy of carbon materials and their composites: Graphene, nanotubes and fibres," *Prog. Mater. Sci.*, 135, Art. no. 101089, Jun. 2023. [Online]. Available: https://doi.org/10.1016/j.pmatsci.2023.101089

[59] C. Hu et al., "Raman spectroscopy study of the transformation of the carbonaceous skeleton of a polymer-based nanoporous carbon along the thermal annealing pathway," *Carbon*, 85, pp. 147–158, 2015. [Online]. Available: https://doi.org/10.1016/j.carbon.2014.12.098

[60] M. E. Pérez-Ojeda *et al.*, "Carbon Nano-onions: Potassium Intercalation and Reductive Covalent Functionalization," *J Am Chem Soc*, 143, pp. 18997–19007, Nov. 2021, doi: 10.1021/jacs.1c07604.

[61] J. Cebik, J. K. McDonough, F. Peerally, R. Medrano, I. Neitzel, Y. Gogotsi, and S. Osswald, "Raman spectroscopy study of the nanodiamond-to-carbon onion transformation," *Nanotechnology*, 24, Art. no. 205703, May 2013. [Online]. Available: https://doi.org/10.1088/0957-4484/24/20/205703

[62] Y. Lin, Y. Zhu, B. Zhang, Y. A. Kim, M. Endo, and D. S. Su, "Boron-doped onion-like carbon with enriched substitutional boron: the relationship between electronic properties and catalytic performance," *J Mater Chem A Mater*, 3, pp. 21805–21814, 2015, doi: 10.1039/C5TA03141A.

[63] A. C. Ferrari, "Raman spectroscopy of graphene and graphite: Disorder, electron–phonon coupling, doping and nonadiabatic effects," *Solid State Commun*, 143, pp. 47–57, Jul. 2007, doi: 10.1016/j.ssc.2007.03.052.

[64] A. Das *et al.*, "Monitoring dopants by Raman scattering in an electrochemically top-gated graphene transistor," *Nat Nanotechnol*, 3, pp. 210–215, Apr. 2008, doi: 10.1038/nnano.2008.67.

[65] A. Das *et al.*, "Monitoring dopants by Raman scattering in an electrochemically top-gated graphene transistor," *Nat Nanotechnol*, 3, pp. 210–215, Apr. 2008, doi: 10.1038/nnano.2008.67.

[66] F. Allali, H. Chadli, M. Bentaleb, P. Hermet, and A. Rahmani, "Nonresonant Polarized Raman Spectra Calculations of Nitrogen-Doped Single-Walled Carbon Nanotubes: Diameter, Chirality, and Doping Concentration Effects," *The Scientific World Journal*, 2020, pp. 1–10, Apr. 2020, doi: 10.1155/2020/1409581.

[67] U. S. Kodithuwakku, N. Wanninayake, M. P. Thomas, B. S. Guiton, and D. Y. Kim, "Unlocking efficiency in oxygen reduction reaction: Synergistic edge dopants of nitrogen and boron in carbon nano onions," *Electrochim. Acta*, 471, Art. no. 143365, Dec. 2023. [Online]. Available: https://doi.org/10.1016/j.electacta.2023.143365

[68] J. C. Chacón-Torres, L. Wirtz, and T. Pichler, "Manifestation of charged and strained graphene layers in the Raman response of graphite intercalation compounds," *ACS Nano*, 7, pp. 9249–9259, Oct. 2013, doi: 10.1021/nn403885k.

[69] J. C. Chacón-Torres, L. Wirtz, and T. Pichler, "Manifestation of Charged and Strained Graphene Layers in the Raman Response of Graphite Intercalation Compounds," *ACS Nano*, vol. 7, pp. 9249–9259, Oct. 2013, doi: 10.1021/nn403885k.

[70] Z. Li, L. Deng, I. A. Kinloch, and R. J. Young, "Raman spectroscopy of carbon materials and their composites: Graphene, nanotubes and fibres," *Prog Mater Sci*, 135, Art no. 101089, Jun. 2023, doi: 10.1016/j.pmatsci.2023.101089.

[71] A. D. C. Permana *et al.*, "Comparative Study of Onion-like Carbons Prepared from Different Synthesis Routes towards Li-Ion Capacitor Application," *Batteries*, 8, p. 160, Oct. 2022, doi: 10.3390/batteries8100160.

[72] Y.-J. Ko *et al.*, "Inherently-Forced Tensile Strain in Nanodiamond-Derived Onion-like Carbon: Consequences in Defect-Induced Electrochemical Activation," *Sci Rep*, 6, p. 23913, Apr. 2016, doi: 10.1038/srep23913.

[73] J. P. Paraknowitsch and A. Thomas, "Doping carbons beyond nitrogen: An overview of advanced heteroatom-doped carbons with boron, sulfur, and phosphorus for energy applications," *Energy Environ. Sci.*, 6, pp. 2839–2855, Oct. 2013. [Online]. Available: https://doi.org/10.1039/C3EE41444B

[74] Z. H. Sheng, H. L. Gao, W. J. Bao, F. Bin Wang, and X. H. Xia, "Synthesis of boron doped graphene for oxygen reduction reaction in fuel cells," *J Mater Chem*, 22, pp. 390–395, Jan. 2012, doi: 10.1039/c1jm14694g.

[75] L. Lai *et al.*, "Exploration of the active center structure of nitrogen-doped graphene-based catalysts for oxygen reduction reaction," *Energy Environ Sci*, 5, pp. 7936–7942, Jul. 2012, doi: 10.1039/c2ee21802j.

[76] J. Laverde, N. C. Rosero-Navarro, R. Buitrago-Sierra, and D. López, "Nitrogen functionalities in mesoporous carbons and their impact on the sulfur infiltration efficiency and in the electrochemical performance of Li–S cells," *Solid State Ionics*, 399, Art. no. 116303, Oct. 2023. [Online]. Available: https://doi.org/10.1016/j.ssi.2023.116303

[77] D. Zhang et al., "Preparation of nitrogen-doped lignin-based porous carbon materials and their application in a supercapacitor," *J. Mater. Sci.*, 59, pp. 19161–19174, Oct. 2024. [Online]. Available: https://doi.org/10.1007/s10853-024-10317-z

[78] D. J. Morgan, "Comments on the XPS Analysis of Carbon Materials," *C (Basel)*, vol. 7, Art no. 51, Jul. 2021, doi: 10.3390/c7030051.

[79] M. Ayiania, M. Smith, A. J. R. Hensley, L. Scudiero, J. S. McEwen, and M. Garcia-Perez, "Deconvoluting the XPS spectra for nitrogen-doped chars: An analysis from first principles," *Carbon N Y*, 162, pp. 528–544, Jun. 2020, doi: 10.1016/j.carbon.2020.02.065.

[80] Z. Yang, X. Lu, W. Tan, J. Zhao, D. Yang, Y. Yang, Y. He, and K. Zhou, "XPS studies of nitrogen doping niobium used for accelerator applications," *Appl. Surf. Sci.*, 439, pp. 1119–1126, 2018. [Online]. Available: https://doi.org/10.1016/j.apsusc.2017.12.214

[81] A. D. Lueking, H. R. Gutierrez, P. Jain, D. T. Van Essandelft, and C. E. Burgess-Clifford, "The effect of HCl and NaOH treatment on structural transformations in a ball-milled anthracite after thermal and chemical processing," *Carbon N Y*, 45, pp. 2297–2306, Oct. 2007, doi: 10.1016/J.CARBON.2007.04.027.

[82] I. Kriegel and F. Scotognella, "Tunable light filtering by a Bragg mirror/heavily doped semiconducting nanocrystal composite," *Beilstein Journal of Nanotechnology*, 6, pp. 193–200, 2015, doi: 10.3762/bjnano.6.18.

[83] Z. Wang, "Nitrogen-doped carbon nanomaterials as efficient electrocatalysts for oxygen reduction reaction," *J. Mater. Chem. A*, 4, pp. 4038–4055, 2016. [Online]. Available: https://doi.org/10.1039/C6TA00457A

[84] H. Peng, "Oxygen vacancy engineering in $Ni(OH)_2$ nanosheets for enhanced supercapacitor performance," *ACS Appl Mater Interfaces*, 9, pp. 35057–35066, 2017.

[85] T. Kato, Y. Yamada, Y. Nishikawa, T. Otomo, H. Sato, and S. Sato, "Origins of peaks of graphitic and pyrrolic nitrogen in N1s X-ray photoelectron spectra of carbon materials: quaternary nitrogen, tertiary amine, or secondary amine?," *J Mater Sci*, 56, pp. 15798–15811, Oct. 2021, doi: 10.1007/s10853-021-06283-5.

[86] M. Cheng, H. Fan, Y. Song, Y. Cui, and R. Wang, "Interconnected hierarchical NiCo2O4 microspheres as high-performance electrode materials for supercapacitors," *Dalton Transactions*, 46, pp. 9201–9209, 2017, doi: 10.1039/c7dt01289f.

[87] Y. Rangraz and M. M. Heravi, "Recent advances in metal-free heteroatom-doped carbon heterogeneous catalysts," *RSC Adv.*, 11, pp. 23725–23778, Jul. 2021. [Online]. Available: https://doi.org/10.1039/D1RA03446D

[88] O. Mykhailiv *et al.*, "Boron-Doped Polygonal Carbon Nano-Onions: Synthesis and Applications in Electrochemical Energy Storage," *Chemistry - A European Journal*, vol. 23, pp. 7132–7141, May 2017, doi: 10.1002/chem.201700914.

[89] A. R. Santos, R. K. Blundell, and P. Licence, "XPS of guanidinium ionic liquids: A comparison of charge distribution in nitrogenous cations," *Physical Chemistry Chemical Physics*, 17, pp. 11839–11847, May 2015, doi: 10.1039/c5cp01069a.

[90] A. Camisasca, A. Sacco, R. Brescia, and S. Giordani, "Boron/Nitrogen-Codoped Carbon Nano-Onion Electrocatalysts for the Oxygen Reduction Reaction," *ACS Appl Nano Mater*, 1, pp. 5763–5773, Oct. 2018, doi: 10.1021/acsanm.8b01430.

[91] Y. Lin, Y. Zhu, B. Zhang, Y. A. Kim, M. Endo, and D. S. Su, "Boron-doped onion-like carbon with enriched substitutional boron: The relationship between electronic properties and catalytic performance," *J Mater Chem A Mater*, 3, pp. 21805–21814, 2015, doi: 10.1039/c5ta03141a.

[92] S. Bokome, *Synthesis and Application of Boron-Nitrogen Doped Carbon Nano-Onions in Supercapacitors*, MSc dissertation, University of the Witwatersrand, Johannesburg, South Africa, Jan. 28, 2020. [Online]. Available: https://wiredspace.wits.ac.za/items/57d17f63-6fd1-45a2-8c1d-cbe0f74580ad. Accessed: Mar. 2025.

[93] T. H. Mongwe, B. J. Matsoso, B. K. Mutuma, N. J. Coville, and M. S. Maubane, "Synthesis of chain-like carbon nano-onions by a flame assisted pyrolysis technique using different collecting plates," *Diam Relat Mater*, 90, pp. 135–143, Nov. 2018, doi: 10.1016/j.diamond.2018.10.002.

Chapter 5

Exploring the electrochemical performance of OLCs/Ni $(OH)_2$ electrode materials for hybrid supercapacitor application

This chapter delineates electrochemical findings from investigations of functionalized Ox-OLCs, doped N-OLCs, doped B-OLCs, and co-doped B, N-OLCs, all of which are adorned with Ni $(OH)_2$ and activated and functionalized AcOx-OLCs, utilizing a symmetric structure formed in 6M KOH.

5.0. Introduction

The contemporary world requires energy; however, this energy is predominantly derived from the combustion of fossil fuels, particularly coal. Storage systems are essential in modern civilization if energy is to be generated from renewable sources such as solar and wind, as they store excess power for use when production drops. This study concentrates on energy storage utilizing supercapacitors. This is due to the ability of SCs to function across an extensive temperature spectrum, leading to elevated power densities and prolonged life cycles [1]. Supercapacitors employ three processes for energy storage. As stated in **Chapter 2 (Section 2.3.1)**, EDLCs represent one method by which SCs accumulate energy. Carbon materials are predominantly utilized in EDLCs owing to their extensive surface area, which may host many electrolyte ions[2].

Electrochemical pseudocapacitors represent the second category of supercapacitors (SCs) that store energy, utilizing metal oxide or conducting polymer electrodes that include a significant degree of electrochemical pseudocapacitance and double-layer capacitance.

Pseudocapacitance is attained through electrochemical charge transfer via reduction-oxidation reactions, electrosorption, or intercalation[3]. In contrast, hybrid capacitors, such as lithium-ion capacitors, utilize electrodes with distinct properties, one primarily demonstrating electrostatic capacitance and the other electrochemical capacitance[4]. The distinction between pseudocapacitive and battery-like electrodes remains one of the most debated topics in electrochemistry. Due to overlapping electrochemical behaviors, this controversy stems from the frequent misclassification of battery-type electrodes as pseudocapacitive materials. It is recommended that, when evaluating the electrochemical characteristics of a novel nanomaterial, researchers should first establish whether its charge storage mechanism aligns with diffusion-controlled faradaic redox reactions characteristic of battery-type electrodes or the surface-limited, fast redox processes typical of pseudocapacitors. [5].

In redox reactions, conventional battery-like electrode materials differ from capacitor-like electrode materials due to phase change transitions occurring during the electrochemical process. Consequently, battery-like electrodes exhibit independent reductive and oxidative peaks in their cyclic voltammetry profiles or constant-current discharge curves, which are characterized by well-defined plateaus. Typical battery materials include $Ni(OH)_2$ and metals including Cu, Co, and Cd, along with their respective oxides and hydroxides. Unlike capacitive

charge retention, charge storage in battery-type electrodes follows a non-linear dependence on the applied voltage, making conventional capacitance values an inaccurate metric for these materials. [7].

This study primarily concentrates on OLCs/Ni $(OH)_2$ suitable for application in battery-like supercapacitors. The primary critical issue in solid-state batteries is the interaction at the cathode interface, anode, and electrolyte interface. Therefore, it is essential to align the dimensions of the electrolyte particles with the pore sizes of the cathode and anode materials, as the specific capacitance is influenced by the diffusion of electrolyte ions into the pores of the active electrode material[8].

Furthermore, the internal resistance of the active material in supercapacitors significantly influences the energy storage capacity, determined mainly by the ionic conductivity of the electrolyte ions[9]. Optimal electrolytes are crucial in using supercapacitors despite each possessing distinct advantages and downsides. For instance, aqueous electrolytes, including alkaline, acidic, and neutral solutions such as H_2SO_4, KOH, and Na_2SO_4, can be utilized. Consequently, this research uses a fully asymmetric device to examine KOH for supercapacitor applications. The decomposition of electrolytes must be assessed in supercapacitors, as it can occasionally cause operational failures, leading to diminished capacitance values[10].

Among the various aqueous electrolytes, 6 M KOH was selected owing to its numerous advantages. Initially, KOH exhibits elevated ionic conductivity, facilitating swift ion transport

and diminishing internal resistance, thereby enhancing rate capability. Secondly, KOH demonstrates a broad electrochemical stability window in contrast to neutral electrolytes such as Na_2SO_4, facilitating elevated operating voltages and consequently enhancing energy density. Third, it exhibits a reduced corrosive effect on carbon-based electrodes compared to strong acids such as H_2SO_4, thereby minimising electrode degradation and promoting an extended cycle life, discussed in the literature review **Chapter 2 (pg. 69-77)** . Ultimately, the 6 M concentration guarantees an ample supply of ions, thereby enhancing the formation of the double layer and subsequently increasing the specific capacitance of the device.

N-OLCs/Ni $(OH)_2$ was examined for supercapacitor applications utilizing a two-electrode setup. N-OLCs/Ni $(OH)_2$ was used for energy storage in supercapacitors employing 6M KOH in a fully asymmetric cell. The B, N-OLCs/Ni $(OH)_2$, B-OLCs/Ni $(OH)_2$, Ox-OLCs/Ni $(OH)_2$, and P-OLCs/Ni $(OH)_2$ synthesized were excluded from this investigation due to their impurity and low specific surface area.

5.1. Development of enhanced Ox- OLCs/Ni $(OH)_2$, N- OLCs/Ni $(OH)_2$, B, N-OLCs/Ni $(OH)_2$, B-OLCs/Ni $(OH)_2$, and AcOx-OLCs electrode material used for three-electrode systems and two electrode systems applications.

Electrochemical measurements were conducted using a three-electrode system (half-cell) setup in a 6M KOH electrolyte. A silver wire was the reference electrode, while nickel foam was the

counter electrode. The electrode materials were synthesized by formulating a paste for each composite material, combined with PVDF binder (polyvinylidene fluoride) in a 9:1 ratio, wherein 90% of the mixture comprised the composite material from each distinct sample and 10% consisted of the PVDF binder, resulting in a total of 10 mg of the mix for each sample. Several drops of N-methyl-2-pyrrolidone (NMP) were incorporated into each sample to create a slurry, and all sample combinations were sonicated for two hours.

The resultant slurry was applied to several carbon papers for each sample created via drop coating with a glass dropper. The produced working electrodes were dried at 60°C in an oven overnight before electrochemical testing. A Whatman microfiber filter paper, utilized as a separator, was immersed in a 6M KOH electrolyte and positioned between the coated electrode and the counter electrode (Nickel foam) for application in supercapacitors for all individual samples, as illustrated in the configuration below in **Figure 5.1.**

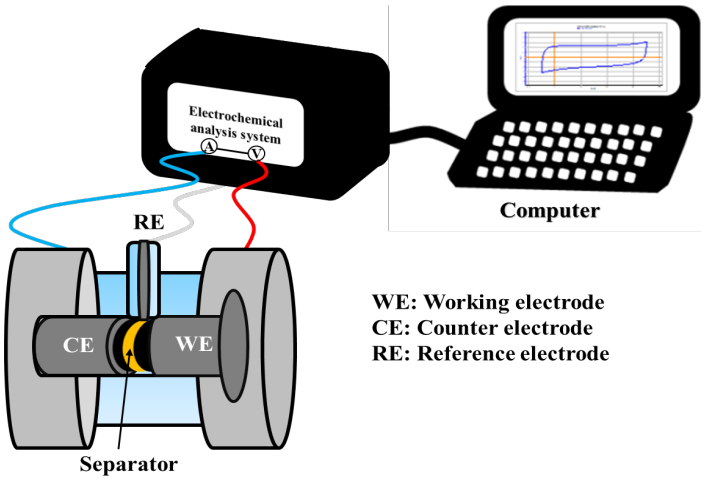


Figure 5. 1: Schematic diagram for three-electrode system [11]

In the applications of a two-electrode system (full-cell), the sole electrode evaluated was N-doped OLCs adorned with nickel hydroxide (N-OLCs/Ni $(OH)_2$) prepared and utilized as the positive electrode, while activated functionalized OLCs (AcOx-OLCs) served as the negative electrode, as illustrated in the setup below in **Figure 5.2**.

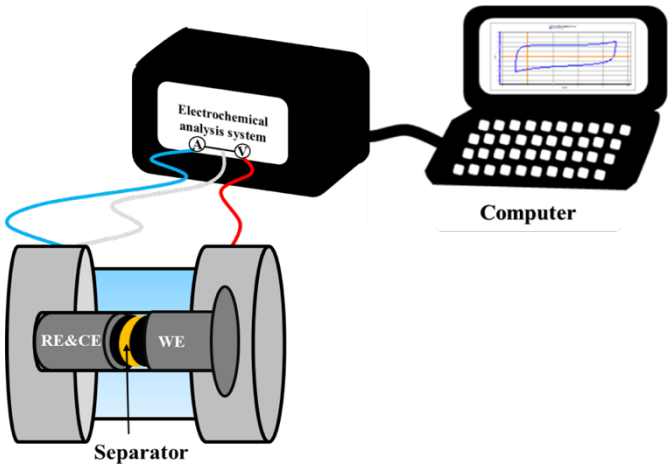


Figure 5. 2: Schematic diagram for two- electrode system [11]

5.2. Results and discussion.

5.2.1. Cyclic voltammetry for a three-electrode system for Ox-OLCs/Ni $(OH)_2$, N-OLCs/Ni $(OH)_2$, B-OLCs/Ni $(OH)_2$, B, N-OLCs/Ni $(OH)_2$, and AcOx-OLCs.

A biological SP 300 potentiostat, operated with EC-LAB® version 11.52 software, was utilized for electrochemical measurements in a three-electrode system within 6M KOH. The cyclic voltammetry (CV) curves of the four samples for three electrodes were carried out at a scan rate of 1.0-50mVs^{-1} and potential window of (-0.2-0.4V) as shown in **Figures 5.3a-d**, while for AcOx-OLCs were carried out at a scan rate of 10-50 mVs^{-1} and potential window of (0.0V) – (-0.8V) as depicted in **Figure 5.4b** indicating that nitrogen-doped onion-like carbon adorned with nickel hydroxide exhibits the most robust current response signifying high capacitance in comparison to Ox-OLCs/Ni $(OH)_2$, B-OLCs/Ni $(OH)_2$, B, N-OLCs/Ni $(OH)_2$, and AcOx-OLCs as depicted in **Figures 5.3a-d and 5.4b**.

The voltammograms of four samples at 1.0 mVs^{-1}, illustrated in **Figure 5.4a**, exhibit redox features indicative of battery-like behavior (Faradaic redox processes). The mechanistic process primarily involves single-electron transfer between +2 and +3 oxidation states of nickel (Ni^{2+}/Ni^{3+}) in ∝-like crystals, including the de-intercalation and intercalation of OH^- ions, aligning with prior findings for Ni-based electrodes as depicted in **Equation 5.1** [12]. The redox peak in all four samples, as represented in **Figure 5.4a**, escalates with an intensification in scan rate. This is characteristic of the electrochemical signature of Ni-based electrodes. The facile transport of OH^- the increase in

the peaks of anodic and cathodic current responses corroborates ions[13]. The AcOx-OLCs electrode material was the anode used to evaluate the full-asymmetric cell.

The CV curve of the AcOx-OLCs, as depicted in **Figure 5.4b**, has a quasi-rectangular form, indicating that the energy storage mechanism is characterized by electric double-layer capacitance (EDLC). B, N-OLCs/Ni $(OH)_2$ exhibited the subsequent highest current response, succeeded by AcOx-OLCs, then B-OLCs/Ni $(OH)_2$, and finally OX-OLCs/Ni $(OH)_2$. All four materials, excluding AcOx-OLCs, were evaluated at a scan rate of 1.0 mVs^{-1} under a potential window of (-0.2 - 0.4V), as illustrated in **Figure 5.4a**. N-OLCs/Ni $(OH)_2$ exhibited a superior current response to the other electrode materials. This can be attributed to various factors, including charge transfer, where nitrogen functions as an N-type dopant, polarizing adjacent carbon atoms and generating charged sites that enhance electron transfer[14].

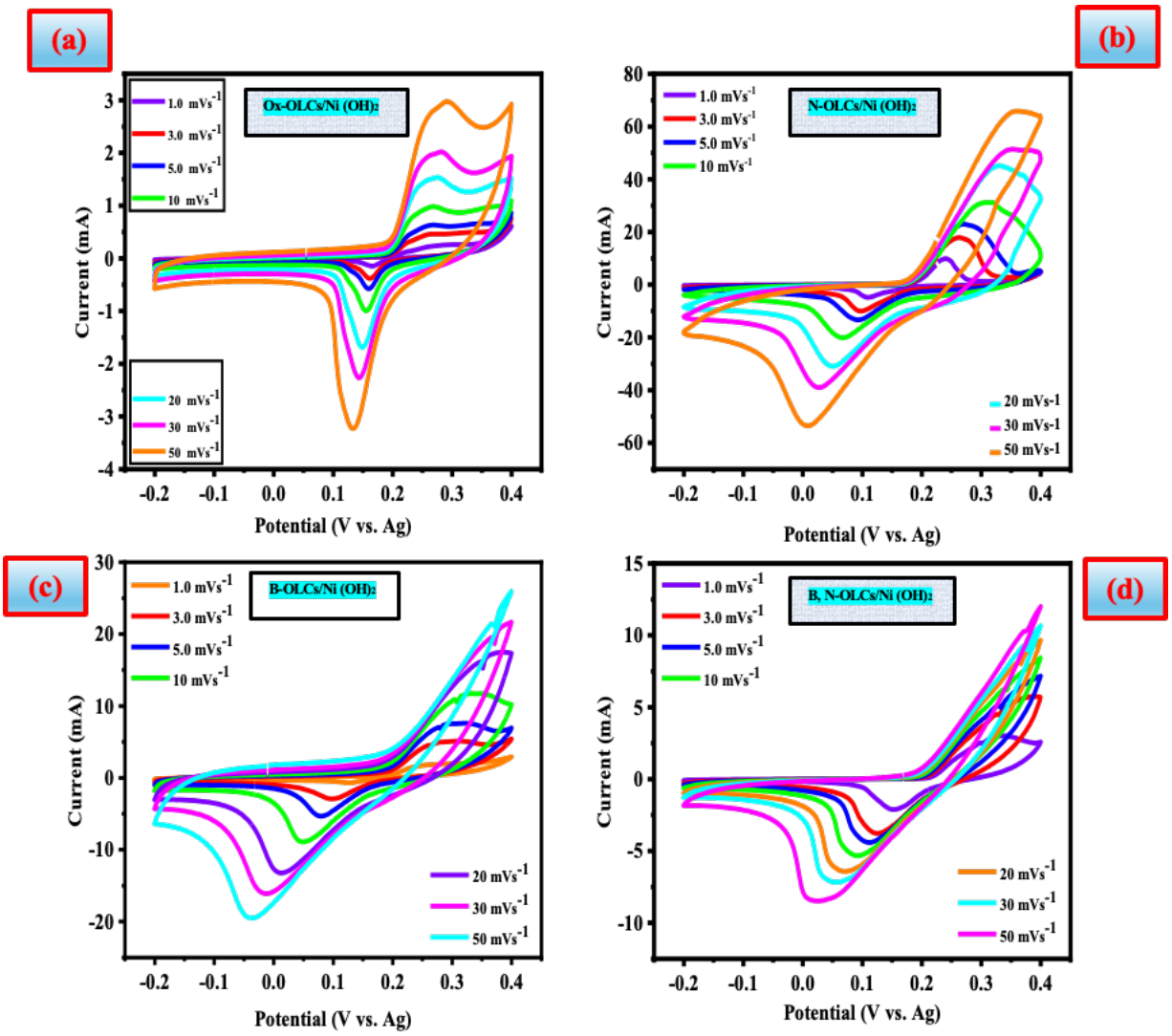


Figure 5. 3: CV graphs for three-electrode system (a) OX-OLCs/Ni (OH)$_2$ (b) N-OLCs/Ni (OH)$_2$ (c) B- OLCs/Ni (OH)$_2$ (d) B, N-OLCs/Ni (OH)$_2$.

These augment electrochemical activity and accelerate the kinetics of redox processes. Incorporating nitrogen introduces several functional groups, such as pyridinic and pyrrolic nitrogen, which can be active sites for electrochemical reactions, enhancing the overall current responsiveness[15].

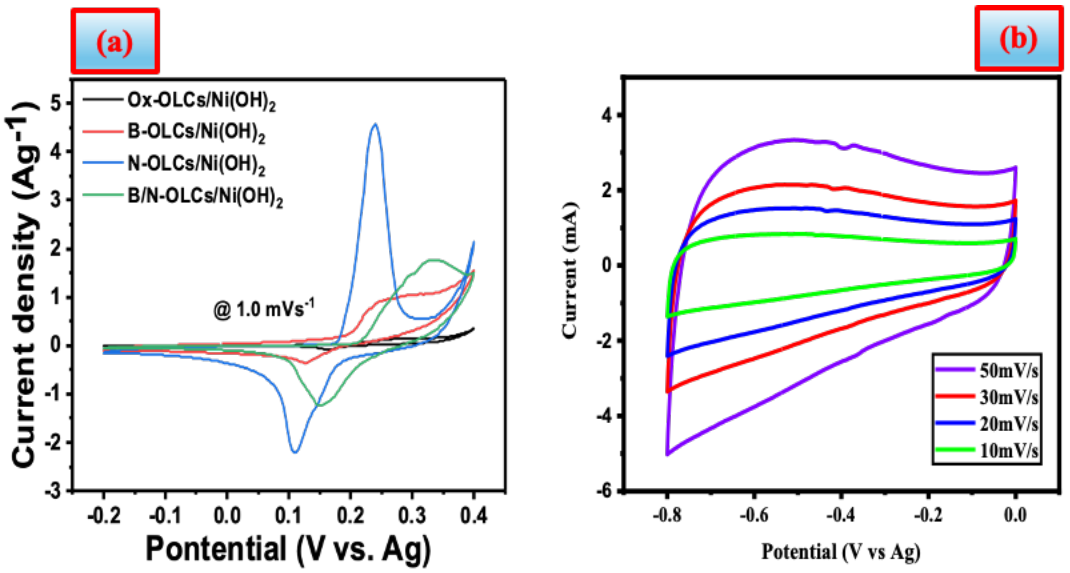


Figure 5. 4: (a) CV graphs comparison for the three-electrode system at 1.0 mV/s (b) CV graphs for AcOx-OLCs at different scan rates.

$$(Charging)\ Ni\ (OH)2\ +\ OH-\ \leftrightarrow\ NiOOH\ +\ H2O\ +\ e-\ (Discharging) \qquad Eqn\ (5.\ 1)$$

Nitrogen doping introduces functional groups that boost reactant adsorption and improve interaction with nickel hydroxide, resulting in superior electrolytic performance. N-O-C generally maintains a significant level of graphitic character, which is advantageous for conductivity and charge transport, improving the current response[16].

The amalgamation of N-O-C with nickel hydroxide can provide a synergistic effect, wherein the attributes of both substances enhance one another, resulting in superior electrochemical performance. Nickel hydroxide is recognized for its significant electrochemical activity, particularly in alkaline environments. Although boron doping can augment conductivity, it does not offer the same active sites as nitrogen[17][18].

The co-doping of boron and nitrogen may confer certain benefits; nonetheless, the specific advantages of nitrogen regarding charge transfer and the availability of active sites frequently surpass those of boron[19]. Despite activated functionalized carbon possessing the largest surface area, as depicted in BET results in **Chapter 4**, electrochemical activity is not exclusively contingent upon surface area. The active sites' characteristics and electrical properties influence the current response.

5.2.2. Galvanostatic charge-discharge and specific capacitance of a three-electrode system

The GCD curves of Ox-OLCs/Ni $(OH)_2$, N-OLCs/Ni $(OH)_2$, B-OLCs/Ni $(OH)_2$, and B, N-OLCs/Ni $(OH)_2$ exhibited asymmetry, indicative of battery-like nanostructured Ni-based electrode materials that facilitate the energy retention mechanism of battery-like electrodes, as illustrated in the GCD curves in **Figure 5.5 (a-d)**. In contrast, AcOx-OLCs displayed asymmetrical curves within the potential voltage of 0.6V, measured at varying current densities from 0.30 to 3.00 A/g, further corroborating the energy storage mechanism of the EDLC, as depicted in the CV curve in **Figure 5.6b**. The GCD of the composite materials was evaluated and illustrated in **Figure 5.6a** at a current density of 0.5 A/g in 6M KOH. The data from the GCD curves corroborate the findings from the CV plots, indicating that B, N-OLCs/Ni $(OH)_2$, and N-OLCs/Ni $(OH)_2$ exhibit superior electrochemical performance in comparison to the other carbon compounds illustrated in **Figure 5.6a**.

The N-OLCs/Ni $(OH)_2$ exhibited the most prolonged discharge duration at a current density of 0.5 A/g, as indicated by the red GCD curve **Figure 5.6a**. The specific capacitance of the materials,

derived from the GCD curves in **Figure 5.6a**, is presented in **Figure 5.6c**. This corroborates CV data, indicating that an increase in current leads to decreased capacitance due to the restricted time available for electrolyte ions to reach the anode and cathode surfaces. Additional factors affecting charge-discharge duration include increased surface area and porosity, facilitating more efficient ion transport and storage.

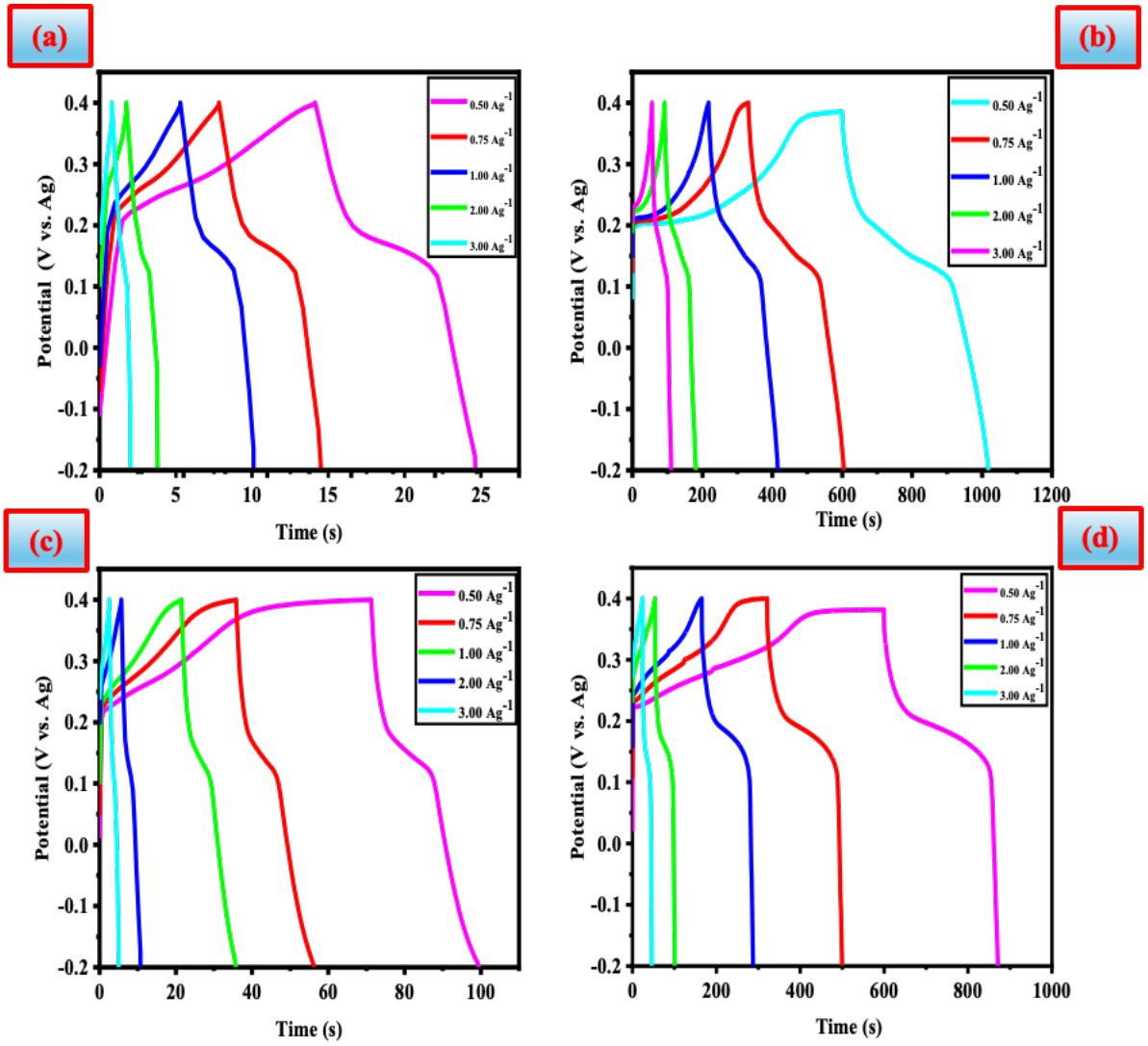


Figure 5. 5: GCD graphs for the three-electrode system at different current densities (a) Ox-OLCs/Ni $(OH)_2$ (b) N-OLCs/Ni $(OH)_2$ (c) B-OLCs/Ni $(OH)_2$ (d) B, N-OLCs/Ni $(OH)_2$.

The incorporation of doping elements such as nitrogen and boron, which can enhance active sites and improve electronic conductivity; the selection of electrolyte, which can impact ion mobility and its interaction with the carbon surface; elevated current densities, which generally lead to reduced charge-discharge times due to accelerated ion movement; and functional groups on the carbon surface, which can augment interactions with the electrolyte, thereby influencing overall electronic performance[20][21].

The calculated values of the specific capacitances are provided in **Table 5.1**. The enhanced specific capacitance values of the N-OLCs/Ni $(OH)_2$ and B, N-OLCs/Ni $(OH)_2$ can be ascribed to the elevated I_D/I_G ratios (results reported in **Chapter 4**). Nitrogen atoms create supplementary active sites and augment the carbon matrix's electrical conductivity, enhancing charge storage capacity[22]. Nickel hydroxide contributes faradaic pseudo capacitance, which markedly increases the overall capacitance. Integrating nitrogen doping and nickel hydroxide decorating produces a synergistic effect that improves chemical performance. Co-doping with boron and nitrogen enhances the availability of active sites and increases the wettability of the carbon surface, hence permitting improved electrolyte accessibility[13].

The activation process of functionalized OLCs augments the surface area and porosity of the carbon material, hence improving its electrochemical characteristics. Introducing functional groups on the carbon surface enhances interaction with the electrolyte, resulting in improved charge storage[23]. These results corroborate the CV data, indicating that an increase in current

leads to a reduction in contact time for the transport of electrolyte ions. This subsequently resulted in reduced capacitance values at elevated current densities.

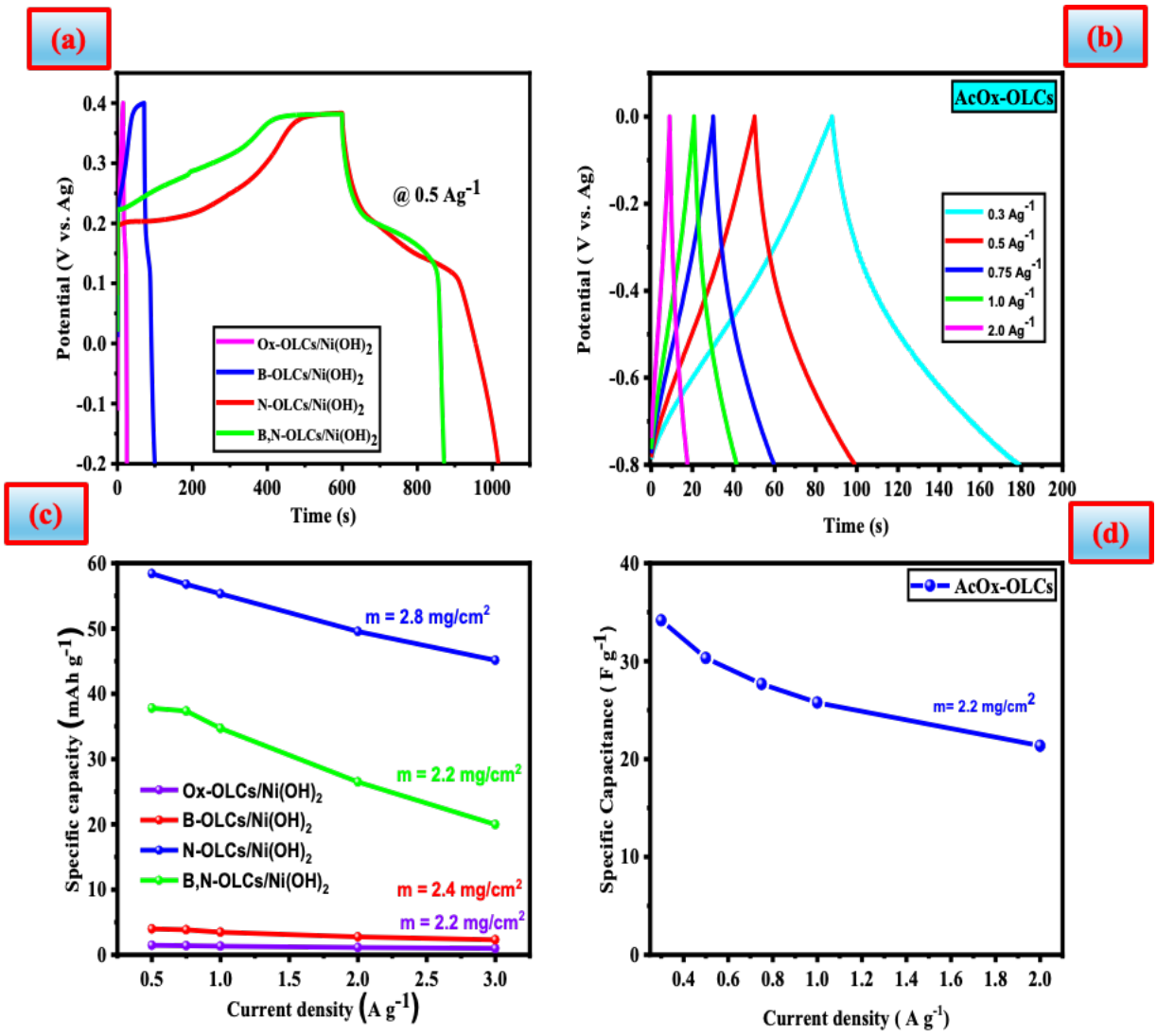


Figure 5. 6: (a) GCD graphs comparison for three-electrode systems at different current densities (b) GCD graphs for AcOx-OLCs at different current densities (c) specific capacity comparison graphs (d) specific capacitance graph for AcOx-OLCs.

Table 5. 1: Specific Capacity and Capacitance of different OLCs at various current densities.

Specific capacitance at various current densities						
Samples	**0.30 A/g**	**0.50 A/g**	**0.75 A/g**	**1.00 A/g**	**2.00 A/g**	**3.00 A/g**
Ox-OLCs/Ni $(OH)_2$	N/A	1.46 mAh/g	1.40 mAh/g	1.32 mAh/g	1.12 mAh/g	1.00 mAh/g
B-OLCs/Ni $(OH)_2$	N/A	3.97 mAh/g	3.84 mAh/g	3.46 mAh/g	2.76 mAh/g	2.30 mAh/g
B,N-OLCs/Ni $(OH)_2$	N/A	37.78 mAh/g	37.33 mAh/g	34.71 mAh/g	26.47 mAh/g	19.95 mAh/g
N-OLCs/Ni $(OH)_2$	N/A	58.41 mAh/g	56.77 mAh/g	55.32 mAh/g	49.55 mAh/g	45.14 mAh/g
AcOx-OLCs	34.16 F/g	30.31 F/g	27.66 F/g	25.75 F/g	21.35 F/g	N/A

5.2.3. Electrochemical impedance spectroscopy (EIS) for three-electrode system

EIS is employed to appraise the electrochemical efficiency of energy retention devices. Researchers employed this technique to evaluate electrode materials for SCs; frequency sweeps must be steered at distinctive voltage intensities and distinctive temperatures. EIS facilitates the examination of frequency's impact on electrode series resistance and specific capacitance[24]. The EIS measurements of Ox-OLCs/Ni $(OH)_2$, N-OLCs/Ni $(OH)_2$, B-OLCs/Ni $(OH)_2$, B, N-OLCs/Ni $(OH)_2$, and AcOx-OLCs utilizing an electrical equivalent circuit are depicted in **Figure 5.7 (a-d), Figure 5.8 (a-b) and Figure 5.9 (a-e)**. The Nyquist plot is described by a composite RC/Randle's circuit comprising solution resistance R_s, double-layer capacitanceC_{dl}, interfacial resistance R_{int}, attributed to internal resistance drop R_{ct} charge-transfer resistance attributed to electron transportation, Warburg diffusion region Z_ω representing resistance to ion diffusion and the

constant phase element CPE reflecting surface inhomogeneity. A CPE is a capacitive component characterized by a continuous phase angle. The impedance is expressed as:

$$Z_{CPE} = [Q_0(j\omega)^a]^{-1} \quad \textit{Eqn (5. 2)}$$

Where Q_0 is the frequency-independent continual related to the electrolyte/electrode interface, $j = \sqrt{-1}$, w denotes the radial frequency, and the exponent a reflects the gradient of the log z vs. Log F, where the values satisfy $-1 \leq a \leq 1$. When $a = 0$, the Constant phase element (CPE) performs as a pure resistor; when $a = 1$, it functions as a pure capacitor; when $a = -1$, it acts as an inductor; and at $a = 0.5$, the CPE is analogous to Warburg resistance Z_ω[25].

The Nyquist plots indicate a greater semicircle diameter for N-OLCs/Ni $(OH)_2$ and B, N-OLCs/Ni $(OH)_2$, implying a reduction in Faradaic reactions at the surface of the active material. Moreover, the Ox-OLCs/Ni $(OH)_2$ and B-OLCs/Ni $(OH)_2$ exhibit small semicircles, signifying minimal charge transfer resistance. The low-frequency area of Ox-OLCs/Ni $(OH)_2$ and N-OLCs/Ni $(OH)_2$ electrodes exhibited a steeper gradient compared to B-OLCs/Ni $(OH)_2$, B, N-OLCs/Ni $(OH)_2$, and AcOx-OLCs as depicted in **Figure 5.8b**, signifying enhanced ion diffusion and superior contact between the surfaces of Ox-OLCs/Ni $(OH)_2$ and N-OLCs/Ni $(OH)_2$ with the electrolyte.

The cumulative series resistance $R_s + R_{int} + R_{ct}$ values for Ox-OLCs/Ni $(OH)_2$, N-OLCs/Ni $(OH)_2$, B-OLCs/Ni $(OH)_2$, B, N-OLCs/Ni $(OH)_2$, and AcOx-OLCs are 11.86 Ω, 9.84 Ω, 1.091×10^{-36} Ω, 29.92 Ω, and 43.29 Ω, respectively, as indicated in **Table 5.2**. These findings suggest that N-OLCs/Ni $(OH)_2$ exhibits a lower resistance value, signifying enhanced conductivity

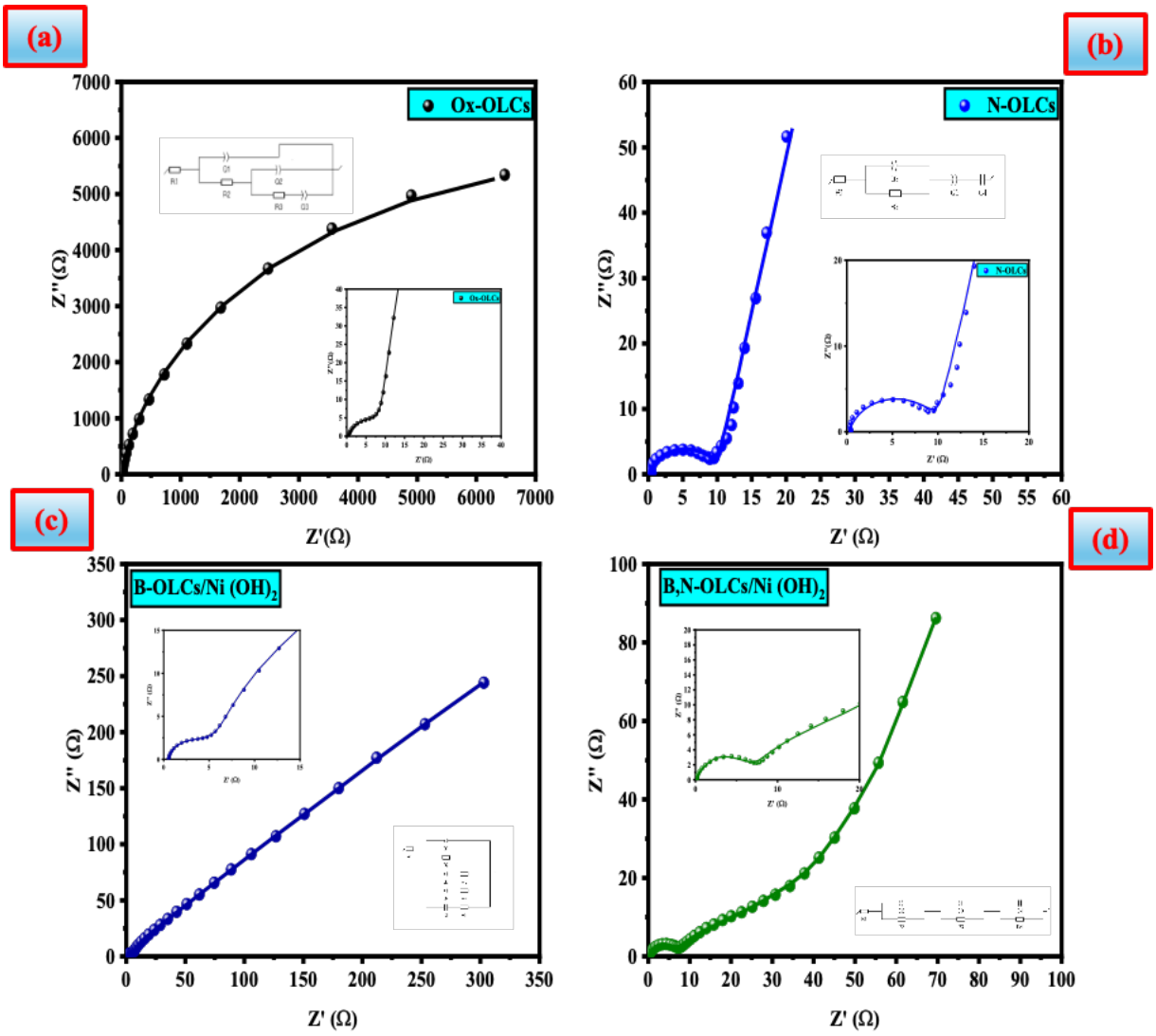


Figure 5. 7: EIS graphs and series circuits for (a) Ox-OLCs/Ni (OH)₂ (b) N-OLCs/Ni (OH)₂ (c) B-OLCs/Ni (OH)₂ (d) B, N-OLCs/Ni (OH)₂

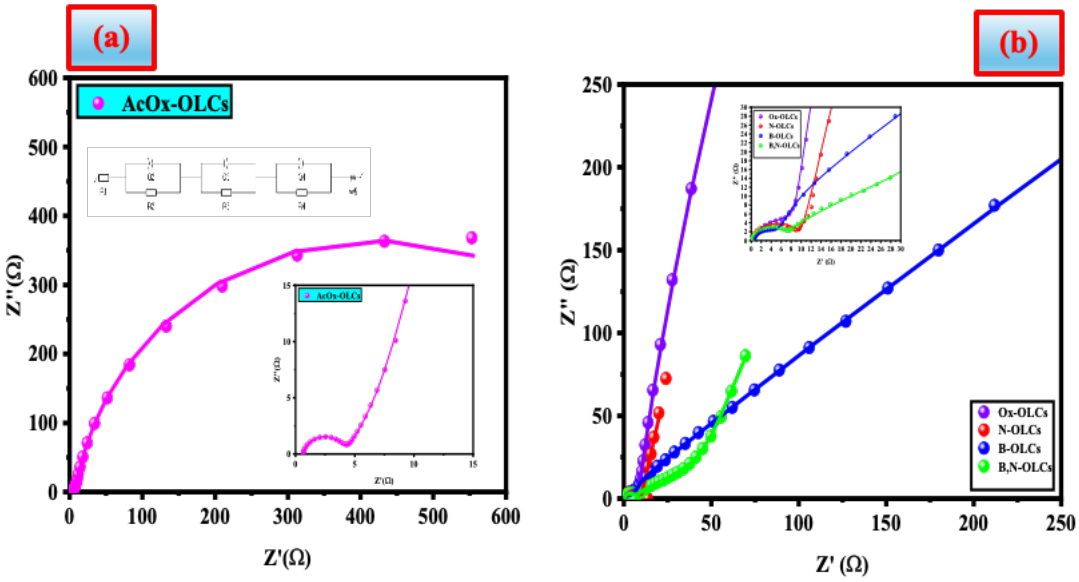


Figure 5. 8: EIS graphs and series circuit for (a) AcOx-OLCs (b) EIS Comparison graphs

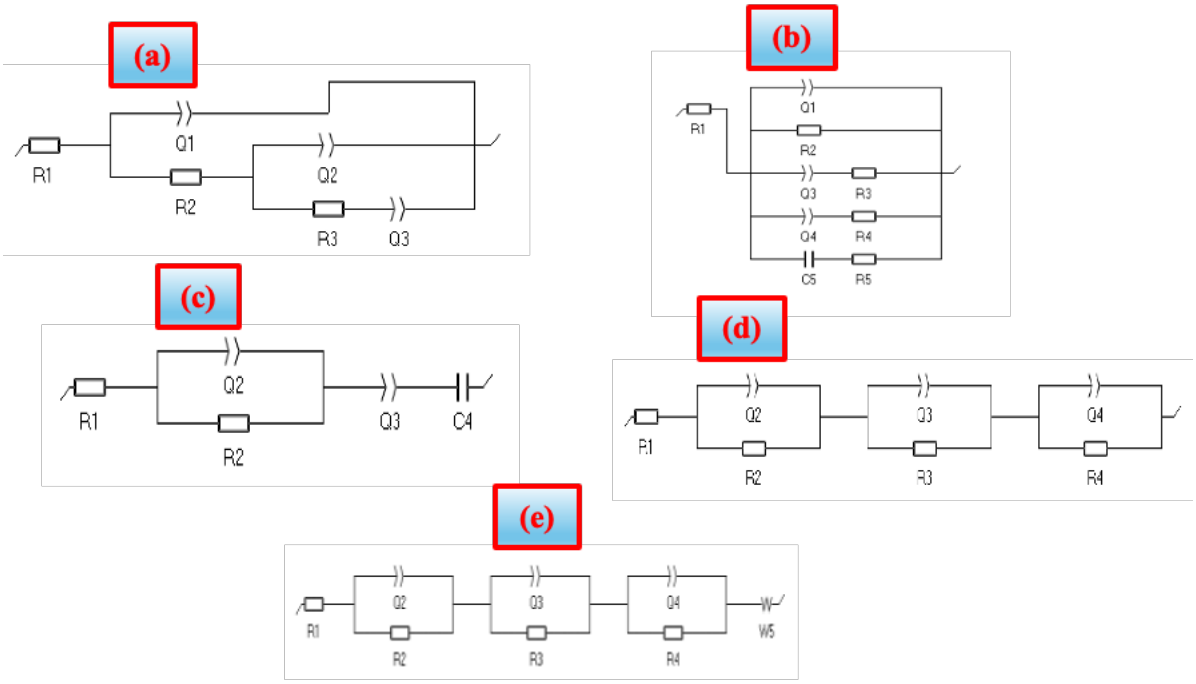


Figure 5. 9: EIS series circuits for three-electrode system (a) Ox-OLCs/Ni $(OH)_2$ (b) N-OLCs/Ni $(OH)_2$ (c) B-OLCs/Ni $(OH)_2$ (d) B, N-OLCs/Ni $(OH)_2$ (e) AcOx-OLCs/Ni $(OH)_2$

The interfacial impedance of passive nickel hydroxides to electron transport has been previously documented[16]. The Z_ω reading of $3.981 s^{-1/2}$ It was recorded for AcOx-OLCs, as depicted in **Table 5.2**. The corresponding values of a for Ox-OLCs/Ni $(OH)_2$, N-OLCs/Ni $(OH)_2$, B-OLCs/Ni $(OH)_2$, B, N-OLCs/Ni $(OH)_2$, and AcOx-OLCs are as follows: for Ox-OLCs/Ni $(OH)_2$, $a1$, $a2$, and $a3$ are 0.1729, 0.8415, and 0.9382, respectively **(Table 5.2)**; for N-OLCs/Ni $(OH)_2$, $a2$ and $a3$ are 0.829 and 0.8578, respectively **(Table 5.2)**; for B-OLCs/Ni $(OH)_2$, $a1$, $a3$, and $a4$ are 1, 0, and 0.4541, respectively **(Table 5.2)**; for B, N-OLCs/Ni $(OH)_2$, $a2$, $a3$, and $a4$ are 0.9258, 0.9257, and 0.3536, respectively **(Table 5.2)**; and for AcOx-OLCs, $a2$, $a3$, and $a4$ are 0.05932, 0.01074, and 0.01027, respectively **(Table 5.2)**. For B-OLCs/Ni $(OH)_2$, the values of $a1$ and $a3$ were 1 and 0, respectively, as illustrated in **Table 5.2**.

Table 5. 2: EIS parameters of different electrode materials

EIS parameters	Electrode materials									
	Ox-OLCs/Ni $(OH)_2$	Standard deviation	N-OLCs/Ni $(OH)_2$	Standard deviation	B-OLCs/Ni $(OH)_2$	Standard deviation	B, N-OLCs/Ni $(OH)_2$	Standard deviation	AcOx-OLCs	Standard deviation
Rs/Ω	0.3684	± 0.0138	0.2589	±0.138	0.5514	0.01102	5.452×10^{-6}	± 7.7×10^{-3}	0.6166	± 0.01882
Q1/*CPE* F. s^(*a*-1)	1.431×10^{-4}	± 3.5×10^{-3}	-	-	3.01×10^{-5}	± 1.7×10^{-6}	-	-	-	-
a1	0.1729	± 7.7×10^{-3}	-	-	1	± 4.2×10^{-3}	-	-	-	-
R_{ct}/Ω	1.6×10^{-3}	± 6.0×10^{-4}	9.584	±0.2742	1.091×10^{-36}	± 3.4×10^{-54}	3.126	± 0.2611	3.658	± 5.579
Q2/ *CPE* F. s^(*a*-1)	1.734×10^{-4}	± 1.6×10^{-5}	1.334×10^{-3}	±0.215	-	-	1.876×10^{-4}	± 6.2×10^{-5}	0.04206	± 0.03255
a2	0.8415	± 0.01019	0.829	±0.03052	-	-	0.9258	± 0.04368	0.5899	± 0.05932
R_{int}/Ω	11.49	± 0.3002	-	-	6.84×10^{-225}	± 1.4×10^{-102}	2.331	± 252.3	3.369	± 0.08328
Q3/ *CPE* F. s^(*a*-1)	5.094×10^{-4}	± 1.5×10^{-5}	0.05763	±1.5×10^{-3}	1.452×10^{-4}	± 2.4×10^{-5}	0.126	± 1.7×10^{-3}	5.01×10^{-6}	± 4.6×10^{-6}
a3	0.9382	± 4.5×10^{-3}	0.8578	±6.0×10^{-3}	0	0	0.9257	± 4.5×10^{-3}	0.9023	± 0.01074
R_{int}/Ω	-	-	-	-	3.083	±0.1417	24.46	± 0.9934	789.2	± 37.61
Q4/ *CPE* F. s^(*a*-1)	-	-	-	-	7.27×10^{-3}	± 1.8×10^{-5}	0.02704	± 9.6×10^{-4}	0.01092	± 4.0×10^{-4}
a4	-	-	-	-	0.4541	± 2.4×10^{-3}	0.3536	± 9.8×10^{-3}	0.9264	± 0.01027
R5/R_{int}/Ω	-	-	-	-	17.36	± 0.313	-	-	-	-
C4/C_{dl}/µF	-	-	8.269×10^{5}	±1283	-	-	-	-	-	-
C5/C_{dl}/µF	-	-	-	-	236.8	± 4.4×10^{-6}	-	-	-	-
***Z*w / Ω s^-1/2**	-	-	-	-	-	-	-	-	3.981	± 2.604

This indicates that the electrode functions as a pure capacitor when $a1 = 1$, implying ideal capacitive performance with negligible surface roughness or inhomogeneity[27]. It generally signifies a double-layer capacitor C_{dl} At the electrode/electrolyte interface or dielectric behavior in an interface that is clearly defined. The value of 0 at $a3$ indicates that the CPE functions as a pure resistor rather than a capacitor, resulting in a total resistance value of 1.091×10^{-36}, as recorded in **Table 5.2**. This indicates that the element linked to Q_3, $a3$ functions as a purely resistive mechanism instead of a capacitive or diffusive one. In search case, capacitance is absent in B-OLCs/Ni $(OH)_2$ electrodes, or it may signify a completely blocked interface where no capacitive impacts are seen due to inadequate electrical contact between the B-OLCs and Ni $(OH)_2$, resulting in high resistance or even open circuit situations[28].

The results for B, N-OLCs/Ni $(OH)_2$, N-OLCs/Ni $(OH)_2$, Ox-OLCs/Ni $(OH)_2$, and AcOx-OLCs were below 1.0 as illustrated in **Table 5.2**, indicating an optimal capacitor exhibiting a combination of electric double layer lapacitive and pseudocapacitive behavior. For AcOx-OLCs, the a values were significantly low, demonstrating distribution and suggesting relatively low resistance or capacitance, which implies efficient charge transfer and favorable electrochemical activity. This may also signify negligible diffusion resistance, indicating that ions can circulate readily inside the electrolyte, thus improving overall electrochemical performance[29].

Consequently, the tabulated a value indicated that N-OLCs/Ni $(OH)_2$ and AcOx-OLCs exhibited elevated specific capacity, with N-OLCs/Ni $(OH)_2$ demonstrating enhanced diffusion of OH- ions

and improved electrochemical conductivity within a three-electrode system[30]. Consequently, only N-OLCs/ Ni $(OH)_2$ served as the cathode electrode component, while AcOx-OLCs functioned as the anode electrode component in the ensuing two-electrode system.

5.2.4. Graphs of Trasatti and Dunn differentiation and the Randles-Sevcik plot

The charge storage process was elucidated utilizing Trasatti and Dunn differentiation alongside Randles-Sevcik plot methodologies. The Log (i) vs Log (V) graphs in **Figure 5.10a** demonstrate that the b value exceeds 0.5, namely $b = 0.53$ for N-OLCs/Ni $(OH)_2$, showing that N-OLCs/Ni $(OH)_2$ exhibit a diffusion-controlled storage mechanism. A b value near 0.5 indicates that the charge storage process at the anode and cathode is governed by diffusion, as shown in **Figure 5.10a**. The electrochemical reaction rate is constrained by the migration of ions to the electrode surface. A b value of 0.51 ± 0.06 at the cathode and 0.53 ± 0.08 at the anode implies a diffusion-controlled surface, as shown in **Figure 5.10a**. Consequently, this indicates that the anodic and cathodic processes are predominantly controlled by the diffusion of electroactive molecules in N-OLCs/Ni $(OH)_2$[31].

The amalgamation of b values is approximately 0.5 and elevated R^2 Values (0.9521 and 0.9115) indicate that the electrochemical reactions at both the anode and cathode are governed by diffusion. The rate of redox reactions is predominantly dictated by the diffusion rate of ions to and from the electrode surfaces[32]. The elevated R^2 Values (0.9521 and 0.9115) signify that the Randle-Sevcik equation effectively characterizes the correlation between the logarithm of peak current and the scan rate, substantiating the diffusion-controlled mechanism[33].

At a scan rate of 1 mV/s, **Figure 5.10b** illustrates the voltage curve for diffusion-governed current compared to surface-controlled (capacitive) current in N-OLCs/Ni $(OH)_2$. The histograms in **Figure 5.10c**, which compare the percentage contributions of non-Faradaic and Faradaic processes, demonstrating that at lower scan rates, battery-like storage prevails, while EDLC-type is prominent at elevated scan rates. This suggests the N-OLCs/Ni $(OH)_2$ electrode material possesses distinctive elevated-energy and elevated-power properties[34].

Contrary to other reports, the energy retention method of Ni-based battery-like electrode material involves a synergistic Faradaic and capacitive process[13]. At reduced scan speeds, ions possess increased time to permeate the porous architecture of the electrode materials. This facilitates enhanced ion penetration into the material's bulk, resulting in a more significant influence from diffusion-controlled mechanisms. The diffusion-controlled process (68%) is generally linked to Faradaic reactions, wherein ions intercalate into the electrode material, facilitating battery-type storage as depicted in **Figure 5.10c** [35]. At elevated scan rates, the predominant portion of charge storage (85%) is governed by surface control, as depicted in **Figure 5.10c**. This signifies that charge storage is primarily governed by Electric double-layer capacitors (EDLC), wherein ions adhere to the surface of the electrode material. The fast charge-discharge cycles promote surface reactions rather than bulk diffusion.

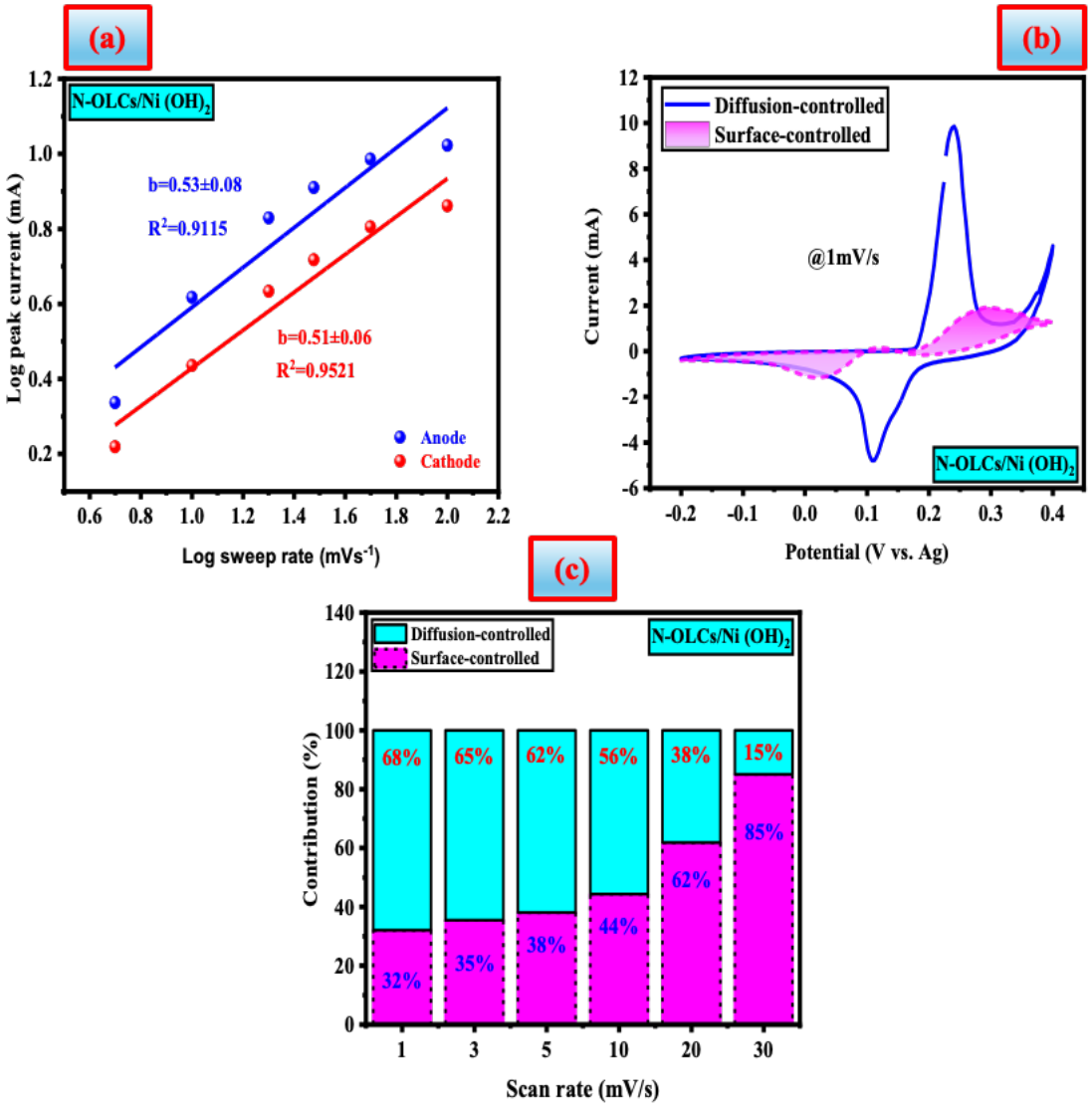


Figure 5. 10: (a) Randles-Sevcik plot for N-OLCs/Ni (OH)₂ (b) Trasatti and Dunn differentiation method for N-OLCs/Ni (OH)₂ (c) Histogram for percentage contributions of Faradaic and non-Faradaic process for N-OLCs/Ni (OH)₂.

5.3. Cyclic voltammetry for two electrode system for N-OLCs/Ni $(OH)_2$

Electrochemical evaluations in a two-electrode setup (full cell) were conducted in utilizing a biological SP 300 potentiostat, operated with EC-LAB version 11.52 software. The experiment to acquire the CV curves was performed in a 6M KOH solution, and a comparison was made. To enhance comprehension of the battery-type electrode potential of the N-OLCs/Ni $(OH)_2$, a hybrid supercapacitor (HSC) was constructed. The N-OLCs/Ni $(OH)_2$ was the positive electrode (cathode) and AcOx-OLC as the negative electrode (anode). For the fabrication of the asymmetric device, it is essential to perform the mass balancing according to **Equation 2.15 (Chapter 2).** The mass ratio was found to be 2.68 using the CV profiles of AcOx-OLCs and N-OLCs/Ni$(OH)_2$ obtained from three-electrode systems. For the configuration of the asymmetric device, the electrode mass utilized for the cathode electrode was 1.5 mg, while for the anode was 4.1mg with an active mass being 5.04 mg. This means that the anode AcOx-OLCs should have approximately 2.68 times more mass than the cathode N-OLCs/Ni $(OH)_2$ to maintain charge balance in the asymmetric cell.

The voltage ranges of the N-OLCs/Ni $(OH)_2$ and AcOx-OLCs electrodes at different scan rates are depicted in **Figure 5. 11b**. The charge balance of the two electrode system was considered using the **Equation 5.3**:

$$q^+ = q^- \qquad \textit{Eqn 5. 3}$$

The calculated (0.0019 C) charge imbalance between the electrodes may be attributed to several factors, including an improper mass ratio between the anode and cathode, differences in electrochemical behavior, and discrepancies between theoretical and practical capacitance values.

Pseudocapacitive materials such as Ni $(OH)_2$ often exhibit slower charge–discharge kinetics compared to electric double-layer capacitive (EDLC) materials like carbon, leading to kinetic mismatches [34]. Additionally, capacitance measured in three-electrode systems may overestimate performance in full-cell configurations due to internal resistance and electrode–electrolyte interactions[35].

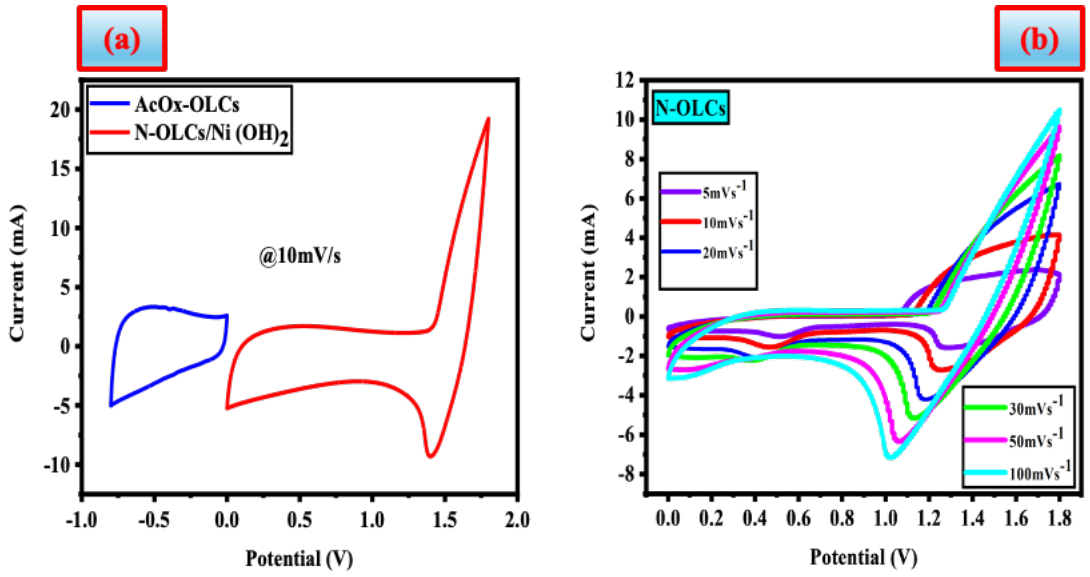


Figure 5. 11: (a) CV graph combination of three-electrode system AcOx-OLCs and two- Electrode system N-OLCs/Ni $(OH)_2$. (b) Two-electrode system CV graphs for N-OLCs/Ni $(OH)_2$ at different scan rates

These factors collectively contribute to unequal charge storage in the asymmetric device. CV parameters over several voltage ranges were employed to assess the constant electrochemical range of the HSC. The HSC employs two electrodes with differing potentials to elevate the operational voltage of its apparatus, hence achieving a greater density. The electrochemical

function of the HSC components was further examined within a potential range of (0.0 - 1.8V), utilizing CV measurements conducted at diverse scan speeds and current densities. The CV curves for N-OLCs/Ni $(OH)_2$ indicated that the energy storage mechanism resembles a battery-type electrode. The outcomes shown in **Figure 5.11b** indicate that doping with nitrogen has augmented the electrochemical performance of the pure material, leading to an enhanced specific capacitance.

The CV curves of AcOx-OLCs//N-OLCs/Ni $(OH)_2$ asymmetric cell exhibited increased current densities as illustrated in **Figure 5.11b**, suggesting that the expanded surface area of 260 m^2/g offered additional active sites for electrochemical processes, hence augmenting the total current densities depicted in the CV graph presented in **Figure 5.11b**. Incorporating nitrogen atoms into the carbon framework may enhance electrical conductivity, while these nitrogen atoms promote superior contact with nickel hydroxide, resulting in increased charge transfer and electrochemical activity[36].

The AcOx-OLCs anode electrode was compared to the N-OLCs/Ni $(OH)_2$ at a scan rate of 10 mV/s, as depicted in **Figure 5.11a**. Both materials preserved their forms, of which N-OLCs/Ni $(OH)_2$ maintained a quasi-rectangular shape with the characteristic behavior of psuedocapacitor. In contrast, AcOx-OLCs maintained a quasi-rectangular shape with the characteristic behavior of electrochemical double-layer capacitance at that rate. **Figure 5.11b** depicts the CV curves for N-OLCs/Ni $(OH)_2$ retained a consistent form at elevated scan rates of 100 mV/s, demonstrating favorable capacitive behavior and suggesting that this material is an attractive candidate for high-rate supercapacitor applications.

5.3.1. Galvanostatic charge-discharge, specific capacity, electrochemical impedance spectroscopy, bode plots, cyclic performance plot

To enhance comprehension of the battery-like electrode potential of the N-OLCs/Ni $(OH)_2$, a hybrid supercapacitor (HSC) was constructed. The N-OLCs/Ni $(OH)_2$ and AcOx-OLCs served as the positive and negative electrodes to build a straightforward HSC framework in a 6M KOH electrolyte. The HSC employs two electrodes with differing potentials to augment the device's operating voltage, achieving greater density. The electrochemical performance of the HSC device was further examined within a potential range of 0.0 - 1.8 V, with GCD curves at varied current densities illustrated in **Figure 5.12a**.

All GCD asymmetrical curves attained a maximum potential of 1.8V, signifying the elevated Coulombic efficiency of the device. **Figure 5.12b** illustrates the specific capacitance of N-OLCs/Ni $(OH)_2$ at various scan rates, while **Table 5.3** presents the recorded specific capacity values corresponding to these scan rates. The specific capacity at a scan rate of 0.1 A/g was 20.38 mAh/g, whereas at a scan rate of 2.0 A/g, it was 5.15 mAh/g as recorded in **Table 5.3**. The reduction in specific capacity may be ascribed to the fact that at lower current density, ions have adequate time to flow into the porous architecture of the N-OLCs/Ni $(OH)_2$ electrode, facilitating optimal utilization of the active sites[16]. At elevated current densities, ion diffusion is constrained, preventing ions from penetrating deeply into the pores. This results in diminished active material utilization and reduced specific capacitance, as illustrated in **Table 5.3**. Cycling stability is crucial for any electrochemical energy storage system[37]. **Figure 5.12d** illustrates the capacitive

retention and Coulombic efficiency of the AcOx-OLC//N-OLCs/Ni $(OH)_2$ device evaluated at 1.0 A/g within a voltage window of 0.0 to 1.8 V.

Following 1000 charge/discharge cycles, the HSC device demonstrated cycle stability with a capacity retention of 22.45% and a high Coulombic efficiency of roughly 97.61%, as depicted in **Figure 5.12d**. The substantial decline in capacity retention may be ascribed to the deterioration of the underlying structure of the N-OLCs/Ni $(OH)_2$, resulting in reduced capacity. Repeated cycling may lead to the electrolyte's decomposition, impacting the electrode material's overall performance and stability. Side reactions during cycling can generate by-products obstructing active sites or elevating internal resistance, diminishing capacitance[38]. Developing a passivation layer on the electrode surface may impede ion transport, diminishing the effective surface area for charge storage. Additionally, nickel hydroxide may experience phase transitions or dissolution during cycling, adversely affecting its capacitance retention[39].

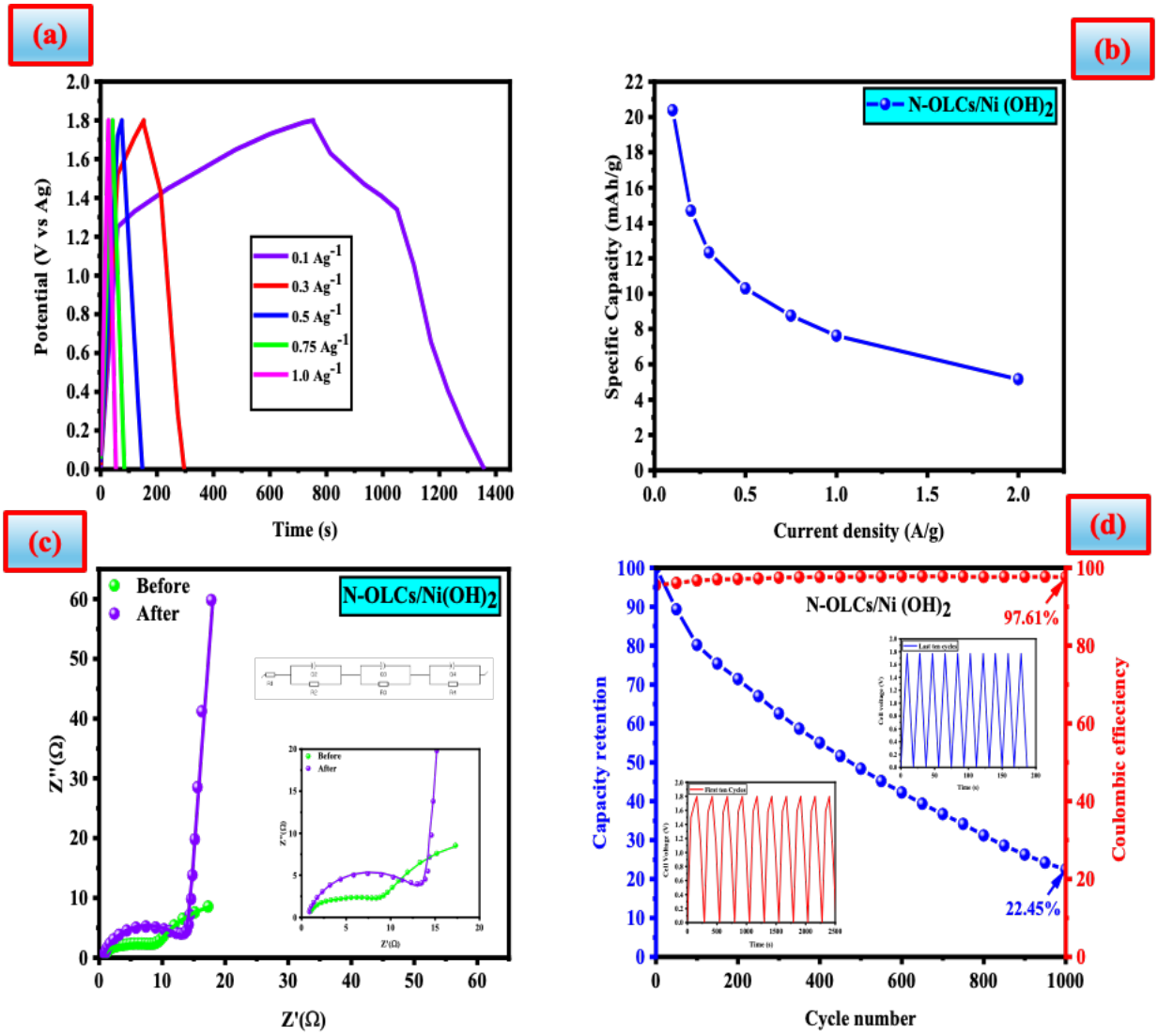


Figure 5. 12: (a) GCD graphs for N-OLCs/Ni (OH)₂ (b) Specific Capacity graph for N-OLCs/Ni (OH)₂ (c) Nyquist plot obtained before and after 6000 cycles and a series circuit of N-OLCs/Ni (OH)₂ (d) Electrochemical performance for N-OLCs/Ni (OH)₂.

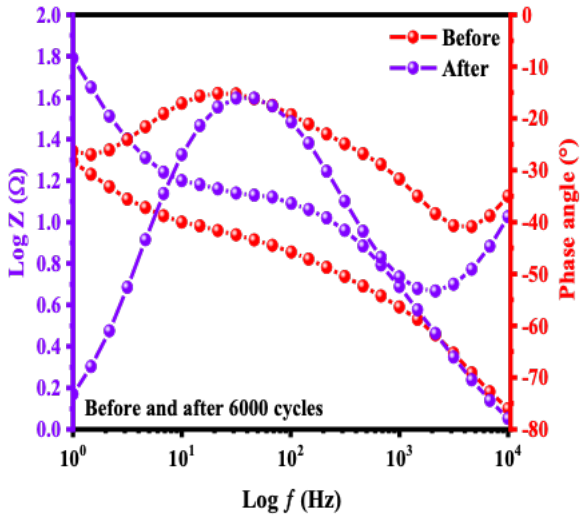


Figure 5. 13: Bode plots comparison obtained before and after 6000 cycles for N-OLCs/Ni (OH)₂

Electrochemical impedance spectroscopy (EIS) can elucidate interfacial electrochemistry and characterize the cycling stability of materials. **Figure 5.12c** illustrates the Nyquist plots obtained before and after 6000 cycles. The simple Randles electrical equivalent circuit modeled the EIS parameters before and after 6000 cycles.

Table 5. 3: Specific capacity at different current densities for the two-electrode device

Material	Specific capacity at different current densities						
	0.1 A/g	0.2 A/g	0.3 A/g	0.5 A/g	0.75 A/g	1 A/g	2 A/g
N-OLCs/Ni $(OH)_2$	20.38 mAh/g	14.69 mAh/g	12.32 mAh/g	10.30 mAh/g	8.75 mAh/g	7.62 mAh/g	5.15 mAh/g

Specific capacities shown in **Table 5.3** were calculated using the **Equation 5.4**:

$$C_s = \frac{Q}{m} \qquad Eqn\ 5.4$$

Where:

Q =charge/discharge $capacity$ (mAh)

$m = Active\ mass\ (g)$

Figure 5.12c encompasses the bulk resistance R_s resulting from the aggregate resistances of electrolytes, electrodes, current collectors, and separators, the charge-transfer resistance R_{ct} associated with electron transport, interfacial resistance R_{int} attributed to IR drop and the constant phase element CPE arising from the inhomogeneous or irregular structure of the electrode surfaces, as previously elucidated.

The modelled characteristics are presented in **Table 5.4**, including the R_s and R_{ct} values before and after cycling. Before 6000 cycles, the R_s value was 0.6858 Ohms, whereas after 6000 cycles, the R_s value decreased to 0.6508 Ohms. The R_{ct} value before 6000 cycles was 7.217 Ohms, whereas after 6000 cycles, the R_{ct} value increased to 13.3 Ohms. The reduction in R_s may indicate a minor enhancement in the material's conductivity after 6000 cycles. This may result from enhanced contact between the active materials and the current collector or the developing of a more conductive network within the electrode.

Additionally, the gradual reduction of R_s over multiple cycles, which implies that the HSC preserves commendable electrochemical performance and facilitates more efficient charge transfer within the HSC. The substantial rise in R_{ct} indicates a decline in charge transfer efficiency inside

the HSC, potentially impacting the overall performance of the HSC, as illustrated in **Figure 5.12d** regarding capacity retention. The electrode's degradation may also be ascribed to the rise in R_{ct} , seen in **Table 5.4**, which could impact the overall stability of the HSC. Additionally, the $CPE\ a$ value before and after 6000 cycles were $a2$ (0.6512 to 0.8367), $a3$ (0.999 to 0.9567), and $a4$ (0.8271 to 0.371) as shown in **Table 5.4**.

Table 5.4 illustrates an increase in $a2$ signifies an enhancement in the material's capacitive performance. The slight decline in $a3$ suggests a minor reduction in ideal capacitive behavior, potentially due to the formation of resistive layers or degradation of the active material. The substantial decrease in $a4$ indicates a significant loss in capacitive behavior, as evidenced by the reduction in capacity retention illustrated in **Figure 5.12d**, likely resulting from the degradation of nickel hydroxide and the formation of insulating layers that impede charge storage[40].

Table 5. 4: EIS parameters for the two-electrode material

EIS parameters	N-OLCs/Ni $(OH)_2$ electrode material			
	Before 6000 cycles	**Standard deviation**	**After 6000 cycles**	**Standard deviation**
Rs/Ω	0.6858	± 0.0294	0.6508	± 0.02822
R_{ct}/Ω	7.217	± 0.2214	13.3	± 0.1156
Q2/ *CPE* F. s^(*a*-1)	1.474×10^{-3}	$\pm 1.036\times 10^{-4}$	1.292×10^{-4}	$\pm 6.772\times 10^{-6}$
a2	0.6512	± 0.01358	0.8367	$\pm 6.221\times 10^{-3}$
R_{int}/Ω	1.592	± 0.07869	2.13×10^{-34}	$\pm 1.927\times 10^{-47}$
Q3/ *CPE* F. s^(*a*-1)	49.81×10^{-5}	$\pm 3.05\times 10^{-6}$	2.908×10^{-3}	$\pm 2.66\times 10^{-5}$
a3	0.9999	$\pm 1.57\times 10^{-3}$	0.9567	$\pm 3.243\times 10^{-3}$
R_{int}/Ω	23.9	± 1.05	7.138	± 2.772
Q4/ *CPE* F. s^(*a*-1)	0.0138	$\pm 5.527\times 10^{-4}$	1.185×10^{-28}	$\pm 2.056\times 10^{-35}$
a4	0.8271	± 0.01729	0.3142	± 0.01715
Phase angle	-26.15°	-	-73.28°	-

The alterations in the CPE parameters, as shown in **Table 5.4**, indicate that the Electrode-Electrolyte Interface (EEI) experienced substantial structural modifications over time, resulting in diminished capacity retention in the HSC. This degradation of the EEI caused a loss of active sites due to obstruction, thereby decreasing the overall capacitance and efficiency of the HSC. The alterations in CPE parameters indicate the EEI layer's dynamic characteristics, wherein initial capacity performance enhancements are eclipsed by prolonged deterioration and a decline in electrochemical efficiency[41].

Figure 5.13 illustrates the Bode plot of N-OLCs/Ni $(OH)_2$ before and after 6000 cycles. The phase angle of -26.15° indicates a blend of resistive and capacitive characteristics, signifying adequate charge storage and transmission, as shown in **Table 5.4**. After 6000 cycles, the phase angle markedly diminishes to -73.28°, signifying a transition towards increased capacitive behavior as recorded in **Table 5.4**. This indicates that the material's charge storage capacity has been impaired, probably due to the deterioration of the active components and the development of resistant layers[11]. The notable alteration in phase angle at low frequencies signifies a decline in capacitive behavior, directly affecting the material's capacity to store and release charge effectively. The modifications in phase angle at elevated frequencies indicate a rise in internal resistance, resulting in increased energy losses and diminished overall performance of the HSC[27].

5.3.2. The Ragone Plot of N-OLCs/Ni $(OH)_2$

The Ragone plot of the HSC device was examined, as illustrated in **Figure 5.14**. The AcOx-OLCs//N-OLCs/Ni $(OH)_2$ device demonstrates an elevated energy density of 18.34 Wh/Kg and a power density of 108.20 W/Kg at a current density of 0.1 A/g over discharging time of 610.05s. At a current density of 2 A/g, the energy density was 4.64 Wh/Kg, and the power density was 1856 W/kg over discharge time of 9.2s, as seen in **Table 5.5**. the energy density and power densities at scan rate 0.1 A/g were considered with the **Equation 2.35 and 2.36** in **Chapter 2**, respectively. A specific capacity of 20.38 mAh/g corresponds to a specific capacitance of 40.76 F/g over a 1.8V voltage window. To compute the energy density of the hybrid supercapacitor with a specific capacitance of 40.76 F/g operating within a 1.8V voltage window, **Equation 2.35** was used, then, energy density was used to find the power density using **Equation 2.36.** At this low current density (0.1 A/g), the energy density is elevated at 18.34 Wh/kg and power density 108.20 W/kg due to ions having adequate time to flow into the electrode material, facilitating optimal utilization of the active sites [42]. This signifies a substantial contribution from diffusion-controlled processes linked to psuedocapacitance (battery-type energy storage). As the current density escalates, energy density diminishes, but power density amplifies to 1856 W/kg and energy density to 4.64 Wh/kg at current density of 2.00 A/g, as depicted in **Figure 5.15 and Table 5.5**. This indicates a transition towards expedited charge-discharge cycles, characterized by a combination of diffusion-controlled and surface-controlled processes [43].

The energy density further diminishes, whereas the power density escalates, as illustrated in **Table 5.5**. The electrochemical performance is governed by a surface-controlled mechanism

characterized by fast ion adsorption and desorption at the electrode interface. At the maximum current density, the energy density is minimized while the power density is maximized. The charge storage is generally governed by a surface-controlled process, signifying that ions predominantly interact with the electrode material's surface, with minimal diffusion into the bulk[44].

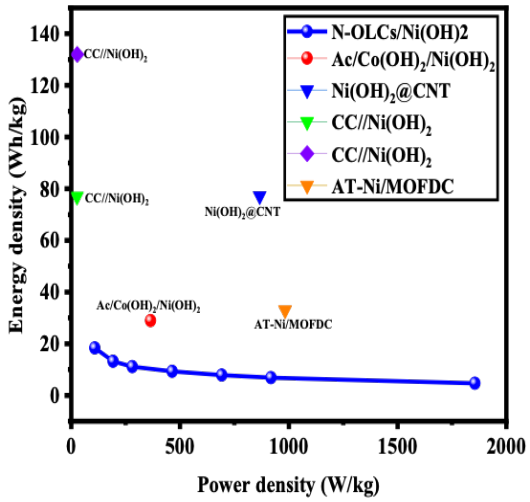


Figure 5. 14: Ragone plot for N-OLCs/Ni (OH)₂ (Energy density vs Power density)

The energy storage is predominantly diffusion-controlled at a current density of 0.1 to 0.2 A/g, as illustrated in **Table 5.5**, and is linked to psuedocapacitance (battery-type storage device). This pertains to Faradaic processes in which ions intercalate into the electrode material, enhancing energy density. At an elevated current density of 0.3 to 2 A/g, as illustrated in **Table 5.5**, energy storage is primarily governed by surface mechanisms linked to electric double-layer capacitance (EDLC). This entails the adsorption of ions onto the electrode material's surface, which occurs more rapidly but yields a reduced energy density[45].

The results were juxtaposed with existing literature, as illustrated in **Figure 5.14**. For Ac/Co $(OH)_2$/Ni $(OH)_2$//Ac, the power density was 364.5 W/Kg, and the energy density was 28.9 Wh/Kg [12]. The energy density of Ni $(OH)_2$@CNT was 77.2 Wh/Kg, while the power density was 866 W/Kg [46]. The power densities for CC//Ni $(OH)_2$ utilized as both anode and cathode in various devices were 26.6 W/Kg and 27.7 W/Kg, while the energy densities were 77 Wh/Kg and 132.7 Wh/Kg, respectively[5].

Table 5. 5: Energy density vs power density data at different current densities

Current density (A/g)	Energy density (Wh/Kg)	Power density (W/Kg)
0.1	18.34	108.2
0.2	13.20	192.79
0.3	11.08	281.22
0.5	9.27	464.20
0.75	7.88	692.44
1	6.86	918.09
2	4.64	1856

For AT-Ni/MOFDC, the energy density was 33 Wh/Kg , while the power density was 983 W/Kg [11]. The Ragone data in **Table 5.5** and **Figure 5.14** illustrates the trade-off between energy and power density in hybrid supercapacitors. The N-OLCs/Ni $(OH)_2$ demonstrated commendable performance at various current densities. Rendering is adaptable for many uses.

5.4. Summary

The flame pyrolysis approach was effectively employed to synthesize onion-like carbon, which was later investigated and functionalized to produce Ox-OLCs, followed by nitrogen doping using melamine to obtain N-OLCs. Subsequently, it was adorned with nickel hydroxide to produce N-OLCs/Ni $(OH)_2$. Compared to Ox-OLCs/Ni $(OH)_2$, B-OLCs/Ni $(OH)_2$, and B, N-OLCs/Ni $(OH)_2$, N-OLCs/Ni $(OH)_2$ demonstrates enhanced physicochemical and electrochemical properties. N-OLCs/Ni $(OH)_2$ exhibits superior battery-like energy retention in a three-electrode setup, with reduced series resistance and enhanced specific capacity. Non-Faradaic and Faradaic mechanisms have been demonstrated to regulate the energy retention mechanism of N-OLCs/Ni $(OH)_2$. At a current density of 0.1 A/g, the constructed AcOx-OLCs//N-OLCs/Ni $(OH)_2$ hybrid unit exhibits a specific capacity of 20.38 mAh/g. The HSC exhibits an energy density of 18.34 Wh/Kg and a power density of 108.20 W/Kg at a current density of 0.1 A/g, and an energy density of 4.64 Wh/Kg with a power density of 1856 W/Kg at a current density of 2.0 A/g, alongside a cycling performance of 22.45% capacity retention after 1000 cycles. This research introduces a novel approach for exploring metal hydroxide to produce high-performance battery-type energy storage materials with functionalized doped onion-like carbon as a support material.

5.5. References

[1] W. Gu and G. Yushin, "Review of nanostructured carbon materials for electrochemical capacitor applications: advantages and limitations of activated carbon, carbide-derived carbon, zeolite-templated carbon, carbon aerogels, carbon nanotubes, onion-like carbon, and graphene," *WIREs Energy and Environment*, 3, pp. 424–473, Sep. 2014, doi: 10.1002/wene.102.

[2] P. Simon and Y. Gogotsi, "Materials for electrochemical capacitors," *Nat. Mater.*, vol. 7, pp. 845–854, Nov. 2008. [Online]. Available: https://doi.org/10.1038/nmat2297

[3] T. S. Mathis, N. Kurra, X. Wang, D. Pinto, P. Simon, and Y. Gogotsi, "Energy storage data reporting in perspective—Guidelines for interpreting the performance of electrochemical energy storage systems," *Adv. Energy Mater.*, 9, Art. no. 1902007, Oct. 2019. [Online]. Available: https://doi.org/10.1002/aenm.201902007

[4] F. Béguin, V. Presser, A. Balducci, and E. Frackowiak, "Carbons and Electrolytes for Advanced Supercapacitors," *Advanced Materials*, 26, pp. 2219–2251, Apr. 2014, doi: 10.1002/adma.201304137.

[5] M. M. Ovhal, N. Kumar, S. K. Hong, H. W. Lee, and J. W. Kang, "Asymmetric supercapacitor featuring carbon nanotubes and nickel hydroxide grown on carbon fabric: A study of self-discharging characteristics," *J Alloys Compd*, 828, Art no. 154447, Jul. 2020, doi: 10.1016/J.JALLCOM.2020.154447.

[6] Y. Jiao *et al.*, "Mixed-metallic MOF based electrode materials for high performance hybrid supercapacitors," *J Mater Chem A Mater*, 5, pp. 1094–1102, 2017, doi: 10.1039/C6TA09805C.

[7] S. B. Ma *et al.*, "A novel concept of hybrid capacitor based on manganese oxide materials," *Electrochem commun*, 9, pp. 2807–2811, Dec. 2007, doi: 10.1016/J.ELECOM.2007.09.015.

[8] V. Ruiz, C. Blanco, E. Raymundo-Piñero, V. Khomenko, F. Béguin, and R. Santamaría, "Effects of thermal treatment of activated carbon on the electrochemical behaviour in supercapacitors," *Electrochim. Acta*, 52, pp. 4969-4973, Apr. 2007, doi: 10.1016/j.electacta.2007.01.071. [Accessed: Mar. 9, 2025].

[9] E. R. Nightingale, "Phenomenological Theory of Ion Solvation. Effective Radii of Hydrated Ions," *J Phys Chem*, 63, pp. 1381–1387, Sep. 1959, doi: 10.1021/j150579a011.

[10] K. Naoi, W. Naoi, S. Aoyagi, J. I. Miyamoto, and T. Kamino, "New generation 'nanohybrid supercapacitor,'" *Acc Chem Res*, 46, pp. 1075–1083, May 2013, doi: 10.1021/ar200308h.

[11] T. P. Mofokeng, "Hierarchical nitrogen-doped carbon nanotube-carbon nanofiber-based networks for electrochemical capacitors," M.S. thesis, Dept. Chem. Sci., Univ. Johannesburg, Johannesburg, South Africa, 2021. [Online]. Available: https://ujcontent.uj.ac.za/. [Accessed: Mar. 9, 2025].

[12] Y. Li et al., "Sandwich-like activated carbon/$Co(OH)_2$/$Ni(OH)_2$ composites prepared by electrodeposition for high-performance supercapacitors," *J. Energy Storage*, 112, Art. no. 115529, Mar. 2025. [Online]. Available: https://doi.org/10.1016/j.est.2025.115529

[13] X. Yi, C. Kirk, and N. Robertson, "Nickel hydroxide-based energy storage devices: nickel-metal hydride batteries vs. nickel hydroxide hybrid supercapacitors," *Carbon Neutrality*, 3, Art. no. 39, Dec. 2024. [Online]. Available: https://doi.org/10.1007/s43979-024-00114-7

[14] A. Shaikh, B. K. Singh, D. Mohapatra, and S. Parida, "Nitrogen-Doped Carbon Nano-Onions as a Metal-Free Electrocatalyst," *Electrocatalysis*, 10, pp. 222–231, May 2019, doi: 10.1007/s12678-019-00514-9.

[15] M. Serhan, M. Sprowls, D. Jackemeyer, M. Long, I. D. Perez, W. Maret, N. Tao, and E. Forzani, "Total iron measurement in human serum with a smartphone," in *2019 AIChE Annual Meeting*, American Institute of Chemical Engineers, 2019. [Online]. Available: https://doi.org/10.1039/x0xx00000x. Accessed: Feb. 18, 2025.

[16] X. Yi, C. Kirk, and N. Robertson, "Nickel hydroxide-based energy storage devices: nickel-metal hydride batteries vs. nickel hydroxide hybrid supercapacitors," *Carbon Neutrality*, 3, Art. no. 39, Dec. 2024. [Online]. Available: https://doi.org/10.1007/s43979-024-00114-7.

[17] D. Hulicova-Jurcakova, M. Kodama, S. Shiraishi, H. Hatori, Z. H. Zhu, and G. Q. Lu, "Nitrogen-enriched nonporous carbon electrodes with extraordinary supercapacitance," *Adv Funct Mater*, 19, pp. 1800–1809, Jun. 2009, doi: 10.1002/adfm.200801100.

[18] U. S. Kodithuwakku, N. Wanninayake, M. P. Thomas, B. S. Guiton, and D. Y. Kim, "Unlocking efficiency in oxygen reduction reaction: Synergistic edge dopants of nitrogen and boron in carbon nano onions," *Electrochim. Acta*, 471, Art. no. 143365, Dec. 2023. [Online]. Available: https://doi.org/10.1016/j.electacta.2023.143365

[19] A. Camisasca, A. Sacco, R. Brescia, and S. Giordani, "Boron/Nitrogen-Codoped Carbon Nano-Onion Electrocatalysts for the Oxygen Reduction Reaction," *ACS Appl Nano Mater*, 1, pp. 5763–5773, Oct. 2018, doi: 10.1021/acsanm.8b01430.

[20] N. M. Musyoka, B. K. Mutuma, and N. Manyala, "Onion-derived activated carbons with enhanced surface area for improved hydrogen storage and electrochemical energy application," *RSC Adv*, 10, pp. 26928–26936, Jul. 2020, doi: 10.1039/d0ra04556j.

[21] Y. Lin, Y. Zhu, B. Zhang, Y. A. Kim, M. Endo, and D. S. Su, "Boron-doped onion-like carbon with enriched substitutional boron: The relationship between electronic properties and catalytic performance," *J Mater Chem A Mater*, 3, pp. 21805–21814, 2015, doi: 10.1039/c5ta03141a.

[22] A. Camisasca, A. Sacco, R. Brescia, and S. Giordani, "Boron/Nitrogen-Codoped Carbon Nano-Onion Electrocatalysts for the Oxygen Reduction Reaction," *ACS Appl Nano Mater*, 1 , pp. 5763–5773, Oct. 2018, doi: 10.1021/acsanm.8b01430.

[23] S. Rathinavel, K. Priyadharshini, and D. Panda, "A review on carbon nanotube: An overview of synthesis, properties, functionalization, characterization, and the application," *Mater. Sci. Eng. B*, 268, Art. no. 115095, Jun. 2021. [Online]. Available: https://doi.org/10.1016/j.mseb.2021.115095

[24] F. Rafik, H. Gualous, R. Gallay, A. Crausaz, and A. Berthon, "Frequency, thermal and voltage supercapacitor characterization and modeling," *J Power Sources*, 165, pp. 928–934, Mar. 2007, doi: 10.1016/j.jpowsour.2006.12.021.

[25] T. P. Mofokeng, Z. N. Tetana, and K. I. Ozoemena, "Defective 3D nitrogen-doped carbon nanotube-carbon fibre networks for high-performance supercapacitor: Transformative role of nitrogen-doping from surface-confined to diffusive kinetics," *Carbon N Y*, 169, pp. 312–326, Nov. 2020, doi: 10.1016/j.carbon.2020.07.049.

[26] Y.-R. Wang et al., "Superhydrophilic nickel hydroxide ultrathin nanosheets enable high-performance asymmetric supercapacitors," *Rare Metals*, 43, Art. no. 138, Nov. 2023. [Online]. Available: https://doi.org/10.1007/s12598-023-02386-x.

[27] X. F. Sánchez-Romate, A. Del Bosque, J. Artigas-Arnaudas, B. K. Muñoz, M. Sánchez, and A. Ureña, "A proof of concept of a structural supercapacitor made of graphene coated woven

carbon fibers: EIS study and mechanical performance," *Electrochim. Acta*, 370, Art. no. 137746, Jan. 2021, doi: 10.1016/j.electacta.2021.137746. [Accessed: Mar. 9, 2025].

[28] M. Catelani *et al.*, "Experimental Characterization of Hybrid Supercapacitor Under Different Operating Conditions Using EIS Measurements," *IEEE Trans Instrum Meas*, 73, Art no. 2024, 2023, doi: 10.6084/m9.figshare.24321496.

[29] A. D. Su *et al.*, "Hierarchical porous nickel oxide–carbon nanotubes as advanced pseudocapacitor materials for supercapacitors," *Chem Phys Lett*, 561–562, pp. 68–73, Mar. 2013, doi: 10.1016/J.CPLETT.2013.01.023.

[30] A. K. Mondal, D. Su, S. Chen, B. Sun, K. Li, and G. Wang, "A simple approach to prepare nickel hydroxide nanosheets for enhanced pseudocapacitive performance," *RSC Adv*, 4, pp. 19476–19481, 2014, doi: 10.1039/c4ra01719f.

[31] D. Harvey, *Modern Analytical Chemistry* (formerly *Instrumental Analysis*), LibreTexts, 2020. [Online].

Available: https://chem.libretexts.org/Bookshelves/Analytical_Chemistry. [Accessed: Mar. 9, 2025].

[32] J. C. Dunn, "A Fuzzy Relative of the ISODATA Process and Its Use in Detecting Compact Well-Separated Clusters," *J. Cybern.*, 3, pp. 32-57, 1973, doi: 10.1080/01969727308546046.

[33] G. Macias, "Understanding the Randles-Sevcik Equation: A Powerful Tool for Electrochemistry Research," *Electrochem. Sci. Adv.*, 3, Art. no. e2200213, 2023, doi: 10.1002/elsa.202200213.

[34] W. Zuo, R. Li, C. Zhou, Y. Li, J. Xia, and J. Liu, "Battery-supercapacitor hybrid devices: Recent progress and future prospects," *Adv. Sci.*, 4, Art. no. 1600539, Jul. 2017. [Online]. Available: https://doi.org/10.1002/advs.201600539.

[35] S. E. Berrabah, A. Benchettara, F. Smaili, A. Benchettara, and A. Mahieddine, "High performance hybrid supercapacitor based on electrochemical deposed of nickel hydroxide on zinc oxide supported by graphite electrode," *J Alloys Compd*, 942, Art no. 169112, May 2023, doi: 10.1016/J.JALLCOM.2023.169112.

[36] D. Hulicova-Jurcakova, M. Kodama, S. Shiraishi, H. Hatori, Z. H. Zhu, and G. Q. Lu, "Nitrogen-enriched nonporous carbon electrodes with extraordinary supercapacitance," *Adv Funct Mater*, 19, pp. 1800–1809, Jun. 2009, doi: 10.1002/adfm.200801100.

[37] K. Watanabe, T. Kikuoka, and N. Kumagai, "Physical and electrochemical characteristics of nickel hydroxide as a positive material for rechargeable alkaline batteries," *J. Appl. Electrochem.*, 25, pp. 219–226, Mar. 1995, doi: 10.1007/BF00262956. [Accessed: Mar. 10, 2025].

[38] C. K. Sarangi, G. L. Achary, T. Subbaiah, R. K. Paramguru, and S. K. Roy, "Role of electrochemical precipitation parameters in developing mixed-phase battery-grade nickel hydroxide," *Electrochem*, 6, Art. no. 2, Jan. 2025. [Online]. Available: https://doi.org/10.3390/electrochem6010002.

[39] M. Wu, S. Xie, and Y. Zhou, "Enhancing safety and performance of hybrid supercapacitors through material system optimization," *Ionics (Kiel)*, Dec. 2024. [Online]. Available: https://doi.org/10.1007/s11581-024-05895-6. Accessed: Feb. 18, 2025.

[40] M. Libber, N. Gariya, and M. Kumar, "A comprehensive analysis of supercapacitors with current limitations and emerging trends in research," *J. Solid State Electrochem.*, 29, pp. 513–527, Oct. 2024. [Online]. Available: https://doi.org/10.1007/s10008-024-06107-x. Accessed: Aug. 18, 2025.

[41] I. Letchumanan, C. P. Leo, S. Y. Pung, C. M. Koe, N. Shaari, and Y. N. Yusoff, "Fabrication of hybrid tin oxide-cellulose nanocomposite as the flexible and thin supercapacitor," *Energy Storage*, 6, Feb. 2024, doi: 10.1002/est2.508.

[42] BioLogic, "EC-Lab Application Note #06: Electrochemical Impedance Spectroscopy (EIS) - Theory and Applications," Bio-Logic SAS, Seyssinet-Pariset, France, AN-06, 2005. [Online]. Available: https://www.biologic.net/topics/media/application-notes/. [Accessed: Mar. 9, 2025].

[43] A. S. Raut, C. B. Parker, and J. T. Glass, "A method to obtain a Ragone plot for evaluation of carbon nanotube supercapacitor electrodes," *J Mater Res*, 25, pp. 1500–1506, Aug. 2010, doi: 10.1557/jmr.2010.0192.

[44] R. Vicentini *et al.*, "Ragone Plots for Electrochemical Double-Layer Capacitors," *Batter Supercaps*, 4, pp. 1291–1303, Aug. 2021, doi: 10.1002/batt.202100093.

[45] A. Allagui, M. E. Fouda, and A. S. Elwakil, "Communication—The Ragone Plot of Supercapacitors Under Different Loading Conditions," *J Electrochem Soc*, 167, p. 020533, Jan. 2020, doi: 10.1149/1945-7111/ab6bb9.

[46] M. Thangarasu *et al.*, "Porous 3D honeycomb structures formed from interconnected Ni(OH2) sheets on CNT-coated hybrid framework as high-performance electrodes for supercapacitors," *J Energy Storage*, 83, Art no. 110766, Apr. 2024, doi: 10.1016/j.est.2024.110766.

Chapter 6

Conclusions and recommendation

6.1. Conclusions

- The synthesis of onion-like carbons (OLCs) through flame pyrolysis was accomplished effectively, subsequently leading to functionalisation, doping, and co-doping with boron and nitrogen, along with the integration of $Ni(OH)_2$ to create battery-type electrodes. The thorough characterisation utilising BET, XRD, XPS, TEM, SEM, and Raman techniques validated the intended structural, morphological, and compositional attributes.

- The electrochemical performance of the AcOx-OLC//N-OLCs/$Ni(OH)_2$ asymmetric supercapacitor in a 6 M KOH solution demonstrated impressive energy and power densities of 18.34 Wh/kg and 108.20 W/kg at a current density of 0.1 A/g, although a decline in performance was observed at elevated current densities. The co-doping of B and N in $Ni(OH)_2$ composites resulted in an improved capacity and reduced resistance when compared to samples that were either singly doped or oxidised.

- The effects of doping reveal that nitrogen doping and B,N co-doping markedly enhance electrochemical performance by improving electrical conductivity, optimising pore structure, and facilitating synergistic Faradaic and non-Faradaic charge storage mechanisms. Conversely, B-OLCs/$Ni(OH)_2$ and Ox-OLCs/$Ni(OH)_2$ exhibited diminished

capacitance and cycling stability, highlighting the significance of nitrogen in enhancing performance.

- The AcOx-OLC//N-OLCs/$Ni(OH)_2$ device exhibited a retention of merely 22.45% capacity following 1000 cycles, a decline likely attributable to material degradation, irreversible reactions, or loss of contact. Future investigations ought to concentrate on enhancing structural integrity, refining interfaces, and devising more resilient electrode architectures to ensure sustained long-term performance.

6.2. Future Works and Recommendations

Further study is required to improve the synthesized materials' electrochemical characteristics and practical uses. The subsequent recommendations and prospective research avenues are suggested:

- Enhance Operating Conditions for Durability: Examine the ideal voltage range in KOH electrolyte for N-OLCs/Ni $(OH)_2$ electrodes to reduce structural deterioration, improve capacitance retention, and prolong cycling stability in practical operating scenarios. This ought to be accompanied by investigations into the reusability of electrolytes and the assembly of cells with minimal waste to enhance sustainability.
- Customize Composite Ratios and Assess Alternatives: Methodically analyze and evaluate different OLC/Ni $(OH)_2$ ratios to identify the composition that optimizes both energy and power densities. Simultaneously, synthesize nickel oxide (NiO) composites from Ni $(OH)_2$ precursors and evaluate their electrochemical performance against hydroxide-based

materials, considering the energy expenditure and environmental implications of each synthesis method.

- Advance Sustainable Synthesis Approaches: Seek low-energy, solvent-efficient, and economically viable synthesis techniques for boron-doped and boron–nitrogen co-doped OLCs to enhance scalability and commercial viability. It is imperative to prioritize the minimization of hazardous by-products, the integration of renewable feedstocks, and the enhancement of waste management practices.
- Improve the stability of anode materials via the principles of composite engineering: Incorporate N-OLCs/$Ni(OH)_2$ anode material alongside secondary stabilizing agents or coatings to enhance cycling stability, energy density, and power density. The choice of additives ought to emphasize materials that are environmentally friendly and cost-effective, ensuring that they do not substantially expand the process footprint.
- Broaden Utilization Examination of Nickel-Based Anodes: Considering their elevated power density and capacitance, evaluate N-OLCs/Ni $(OH)_2$ as anode materials within the context of more extensive electrochemical devices. It is essential for comparative studies involving other nickel-based materials to include life cycle and techno-economic analyses to assess their long-term industrial viability.
- Conduct an advanced structural and compositional analysis through XPS examination of P-OLCs to attain a more profound understanding of functionalization and heteroatom integration, thereby informing the optimization of doping techniques. Whenever feasible, implement analytical protocols that reduce chemical waste and conserve energy.

- Investigate Advanced Techniques for Doping and Decoration: Examine diverse doping techniques and composite embellishment involving nitrogen, nickel oxide, and nickel hydroxide, focusing on optimizing process efficiency and minimizing the necessity for high-temperature, high-energy synthesis procedures.
- Exhibit Practical Device Integration: Assess the feasibility of N-OLCs/Ni $(OH)_2$ electrodes in energizing small devices (e.g., LED bulbs) to confirm their real-world relevance. Prototyping must be paired with environmental impact assessments to guarantee scalability while minimizing energy and material waste.

Appendix A

Auxiliary data for chapter 4.

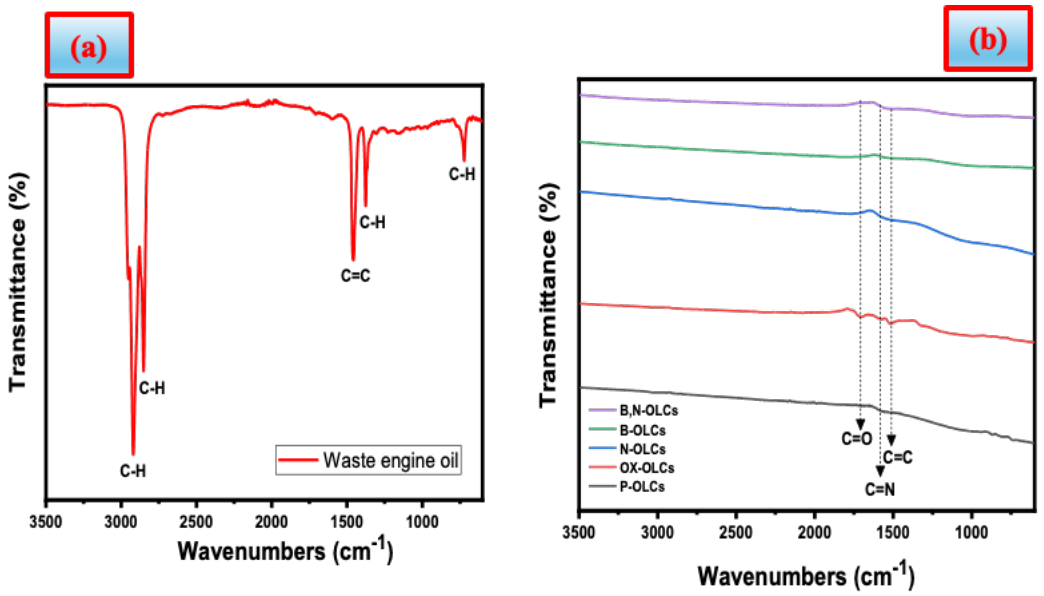


Figure S 1: Fourier transformed infrared (FTIR) of (a) waste engine oil, (b) onion-like carbons for (pristine, N-doped, B-doped, and B, N-co-doped)

Waste engine oil, the precursor for synthesizing onion-like carbon, was subjected to Fourier Transform Infrared (FTIR) examination. The aliphatic C-H stretching vibrations that correspond to the peaks at 2914 cm^{-1} and 2848 cm^{-1} in the waste oil's FTIR spectra indicate hydrocarbon molecules such as alkenes, alkanes, and alkynes. Additional peaks at 1453 cm^{-1}, 1373 cm^{-1}, and 718 cm^{-1} indicate the presence of C-H bending and C=C stretching vibrations, which are frequently present in materials derived from petroleum, as illustrated in **Figure S1(a)**. In their FTIR spectra, the resultant carbon nanomaterials showed peaks at 1704 cm^{-1}, 1586 cm^{-1}, and 1509 cm^{-1}. These are the functional groups C=C, nitrile (C=N), and carbonyl (C=O), respectively. A carbonyl group

indicates that the synthesized carbon structures have been oxidized or functionalized, as depicted in **Figure S1(b)**.

Appendix B

Auxiliary data for Chapter 5.

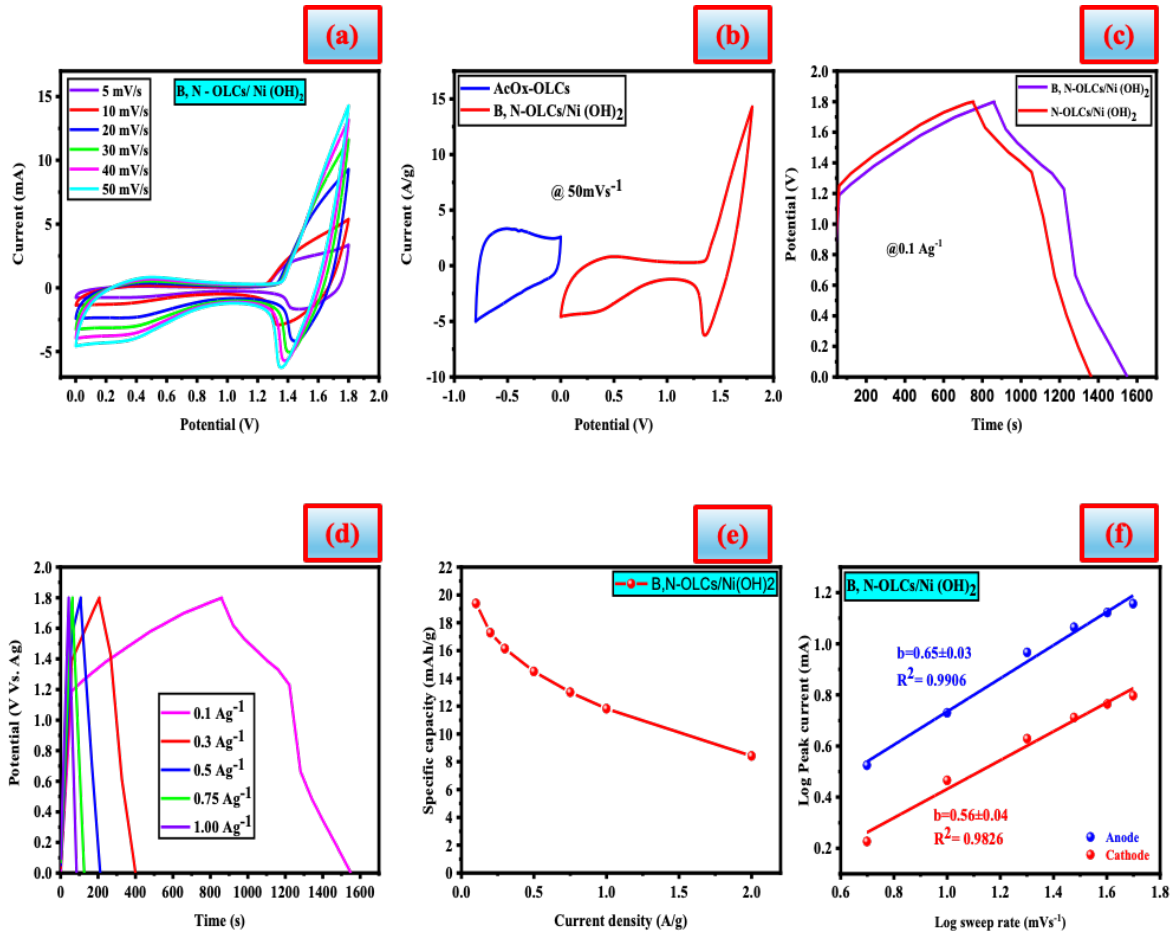


Figure S 2: Two electrode cell data for B, N-OLCs/Ni (OH)2 (a) CV data (b) CV comparison with the anode electrode material (AcOx-OLCs) (c) GCD plot comparison with N-OLCs/Ni $(OH)_2$ (d) GCD plot for B, N-OLCs/Ni $(OH)_2$ (e) specific capacitance graph (f) Log sweep rate vs. Log peak current graph

Appendix C

Auxiliary data for chapter 5

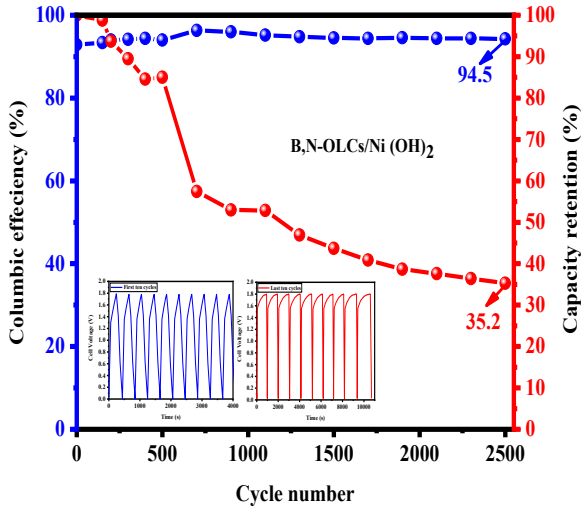


Figure S 3: capacity retention plot for B, N-OLCs/Ni $(OH)_2$ in two electrode cells